ScuDo
Scuola di Dottorato ~ Doctoral School
WHAT YOU ARE, TAKES YOU FAR

Doctoral Dissertation
Doctoral Program in Aerospace Engineering (31st cycle)

A Comprehensive Modeling Framework for Integrated Mission Analysis and Design of a Reusable Electric Space Tug

Martina Mammarella

* * * * * *

Supervisors
Prof. Giorgio Guglieri, Supervisor
Prof. Nicole Viola, Co-Supervisor

Doctoral Examination Committee:
Prof. Teodoro Alamo, Referee, University of Sevilla
Prof. Riccardo Scattolini, Referee, Politecnico di Milano
Prof. Kimon Valavanis, University of Denver
Prof. Paolo Maggiore, Politecnico di Torino
Prof. Alessandro Rizzo, Politecnico di Torino

Politecnico di Torino
February 11th, 2019

I hereby declare that, the contents and organization of this dissertation constitute my own original work and does not compromise in any way the rights of third parties, including those relating to the security of personal data.

....
Martina Mammarella
Turin, February 11th, 2019

To my persistence.

Acknowledgements

First and foremost, I would like to express my gratitude to my advisors Prof. Giorgio Guglieri and Prof. Nicole Viola for giving me the possibility of exploring and traveling, the wisdom to make the right choice, the freedom of following my dreams, the bravery to go beyond my limits, the support to get on this thrilling roller coaster and to successfully complete the ride. I owe a debt of gratitude to Prof. Elisa Capello, whose inestimable advices, priceless support, and invaluable friendship have allowed me to overcome most of the obstacles encountered along this long and devious journey. Without her, I would have given up. I would like to deeply acknowledge Dr. Fabrizio Dabbene for being a valuable mentor, guiding me in a new world of (control) laws and maths. It has been an honor to work with him, side by side, getting out of abstruse definitions and improbable demonstrations. I would like to thank Prof. Frank Allgöwer for giving me the possibility to collaborate with him and his research group, in the person of Dr. Matthias Lorenzen. It has been a privilege and a great pleasure to work under his (patient) supervision. I need to acknowledge Prof. Marcello Romano for hosting me and supervising my research during the six months spent at the Spacecraft Robotics Laboratory of the Naval Postgraduate School. It was one of the best experience I have ever had. I have to thank Prof. Hyeongjun Park to support and endure me, not only during the period I spent working with him. He taught me so much and he was a great friend. I will always be grateful to him. An essential thank goes also to Dr. Josep Virgili-Llop and Dr. Costantinos Zagaris that helped us performing the long and exhausting experimental campaigns. Special thanks to Mr. Giorgio Saccoccia and Mr. José Gonzalez del Amo for guiding me through the sparkling world of electric propulsion. It was an amazing journey and I had the opportunity to learn so many things. It was an honor having you as supervisors for part of my research. I must thank my BRO and all my friends, near and far. They have been my strength, my laughs, my home, my CICOS. They have been my step-family all these years, never making me feel alone, wherever I was. And, of course, they have been amazing traveling companion. I owe them so much. Last but not least, I need to thank my whole family. The distance did not stop you from making me feel your support during all these years away. Words would never do justice to gratitude towards you. It has been a tough journey but the best is yet to come.

Abstract

"Earth is a small town with many neighborhoods in a very big universe." The quote of the American Astronaut Ronald John Garan Jr. perfectly summarizes the universal and enduring mankind's interest in exploring the unknown, discovering new worlds, pushing the boundaries of scientific and technical limits further and beyond. More than a half century ago, during a speech delivered at Rice University in Houston, President John F. Kennedy claimed the Moon as the new frontier for the human space exploration. The outstanding achievements of the Apollo mission pushed the research in space across the second part of the last century with new goals, as the permanent presence of the human in space. The evolutionary space program built up around that promise was, to say the least, challenging and involved the development of several revolutionary elements. Due to the significant economic effort required by the Apollo mission, only two elements were realized: the Space Shuttle on one side and the Skylab space station on the other. While the Shuttle remained operative until 2011, Skylab was short-lived and disposed after about six years. Only by joining forces with other international partners, NASA was able to realize a long lasting permanent outpost orbiting around Earth, i.e. the International Space Station (ISS). But again, due to the considerable efforts dedicated to build up the ISS and to keep the Space Shuttle operative, the space race suffered a second setback. Until 2007, when the international community drew up a new visionary program. Moon exploration stepped again into the spotlight to extend and sustain human activities beyond Low Earth Orbit (LEO) towards Mars. The new era of space exploration has begun with the intent of expanding the frontiers of knowledge, capability, and opportunities in space. One of the first milestones is represented by the settlement of the so-called Lunar Orbital Platform-Gateway (LOP-G) by the mid 2020's. The Gateway will serve as a manned outpost in the lunar vicinity to support activities on and around the Moon while also servicing as technological and operational testbed to open the frontier for human exploration of Mars, thanks to the exploitation of key technologies, such as high-power electric propulsion. To sustain the LOP-G and its future visiting crews, the Orion spacecraft is currently under development. However, the usability of the Gateway could be extended if new transportation systems would be available

to support the station transferring additional supplies and equipment. In compliance with the current plans to efficiently reduce the number of development and validation economic efforts by designing and exploiting same elements for multiple missions, a reusable, high-power electric space tug, i.e. the Lunar Space Tug (LST), is proposed in this Thesis to support the replenishment of the LOP-G. This innovative transportation system should be flexible enough to be adopted in different phases of the Gateway lifetime and for evolving needs. The LST should be in charge of recovering cargo modules released in Earth proximity and transfer them up to the Gateway performing a low-thrust transfer, before return to its operational orbit, ready for the next delivery mission, envisioning a closed-loop mission profile. A tailored multi-input/multi-output design tool has been developed to obtain the preliminary and detailed design, at component level, of the LST spacecraft for several propulsion subsystem architectures. The impact of adopting this technology on the platform design is investigated with respect to several thruster working points and case studies, each one characterized by different refurbishment needs. Then, the optimal LST configuration able to support the Gateway crew for different resupply needs is selected, performing a trade-off analysis among the design solutions that comply with all mission and system constraints previously defined in order to minimize the spacecraft mass, propellant consumption and overall mission cost. From an operational viewpoint, the LST should significantly rely on the Automated Rendezvous and Docking (ARVD) technology, which has been identified as crucial for the transition of space missions from geocentric architectures to self-sustainable, autonomy and independent. At this end, new Guidance Navigation and Control (GNC) algorithms shall be investigated to allow ARVD maneuvers to become reliable routine. In particular, the control problem encapsulates safety restrictions and performance specification that shall be properly addressed verifying the effectiveness and real-time implementability of innovative control strategies. Thus, a 6 Degrees-of-Freedom (DoF) orbital simulator has been developed to simulate the rotational and translational dynamics of the LST and its target vehicles in both Earth orbit and Lunar proximity. Moreover, to reproduce a realistic simulation environment, uncertainty and disturbance affecting the spacecraft dynamics during the maneuver have been modeled and included in the simulator. For attitude and orbital control, three different Model Predictive Control (MPC) algorithms have been implemented and their performance evaluated in the presence of disturbance and parametric uncertainty. In particular, a sampling-based stochastic MPC algorithm is proposed and the typical binding computational effort required by these type of stochastic algorithms, especially when running on low-performing hardware, has been overcome shifting the intensive computations to the offline phase, thus greatly reducing the online computational cost. To complete the algorithms verification process, all three MPC strategies have been experimentally validated exploiting spacecraft mock-up and running the algorithms on the on-board micro-controller, demonstrating their effectiveness and real-time computational applicability.

Contents

List of Figures xv

List of Tables xxiii

List of Abbreviations xxv

1 Introduction 1

2 The Lunar Space Tug 15

2.1 The Lunar Space Tug Mission Definition 15
  2.1.1 Ground Segment 17
  2.1.2 Launch Segment 19
  2.1.3 The Lunar Orbital Platform - Gateway 21
  2.1.4 Cargo Module 25
  2.1.5 On-Orbit Refueling System 28
2.2 The Lunar Space Tug Spacecraft 31
  2.2.1 Propulsion Subsystem 31
  2.2.2 Electrical Power Subsystem 36
  2.2.3 Attitude and Orbit Control Subsystem 37
  2.2.4 Thermal Control Subsystem 39
  2.2.5 Telemetry, Tracking and Control Subsystem 39
  2.2.6 Command and Data Handling Subsystem 40
  2.2.7 Structures and Mechanisms Subsystem 41
2.3 The Lunar Space Tug Scenario 42
  2.3.1 Mission Phases 42
  2.3.2 Modes of Operations 46
  2.3.3 Traffic Plan 46

3 Mission and Space Systems Design Tool 51

3.1 MISS Design Tool Architecture 51
  3.1.1 Mission Scenario Definition 52
  3.1.2 Delta-v Budget 55
  3.1.3 Spacecraft Design 57

3.1.4 Optimal Solution Selection 59
3.1.5 Mission Cost Estimate 60
3.2 Spacecraft Design Analytical Models 60
3.2.1 Attitude and Orbit Control Subsystem 60
3.2.2 Propulsion Subsystem 62
3.2.3 Electrical Power Subsystem 64
3.2.4 Thermal Control Subsystem 65
3.2.5 Other Subsystems 68
3.2.6 Propellant Consumption and Tank Design 68

4 Simulated Trajectories for Automated Rendezvous Tool 71
4.1 Automated Rendezvous Maneuver 71
4.2 STAR Orbital Simulator 78
4.2.1 Coordinate Reference Frames 79
4.2.2 STAR Initialization 81
4.2.3 STAR Simulation Environment 84
4.2.4 Model Parametric Uncertainty 90
4.2.5 Internal and External Additive Disturbances 94
4.2.6 Attitude Control 98
4.2.7 Orbital Control 99

5 Control Strategies for Automated Rendezvous Maneuver 103
5.1 Controllers for Rendezvous Maneuver 103
5.1.1 Control Techniques for Orbital Control 104
5.2 Linear-Quadratic MPC 112
5.3 Tube-based Robust MPC 114
5.4 Offline Sampling-based Stochastic MPC 121
5.4.1 SMPC Algorithm Based on Offline Sampling 130
5.4.2 Theoretical Guarantees of OS-SMPC 131

6 MISS STAR Results 137
6.1 MISS Results 137
6.1.1 Lunar Space Tug Design 138
6.1.2 Optimal Design Selection 150
6.2 STAR Results 154
6.2.1 LQMPC vs TRMPC 157
6.2.2 OS-SMPC 166
6.3 Experimental Validation of MPC Schemes 173
6.3.1 POSEIDYN Testbed and Experimental Setup 174
6.3.2 Model Setup 179
6.3.3 LQMPC and TRMPC 182
6.3.4 Fuel-Efficient LQMPC and TRMPC 186

6.3.5 OS-SMPC 189

7 Conclusions 195

A Multi-Scenario SEP Platforms Design Exploiting MISS 203
A.1 Transfer Duration 207
A.2 Optimal Nominal Operational Points 209

B Real-Time Implementability Validation of Proposed MPC Schemes for Fixed-Wing UAVs 215
B.1 MH850 Fixed-Wing Mini-Unamnned Aerial Vehicle (UAV) and On-Board Systems 216
B.2 Guidance and Control Strategies 218
B.2.1 Guidance Algorithm 219
B.2.2 Tube-based Robust Model Predictive Control (MPC) for Precision Farming 220
B.2.3 Offline-Sampling Stochastic MPC for Multi-Scenario Mapping 228

List of Figures

1.1 (a) Astronaut Edwin E. Aldrin Jr. poses for a photograph beside the deployed United States flag during an EVA on the lunar surface. (b) A close-up view of astronaut Buzz Aldrin's bootprint in the lunar soil (credit: NASA). 1
1.2 Extended Integrated Program Plan traffic model [3] (credit: NASA). 2
1.3 Space Shuttle launch as represented in [3] (a) and Space shuttle Atlantis as standing on Launch Pad 39A at NASA's Kennedy Space Center in Florida, where it is set to liftoff on STS-135, the final shuttle mission. (b) (credit: NASA). 3
1.4 Skylab as represented in [3] (a) and as photographed from the Skylab 4 Command and Service Modules during the final fly-around before returning home (b) (credit: NASA). 4
1.5 The evolution of the Global Exploration Roadmap mission scenario from 2011 to 2018. 6
1.6 (a) Earth-Moon mission scenario according to the Integrated Program Plan (1970). (b) Earth-Moon mission scenario according to the Global Exploration Roadmap (2017) (credit: NASA). 7
1.7 Earth-Moon mission scenario main elements (credit: NASA/Boeing). 8
1.8 (a) A reusable space tug to augment Space Shuttle capability and to support the space station in LEO according to the Integrated Program Plan (1970) (credit: NASA). (b) The Lockheed Martin space tug, i.e. Jupiter, to support the ISS (2015) (credit: Lockheed Martin). 10

2.1 Function block diagram at system level. 17
2.2 ESA tracking station network (credit: ESA). 19
2.3 (a) Launch of Orion Exploration Flight Test 1 by Delta IV Heavy, December 2014 (credit: ULA); (b) Proton-M launching AsiaSat 9 on September 2017 (credit: Roscosmos); (c) SpaceX Falcon Heavy first flight on February 2018 (credit: SpaceX); and (d) rendering of the NASA SLS (credit: NASA). 20

2.4 The synchronized landings of two of the Falcon Heavy boosters on the Landing Zone 1 and 2 of the Cape Canaveral Force Station on February 6th, 2018 (credit: SpaceX). 21
2.5 Ariane V ECA VA 242 (launch date: April 6th 2018, payload: DSN-1/Superbird-8 and HYLAS 4 satellites, injection orbit: GTO) and a rendering of Ariane VI. (credit: ArianeSpace). 22
2.6 (a) Early concept rendering of Lockheed Martin's LOP-G, with an Orion crew vehicle docked (credit: Lockheed Martin); (b) Lockheed Martin artist's rendering of the NextSTEP habitat docked with Orion as part of a concept for the LOP-G. (credit: PRNewsfoto / Lockheed Martin). 23
2.7 Canadarm2 attached to the ISS with an aurora in the background. (credit: NASA). 23
2.8 Total habitable volume per astronaut guidelines [33]. 24
2.9 Logistics mission to the ISS grouped according to the spacecraft that carried out the mission (updated at: August 2018, source: NASA). . 25
2.10 (a) Inside Progress spacecraft (credit: Roscosmos); (b) Inside HTV (credit: NASA); (c) Inside Cygnus spacecraft (credit: NASA); (d) Inside Dragon spacecraft (credit: NASA); and (e) Inside ATV spacecraft (credit: ESA). 26
2.11 (a) Leonardo MPLM; (b) Raffaello MPLM; and (c) Donatello MPLM (credit: NASA). 27
2.12 The rendering of a space tug refueling operation through one Shuttle orbiter (credit: NASA). 28
2.13 The RRM and Dextre outside the ISS (credit: NASA). 29
2.14 (a) Boeing multi-launch dual-fluid depot (credit: Boeing); (b) ULA single-fluid single-launch concept (credit: ULA); (c) Shackleton Energy proposal; (d) rendering of propellant depot evolution [41] (credit: NASA). 30
2.15 HET reference performance map: iso-power black curves and iso-voltage red-curves. 33
2.16 e-PROP physical block diagram [48]. 34
2.17 HT20k development model with magnetic shielding (credit: SITAEL). 35
2.18 The Cygnus spacecraft with its cymbal-like UltraFlex solar arrays deployed (credit: NASA). 37
2.19 (a) AOCS architecture; (b) Monopropellant thrusters allocation in front (left) and rear (right) pods. 38
2.20 Four Rockwell Collins RDR 68-3 Reaction Wheels arranged in the NASA Standard configuration. 39
2.21 LST Design reference Mission. 45
2.22 ATV-like rendezvous mission profile. 45
2.23 LST operational timeline for different fleet configurations. 48

2.24 LST operational timelines with respect to three fleet configurations. 49

3.1 MISS high-level algorithm block diagram. 52
3.2 Example of payload setup during the MISS algorithm initialization phase. 53
3.3 Transfer duration as a function of the thrust-over-mass ratio. The red dot highlights the T/m value, i.e. $2 \cdot 10^{-4}$ N/kg, corresponding to one year transfer. 55
3.4 MISS detailed architecture and algorithm logic. The mass budget links are represented with dashed lines whereas the power budget links are in dotted lines. 58
3.5 MISS PROP algorithm block diagram. The mass budget links are represented with dashed lines whereas the power budget links are in dotted lines. 63

4.1 Gemini VII photographed by Gemini VI during the first manned rendezvous maneuver, December 15, 1965 (left) and view from Gemini VIII just 0.6 m from an Agena target vehicle before achieving the first docking, March 16, 1966 (right) (credit: NASA). 72
4.2 Kosmos 186 and Kosmos 188 performing the first automatic docking in space. (credit: collectSPACE). 72
4.3 LST rendezvous mission profile including closing phase and final approach. 74
4.4 LST close-range rendezvous: (a) closing phase and (b) final approach ([79]). 75
4.5 ECI and MCI inertial reference frames. 79
4.6 Perifocal reference frames for (a) GTO and (b) NRHO. 80
4.7 LVLH reference frame with respect to the target vehicle. 81
4.8 LST body reference frame. 82
4.9 STAR simulation environment high-level architecture. 85
4.10 LOS approach corridor with entry radius r_i and final radius r_f corresponding respectively at -500 m and -2 m along V-bar. 100

5.1 An illustration of the state tube, the sequence of constraint set and the nominal trajectory. 115
5.2 Example of outer-bounding tube representation at the k-th time step over a prediction horizon of T for $x \in \mathbb{R}^2$. 118

6.1 LST design solutions for all 9 subcases, highlighting in green those compliant with both system and mission constraints, in yellow those that are compliant with either one of the constraint and in red those that are not feasible. 140

6.2 e-PROP architecture with respect to the corresponding HET operational point over the performance envelope for the three case studies: (i) 30-days (black circles); (ii) 60-days (red circles); (iii) 90-days (yellow circles). 141
6.3 Thruster lifetime with respect to the corresponding HET operational point over the performance envelope for the three case studies: (i) 30-days (black circles); (ii) 60-days (red circles); (iii) 90-days (yellow circles). 142
6.4 e-PROP architecture in terms of $N_{HET_{op}}$ and cluster architecture for the three case studies: (i) 30-days (black circles); (ii) 60-days (red circles); (iii) 90-days (yellow circles). 143
6.5 e-PROP architecture in terms of cluster architecture and number of PPU for the three case studies: (i) 30-days (black circles); (ii) 60-days (red circles); (iii) 90-days (yellow circles). 144
6.6 EPS design features in terms of solar array area as a function of the total power demand for the three case studies: (i) 30-days (black circles); (ii) 60-days (red circles); (iii) 90-days (yellow circles). . . . 144
6.7 EPS design features in terms of secondary battery mass as a function of the total power demand for the three case studies: (i) 30-days (black circles); (ii) 60-days (red circles); (iii) 90-days (yellow circles). 145
6.8 TCS design features in terms of radiator panels area as a function of the total power demand for the three case studies: (i) 30-days (black circles); (ii) 60-days (red circles); (iii) 90-days (yellow circles). . . . 146
6.9 LST transfer duration as a function of its total wet mass and thrust available for the three case studies: (i) 30-days (black circles); (ii) 60-days (red circles); (iii) 90-days (yellow circles). 147
6.10 LST transfer duration as a function of its total wet mass and power demand for the three case studies: (i) 30-days (black circles); (ii) 60-days (red circles); (iii) 90-days (yellow circles). 148
6.11 LST transfer duration as a function of its total power demand and thrust available for the three case studies: (i) 30-days (black circles); (ii) 60-days (red circles); (iii) 90-days (yellow circles). 148
6.12 LST Hydrazine consumption during ARVD maneuvers and corresponding tanks sizing for the three case studies: (i) 30-days (black circles); (ii) 60-days (red circles); (iii) 90-days (yellow circles). . . . 149
6.13 LST Xenon consumption during ARVD maneuvers and corresponding tanks sizing for the three case studies: (i) 30-days (black circles); (ii) 60-days (red circles); (iii) 90-days (yellow circles). 150
6.14 LST e-PROP architectures for all three cases design solutions compliant with mission and system constraints for the 3-LST fleet configuration. 151

6.15 LST Euler angles during the ARVD maneuver with cargo module (a) and LOP-G (b). 159
6.16 LST angular velocity during the ARVD maneuver with cargo module (a) and LOP-G (b). 160
6.17 LST RWs angular velocity during the ARVD maneuver with cargo module (a) and LOP-G (b). 160
6.18 LST ARVD trajectories in the Local-Vartical/Local-Horizontal (LVLH) frame with cargo module (a) and the LOP-G (b) obtained exploiting LQMPC (black lines) and TRMPC (red lines) for the orbital control. 161
6.19 LST ARVD trajectories in the LVLH frame with cargo module (a) and the LOP-G (b) obtained exploiting LQMPC (black lines) and TRMPC (red lines) for the orbital control. 162
6.20 LST ARVD trajectories in the perifocal frame with cargo module (a) and the LOP-G (b). 163
6.21 LST velocity profile during the ARVD maneuver in the LVLH frame with cargo module (a) and the LOP-G (b). 164
6.22 Thrusters actuation during the ARVD maneuvers with cargo module (red lines) and the LOP-G (black lines). 164
6.23 Fuel consumption during the ARVD maneuvers exploiting LQMPC and TRMPC: (a) total Hydrazine demand in GTO (red bars) and in NRHO (green bars) and (b) time evolution over the entire maneuver. 165
6.24 LST Euler angles during the ARVD maneuver with cargo module (a) and LOP-G (b). 167
6.25 LST angular velocity during the ARVD maneuver with cargo module (a) and LOP-G (b). 167
6.26 LST ARVD trajectories in the perifocal frame with cargo module (a) and the LOP-G (b). 168
6.27 LST ARVD trajectories in the LVLH frame with the cargo module: (a) complete trajectory and (b) final approach. 169
6.28 LST ARVD trajectories in the LVLH frame with the cargo module: (a) complete trajectory and (b) final approach. 170
6.29 LST velocity profile during the ARVD maneuver in the LVLH frame with cargo module (a) and the LOP-G (b). 171
6.30 Time evolution of the fuel consumption during the ARVD maneuvers exploiting OS-SMPC over the entire maneuver and total Hydrazine demand in GTO and in NRHO. 172
6.31 Execution time for solving on-line the OS-SMPC problem for both attitude and trajectory control in GTO and NRHO. 173
6.32 POSEIDYN testbed in the NPS Spacecraft Robotics Laboratory. On the granite table, the two FSS and, in the background, three of the Vicon cameras. 175

6.33 The FSS chaser vehicle (left) is equipped with a male conic docking interface while on the right the target FSS with a female funnel-like interface. 176
6.34 NPS-POSEIDYN testbed environmental disturbance. 179
6.35 NPS-POSEIDYN testbed with the cone constraints. The chaser initial condition has to be chosen within the feasible region (light green) whereas the target spacecraft can be located within the feasible terminal region (dark green). ϕ defines the cone half-angle, whereas θ represents the chaser FSS attitude with respect to the testbed reference system. 182
6.36 Comparison of simulation and experimental trajectories in Case A. Three different experimental results are represented for each approach. The Chaser is represented at time $t_0 = 0s, t_1 = 20s$, $t_2 = 100s$, $t_3 = 200s$. 185
6.37 Comparison of simulation and experimental trajectories in Case B. Three different experimental results are represented for each approach. The Chaser is represented at time $t_0 = 0s, t_1 = 20s$, $t_2 = 100s$, $t_3 = 200s$. 186
6.38 Zoomed-in trajectory of Case B for LQMPC and TRMPC. 187
6.39 Experimental results comparison with and without fuel saving strategy applied. 188
6.40 Numerical results for 100 trajectories (a) and zoom-in around the target FSS (b). 190
6.41 Simulation and experimental results for 3 different ICs, considering 20 repetitions for each one. 191
6.42 Zoom-in on the terminal region of both simulation and experimental results. 192
6.43 Control effort with respect to the time-to-dock results for 60 experiments. 193
6.44 Average and maximum computational cost of all 60 experiments. . . 194

A.1 HT20k XC expected performance. 205
A.2 Telecommunication scenario #2, Disposal scenario #6 and Transportation scenario #3 with 5/10/15/20 t cargo modules – Feasible working points over the reference performance map and with respect to the total number of HT20k in the e-PROP cluster. Three lifetime level for HT20k: (i) 20000 h (black circle); (ii) 25000 h (red circle); (iii) 30000 h (yellow circle). 206

A.3 Telecommunication scenario #2, Disposal scenario #6 and Transportation scenario #3 with 5/10/15/20 t cargo modules – Transfer duration with respect to total thrust available (left), total wet mass (center), and total power demand (right). Three lifetime levels for HT20k: (i) 20000 h (black circle); (ii) 25000 h (red circle); (iii) 30000 h (yellow circle). 208
A.4 Performance map for transportation, disposal and telecommunication scenarios. 210
A.5 Performance map for LOP-G replenishment scenarios. 211
A.6 Overlapped performance maps for all 10 selected scenarios. The red dashed rectangle highlights the area of the map shared among all the feasible concepts. 213

B.1 The MH850 mini-UAV [197] and the custome-made autopilot (credit: Politecnico di Torino). 216
B.2 CTE and reference distances. 219
B.3 Guidance phases. 220
B.4 Inner and outer variables behavior and control actions for both linear (left column) and nonlinear (right column) models exploiting TRMPC. 221
B.5 SIL vs HIL for a square pattern. 224
B.6 SIL vs HIL for a butterfly pattern. 225
B.7 SIL vs HIL for a 8-waypoints snake pattern. 225
B.8 Zoom-in on the square, butterfly and snake patterns. 226
B.9 Elapsed-over-simulated time for the three case study. 226
B.10 (a) Monitored portion of field at Olcenengo, Italy, overlapped with a snake-path. (b) Comparison among SIL (red line) and HIL (dotted black line) trajectories. 227
B.11 Deviations between actual airspeed and altitude with respect to the references, and CTE for the UAV position. 228
B.12 20 different square-trajectories over the Taro River, Borgo Val di Taro, Parma, Italy. The area covered has an extension of about 180 ha. 229
B.13 20 different snake-trajectories over a paddy field in Olcenengo, Vercelli, Italy. 229
B.14 20 different piecewise-linear trajectories over Downtown Miami's Brickell Financial District, around the Four Season Hotel and Tower - 2D trajectories. 230
B.15 LQMPC 3D trajectory (black line) and OS-SMPC 3D trajectory (red line). 231

List of Tables

2.1 Mission segments and related building blocks. 18
2.2 ISS annual replenishment since and average daily need per crewmember since 2012 (after Space Shuttle program closed). 28
2.3 Performance of the HT20k without magnetic shielding. 36
2.4 LST mission phases characterization in terms of starting and ending events. 44
2.5 LST mission phases characterization in terms of starting and ending events. 47

3.1 Mass breakdown exploited for LST design. 57
3.2 Figures of Merit for LST trade-off analysis. 60
3.3 AOCS sensors main features. 62
3.4 e-PROP components main features. The mass of the PR is a function of the HET propellant flow rate $\dot{m}_{flow}$. 64
3.5 TCS thermal parameters for HOT and COLD assessment in Earth and Lunar orbits. 67

6.1 LST case studies and related resupply need and cargo module geometry. 138
6.2 LST operational orbits parameters. 138
6.3 LST preliminary Δv budgets. 139
6.4 HET reference operational points. 139
6.5 AOCS design feature in terms of mass and power budget at component level. 146
6.6 LST trade-off analysis results. 152
6.7 Optimal LST design sizing at subsystem level. 152
6.8 Optimal LST design sizing at component level. 153
6.9 Optimal LST design sizing peculiar for each case study. 153
6.10 STAR initialization data. 154
6.11 LST moment of inertia and center-of-mass location. 155
6.12 LST orbital position and velocity in LVLH, Earth-Centered Inertial Frame (ECI) and perifocal frames. 156

6.13 TRMPC tightened constraints for attitude and orbital control in terms of upper and lower bounds identified as *ub* and *lb*, respectively. 158
6.14 LQMPC and TRMPC setting parameters. 159
6.15 OS-SMPC setting parameters. 166
6.16 Summary of relevant FSS Physical Properties. 175
6.17 State and Control constraints. 184
6.18 MPC design parameters and model initialization settings. 184
6.19 Performance of controllers in Case A. 185
6.20 Performance of controllers in Case B (LQ=LQMPC, TR=TRMPC). 187
6.21 Performance comparison of controllers in Case A with respect to fuel saving approach, both in simulation and experiment setup. 189
6.22 Comparison of the average control effort for three different MPC approaches adopted to control the Floating Spacecraft Simulator (FSS) during a rendezvous maneuvers on the NPS POSEIDYN testbed: (i) LQMPC; (ii) TRMPC; (iii) OS-SMPC. 193

B.1 TRMPC parameters. 223
B.2 Additive disturbances considered. 223

List of Abbreviations

AEPS Advanced Electric Propulsion System

AOCS Attitude and Orbit Control Subsystem

APF Artificial Potential Field

ARVD Automated Rendezvous and Docking

ARRM Asteroid Redirect Robotic Mission

ATV Automated Trasfer Vehicle

BOL Beginnig of Life

CDH Command and Data Handling

ConOps Concept of Operations

CSA Canadian Space Agency

CTE Cross-Track Error

CW Clohessy-Wiltshire

DoD Depth of Discharge

DoF Degrees of Freedom

DRM Design Reference Mission

DRO Distant Retrograde Orbit

ECI Earth-Centered Inertial Frame

EML Earth-Moon Lagrangian Point

EOL End Of Life

EOR Electric Orbit Raising

e-PROP Electric Propulsion Subsystem

EPS Electrical Power Subsystem

ESA European Space Agency

EVA Extra-Vehicular Activity

FCU Flow Control Unit

FSS Floating Spacecraft Simulator

GEO Geostationary Earth Orbit

GNC Guidance Navigation and Control

GTO Geostationary Transfer Orbit

HET Hall Effect Thruster

HIL Hardware-In-the-Loop

HTV H-II Transfer Vehicle

iid independent and identically distributed

IMU Inertial Measurement Unit

INCOSE International Council on System Engineering

ISECG International Space Exploration Coordination Group

Isp Specific Impulse

ISRU In-Situ Resources Utilization

ISS International Space Station

JAXA Japanese Aerospace Exploration Agency

LASSO Least Absolute Shrinkage and Selection Operator

LEO Low Earth Orbit

LMI Linear Matrix Inequality

LOP-G Lunar Orbital Platform-Gateway

LOS Line-Of-Sight

LQMPC Linear-Quadratic Model Predictive Control

LQR Linear-Quadratic Regulator

LST Lunar Space Tug

LSTCM Lunar Space Tug Cost Model

LVLH Local-Vartical/Local-Horizontal

MCC Mission Control Center

MCI Moon-Centered Inertial Frame

MIB Minimum Impulse Bit

MISS MIssion and Space Systems

MLI Multi-Layer Insulation

MMOD Micrometeoroids and Orbital Debris

MPC Model Predictive Control

MPCV Multi-Purpose Crew Vehicle

MPLM Multi-Purpose Logistic Module

NASA National Aeronautics and Space Administration

NPS Naval Postgraduate School

NRHO Near Rectilinear Halo Orbit

OBC On-Board Computer

OCT Office of the Chief Technologist

ORS On-Orbit Refueling System

OS-SMPC Offline Sampling Stochastic Model Predictive Control

PID Proportional Integral Derivative

PM Pointing Mechanism

PMM Permanent Multipurpose Module

POCC Payload Operations Control Center

POSEIDYN Proximity Operation of Spacecraft: Experimental hardware-In-the-loop DYNamic

PPE Power and Propulsion Element

PPU Power Processing Unit

PR Pressure Regulator

PROP Propulsion Subsystem

RMPC Robust Model Predictive Control

RP Relative Percentage

RPI Robust Positive Invariant

RRM Robotic Refueling Mission

RW Reaction Wheel

SEP Solar Electric Propulsion

SIL Software-In-the-Loop

SLS Space Launch System

SM Safety Margin

SMAD Space Mission Analysis and Design

SMC Sliding Mode Control

SMPC Stochastic Model Predictive Control

SOCC Space Operation Control Center

SPHERES Synchronized Position Hold Engage and Reorient Experimental Satellites

SRP Solar Radiation Pressure

STAR Simulated Trajectories for Automated Rendezvous

StrMech Structures and Mechanisms

TA Technology Area

TCS Thermal Control Subsystem

TH Tschauner–Hempel

TMF Thrust Management Function

TRMPC Tube-Based Robust Model Predictive Control

TTC Telemetry Tracking and Control

UAV Unamnned Aerial Vehicle

ULA United Launch Alliance

Chapter 1

Introduction

"The journey of a thousand miles begins with one step."

September 12, 1962. The President John F. Kennedy made a promise: *"We choose to go to the Moon!"* The first step towards the future of space exploration. The challenge that *"we are willing to accept, one we are unwilling to postpone, and one which we intend to win"*. Seven years later, the promise was kept. July 20, 1969, 02:56:15 UTC. The mission commander Neil Alden Armstrong stepped onto the lunar surface, posing the final and most thrilling milestone to the Space Race started in 1955.

"That's one small step for man, one giant leap for mankind."

Astronaut Neil Armstrong, together with the Command Module pilot Micheal Collins and the Lunar Module pilot Edwin E. Aldrin Jr., made the history.

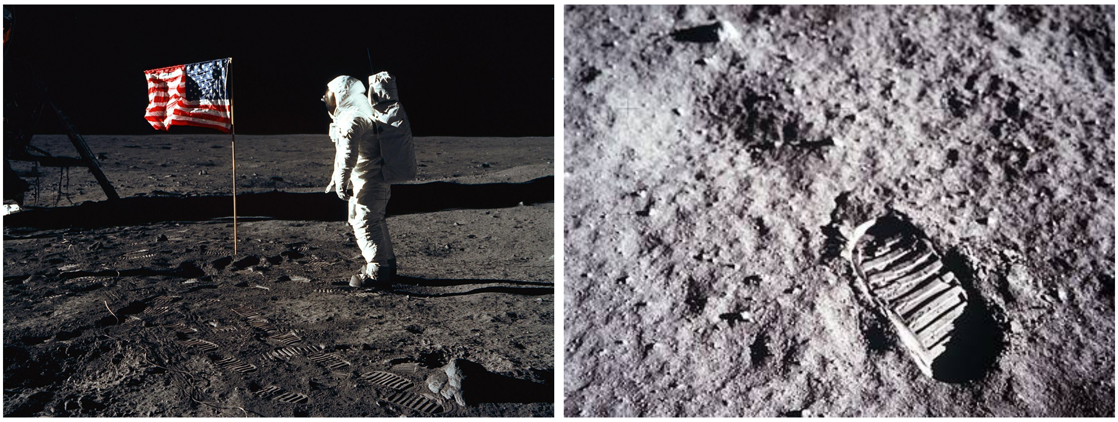

(a) (b)

Figure 1.1: (a) Astronaut Edwin E. Aldrin Jr. poses for a photograph beside the deployed United States flag during an EVA on the lunar surface. (b) A close-up view of astronaut Buzz Aldrin's bootprint in the lunar soil (credit: NASA).

But the journey had just begun. Indeed, in February 1969 the American President Richard Nixon appointed a Space Task Group, headed by Vice President Spiro Agnew, to assess the future direction in space exploration and to support extended operations beyond the Apollo program [1]. This request followed up to the summary report delivered in January, 1965 [2] by the Future Programs Task Group, directed by Francis B. Smith of Langley Research Center to answer inquires made by the (former) President Lyndon B. Johnson as to criteria and priorities for space missions beyond 1960's. The main outcome was represented by the Technical Memorandum produced by the Advanced Systems Analysis Office of National Aeronautics and Space Administration (NASA) Marshall Space in 1970 [3]. This report described a possible comprehensive path of future space flight evolution, following the many achievements culminating in the successful flight of Apollo 11, and envisioned an integrated space program with the objective to *"utilize hardware in multiple application in order to minimize the number of hardware developments and to reuse all major pieces for reduction of operational cost"*. With this evolutionary space program emphasizing the use of existing Apollo capability, two goals were intended to be pursued: (i) to maximize the benefits returned to mankind from space exploration; and (ii) to improve the knowledge of the Solar System.

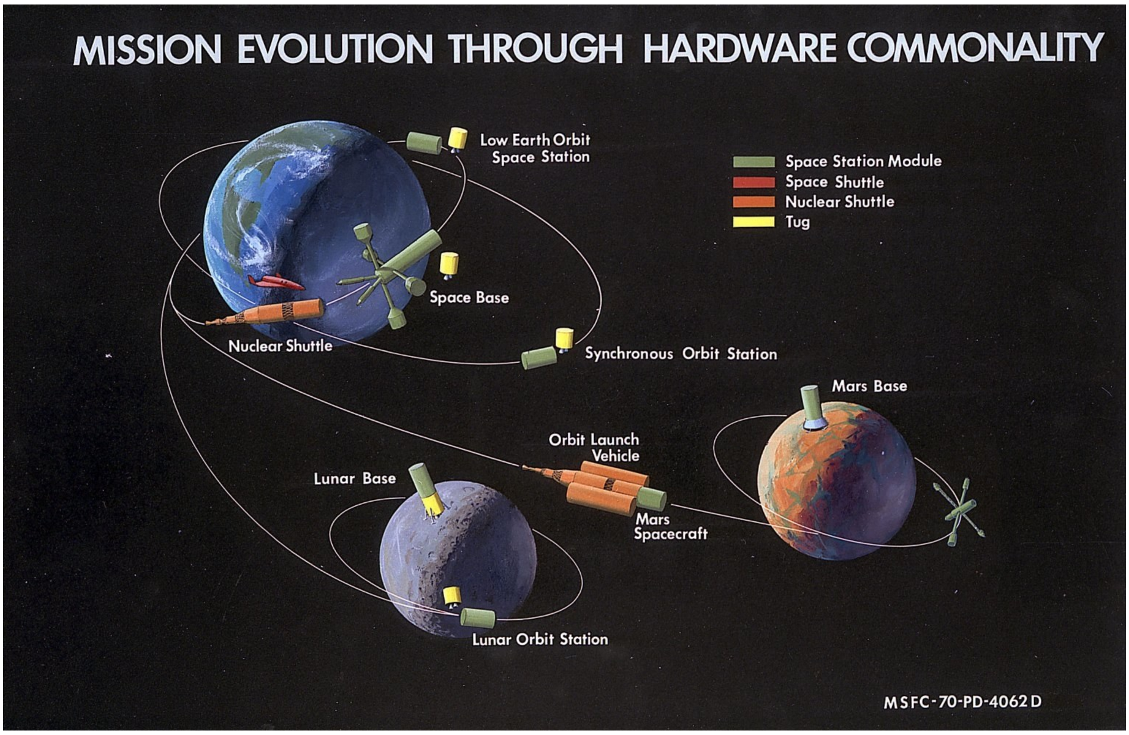

Figure 1.2: Extended Integrated Program Plan traffic model [3] (credit: NASA).

The so-called Integrated Program Plan initially envisioned the settlement of a modular space station, i.e. the Skylab space station, derived from Apollo hardware and placed in Low Earth Orbit (LEO) in the early 1970's, together with improvements of the Apollo systems and Saturn V capability, to extend the Lunar surface mission duration. Moreover, the lunar exploration program should include also a Lunar orbit station to enhance lunar observation and on the location of lunar resources, e.g. water, to support future exploration. Extending lunar mission duration would require to provide lunar orbit to lunar surface transportation, identifying an additional new (un)manned system, i.e. the space tug. With the intent of minimizing the development efforts and cost, the tug could operate also in Earth orbit to support the space station(s) and for on-orbit maintenance of automated satellites and probes. On the other hand, a two-stage fully reusable system, i.e. the well-known Space Shuttle, would provide low-cost transportation between Earth and LEO orbits for astronauts as well as equipment, propellant and supplies. All these elements would allow the possibility to expand the manned program in both Earth and Lunar environments, for example including a synchronous orbit station and a permanent lunar base, which in turn would require a low-cost reusable lunar shuttle based of nuclear propulsion, in analogy to the Space Shuttle and the space tug in Earth proximity. Furthermore, emphasis was placed on the exploration of Mars, with the final goal of landing with humans on its surface and establishing a Mars (semi)permanent base, via precursor missions involving unmanned probes and landers.

(a) (b)

Figure 1.3: Space Shuttle launch as represented in [3] (a) and Space shuttle Atlantis as standing on Launch Pad 39A at NASA's Kennedy Space Center in Florida, where it is set to liftoff on STS-135, the final shuttle mission. (b) (credit: NASA).

Due to the considerable effort expended by NASA in the 1969-1971 period on planning the Integrated Program Plan execution, the attention was posed on those elements considered as the program's first step, while keeping in mind the whole visionary mission architecture: (i) the Space Shuttle (Figure 1.3) and (ii) the Skylab space station (Figure 1.4). On one side, the Space Transportation System program saw the light at the beginning of 1972 while the first Space Shuttle orbital flight test took place in 1981. 135 missions were performed by the Shuttle fleet, composed by five vehicles, between 1981 and 2011, delivering numerous satellites, interplanetary probes, as well as the Hubble Space Telescope (1990), conducting science experiments and providing on-orbit servicing capability supporting the construction and replenishment of the International Space Station (ISS).

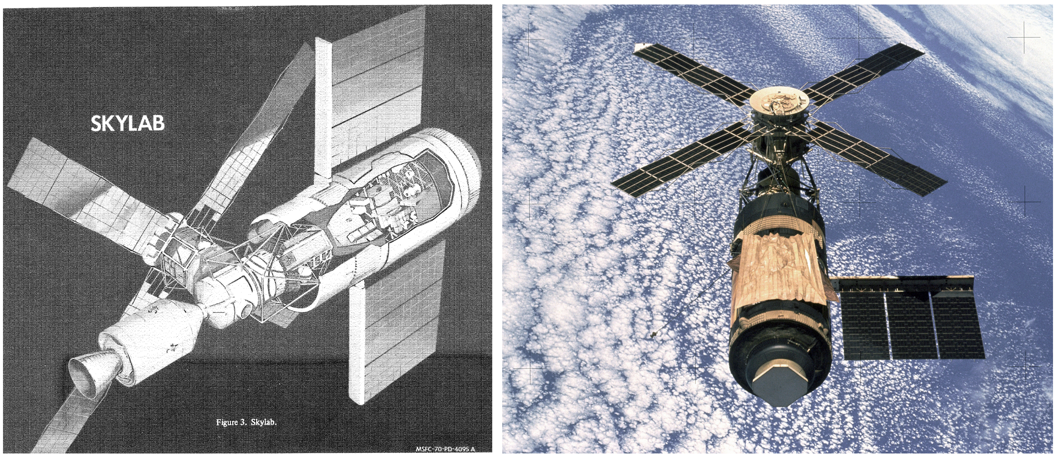

(a) (b)

Figure 1.4: Skylab as represented in [3] (a) and as photographed from the Skylab 4 Command and Service Modules during the final fly-around before returning home (b) (credit: NASA).

On the other side, the American space station called Skylab was built starting from Saturn V and Apollo systems hardware and was launched on board a redesigned Saturn V on May 14, 1973. Over the period from May 25, 1973 and February 8, 1974, three manned missions took place, each one with a crew composed by three astronauts and with increasing permanence on-board the station. After the third manned mission, several plans on reusing the station were made, addressing the economical benefits in reactivating Skylab instead of building up a new orbiting station, also relying on the possibility to exploit the still under-development Space Shuttle to re-boost, refurbish and expand the station. Due to continuous delays in completing the Shuttle development and a greater-than-expected solar activity that increased drag on Skylab, the station demise occurred ahead schedule on July 11, 1979. After the re-entry of Skylab, NASA efforts in designing and building a new space station were initially represented by the so-called Space Station Freedom, i.e. a presumably permanently manned Earth-orbiting space station. After several cutbacks the project evolved into the ISS in 1993, launched starting from 1998 thanks to the collaboration with other four participating space agencies, i.e. Roscosmos, Japanese Aerospace Exploration Agency (JAXA), European Space Agency (ESA), and Canadian Space Agency (CSA).

The economic efforts required by both the Space Shuttle and the ISS caused a relevant setback in the space exploration program for a quite long period. Until 2006, when fourteen space agencies founded the International Space Exploration Coordination Group (ISECG) to begin an unprecedented international collaboration and to elaborate a common, global vision for peaceful robotic and human space exploration, focusing on destinations within the Solar System. This visionary program was first articulated in [4] released in May, 2007. During the second ISECG meeting held in Montreal, Canada, on July 2008, the Moon exploration stepped again into the spotlight. A series of Lunar Architecture workshops were organized between 2008 and 2009 to discuss the possibility of developing a reference lunar surface architecture as the result of a robust international collaboration. The reference architecture was neither intended as a lunar base nor a series of Apollo-style missions but composed by several precursor robotic missions enhancing a future framework for a human lunar exploration program. Moreover, the ISECG group highlighted how all these common objectives could be envisioned as a preparation plan for providing additional capability for crew habitation, science and demonstration of technologies necessary for human missions to Mars. The major outcome derived by this international effort is represented by the Global Exploration Roadmap, first delivered in September 2011 [5]. Feasible and sustainable exploration pathways to the Moon, near-Earth asteroids, and Mars have been defined, starting from the ISS experience and examining possible roadmaps in the next 25 years. The following updates released in 2013 [6] and 2018 [7] confirmed the intent of the global community on preparing to push the boundaries of space missions even further, to reach, explore and, eventually, colonize the Mars surface. The strategic goals focus on the expansion of the frontiers of knowledge, capability, and opportunities in space, enhancing robotics missions in the Solar System and returning humans to the Moon before sending them to Mars. Extended lunar stays build the experience and expertise needed for the long-term space missions required to reach the final goal, the Red Planet. As represented in Figure 1.5, the current plans for the new space exploration era share several commonalities with the Integrated Program Plan of 50 years ago: (i) an innovative launch vehicle with improved capabilities, i.e. the Space Launch System (SLS); (ii) transportation system, e.g. the Orion Multi-Purpose Crew Vehicle (MPCV), connecting Earth, Moon and Mars; (iii) robotics elements operating on Lunar and Mars surface; and (iv) a Lunar orbital station i.e. the so-called Deep Space Gateway. To achieve this exceptional goal, summarized by the NASA's Office of the Chief Technologist (OCT) as the technological objective *"extend and sustain human activities beyond Low Earth Orbits"*, international collaboration has been intensively promoted between space agencies, ISS commercial partners and industry to fulfill the technological gap, advancing and maturing technologies critical to future human exploration. In [8], all these enabling technologies have been arranged in 14 Technology Area (TA), each one representing a different roadmap. Dedicated study panels identified for each

TA the top technical challenges via a prioritization process, in order to comply with limited resources and multiple objectives.

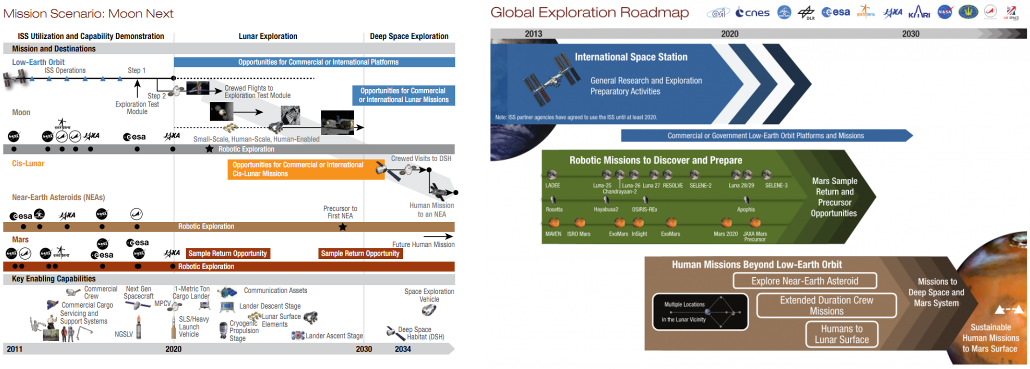

(a) 2011 (b) 2013

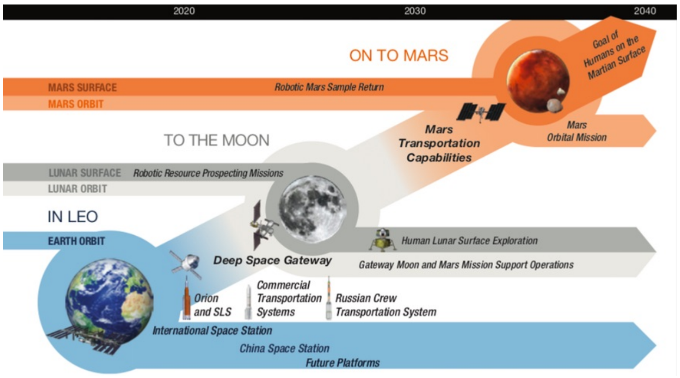

(c) 2018

Figure 1.5: The evolution of the Global Exploration Roadmap mission scenario from 2011 to 2018.

The envisioned incremental approach is based on several intermediate steps, among which the Cislunar station, also known as Lunar Orbital Platform-Gateway (LOP-G), has been identified as one of the first step to pave the way towards the Deep Space, opening new frontiers for the human exploration of the Moon and Mars and expanding human presence and commerce beyond LEO. Thus, focusing on the current Earth-Moon mission scenario represented in Figure 1.6b in comparison with the Integrated Program Plan one in Figure 1.6a, the SLS will replace the retired Space Shuttle, providing a total thrust greater than the Saturn V although a lower payload mass, to take humans further into deep space than ever before. The LOP-G, corresponding to the envisioned Lunar orbit station, will represent a human-tended vehicle that would serve as a staging point for exploration missions in cislunar space and beyond. The presence of crews implies the need to resupply the station with life support items such as food, water, and oxygen. This, in turn, requires the presence of cargo ships to transport and delivery not only astronauts but also resupply to the Gateway. Considering the present station-refurbishment scenario, cargo spacecraft support ISS operation by transporting equipment, propellant and other supplies, to sustain human presence in orbit. Thus, the third crucial element, i.e. the Orion MPCV, will allow not only the transfer of astronauts but also resupply and equipment up to the LOP-G, thanks to the SLS Interim Cryogenic Propulsion Stage that will provide enough thrust to circularize orbit and commit Orion to a Trans-Lunar Injection, retracing the capabilities previously allocated to a nuclear shuttle.

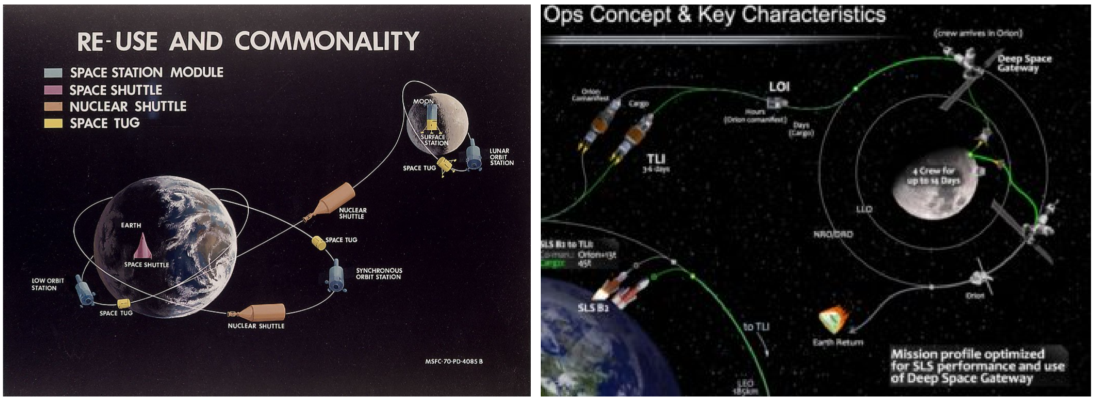

(a) (b)

Figure 1.6: (a) Earth-Moon mission scenario according to the Integrated Program Plan (1970). (b) Earth-Moon mission scenario according to the Global Exploration Roadmap (2017) (credit: NASA).

The initial Gateway architecture will include four main blocks, a Power and Propulsion Element (PPE), a small habitat, an airlock, and a logistic module to enable research, in addition to a robotic arm and capability for spacewalks, each one launched by a SLS co-manifested with an Orion MPCV during the 2023-2026 timeframe. Initially, according to the current transfer capability allocated to the Orion vehicle, the LOP-G will host a 4-members crew every year for missions of at least 30 days at a time. On the other hand, as stated in [7], duration and frequency of crew missions could increase as the Gateway would evolve and additional transportation systems would become available.

Among all the enabling technologies of particular interest for the Earth-Moon mission scenario, the TA2 *In-Space Propulsion Technologies* result of crucial importance [8]. Indeed, it involves all propulsion-related technologies required by space missions after the spacecraft leaves the launch vehicle from Earth, including low-thrust cargo transfer for human exploration support and high-thrust Earth orbit departure for crewed vehicles. These latter two tasks correspond to the first two top technical challenges identified within the TA2, in priority order:

(a) SLS (b) LOP-G

(c) Orion MPCV

Figure 1.7: Earth-Moon mission scenario main elements (credit: NASA/Boeing).

1. *High-Power Electric Propulsion Systems*: develop high-power electric propulsion system technologies and more efficient in-space transportation systems, thanks to the higher propellant efficiency than other in-space propulsion technologies, enabling high-Δv missions involving station-keeping for a wide range of spacecraft and orbital maintenance, transfer of heavy payloads in Earth proximity and deep space, sample returns, and pre-placement of cargo for human exploration missions.

2. *Cryogenic Storage and Transfer*: Enable long-term storage and transfer of cryogens in space and reliable cryogenic engine operation for all mission phases, including Earth departure, destination arrival and following safe return. It includes also the propulsion systems on spacecraft, upper stages, and Moon/Mars landing and ascent vehicles, as well as the propellant transfer between refueling stations, reducing related operational costs.

The second technical challenge can be directly related not only to the development of the SLS upper stage, i.e. the Interim Cryogenic Propulsion Stage, but also to support human missions towards Mars, which: (i) will require long-term storage of propellants; (ii) will presumably need more cryogenic propellant than can be reasonably carried to orbit in a single launch; (iii) will provide on-orbit refueling of vehicles operating in Lunar or Mars environment, eventually exploiting In-Situ

Resources Utilization (ISRU) propellants; and (iv) will enable launch of deep space vehicles, reducing their mass and corresponding launch costs. On the other hand, NASA, together with the other ISS partner agencies and industries, has selected the high-power Solar Electric Propulsion (SEP) as propulsive core of the PPE to maintain the LOP-G position as well as move it between lunar orbits as needed. Efforts all around the world have been done towards improving the capabilities and exploitability of this enabling technology for different fields of application and considering several class of power, from few Watts up to 20 kW and beyond. The current interest related to enhancing the deployment of the first element of the LOP-G has given a further and more significant push towards the development and following validation and qualification of high-power SEP. In particular, among all different electric thruster typologies, Hall Effect Thruster (HET) seems to represent the most suitable choice thanks to its unique balance among Specific Impulse (Isp) and thrust level, easy scalability, low-risk associated to their operations and low-cost with respect to other possibilities, e.g. Gridded Ion Engines.

As stated in [9], to reduce the number of development and validation efforts and mission costs, as many architecture elements as possible should be common to multiple destinations, such as engines, power systems, habitats, etc.. Moreover, as anticipated before, high-power electric propulsion has been identified as a crucial technology for low-thrust transfer of heavy payloads in high-Δv missions to support human explorations in Deep Space. On the other hand, it is important to highlight that the major drawback of electric thrusters is represented by the capability of generative quite low of thrust at very high power demand. Thus, current technology does not allow to exploit (high-power) SEP for manned spacecraft. However, separating cargo from crew could allow to reduce the crewed vehicle mass, as well as the launch cost, and to relax the transfer duration for the cargo module, recognizing that most of the cargo is not time-critical. Hence, combining the design and validation efforts towards the realization of a reliable high-power HET to propel the LOP-G, the same technology could be also envisioned beyond the development of an innovative transportation system for the transfer of heavy payloads. Moreover, the interest in developing new transportation systems in support to the Orion spacecraft has been confirmed by NASA when on October, 23 2018 published a request-for-information seeking input from US companies regarding logistic requirements to supply the LOP-G at the end of understanding service options to transport cargo, equipment and other goods like food to and from the orbiting spaceship [10]. A first possibility could be represented by modifying the cargo-ships currently exploited to resupply and support the ISS, such as the American Cygnus, the Russian Progress or the Japanese H-II Transfer Vehicle (HTV), improving their capabilities to sustain the higher Δv and radiations amount characterizing the Earth-Moon mission scenario. Another possibility could be inherited, again, from the Integrated Program Plan. Indeed, a reusable space tug was already envisioned as additional transportation system providing sustainment to both Earth and Lunar orbit stations and extending the capability of the Space Shuttle. Being reusable, once released in orbit, it would remain operative for multiple missions, providing on-orbit servicing and manned/unmanned transfer capabilities.

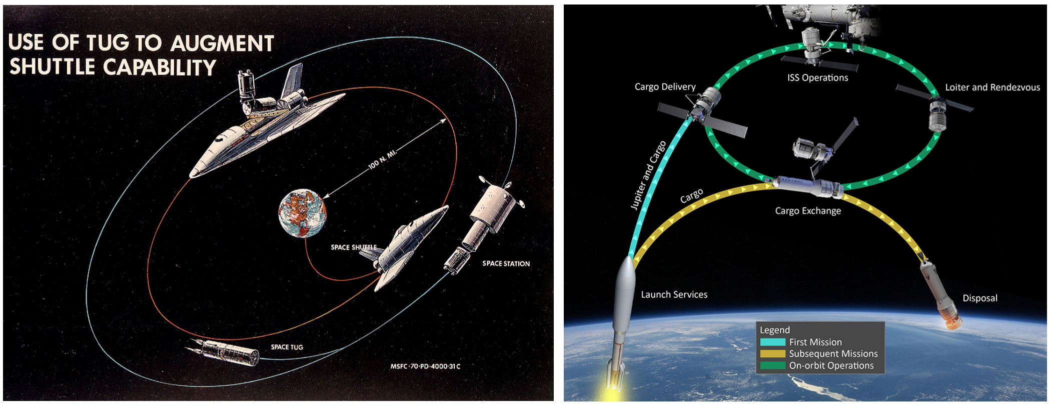

(a) (b)

Figure 1.8: (a) A reusable space tug to augment Space Shuttle capability and to support the space station in LEO according to the Integrated Program Plan (1970) (credit: NASA). (b) The Lockheed Martin space tug, i.e. Jupiter, to support the ISS (2015) (credit: Lockheed Martin).

In particular, for resupply transfer, the space tug was supposed to retrieve cargo modules in LEO directly from the Shuttle cargo bay exploiting a robotic arm, as represented in Figure 1.8a. An analogous concept have been already proposed by Lockheed Martin back in 2015 with the Jupiter spacecraft, i.e. a modular general-purpose space utility vehicle, combining their spacecraft bus with a robotic arm supplied by Canada's MacDonald Dettwiler Associates (MDA) and a pressurized module built by Thales Alenia Space - Italy. This reusable space tug was primarily proposed for cargo delivery to the ISS within a NASA commercial-cargo competition, following a closed-loop mission profile as the one represented in Figure 1.8b. Moreover, Lockheed Martin envisioned to extend the same concept well beyond the ISS and LEO, towards Mars, picturing *"a future of interplanetary shipping lanes to the Moon and to Mars, with autonomous vehicles carrying supplies and scientific instruments and construction materials for habitats, robots in orbit for fueling, repairing, repositioning satellites"*, as stated by James Crocker, Lockheed Martin Vice President.

Combining all the needs previously introduced in technological, operational and economic terms, an innovative space transportation system to support the replenishment of the LOP-G and to extend its usability in terms of crew permanence on board the Gateway is proposed in this Thesis. The so-called Lunar Space Tug (LST) has been conceived as a reusable, unmanned space tug able to transfer heavy payloads among Earth orbits and the Cislunar station thanks to the cargo-transfer capabilities enabled by high-power HETs. Being designed as tug, once reached its nominal orbit, the Lunar Space Tug (LST) should remain operative over a lifespan of at least 10 years, providing the propulsive capabilities to carry multiple times cargo modules, containing equipment and other goods, e.g. water and food, from their injection (Earth) orbit up to the LOP-G, before self-disposal at the end of its lifetime. At this end, the LST should be capable of autonomously rendezvous and mating with both resupply module in Earth proximity and with the LOP-G, eventually exploiting the robotic arm equipped on board the station. Thus, the spacecraft should include Guidance Navigation and Control (GNC) capabilities to properly fulfill Automated Rendezvous and Docking (ARVD) tasks. Moreover, to guarantee the reusability, the LST should be able to perform on-orbit refueling operations, relying either on fuel depot or dedicated refueling systems. Hence, the LST could be launched on commercial rockets (almost) empty and then, be refueled once reached its operative orbit. To extend the usability of this alternative transportation system, the LST should represent a reliable, low-cost solution, able to conform with the already available launch and ground infrastructures and relying on state-of-the art technologies for thrust and on-board power generation. Furthermore, it should be equipped with an International Docking System Standard, to allow both docking with cargo modules and berthing with LOP-G, following the current standards adopted for the ISS and extended to the future Gateway. According to these envisioned capabilities, the LST could represent a valid alternative to fulfill all the requirements identified by NASA as the ones required for the logistic spacecraft capable of carrying pressurized and unpressurized cargo to and from the Gateway, as outlined in [10]. A dedicated multi-input/multi-output design tool, i.e. the so-called MIssion and Space Systems (MISS), has been developed to provide a easy-to-use and reliable software suite able to define a preliminary, detailed design of the LST spacecraft, in compliance with the inputs coming from the high-level mission analysis and the requirements and constraints defined by the stakeholders and intrinsic to the mission itself. The underlying idea was to build a flexible environment where it could be possible to analyze different case studies, each one related to different needs coming from the crew permanence on-board the LOP-G, with respect to several nominal working points of a selected high-power HET and corresponding Propulsion Subsystem (PROP) architecture. The main outputs are given in terms of Δv, mass, power and mission budgets, obtainable thanks to ad-hoc analytical models implemented in a MATLAB environment. Moreover, MISS has been conceived as a flexible design tool, able to assess the sizing, at component level, of different spacecraft based on high-power electric propulsion, thanks to standardize interfaces both for mission definition and propulsive technology envisioned. Last, among all the LST design solutions analyzed, MISS allows to identify the optimal configuration via a trade-off analysis in order to obtain the LST design which not only complies with the mission and system requirements and constraints but also minimize spacecraft mass, propellant consumption and power demand, to reduce the cost of the LST mission.

In terms of enabling technologies, the LST shall mainly rely on two TAs identified in [8]: (i) TA2 *In-space Propulsion Technologies*, in terms of high-power electric propulsion for low-thrust cargo transfer of heavy payloads; and (ii) TA4 *Robotics, Tele-Robotics, and Autonomous Systems*. The latter focuses on several key tasks for the future of robotics and unmanned missions enhancing performance in terms of sensing, piloting, driving, manipulating, and ARVD, developing cooperative and safe human-robot interfaces, and improving autonomy to increase the independence of human crew from Earth-related assets and resources. From an operational viewpoint, nowadays many rendezvous and docking platforms include automation and require very little oversight and interaction from ground mission control. Current unmanned spacecraft visiting the ISS perform a great deal of lower-level functions automatically. However, ground control is still heavily in the loop. The advancement of robotics and autonomous systems will be central to the transition of space missions from current ground-in-the-loop (geocentric) architectures to self-sustainable, independent systems. This represents a key step, necessary for outer-planet exploration and for overcoming the many difficulties of interplanetary travel. In particular, all the scenarios that space agencies have currently envisioned in the new space exploration program have one thing in common: each mission architecture shall heavily rely on the ability to rendezvous and mate multiple elements in space [11]. For example, there is an active interest in orbital debris removal, on-orbit refueling and servicing, and repair missions. As these missions will become more and more popular, the number of rendezvous and docking class operations will increase dramatically. Longer term concepts will also include the assembly of human outposts, e.g. the LOP-G, or supply depots. In order to meet the exploration enterprise goals of affordability, safety and sustainability, the critical capabilities of rendezvous, capture and in-space assembly must become *autonomous*. For these critical capabilities to become routine, a much more reliable ARVD capability must be employed [12]. Moreover, since an always increasing number of proximity operations would be performed in weak-gravity field and non-circular orbits, the classical Hill Clohessy-Wiltshire (CW) paradigm for spacecraft relative motion and GNC algorithms shall be substituted with more flexible and reliable strategies able to deal not only with typical ARVD operational safety and pointing/aligning constraints but also with external disturbances due to the environment, e.g. Solar Radiation Pressure (SRP) or not well-known or well-modeled gravity fields. An additional challenge for ARVD is represented by the need to handle constraints in the presence of *uncertainty*. For example, thruster firings and camera measurements can introduce uncertainties in relative state knowledge and control accuracy. As the spacecraft nears its target, these uncertainties can induce violations in any of the aforementioned mission constraints. Hence, one should embed in new ARVD algorithms the capability to handle any expected uncertainty directly, i.e. incorporating strategies to handle all known unknowns. The control problem formulation encapsulates physical limitations, law- and safety-induced restrictions, and performance specifications. Safety and implementation-related aspects revolve around a number of issues, the most important of which are *reliability*, *verifiability*, and *real-time computational applicability*. Though some of these innovative control techniques may not be implementable on current space-qualified flight computers, the natural increase in on-board computational power and the use of multiple processors with algorithm parallelization could enable their use in the not-too-distant future. Therefore, priority in research must first be to develop (quasi) robust solution methods for the right problems with appropriate constraints. Subsequently, these algorithms should be customized for flight implementation. Finally, a rigorous process (preferably combined with experimental/flight testing) should be established for solution verification and validation.

From an operation viewpoint, the LST would be called to perform multiple ARVD maneuvers in different environments and with different target vehicles during its lifetime. Thus, a relevant part of this Thesis has been dedicated to the design and validation of different MPC techniques aiming to demonstrate the required reliability and ability to satisfy safety and operational constraints in the presence of uncertainty, inherited for instance from inaccurate system dynamics modeling, and persistent disturbance, via simulation and experimental campaigns. First, for design purposes, it is mandatory to have a reliable and realistic simulation environment where: (i) reproducing both chaser and target vehicles dynamics, including all the uncertainty and disturbance sources affecting the spacecraft and its dynamics during the ARVD maneuvers; and (ii) verifying and validating the effectiveness of the control strategies envisioned for LST attitude and orbital control in both Earth environment and Cislunar proximity. Thus, the Simulated Trajectories for Automated Rendezvous (STAR) 6 Degrees of Freedom (DoF) orbital simulator has been developed in a MATLAB/Simulink environment as a reliable and flexible software suite where it is possible to preliminarily validate the different MPC algorithms proposed in this work applied to the optimal LST design solution identified exploiting MISS, combining the features of its Attitude and Orbit Control Subsystem (AOCS) with requirements and constraints coming from the mission and system itself. Moreover, as required by the current guidelines for new GNC algorithms previously introduced, the three MPC control schemes have been further experimentally validated at the Spacecraft Robotics Laboratory of the Naval Postgraduate School (NPS). The main goal was to verify the effectiveness and real-time implementability compliance of these algorithms with space-qualified hardware as the first step for validating their computational applicability.

The reminder of this Thesis is organized as follows. Chapter 2 provides an extensive overview of the LST mission architecture, starting from the detailed description of all systems involved in the space tug scenario and highlighting the interrelations and constraints enforced. Moreover, a preliminary definition of the

LST spacecraft is introduced exploiting the classical tools of System Engineering, outlining the subsystems required to fulfill the functionalities identified and delineating the LST scenario and, consequently, its traffic plan. In Chapter 3, the MISS design tool architecture and mathematical models implemented are thoroughly presented, highlighting the work logic behind the software suite as well as the impact of exploiting high-power electric propulsion on the design of the spacecraft. The peculiarities of the LST ARVD maneuvers are presented in Chapter 4, recalling the main constraints enforced during these proximity operations. Then, a complete and detailed overview of the STAR simulation tool is provided, presenting all the analytical models exploited to: (i) enforce the LST design and all mission and operational constraints; (ii) simulate chaser and target vehicles rotational and translational dynamics in highly-elliptic orbits; (iii) reproduce the disturbance environments and the parametric uncertainty identified; and (iv) control strategies exploited for managing LST AOCS actuators. On the other, the three MPC algorithms proposed and exploited for controlling LST attitude and orbital dynamics are thoroughly described in Chapter 5 from a theoretical point-of-view. In particular, a new general framework for offline-sampling based Stochastic Model Predictive Control (SMPC) is proposed where parametric uncertainty and additive, persistent disturbance are contemporary included. Thus, first the finite horizon receding optimal control problem is introduced, starting with a suitable formulation of the constraints through an offline uncertainty sampling approach. Thereafter, the Offline Sampling Stochastic Model Predictive Control (OS-SMPC) scheme algorithm is introduced, and its main theoretical properties are summarized and proved. Chapter 6 provides the main outcomes of this Thesis. First, the three LST scenarios analyzed are described and the different spacecraft design solutions are presented, once filtered those compliant with mission and system constraints. Then, the optimal LST solution is selected via trade-off analysis to minimize the spacecraft mass, propellant consumption and transfer duration, identifying the corresponding optimal nominal operational point for the propulsive technology and the LST architecture exploitable for evolving resupply needs. For the optimal spacecraft design, the ARVD maneuvers with the cargo module in Earth orbit and with the LOP-G in Lunar proximity have been simulated exploiting STAR and applying the three different MPC strategies proposed. Last, the experimental campaigns performed for the real-time applicability validation of the control algorithms are extensively described. Moreover, the flexibility of the MISS design tool with respect to different mission scenarios, all involving electric spacecraft based on high-power HETs, is validated in Appendix A. On the other hand, Appendix B provides the results obtained via Software-In-the-Loop (SIL) and Hardware-In-the-Loop (HIL) simulations applying the three MPC control strategies proposed for the LST to UAV path planning applications in order to further validate their effectiveness and real-time computational applicability considering systems, i.e. UAVs, typically characterized by faster dynamics and less performing hardware.

Chapter 2

The Lunar Space Tug

2.1 The Lunar Space Tug Mission Definition

System Engineering dates back to 1940's when the Bell Telephone Laboratory used this term for the (presumably) first time once realized that the combination of satisfactory components does not necessarily imply the realization of a satisfactory system. The increased complexity of systems developed between the mid 40's and 50's brought System Engineering to world prominence, as witnessed in [13]. Several American Universities, such as MIT, Harvard, and Standford, introduced courses in System Engineering and industries started training new engineers in this challenging direction to develop new methods and techniques which should have enhanced the System Engineering effectiveness. In 1990, the National Council on System Engineering was founded to address the improvements in System Engineering. In 1995, the increasing involvement of non-US engineers brought the company to change the name in the well-known International Council on System Engineering (INCOSE) [14]. The first INCOSE System Engineering Handbook [15] was published in draft form in 1994 for internal review and then publicly distributed in 1998. In parallel, NASA has released the draft version of the NASA System Engineering Handbook [16]. In the NASA/SP-6105, System Engineering principles and alternative approaches are provided to streamline the System Engineering processes to get from a concept to a design and then, to a final product, following the NASA program/project lice cycle. In 1999, the first version of the Space Mission Analysis and Design (SMAD) [17] was published. It gained widespread use as a text and reference thorough the astronautics community, providing a *user-friendly manual* for designing a space mission to meet a broad set of objectives and making a preliminary assessment of overall performance, size, cost and risk.

The SMAD methodology is based on an iterative and recursive process, which allows to refine the system analysis and design gradually. The conceptual design process, corresponding to the project life-cycle Pre-Phase A (see [16] for further details). It starts with the definition of the mission statement, i.e. a concise and clear representation of the mission purpose and its high-level objectives, including key-performance parameters and technical and programmatic constraints. Applying the SMAD methodology to the LST, the following mission statement has been derived:

To improve deep space access capabilities through reusable transportation systems exploiting Solar Electric Propulsion to support the Lunar Orbital Platform-Gateway replenishment.

It includes the main mission objectives: (i) to support the LOP-G providing he replenishment for the hosted crews; (ii) to develop a reusable transportation system able to transfer heavy resupply modules from Earth environment up to the Cislunar space; and (iii) to exploit SEP to provide Electric Orbit Raising (EOR) capabilities. To establish the foundation of the system design, the stakeholder analysis has been performed. First, the organizations who are affected by or are accountable for the project outcomes have been identified. Since the LST is envisioned to support the future Gateway, which shall be the result of common efforts among the current ISS international partners, i.e. NASA, ESA, Roscosmos, JAXA and CSA. These space agencies have been identified as main sponsors, operators and end-users. Moreover, their commercial partners, private space companies and suppliers have been envisioned as secondary sponsors and operators, providing services and resources for the system operation and developing crucial technologies, in addition to establishing funds availability and schedule bounds. The stakeholders' expectations have been derived starting from two technical reports released in the last couple of years and providing a thorough overview of the current and future space community plans. The newest version of the Global Exploration Roadmaps [7] reaffirms the interest of the 14 space agencies composing the ISECG into enhancing the deep space exploration towards Mars and beyond, pushing humans further than LEO. To achieve this exceptional goal, international collaboration has been intensively promoted between space agencies and private companies, embracing public-private partnerships to fill the technological gap mandatory for the future human exploration. In line with these challenging goals, the NASA OCT and its appointed steering committee have identified three technology objectives collecting the highest-priority technological challenges for the next 5-30 years, as presented in the NASA Space Technology Roadmaps and Priorities [8]: (i) extend and sustain human activities beyond LEO; (ii) explore the evolution of the solar system and the potential for life elsewhere; and (iii) expand our understanding of Earth and the universe in which we live. Furthermore, in the last decade, developing *reusable* space systems, which can rely on existing ground and launch infrastructures, and deriving common standards have become one of the paramount necessity to reduce the cost of new space missions towards the deep space. In compliance with all the aforementioned trends, representing the primary stakeholders' expectations, the secondary objectives have been derived and, together with the primary ones, they represented the main mission and system drivers for the next design phase.

Typically, a space mission can be divided into three segments, each one including several space elements with shared functional commonalities. They are: (i) the *ground segment*, including all those elements supporting the mission operations from ground; (ii) the *launch segment* providing the infrastructures and the systems for the launch phase; and (iii) the *space segment* involving the spacecraft, the satellites and all the infrastructures that contribute to the space operations and on-orbit payload operability. Exploiting the typical tools of the Functional Analysis, such as Functional Tree and Function/Product Matrix (see [18]), the main elements included in each of the former segments, i.e. the so-called building blocks, have been identified with respect to the LST mission objectives and expectations. They are reported in Table 2.1. A thorough overview of all the segments and corresponding building blocks is provided in Sections 2.1.1-2.1.5 whereas the LST spacecraft is described in Section 2.2. Last, Figure 2.1 provides an overview of how the building blocks are interconnected.

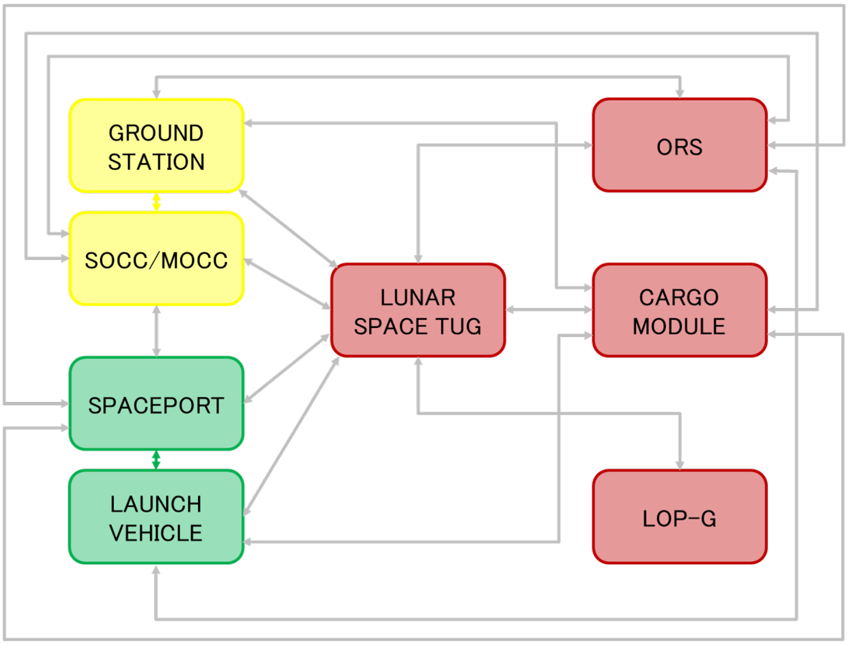

Figure 2.1: Function block diagram at system level.

2.1.1 Ground Segment

The ground segment is in charge of sustaining the elements of the space segment during all the mission phases, collecting data and telemetry, monitoring their

Table 2.1: Mission segments and related building blocks.

Segment	Building Block	Symbol
Ground Segment	Spacecraft Operations Control Center/ Ground Station	
	Mission Control Center	
Launch Segment	Spaceport	
	Launch Vehicle	
Space Segment	Lunar Orbital Platform-Gateway	
	Cargo Module	
	On-orbit Refueling System	
	Lunar Space Tug	

health conditions, tracking them to determine the orbital position, and providing the required command and control capabilities to support mission and logistics operations. It is composed by ground stations, which represent the communication link among Earth and the space segment, and control centers, each one devoted to a precise set of tasks. Typically, three types of control centers can be found, as described in [17]: (i) the Space Operation Control Center (SOCC) devoted to monitor the space segment, analyze data and telemetry, and to command the space elements; (ii) the Payload Operations Control Center (POCC), a control center dedicated to payload and on-board instruments but which commands is dependent from SOCC approval; and (iii) the Mission Control Center (MCC), which is in charge of planning, scheduling and operating the mission and related logistics and resources. In this work, the ground segment has been functionally designed to mainly support the LST and its operations. Since the cargo module has been considered as a *passive* payload, which control and monitoring tasks are directly demanded to the LST itself, the ground segment does not include the POCC. On

Figure 2.2: ESA tracking station network (credit: ESA).

the other hand, several ground stations shall be exploited to support the mission, in combination with both SOCC and MCC. Moreover, since the LST represents the core of the mission and the other elements involved the ground segment have been functionally defined to support the LST mission, the ground segment is assumed to be composed by ground stations, SOCC and MCC. In compliance with the stakeholders' expectations, instead of building dedicated ground systems and facilities, the LST shall rely on existing ground support networks. Moreover, assuming that the tug would be mainly an European asset, in the sense that ESA could represent the principal investigator, Figure 2.2 provides an overview of the ESA's tracking station network, i.e. Estrack, the network of ground stations, which provide links between satellites and the ESA SOCC/MCC, i.e. the European Space Operations Center, located in Darmstadt, Germany.

2.1.2 Launch Segment

The launch segment includes both the launch vehicle and the launch infrastructures, which are typically referred as spaceport. In particular, the spaceport includes all the facilities for support during launch operations from ground and one or more launch pads, from where the space rocket is vertically launched. On the other hand, the launch vehicle provides the required transportation capabilities to carry a space system from Earth surface into space, supplying the proper Δv to inject the payload into the desired orbit with a suitable attitude while protecting the spacecraft from the harsh ascent environment. Typically, the launchers are expendable vehicles designed for carry a payload into space once and, after the separation

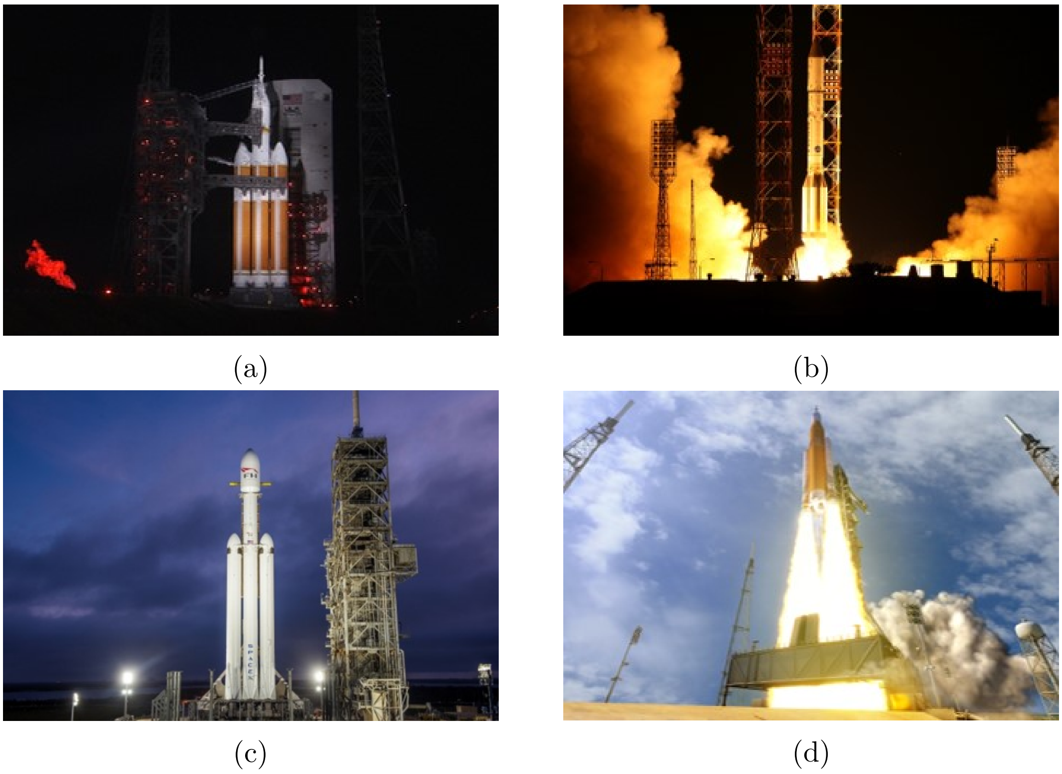

(a) (b) (c) (d)

Figure 2.3: (a) Launch of Orion Exploration Flight Test 1 by Delta IV Heavy, December 2014 (credit: ULA); (b) Proton-M launching AsiaSat 9 on September 2017 (credit: Roscosmos); (c) SpaceX Falcon Heavy first flight on February 2018 (credit: SpaceX); and (d) rendering of the NASA SLS (credit: NASA).

phase, disintegrate during the atmospheric reentry. Following the trend of developing reusable systems to improve the missions cost-effectiveness, space agencies and private companies are currently building reusable launch vehicle, designed to be recovered and launched again. Actually, the NASA Space Shuttle represents the first attempt in this direction, a human spaceflight vehicle composed by the reusable orbital vehicle, the expendable external tank and two reusable solid rocket boosted. On December 2015, after several failing attempts, SpaceX was able to recover for the first time the Falcon 9 upper stage B1021 thanks to a controlled vertical re-entry and landing. The same first stage has been used again in March 2017 and, after the second reentry, it was retired. During the same mission, SpaceX was able to recovery the payload fairing as well. The last challenge was represented by the recovery of both the Falcon Heavy side boosters, which safely and simultaneously landed on the Landing Zone 1 and 2 of the Cape Canaveral Air Force Station (see Figure 2.4).

Moreover, the launch vehicles can be classified according to their size and payload capabilities, as described in [19]: (i) small up to 2 t; (ii) medium from 2 to 20

Figure 2.4: The synchronized landings of two of the Falcon Heavy boosters on the Landing Zone 1 and 2 of the Cape Canaveral Force Station on February 6th, 2018 (credit: SpaceX).

t; (iii) heavy from 20 to 50 t, such as the Delta IV Heavy [20] in Figure 2.3a and the Russian Proton-M [21] in Figure 2.3b; and (iv) super heavy higher than 50t, e.g. the SpaceX Falcon Heavy [22] in Figure 2.3c and the NASA SLS [23], which rendering is depicted in Figure 2.3d. Both super heavy launch vehicles have been conceived to support the future missions towards the deep space.

As anticipated before, the LST is called to transfer heavy resupply modules, i.e. payload mass higher than 2 t, from Earth proximity up to the LOP-G and shall be compatible with multiple launch systems to enhance launch efficiency and providing some leverage in launch cost negotiation, primary exploiting European assets. Thus, the ArianeSpace heavy launch vehicles, i.e. Ariane V ECA (Figure 2.5a) and Ariane VI (Figure 2.5b), have been considered for the next design phase. The performance of these two launchers, used as reference, can be found in [24] and [25], respectively.

2.1.3 The Lunar Orbital Platform - Gateway

The LOP-G is a crew-tended outpost orbiting around the Moon, providing support to the activities of ISS partners and space commercial companies in Lunar proximity. Envisioned as the first step to bring humans beyond LEO again, towards the Moon and Mars, as stated in [6] and confirmed in its newest version [7], the LOP-G can be considered as the natural evolution of the ISS. Born from the combination of knowledge and experience gained in LEO with the technological advancements required to sustain the deep space environment and reduce Earth-dependability, the Gateway is conceived also as the control center to: (i) manage

(a) Ariane V ECA VA242

(b) Ariane VI

Figure 2.5: Ariane V ECA VA 242 (launch date: April 6th 2018, payload: DSN-1/Superbird-8 and HYLAS 4 satellites, injection orbit: GTO) and a rendering of Ariane VI. (credit: ArianeSpace).

tele-operations on the lunar surface; (ii) orbiting spaceport for ascent and descent vehicles, either manned and cargo, traveling between LOP-G and Moon surface as described in [26]; and (iii) Lunar in-situ resources transfer, e.g. propellant to support future human space exploration [27]. Indeed, envisioning the establishment of a semi-permanent outpost on the lunar surface (see [28] for further details), this outpost should be able to rely on ISRU and on the LOP-G support, in line with the current exploration roadmaps [7, 8]. The direct and definitive evidence for surface-exposed water ice in the lunar polar regions, as demonstrated in [29], corroborates the feasibility of these plans. Moreover, a sustainability study has been carried out in [27] relatively to the establishment of a propellant production plant on the Lunar surface that, exploiting large pressurized crew vehicles and fleet of small unmanned rovers, could provide enough propellant to sustain future human space exploration missions.

According to the current plans stated in [30], the Gateway shall host 4 crewmembers for at least 30-days missions once per year, in compliance with the Orion MPCV transfer capabilities (see [31] for further details). According to the current initial plans, the LOP-G shall be composed by 4 elements, as represented in Figure 2.6, providing at least 55 m^3 of habitable volume. The PPE represents the first element of the Gateway to be launched in 2022. The PPE shall provide several key-functionalities, including: (i) power generation and distribution to the LOP-G as well as to the possible external elements/payloads; (ii) attitude control for proper

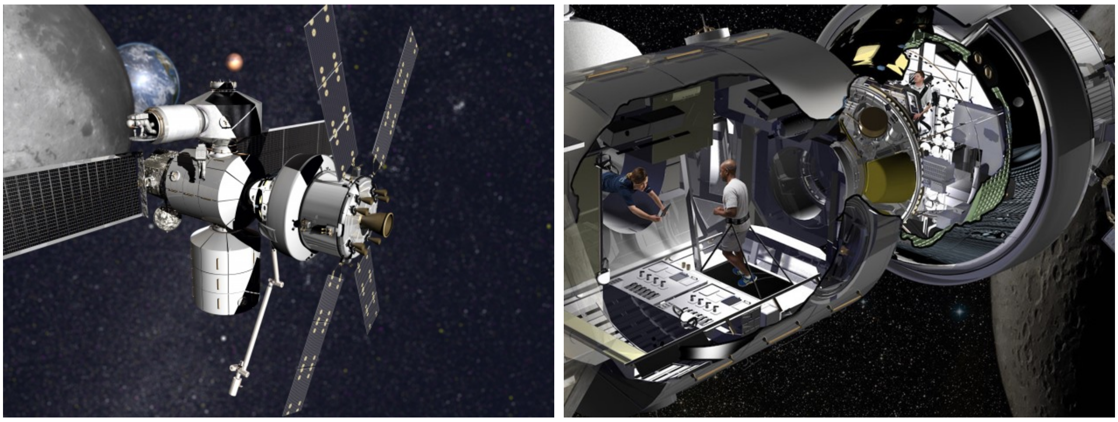

(a) (b)

Figure 2.6: (a) Early concept rendering of Lockheed Martin's LOP-G, with an Orion crew vehicle docked (credit: Lockheed Martin); (b) Lockheed Martin artist's rendering of the NextSTEP habitat docked with Orion as part of a concept for the LOP-G. (credit: PRNewsfoto / Lockheed Martin).

pointing; (iii) propulsive capability for orbit maintenance and possible orbit transfer when the Gateway is uncrewed; and (iv) space-to-ground and space-to-space communication links as well as radio-frequency relay capability to support Extra-Vehicular Activity (EVA) and tele-robotic operation on the Lunar surface. The PPE is intended also as a spaceflight demonstration of advanced SEP technology since the main propulsive core should be based on 50-kW SEP element, composed by multiple either American and European HETs.

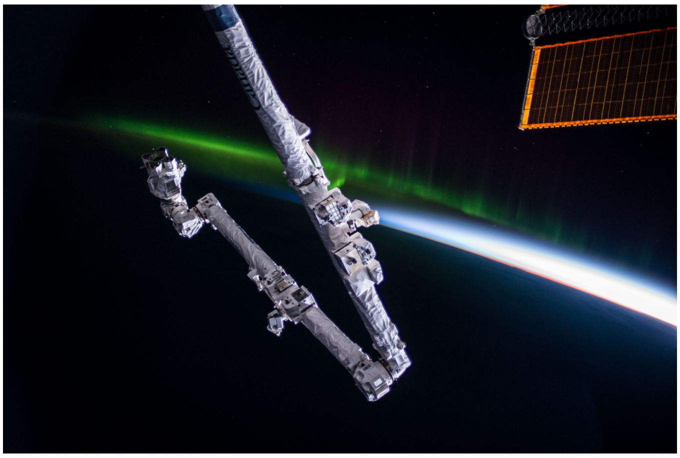

Figure 2.7: Canadarm2 attached to the ISS with an aurora in the background. (credit: NASA).

The second element is represented by the Cislunar Habitation Module, the main habitable module which provides short-duration life support functionalities, docking ports for attachment to the PPE as well as the other Gateway elements and visiting vehicles, and accommodations for crew exercise, scientific tasks and stowage. Moreover, it shall provide external attach points for external science and technology payload. The Gateway Logistics Module allows to extend the habitation capabilities, providing advanced environmental control and life support, waste management, and crew quarters. Moreover, it should be equipped with a Canadarm2-like robotic arm (see Figure 2.7) to extend the LOP-G robotic capabilities for berthing, inspection and maintenance tasks, as described in [31], operated from the Habitation Module.

The Gateway hosting capacity could allow to extend the manned mission duration beyond the minimum, i.e. one month, since its habitable volume corresponds to about 13.75 m^3 per crewmember. Indeed, according to the guidelines provided in NASA-STD-3000 [32], the habitable volume available for each crewmember shall be identified between the top two curves (optimal and performance limit) in Figure 2.8, which delimit the area of the graph in which the crew's performance are enhanced, for mission durations up to 1 year. It is possible to notice that LOP-G available volume (corresponding to the red line in Figure 2.8) is above the optimal curve, for missions up to 2 months, and remains within the designated area up to one year. Hence, the LOP-G exploitation could be enhanced thanks to the adoption of the LST to provide extended replenishment capabilities with respect to the Orion vehicle. Moreover, separating cargo from crew could allow to reduce the crewed vehicle mass, as well as the launch cost, and to relax the transfer duration for the cargo module, recognizing that most of the cargo is not time-critical.

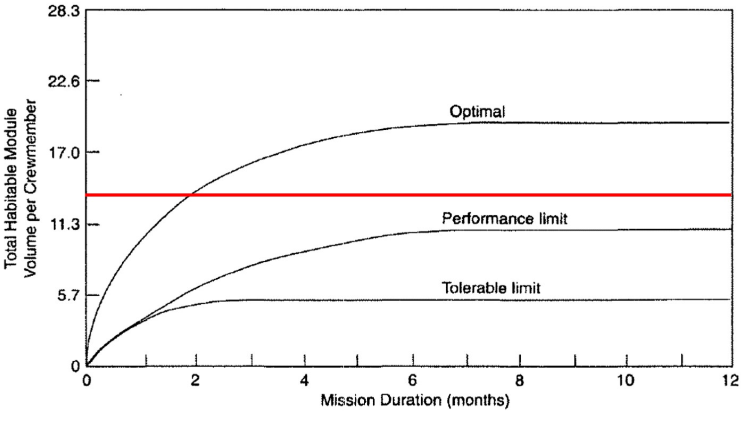

Figure 2.8: Total habitable volume per astronaut guidelines [33].

For the LOP-G location, several studies have been carried on in the last years to select the more suitable orbit with respect to different drivers: (i) stable enough to reduce the attitude and orbit control and maintenance requirements; (ii) easily reachable both from Earth and Moon surface; (iii) guaranteeing the (quasi) permanent communication link with the ground segment, relaying also on Geostationary Earth Orbit (GEO) satellites. At the beginning, the commonly-held ideas was to put the Gateway in the Earth-Moon Lagrangian Point (EML)-1, as presented in [34] and [35]. Then, additional stable orbits such as EML-2 and Distant Retrograde Orbit (DRO) have been proposed [36]. The current strategy envisages that a Near Rectilinear Halo Orbit (NRHO) [37] provides the more suitable conditions, also considering the possibility to move the LOP-G among different locations, such as NRHO and DRO, when Orion is not attached. The reference orbital parameters for the NRHO, set according to [37], are the following: (i) perilune radii: 3232.94 km; (ii) apolune radii: 65799.10 km; (iii) period: 6.66001 days; (iv) 9:2 lunar synodic resonant orbit.

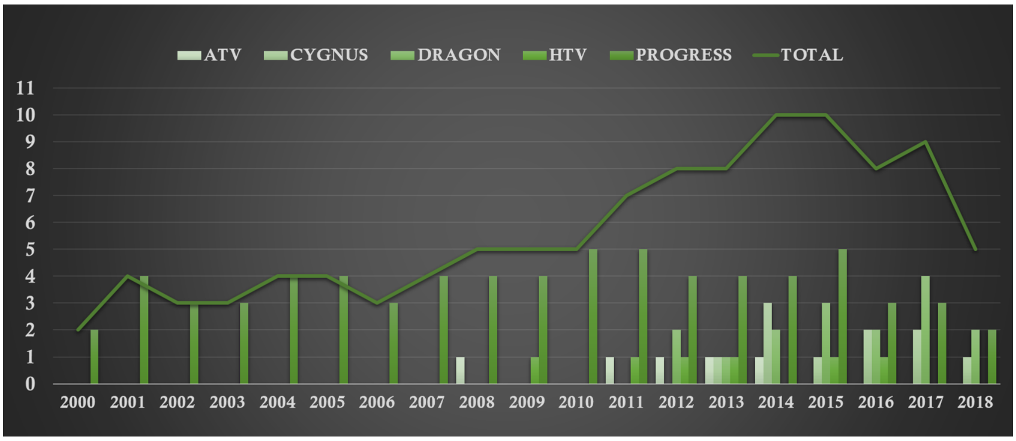

Figure 2.9: Logistics mission to the ISS grouped according to the spacecraft that carried out the mission (updated at: August 2018, source: NASA).

2.1.4 Cargo Module

Since its establishment, every year the ISS has been replenished with the required goods exploiting five different transportation spacecraft: (i) the Russian Progress; (ii) the American Cygnus and Dragon; (iii) the Japanese HTV or Kounotori; and (iv) the European Automated Trasfer Vehicle (ATV). Figure 2.9 provides an overview of all the refurbishment missions since 2000. All these spacecraft share different peculiarities, as anticipated before, among which how food, water, oxygen, and other payloads are transported inside the vehicle. As shown in Figure 2.10, the supplies and experiments are arranged in containers, i.e. cargo transfer bags, stowed inside the pressurized bay of the spacecraft in racks or mid-deck lockers.

Before its mission was shut down in 2011, the Space Shuttle was used as additional resource to transfer resupplies and experiments to the ISS exploiting the

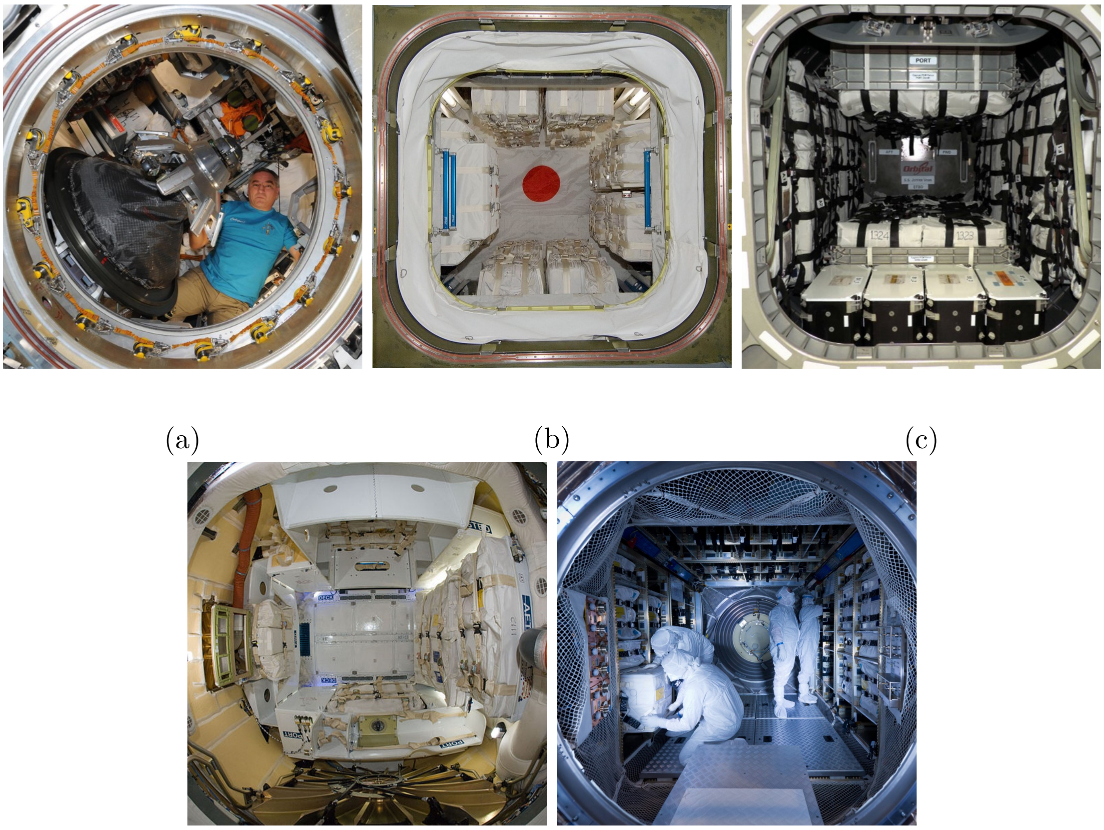

(a) (b) (c)

(d) (e)

Figure 2.10: (a) Inside Progress spacecraft (credit: Roscosmos); (b) Inside HTV (credit: NASA); (c) Inside Cygnus spacecraft (credit: NASA); (d) Inside Dragon spacecraft (credit: NASA); and (e) Inside ATV spacecraft (credit: ESA).

Multi-Purpose Logistic Module (MPLM)s installed in its cargo bay. Three MPLM were designed and built by Thales Alenia Space for the Italian Space Agency (ASI) (see Figure 2.11) and named as famous Italians from history: (a) the Leonardo MPLM, which was used for eight over twelve MPLM missions and has been converted in a Permanent Multipurpose Module (PMM), currently part of the ISS, in 2011; (ii) the Raffaello MPLM, operated for the other four missions, including the last mission of the Space Shuttle; and (iii) the Donatello MPLM, which remained unflown and served to provide spare parts for the other two modules. Analogously to the cargo container of the other transportation systems, the payloads were organized in standardized containers and, once berthed to the ISS, the crew were in charge of unloading the cargo and eventually refill the module with waste and finished experiments, before it was re-berthed in the Shuttle for return to Earth.

Each MPLM is a cylinder-shape container of about 4082 kg of mass, 4.57 m of

(a) (b) (c)

Figure 2.11: (a) Leonardo MPLM; (b) Raffaello MPLM; and (c) Donatello MPLM (credit: NASA).

diameter and 6.6 m of length, providing about 70 m^3 of pressurized volume, 31 of which left for the crew, after the installation of the 16 racks with about 9 tons of payload. They are equipped with a Common Berthing Mechanism (CBM) at one end, as interface with either the Space Shuttle and the ISS, and a grapple fixture for the Canadarm grasping. In the evolved PMM version, additional Multi-Layer Insulation (MLI) blankets, reinforced with Nextel/Kevlar, were installed on the MPLM Leonardo to provide improved protection against micro-meteoroids.

The LST shares some commonalities with both classical transportation systems, such as ATV, being a sort of service module providing the propulsive capabilities to transfer payloads, and the Space Shuttle in the sense of reusability and exploitation of external cargo modules. Indeed, it is not provided with internal pressurized volume dedicated to transfer payloads whereas an external module is attached through the docking/berthing interface to the LST, which provide the thermal, power and communication capabilities to the module during the transfer. For this reason, an MPLM-like cargo module has been considered for the design phase, taking its geometrical and physical features as a reference to estimate the mass of the LST cargo module itself. The main difference is given by the length, which has been assumed as a function of the resupply mass to deliver. In particular, from a statistical analysis of MPLMs data combined with the features of the other space transportation systems pressurized volumes, it has been assumed that 1 m of length allows to store about 1 ton of resupply.

Moreover, combining the data from ISS replenishment mission since 2012, reported in Table 2.2, and the guidelines provided in [33], the presumable resupply demand for the LOP-G has been estimated to about 12.37 kg/person/day (kg/p/d). These references have been adopted during the design phase (see Section 3.1.3 for further details).

Table 2.2: ISS annual replenishment since and average daily need per crewmember since 2012 (after Space Shuttle program closed).

Year	Days	Annual [kg]	Daily [kg/p/d]
2012	366	27900	12.70
2013	365	25700	11.74
2014	365	30900	14.11
2015	366	30100	13.74
2016	365	25000	11.38
2017	365	30400	13.88
2018	212	16300	12.81

2.1.5 On-Orbit Refueling System

The concept of propellant depot dates back to mid 1960's when it was proposed as part of the NASA Integrated Program Plan, as anticipated in Chapter 1. In that scenario, on one side some of the Shuttle orbiters should had served a tanker role refueling the space tugs, as shown in Figure 2.12 and, on the other side, retired space tugs should had been stripped down and turned into tankage to build up a refueling station in lunar orbit. The not-so-visionary scenario was only partially realized over the past 50 years and, in terms of refueling, the orbital depot program was cut back when the NASA short-term goal ceased to include returning humans to the Moon, as stated by the former NASA Administrator Michael Douglas Griffin during a speech to the American Astronautical Society in November 2005.

Figure 2.12: The rendering of a space tug refueling operation through one Shuttle orbiter (credit: NASA).

Since few years ago, once a satellite runs out-of-fuel, the mission is considered terminated. The only two exceptions have been represented by the Hubble Space Telescope and the ISS, both of which are easily to be reached and worth enough to sending people for refueling and extending their lifetime. Until June 2016, when the Chinese Space Agency performed its first satellite-to-satellite the on-orbit refueling test, from the robotic Tianzhou 1 refueling freighter to the China's Tiangong 2 space lab. In the meantime, NASA retraced its steps and in 2011 started the so-called Robotic Refueling Mission (RRM) program, where the ISS twin-armed Canadian robotic handyman, i.e. Dextre, was used in combination to ad-hoc developed tools and an RRM module, containing refueling components and testing interfaces, to demonstrate robotic satellite-servicing technology and techniques. (see Figure 2.13).

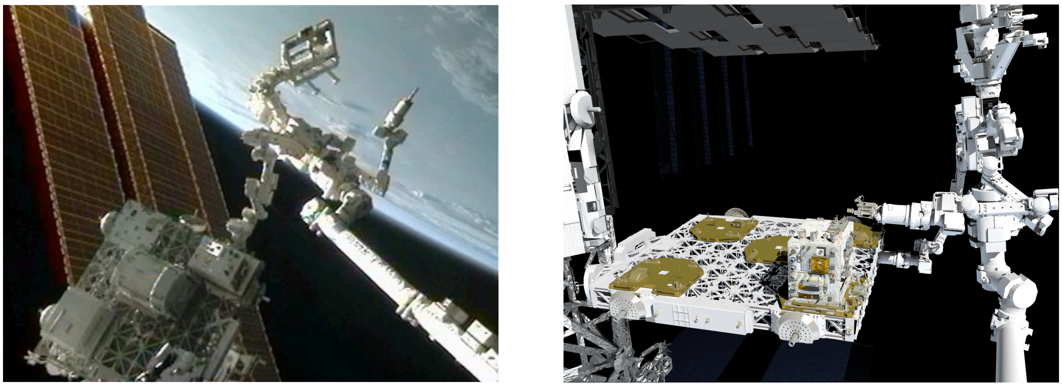

Figure 2.13: The RRM and Dextre outside the ISS (credit: NASA).

As stated in [7], on-orbit servicing and refueling represents one of the crucial enabling technologies to sustain the coming deep space exploration era towards Mars. Significant efforts shall be done in this direction, to establish proper in-space refueling infrastructures, i.e. an orbiting fuel station, providing the required capabilities to enhance also the use of reusable space transportation system while reducing launch costs (see also [38]). Several alternative scenarios, architectures and locations have been proposed in the past years. Some involve very complex assembly operations, as the Boeing multi-launch dual-fluid depot concept proposed in [39]. Others are still innovative but also simpler, e.g. the disposable single-use *pre-depot* and the single-fluid single-launch concepts proposed by the United Launch Alliance (ULA) [40]. Some examples are represented in Figure 2.14.

A second alternative could be represented by a propellant tanker able to deliver single or multiple propellant loads at a specified orbital location and then departs, as proposed in [42]. This last concept has been exploited in this work. The so-called On-Orbit Refueling System (ORS) is first launched and injected in Geostationary Transfer Orbit (GTO), where docks with the LST. Once completed the refueling operation, the LST remains in GTO waiting for the next resupply module while

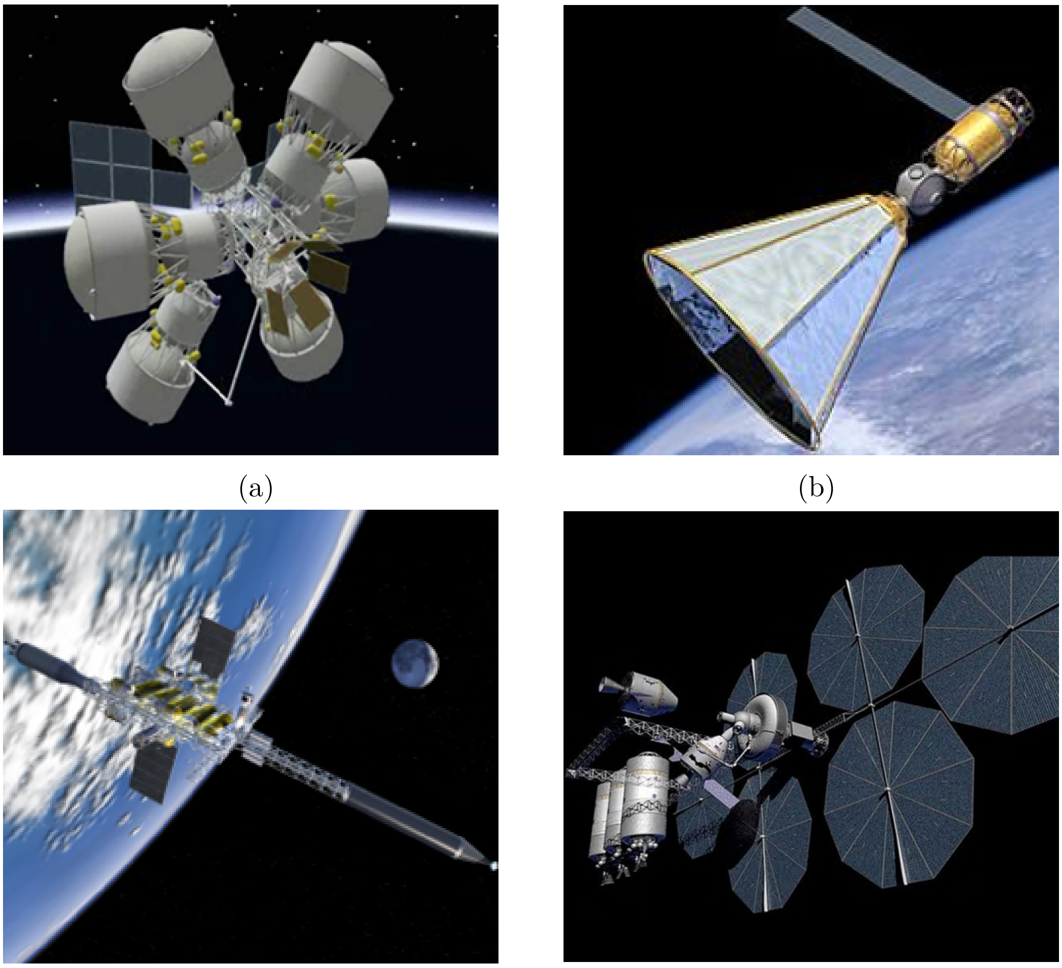

(a) (b)

(c) (d)

Figure 2.14: (a) Boeing multi-launch dual-fluid depot (credit: Boeing); (b) ULA single-fluid single-launch concept (credit: ULA); (c) Shackleton Energy proposal; (d) rendering of propellant depot evolution [41] (credit: NASA).

the tanker departs and eventually burns up in the atmosphere, in a reasonable (and regulated) amount of time. The reasons are multiple, among which the following are the most significant: (i) all the presented fuel station solutions are envisaged to supply chemical-based spacecraft and satellites; (ii) the (still) unknown possible location of the depot does not allow to properly define the LST refueling strategy. Anyway, the on-orbit refueling capabilities of the LST allows to eventually exploit also a future fuel depot for its refueling operations. In this second case, additional analyses should be performed according to the location of the depot and compared with those obtained exploiting a dedicated refueling system.

2.2 The Lunar Space Tug Spacecraft

LST is conceived as a *reusable* transportation system exploiting high-power SEP to rendezvous with heavy cargo modules in Earth environment, make an assessment of their current position, attitude and operational status, capture and move them to the target operative orbit. i.e. the LOP-G NRHO.

As shown in [43], the adoption of SEP has a significant impact not only on the spacecraft design but also on its mission. The use of high-power electric propulsion makes the system less sensitive to mass growth and improves the spacecraft flexibility. Moreover, HETs are characterized by high efficiency, a favorable power-to-thrust ratio and relatively long operation lifetime, which combined with the peculiar high Isp, make this technology favorable with respect to Gridded Ion Engines and less fuel-consuming than chemical thrusters. The cost-effectiveness of this technology is corroborated in [44], where it is highlighted how the significant reduction of propellant demand (with respect to chemical-propelled spacecraft envisioned to perform the same mission) is not only a benefit in itself. Indeed, it also allows to reduces the launch-mass requirements, further decreasing the cost of the mission. All these benefits come at the expense of a much higher power demand, heavier power generators on board to properly convert the solar energy in electric power, and a lower fuel efficiency, which significantly reduces the spacecraft acceleration and broadens the transfer duration. Thus, the classical trajectory and design approaches are not valid anymore and more complex and tailored models have been developed and exploited in this work to properly obtained the preliminary mass, power and transfer duration budgets.

From a functional point-of-view, the LST results composed by the same subsystems typically equipped on-board a chemical-propelled spacecraft. On the other hand, the mass and power breakdowns are significantly affected by the adoption of electric propulsion as described in Chapter 3, where it is highlighted how the considerable power effort moves the typical mass and power balance towards those subsystems that are more influenced, in addition to the PROP itself: (i) the Electrical Power Subsystem (EPS) because of the large amount of power to generate, condition and distribute; (ii) the Thermal Control Subsystem (TCS) due to the large amount of heat to be managed and rejected towards space; and (iii) the AOCS for the precise orientation and control of the spacecraft during both EOR and ARVD maneuvers, in the presence of considerable internal and external disturbances.

2.2.1 Propulsion Subsystem

Exploiting the classical Functional Analysis tools, the main functionalities allocated to the PROP subsystem have been derived to comply with both mission constraints, i.e. adoption of high-power SEP, and stakeholders' expectations, i.e.

maximizing the effectiveness of new technologies development. The PROP subsystem shall provide the thrust for EOR and on-orbit operations, i.e. Δv for orbit corrections, together with steering capabilities to properly orient the thrust direction during the mission according to the mission profile needs. Moreover, it shall support the storage, downstream flowrate and pressure regulation and distribution of the propellant, e.g. Xenon and Krypton. The adoption of high-power SEP requires a cautious handling of the significant amount of electrical power feeding the subsystem. In particular, PROP shall supply the electrical power to its own components while controlling, monitoring and protecting them. Functionally, the PROP subsystem can be renamed as Electric Propulsion Subsystem (e-PROP) subsystem since its core is based on electric thrusters. On the other hand, as thoroughly presented in Section 2.2.3, PROP includes also the AOCS thrusters for the orbit control during ARVD maneuvers and the corresponding Hydrazine tanks, from a physical point of view and internal arrangement. In the follows, this subsystem will be identified as e-PROP.

The e-PROP architecture results strongly affected by the LST primary objective of transferring heavy cargo modules from Earth proximity to the LOP-G. To provide the significant Δv required for this task, the thrust-over-mass ratio shall be maximized. The low-thrust characterizing the electric propulsion technology and the (presumingly) remarkable masses, i.e. cargo plus LST, at stake mean that their ratio is typically very small. Thus, to increase the e-PROP performance, more than one HET shall be exploited. Moreover, to reduce the already strong impact of adopting electric propulsion, a cluster configuration has been envisioned for e-PROP as represented in Figure 2.16. This design choice is corroborated by the need of optimizing the performance of the propulsion subsystem while minimizing mass and cost of the system, as highlighted also in [45]. In this architecture, some components are shared among different thrusters whereas others are dedicated, instead of considering a classical string-architecture, as the one proposed in [46]. Indeed, in the latter configuration, each thruster string includes all the main components whereas only and propellant tanks are shared. Hereafter, a detailed description of the main components included in the e-PROP design and how they are related to each HET equipped on board the LST is provided:

- Thruster Unit: consists of one 20kW-class HET and the corresponding Pointing Mechanism (PM), which provides the thruster with steering capabilities for modifying thrust direction. The number of operative HETs in the cluster, contemporary operated, can vary from 1 up to 4 whereas the number of stand-by thrusters is defined within th MISS design tool, comparing the total mission duration with the HET lifetime. Furthermore, an additional HET is introduced for redundancy. As anticipated before, each e-PROP architecture is characterized not only in terms of number of thrusters but also by peculiar performance related to the working point selected for the HET over

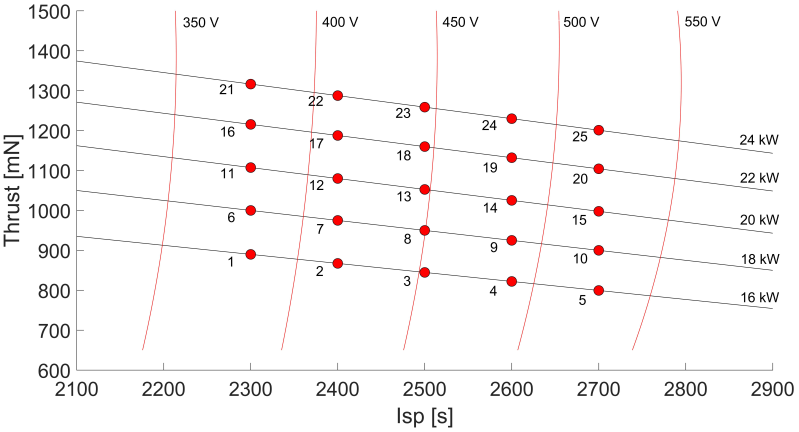

Figure 2.15: HET reference performance map: iso-power black curves and iso-voltage red-curves.

its reference performance map. As shown in Figure 2.15, 25 working points have been identified over the map, each one characterized by peculiar thrust, Isp, input power, input voltage, and propellant mass flow. Moreover, each working point has been differentiated, considering 5 different lifetime levels, from 20000 up to 40000 hours, obtaining a total of 125 design alternatives. The mass of each Thruster Unit is about 45 kg;

- Power Processing Unit (PPU): is in charge of providing electrical power supply, control, monitoring and electrical protection for all the e-PROP components. A power distribution architecture, which allows to connect to the same PPU up to 4 HETs, only one of which operative, has been considered for the design phase. The mass of each PPU is about 40 kg;
- Flow Control Unit: is a highly integrated feed system that accepts unregulated propellant, i.e. typically Xenon, directly from storage tanks and outputs precise, throttleable flow through several channels. Each HET is equipped with its own flow control unit, which mass is about 6 kg;
- Pressure Regulator (PR): is a control valve that guarantees the regulation and control of flow pressure according to the required level, i.e. maximum 150 bar at 55°C if Xenon is adopted. The e-PROP is equipped with one PR plus one for redundancy;
- Tank: is a pressure vessel used for the storage of high-pressure propellant, Xenon in this case, which is later supplied to the electric thruster via a pressure regulator for the entire duration of the mission. The Cobham composite Xenon propellant tank, i.e. the largest ever flown, has been considered, which

main features, inherited from the Bepi Colombo's ones [47], are here reported: (i) fill pressure of 86 bar; (ii) diameter at spacecraft interface of 907 mm; (iii) length of 673 mm; (iv) tank plus skirt weight lower than 22 kg; (v) operating temperature among 25°C and 50°C.

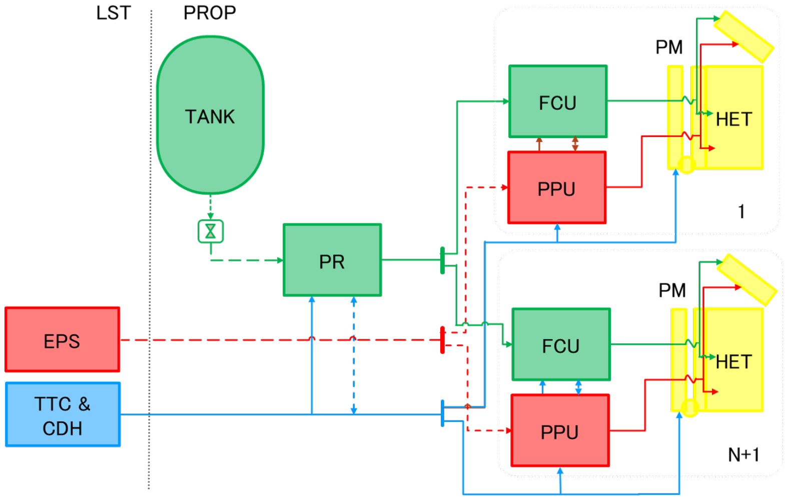

Figure 2.16: e-PROP physical block diagram [48].

HT20k Hall Effect Thruster

HETs are devices in which the propellant particles, ionized by electric discharge, are accelerated through an electrostatic field to generate thrust. The thruster magnetic field, interposed between the electrodes, induces in the plasma the so-called Hall current, which gives the thruster its name, and allows the establishment of the electric field inside the plasma without the need of immersed grids. Among all different e-PROP concepts, HET technology combines a high efficiency, a favorable power-to-thrust ratio and a relatively long operational lifetime. These factors, together with a significant heritage of in-flight operations [49], have contributed to the success of this technology. Thus, it is currently one of the most suitable options for a broad range of applications and exploration scenarios. The significant technological advancement in the on-board power generation has lead to an increasing interest in the development of HET, which input power level is above 5 kW, as proven by the several prototypes that have been developed and tested in the past decades, e.g. [50]-[51]. On the other hand, as the power level increases, the challenges associated with the thruster design, development and qualification increases. The results of combining the high cost for the characterization and endurance tests, which require suitable and very expensive test facilities and diagnostic systems, and the high cost of exploiting Xenon during endurance test campaigns is the main reason why no high-power prototype has yet reached the qualification status for space applications.

Currently, the frontier of high-power e-PROP is represented by the NASA's Advanced Electric Propulsion System (AEPS), an e-PROP based on a 12.5 kW-class HET [52, 53], born from the combined effort of Aerojet Rocketdyne, NASA Glenn Research Center and NASA Jet Propulsion Laboratory, started in 2012 within the Asteroid Redirect Robotic Mission (ARRM) as described in [54]. After the cancellation of the ARRM program, the AEPS was selected as the main propulsion system of the LOP-G, as stated in [53], and is currently under-qualification.

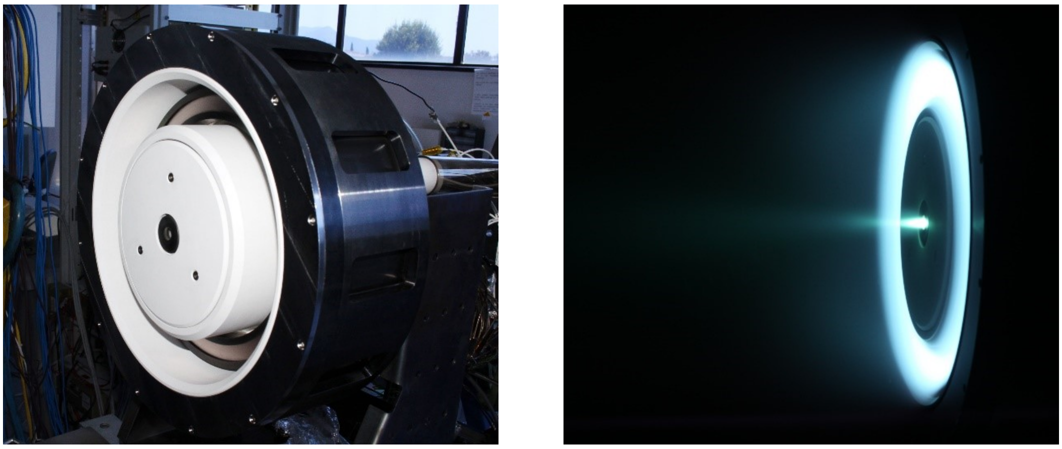

Figure 2.17: HT20k development model with magnetic shielding (credit: SITAEL).

In Europe, SITAEL is one of the center of excellence for development activities on high-power HET [55]. Benefiting from their extended heritage in HET development and thanks to the availability of one of the largest vacuum facilities for electric propulsion testing in the world, i.e. the IV10 space simulator, the development of its 20kW-class HET dated back in 2015. Since then, the thruster and its HC60 hollow cathode have been extensively operated with both Xenon and Krypton. Nowadays, further development activities on the HT20k are ongoing as part of EU's H2020 CHEOPS program, an ESA/GSTP program and a dedicated pre-qualification ESA program.

The current HT20k development model, represented in Figure 2.17, has been designed applying a theoretical scaling methodology to the former HT5k and implementing the magnetic shielding approach to overcome the lifetime limitations associated with the channel erosion. and the preliminary estimation of its performance envelope are reported in [56, 57]. The HT20k performance without magnetic shielding are summarized in Table 2.3. Several test campaigns have been carried out since then considering a wide range of operating conditions. Among them, the long duration wear tests, with both Xenon and Krypton, should allow SITAEL to mitigate risks associated with a future qualification campaign, as described in [55].

Table 2.3: Performance of the HT20k without magnetic shielding.

Parameter	Value
Voltage [V]	300 – 850
Discharge Power [kW]	10 – 26
Anodic Efficiency [-]	up to 68%
Thrust [mN]	400 – 1400
Specific Impulse [s]	2000 – 3450

2.2.2 Electrical Power Subsystem

The subsystem mostly affected by the considerable power demand related to the exploitation of electric propulsion is the EPS. Thus, the first functionality allocated to the EPS is indeed the on-board power generation, which can benefit from the promising improvements obtained in the last years becoming lighter and cheaper per watt, as testified by the new MegaFlex^{TM} Solar Array by Northrop Grumman [58]. Moreover, this subsystem is in charge of distributing the power among all the other subsystems, once the power is properly regulated. Last, EPS shall provide power storage capabilities to overcome the shadow periods when the subsystem cannot count on solar energy to feed the LST.

The EPS design envisions the adoption of deployable solar arrays, arranged in multiple wings, for the power generation and the technology chosen is represented by the Northrop Grumman UltraFlex$^{\text{TM}}$ Solar Arrays [59], characterized by improved specific power (200 W/kg at Beginnig of Life (BOL)) and stowed power density (40 kW/m^3). The UltraFlex has been preferred with respect to the MegaFlex thanks to the higher reliability demonstrated, as in the case of the Cygnus spacecraft (see Figure 2.18). Secondary batteries shall be exploited to store the power required to sustain the LST during shadowed period and to guarantee the adequate performance of e-PROP. Thanks to the advanced capabilities shown on board the ISS, the GSYUASA LSE134 Li-Ion batteries [60] have been chosen to be equipped on the LST. They are characterized by 50% Depth-Of-Discharge for more than 500 cycles life, 148 Ah capacity, 548 Wh energy and a specific energy equal to 155 Wh/kg, all at BOL. Moreover, the Power Control and Distribution Unit is in charge of regulating and distributing electric power among LST subsystems. Further design details can be found in Section 3.2.3.

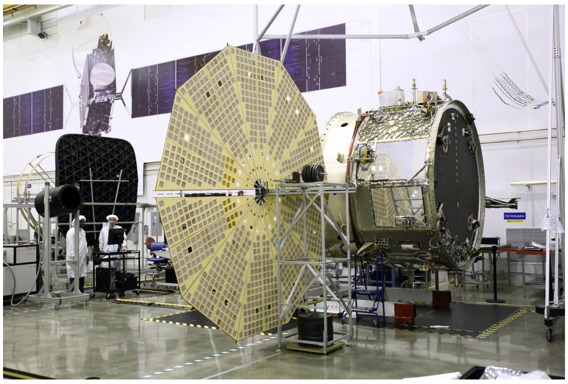

Figure 2.18: The Cygnus spacecraft with its cymbal-like UltraFlex solar arrays deployed (credit: NASA).

2.2.3 Attitude and Orbit Control Subsystem

The AOCS subsystem is in charge of providing attitude and orbit control during the whole mission despite the presence of internal and external disturbances (further details about disturbance sources can be found in Section 4.2.5) while guaranteeing a 3-axis stabilization. Moreover, it incorporates GNC functionalities[1] such as: (i) determining attitude, angular rate, position and velocity; (ii) establishing the optimal/desired trajectory to follow; and (iii) ensuring the compliance with the attitude accuracy requirements as well as additional operations constraints typical of some phases, e.g. ARVD phases (see Section 2.3.1 for further details).

The LST AOCS architecture has been designed considering a 3-axis stabilization control strategy and, as shown in Figure 2.19, includes chemical thruster and Reaction Wheel (RW). In particular, retracing the ATV AOCS design, the LST is equipped with 30 arianeGROUP 20N Chemical Monopropellant Hydrazine Thrusters [63], organized in 4 front pods (G-J) and 6 rear pods (A-F), each one including 3 thrusters mutually orthogonal distributed (see Figure 2.19b). For the attitude control, four Rockwell Collins RDR 68-3 Reaction Wheels [64] are equipped on board, arranged in the typical NASA Standard four-wheel/pyramid configuration (see [65]), i.e., three orthogonal RWs which spinning axes are parallel to the body ones and the fourth RW is equally tilted with respect to them by an angle of 54.7°, as depicted in Figure 2.20.

Moreover, several sensors have been considered for navigation purposes: (i) two Inertial Measurement Unit (IMU) for accurate reference and velocity measurement; (ii) Star sensors and Sun sensors, one for each body axis plus one for redundancy,

---

[1] Sometimes the AOCS and GNC subsystems are presented as complementary whereas, in other cases, the two acronyms are combined, i.e. Attitude and Orbit Guidance, Navigation and Control (AOGNC) (e.g. see ESA Concurrent Design Facility (CDF) studies [61] and [62]).

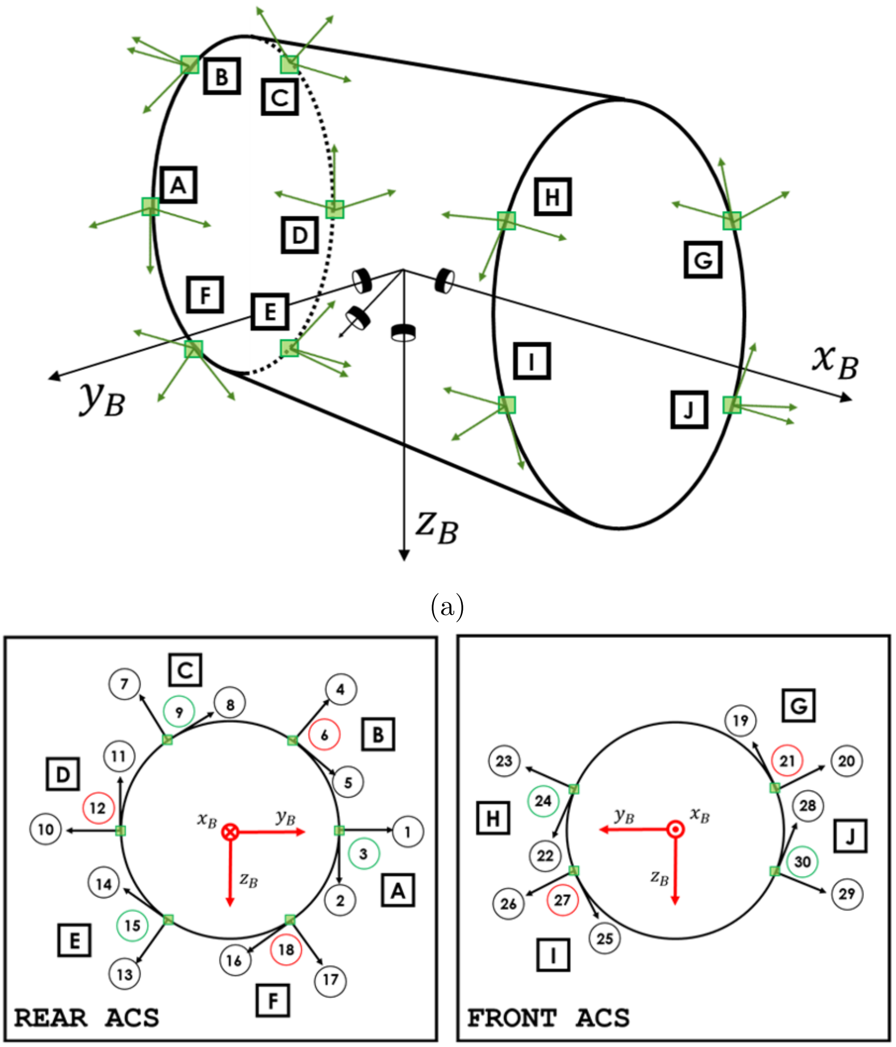

(a)

(b)

Figure 2.19: (a) AOCS architecture; (b) Monopropellant thrusters allocation in front (left) and rear (right) pods.

for attitude determination. A dedicated on-board computer provides the computational capabilities required by the AOCS and it's in charge of defining the optimal Thrust Management Function (TMF) profile of on/off thrusters cycle, during both EOR and ARVD. Indeed, due to the reduced relative distance among the LST and the target vehicles during the proximity operations, it is assumed that chemical thrusters shall be exploited to prove the required thrust instead of HETs, due to their higher reliability. Moreover, the plume impingement on the target vehicles when using electric propulsion could strongly affect the LST controllability leading to possible collision.

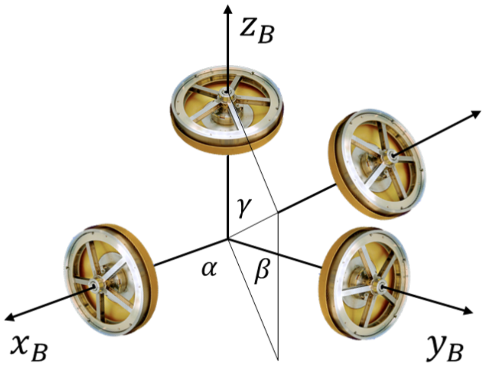

Figure 2.20: Four Rockwell Collins RDR 68-3 Reaction Wheels arranged in the NASA Standard configuration.

2.2.4 Thermal Control Subsystem

The TCS subsystem shall guarantee proper thermal insulation, heat rejection and local heat sink, components temperature control, keeping them within given boundaries. Moreover, it shall provide and heat collection and transportation, suitably distributing the heat within the spacecraft. The significant power demand due to the adoption of a cluster of HETs has a strong fallout also on the management of the internal dissipated heat, and TCS has to properly balance the heat emitted by the LST as infrared radiation against the heat dissipated by its internal components plus the heat absorbed from the Earth and deep space environment. The TCS architecture considers the combination of active and passive control strategies, where radiators are exploited to reject LST waste heat to space via structural panels and deployable structures. Furthermore, heaters are used to protect sensitive components from cold-case environmental conditions, and MLI blankets are adopted to both prevent excessive heat loss from specific components and environmental fluxes. Further details about the TCS architecture and design choice are provided in Section 3.2.4, together with the analytical models exploited to evaluate the environmental heat sources.

2.2.5 Telemetry, Tracking and Control Subsystem

The Telemetry Tracking and Control (TTC) subsystem represents the interface among the spacecraft and the ground segment, providing vital communication to and from the spacecraft itself. It is the only way to observe and control its orbit position, configuration and health status from ground. To allow a reliable connection among the spacecraft and its control centers, the TTC shall guarantee carrier tracking capabilities, generating downlink radio-frequency signals which phases are coherent to the uplink ones coming from the ground, according to a two-way coherent mode. In this way, the ground station would know more precisely the downlink signal frequency and the Doppler shift can be measured to compute the *range rate*, i.e. Line-Of-Sight (LOS) velocity between the spacecraft and the tracking antenna. This choice is particularly recommended, as stated in [17], for spacecraft and satellites operating in deep space, which have significant amount of data to transmit and very short field-of-view time to the ground station. Indeed, knowing the range rate, the ground operators can scan fewer frequencies and acquire the spacecraft more quickly and then determine the range or LOS distance. Moreover, TTC is in charge of: (i) receiving and detecting commands and then forward the uplink carrier to the Command and Data Handling (CDH) subsystem; (ii) receiving telemetry data from CDH and modulating the downlink carrier with either mission and science telemetry; and finally (iii) transmitting the combined carrier to the ground segment. Additional functionalities allocated to TTC are related to the subsystems operations in terms of autonomously detecting system faults and recovering the communication functionality through pre-stored command sequences, monitoring housekeeping and mission data and providing them to the CDH subsystem.

To exploit all this critical functionalities, the TTC is composed by transponders, a dedicated on-board computer for command and telemetry processing and antennas, which guarantee both uplink/downlink with the ground segment and crosslinks with either GEO satellites and the LOP-G.

2.2.6 Command and Data Handling Subsystem

As anticipated in the previous Section, the CDH subsystem shall provide two main functionalities: (i) on one side, CDH shall provide commands validation, decryption, delivery and distribution to the other subsystems, once received from the TTC; and (ii) on the other side, CDH shall gather, process, encrypt, format and then transmit to the TTC housekeeping and mission data. Moreover, data storage capabilities shall be provided, together with spacecraft timekeeping, computer health monitoring and security interfaces.

Typically, the CDH subsystem size is almost proportional to the spacecraft complexity. On the other hand, combining command and data handling functionalities allow to improve the efficiency of spacecraft functions autonomous control. According to the functionalities allocated to this subsystem, the CDH core is represented by its On-Board Computer (OBC), which is in charge of decrypting commands and processing and formatting mission and housekeeping data. The encryption task is entrusted to the commands decoder, together with commands validation, whereas the Remote Interface Unit, usually present on medium-large spacecraft and representing an example of distributed control system implementation, offloads the OBC from analogue and digital data acquisition. Through the Remote Interface

Unit, telemetries are gathered before the OBC elaborates and formats them, together with mission data. Last, multiple data storage units complete the CDH architecture.

2.2.7 Structures and Mechanisms Subsystem

The Structures and Mechanisms (StrMech) subsystem can be envisioned as the functional glue that support structurally and mechanically all the other subsystems, guaranteeing the integrity of the spacecraft during all mission phases. StrMech shall provide also protection from the harsh radiation environment and from Micrometeoroids and Orbital Debris (MMOD). This subsystem shall provide the attachment with the launch vehicle, together with the ordnance-activated separation. Moreover, as highlighted in Figure 2.1, the LST is interconnected with all the other building blocks. In particular, defining each connection in terms of link nature, the LST shall have the following interfaces with the other space segment elements:

- LOP-G: the Gateway provides power to sustain the LST until the spacecraft it's attached, for which structural support is required, and guarantees telemetry and data exchange, also during EOR when the LST is in the LOS of LOP-G.

- The cargo module relies on the LST for thermal protection and power generation and distribution, as anticipated in Section 2.1.4, for which power and mechanical/structural interface is required. Moreover, the cargo telemetry and data are handled by the LST as well, to minimize the complexity of the cargo element, since is has been conceived as a (almost) *passive* payload.

- The ORS can be seen as a cargo module and then it shares the same interconnection with the LST while it requires also a fluidic interface for the refueling operations.

In compliance with the stakeholders' expectations of minimizing efficiently development efforts, the LST is equipped with a standardize docking interface, which is compatible with all three space segments, without requiring any additional adapter, and provides power, data and fluidic connections in addition to the structural one. No dedicated refueling interface has been considered in this work to reduce the (already significant) complexity of the LST design and the ARVD maneuver with the ORS. Moreover, a passive grasping mechanism has been envisioned to provide the berthing capabilities when reaching the LOP-G, exploiting its robotic arm. The structural integrity of the spacecraft is guaranteed by the primary structure whereas the mechanical support to all the subsystems is provided by the secondary structure. Moreover, radiation shielding protects the LST from the radiations whereas the Meteoroid and Debris Protection System, i.e. a metallic shield attached to the spacecraft primary structure, protects the spacecraft from natural and man-made particles during all orbital mission phases.

2.3 The Lunar Space Tug Scenario

Once all the elements involved in the LST mission has been functionally described, the next step of the SMAD methodology consists of defining and characterizing the mission itself to meet primary objectives and stakeholders' expectations. The so-called Concept of Operations (ConOps) analysis allows to derive the *mission concept*, describing how the system will be operated during all life-cycle phases. The first task of the ConOps consists in partitioning the mission into mission phases, each one characterized by peculiar external environment, available resources, expected duration, interfaces with other building blocks and starting/ending events. Then, the system is further detailed through the identification of stable configurations in which it can be operated along the mission, i.e. the spacecraft modes of operations, and the functionalities simultaneously available. It is important to highlight that different modes of operations can be envisaged in the same mission phase. On the other hand, a dynamic view of the system operations is provided through the Design Reference Mission (DRM), a graphical representation of the mission profile described through the mission phases arranged as time sequence. To complete the mission concept description, the operational timeline is defined, combining mission phases and their corresponding expected durations in a sort of graphical chronicle. Following these guidelines, the LST scenario has been derived and the main outcomes are provided in the following Sections.

2.3.1 Mission Phases

According to the LST objectives and functionalities aforementioned, the major mission phases of its mission profile have been identified and described hereafter. In particular, each mission phase has been characterized in terms of starting/ending events (see Table 2.5), environments and reference orbits, and building blocks involved. It is important to highlight that some of the mission phases do not directly involve the LST but they are essential in terms of timeline and mission constraints, such as the launch and injection phase of both cargo module and ORS.

A *cargo module launch and GTO injection*: all the operations the launch vehicle performs to inject the cargo module into GTO;

B *LST close-range rendezvous with cargo module*: the LST starts the close-range rendezvous maneuver when it is 6 km (relative) distant from the cargo module. The continuous-thrust radial boost maneuver ends when the LST is 500 m far from the target. Then, the LST performs the minus V-bar final approach until it docks with the cargo module;

C *LST EOR up to NRHO*: the LST performs the orbit raising maneuver from the GTO up to the LOP-G through a low-thrust spiral trajectory. This phase includes also all the maneuvers required for plane changes and orbit circularization;

D *LST close-range rendezvous with LOP-G*: the LST starts the close-range rendezvous maneuver when it is 30 km (relative) distant from the LOP-G. The continuous-thrust radial boost maneuver ends when the LST is 500 m far from the LOP-G. Then, the LST performs the minus V-bar final approach until it is 2 m far from the station to allow the berthing operations via the LOP-G robotic arm;

X *cargo handling operation*: all the operations related to the cargo module checks and unloading procedures;

E *LST undocking from LOP-G*: the LST undocks from the LOP-G with a classical departure maneuver from the docking port, until it is 6 km far from the station;

F *LST EOR down to GTO*: the LST performs the orbit raising maneuver from the LOP-G down to the GTO through a low-thrust spiral trajectory. This phase includes also all the maneuvers required for plane changes and orbit circularization;

G *LST technical waiting for ORS*: the LST stays in the reference GTO, waiting for ORS arrival;

H *ORS launch and GTO injection*: all the operations required to put the ORS into the reference GTO;

I *LST close-range rendezvous with ORS*: The LST starts the close-range rendezvous maneuver when it is 6 km (relative) distant from the ORS. The continuous-thrust radial boost maneuver ends when the LST is 500 m far from the ORS. Then, the LST performs the minus V-bar final approach until it docks with the ORS;

J *LST on-orbit refueling*: the refueling operation is allowed through the LST and ORS docking interfaces;

K *LST undocking from ORS*: the LST undocks from the ORS with a classical departure maneuver from the docking port, until it is 6 km far from the ORS;

L *LST technical waiting for cargo module*: the LST remains in the reference GTO until the arrival of a new cargo module to deliver. This waiting phase could include maintenance operations.

Table 2.4: LST mission phases characterization in terms of starting and ending events.

	Start Event	**End Event**
A	lift-off launch vehicle with cargo	cargo module GTO orbit injection
B	cargo module GTO orbit injection	LST docks with cargo module
C	LST docks with cargo module	LST ARVD with LOP-G
D	LST ARVD with LOP-G	LST docks with LOP-G
X	LST docks with LOP-G	cargo module unloaded
E	cargo module unloaded	LST undocks and far from LOP-G
F	LST undocks and far from LOP-G	LST back to GTO
G	LST back to GTO	lift-off launch vehicle with ORS
H	lift-off launch vehicle with ORS	ORS GTO orbit injection
I	ORS GTO orbit injection	LST docks ORS
J	LST docks ORS	LST refueled
K	LST refueled	LST undocks and far from ORS
L	LST undocks and far from ORS	lift-off launch vehicle with cargo

Figure 2.21 represents the LST DRM, providing a graphical overview of the tug *closed-loop* missions profile. Indeed, being a reusable transportation system, the LST faces its own launch and injection phase only once, at the beginning of its mission. The reference injection orbit has been set as the Ariane V/VI GTO with a perigee altitude of 250 km, an apogee altitude of 35943, 6° of inclination and an argument of perigee of 178° as stated in [24, 25]. Once it reaches the target orbit, the LST shall remain operative for at least 10 years, along which it will be called to repeat the same mission profile depicted in Figure 2.21 over and over. Once the LST is refueled and undocks from the ORS, it enters in the second technical waiting (phase L), which is followed by the launch and injection of the next cargo module (phase A), ready to start a new transfer towards the LOP-G.

Close-Range Rendezvous

From the DRM represented in Figure 2.21, it is possible to identify three different ARVD maneuvers that the LST shall perform: (i) the first ARVD is in the cargo module GTO injection orbit (phase B); (ii) the second maneuver is necessary to approach the LOP-G in its NRHO (phase D); and (iii) the last one is required to reach the ORS and perform the refueling operation, again in GTO (phase I).

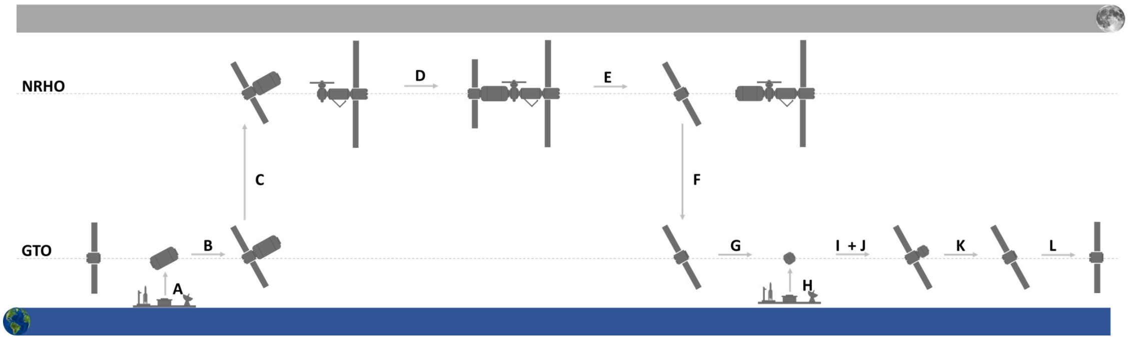

Figure 2.21: LST Design reference Mission.

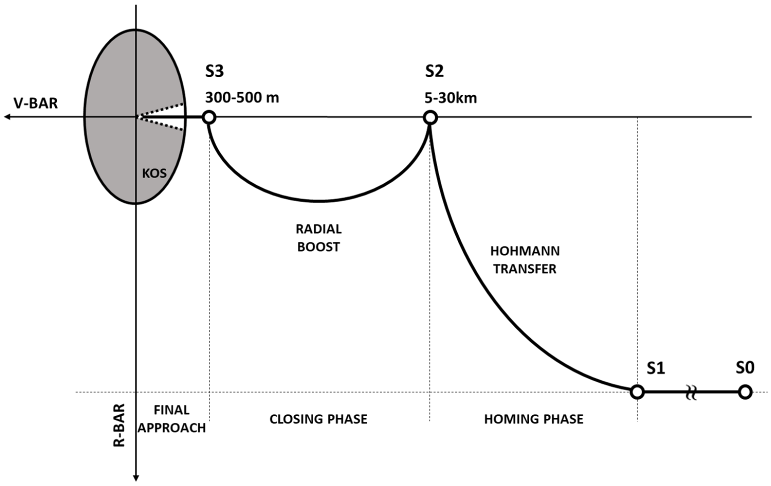

Figure 2.22: ATV-like rendezvous mission profile.

The typical rendezvous mission profile, represented in Figure 2.22, can be split in several sub-phases. Each sub-phase is characterized by regulated starting/ending relative distance among the spacecraft and the target system, velocity and additional safety constraints, as described in [66]. After the launch and later injection into the initial orbital plane, the first step is called *phasing*, corresponding to the S0-S1 phase in Figure 2.22. It allows to reduce the phase angle between the chaser and target vehicles thanks to the difference in orbital period duration. Then, a Hohmann transfer (phase S1-S2) brings the chaser to the target orbit during the so-called *homing phase* or *far-range rendezvous*. Once the spacecraft reaches the desired orbit, the *close-range rendezvous* phase starts, which is typically split into two parts: (i) a preparatory phase, i.e. the *closing phase* (S2-S3), to further reduce the range to the target vehicle; and (ii) the *final approach* (S3-S4) that leads the chaser to reach the desired mating conditions, whether docking or berthing is considered.

Since the LST is an electric spacecraft, the typical rendezvous mission profile cannot be considered. Indeed, the homing phase becomes a low-thrust spiraling trajectory. Moreover, during the close-range rendezvous, the AOCS thrusters are exploited for safety reasons, related to the current electric propulsion reliability and the need to reduce the plume impingement when the two spacecraft are too close, minimizing the probability of collision. Further operational requirements and constraints for the closing phase and final approach are provided in Chapter 4, where the ARVD is thoroughly described.

2.3.2 Modes of Operations

Considering the LST mission profile, sever modes of operations have been identified and reported in Table 2.5, each one representing a stable configuration of the spacecraft.

It is possible to notice that there are four main modes of operations, each of them prevailing in one or more correspondent mission phases. On the other hand, the other modes are mostly related to contingency-plan and safety-critical configurations: (i) NOMINAL mode corresponding to EOR phases C and F and technical waiting phases G and L; (ii) RENDEZVOUS mode for phases B, D, E, I and K; (iii) REFUELING mode for phase J; and last (iv) DOCKING mode for phase X. In particular, the NOMINAL mode representes the core of the LST mission profile, since it corresponds to the EOR phases. Due to the adoption of electric propulsion and its significant impact in terms of power demand and EOR phases duration, this mode of operation has been taken as reference for the preliminary power budget during the design phase (see Section 3.2.3 for further details).

2.3.3 Traffic Plan

As highlighted in the previous Sections, the LST is envisioned to support the replenishment of the future LOP-G and this interdependence significantly affects the traffic plan of the transportation system. Indeed, the operational timeline shall be compliant with the logistics of the Gateway in order to properly provide the sustainment of the outpost and its crew as well. As described in Section 2.1.3, the LOP-G shall host crew of four members once per year. This implies a crucial constraint for the LST operations, since it requires that the LST shall resupply the Gateway at the same time the Orion reaches the LOP-G with the crew on-board. In this way, each crew will be provided with the required refurbishment, in compliance with their mission duration, to carry on the mission on the LOP-G. If the amount of resupply is set according to the amount of days the crew will spend on the Gateway, the timespan between two crew mission is well defined, i.e. 12 months. Thus, one year is the maximum interval that can occur among two consecutive LST mission, assuming that each LST shall provide the resupply sufficient for only one crew at the time. Moreover, additional constraints are inherent to the LST mission profile

Table 2.5: LST mission phases characterization in terms of starting and ending events.

Mode	**Description**
CHECK	This mode is activated either before to switch to the NOMINAL mode or right after the SAFE mode.
DISPOSAL	This mode is activated when the LST is arrived at the EOL and it allows to perform the necessary operations required to dispose the spacecraft in compliance with the disposal strategy selected.
DOCKING	This mode is activated once the LST is docked to the LOP-G.
DORMANT	This mode is activated during the waiting phases, switching all the subsystems at minimum power demand guaranteeing the survival of the LST.
NOMINAL	This mode is activated during the low-thrust transfer and all main functionalities are active.
REFUELING	This mode is activated once the LST is docked to the ORS to allows the refueling operations through the docking interface.
RENDEZVOUS	This mode is activated once the close-range rendezvous phase starts, either with the cargo module, the LOP-G or the ORS until the mating operation is completed.
RIP	This mode is activated when the LST mission is compromised due to a irreversible failure detected during the SAFE mode and it allows to safely end the mission.
SAFE	This mode is entered automatically upon the detection of a predefined operating condition or event that may indicate loss of control or damage to the LST. Consequently, the safety procedure allows either the LST recovery or the activation of the RIP mode.

and functionalities. Indeed, beyond the EOR phases, there are other phases which duration shall be carefully defined, e.g. waiting phases, or are already regulated, as the ARVD maneuvers. In particular, the following assumptions have been taken into considerations for further analysis:

- Being a reusable transportation system, the LST shall be refueled in space, exploiting an ORS. The refueling operation shall last at most 2 days.
- Maintenance activities on the LST shall be provided, if necessary, while the vehicle is in GTO and the operations shall not take more than one month.
- The launch windows for both the cargo module and the ORS shall last at least one month each.

- The close-range rendezvous maneuvers shall last at least 12 hours, both in GTO and NRHO.

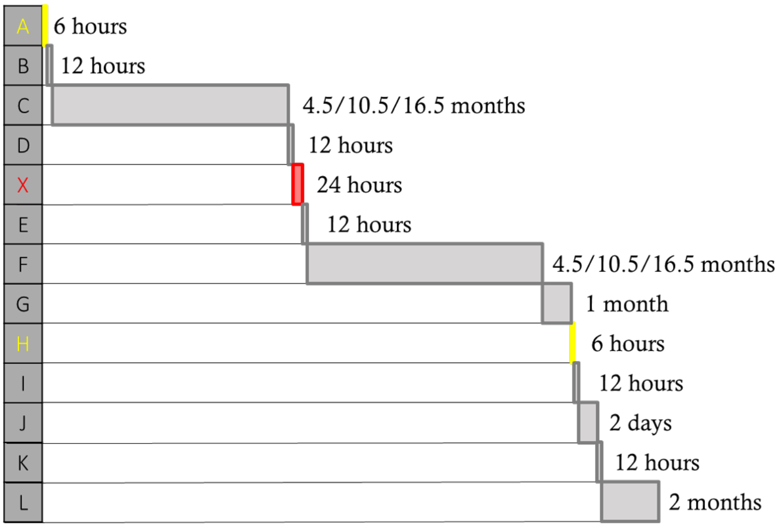

Figure 2.23: LST operational timeline for different fleet configurations.

Moreover, to analyze different replenishment logistic strategies, the possibility to exploit more than one LST to supply the LOP-G has been envisioned, introducing the concept of fleet: multiple tugs sharing the same functionalities and capabilities, as well as the same mission profile, working together to provide the required refurbishment in compliance with the LOP-G operational constraints. Indeed, considering that one LST shall reach the Gateway every 12 months and shall spend at most 3 months in GTO, as anticipated before (refueling, maintenance and technical waiting), and preliminary assuming that the outward and return transfers should take approximately the same time, the LST shall be able to complete the EOR phases to and from the LOP-G in at most 4.5 months. On the other hand, exploiting multiple space tugs can allow to relax this critical mission constraint, mainly because most of the cargo to be transferred can be considered as no time-critical. Indeed, the maximum transfer duration $\Delta t_{MAX_{EOR}}$ in months can be estimated as a function of the number of LST in the fleet N_{LST} by

$$\Delta t_{MAX_{EOR}} = 4.5 + 6(N_{LST} - 1), \tag{2.1}$$

assuming that the departure interval among two consecutive mission within the same fleet is set to one year.

In this work, three different fleet configurations have been considered, composed by a number of LST varying from 1 up to 3 and corresponding to a maximum transfer duration of 4.5, 10.5 and 16.5 months, respectively. Figure 2.23 provides an overview of the preliminary LST operation timeline, which is further detailed in Figure 2.24 with respect to the different fleet configuration. In particular, the red stars represent the Orion arrival at the LOP-G, to which correspond the end of the LST GTO to NRHO EOR phase as well. Indeed, for the 1-LST fleet the tug reaches the Gateway after 4.5 months the first time and again at T= 16.5 months, i.e. exactly one year later. On the other hand, for the 3-LST fleet, the first LST starts its mission at T= 0 and arrives 16.5 months later, while at T= +12 months the second LST is already on its way towards the LOP-G, reaching the station at T= +28.5 months. Then, at T= +40.5 months, also the third LST reaches the LOP-G while the first one is again on its way for its second transfer and the second one has just got back to GTO.

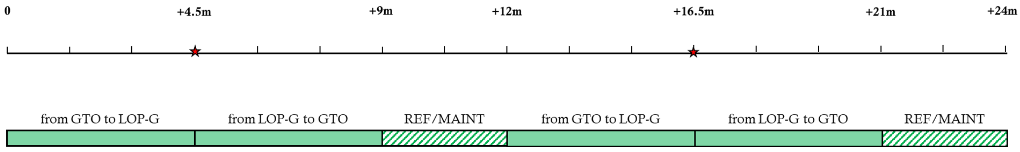

(a) 1-LST fleet

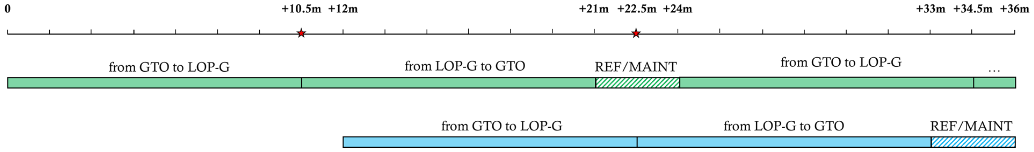

(b) 2-LST fleet

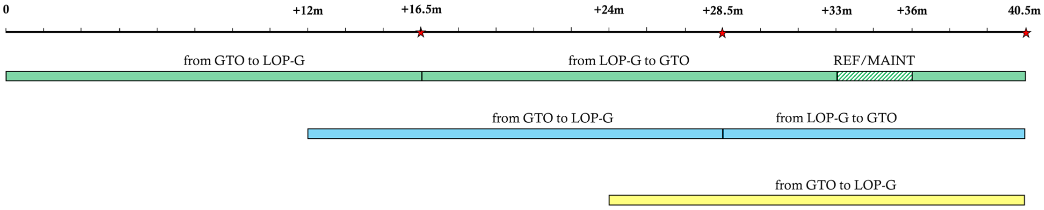

(c) 3-LST fleet

Figure 2.24: LST operational timelines with respect to three fleet configurations.

Chapter 3

Mission and Space Systems Design Tool

3.1 MISS Design Tool Architecture

The design of a spacecraft which propulsive core is based on electric propulsion does not follow the classical guidelines typically adopted for chemical-based satellites, as highlighted in [43]. For this reason, the MISS design tool has been developed to provide a user-friendly and reliable tool to preliminarily assess the sizing of a spacecraft based on high-power electric propulsion to be exploited within the LOP-G replenishment scenario. The second development-driver was the flexibility of the design suite to be exploited for the analysis of different mission concepts in which an electric platform is envisioned. Indeed, the standardization of the different source files, developed in a MATLAB environment, allows to easily change the main features of the scenario to analyze as well as to upload different databases with the performance of the electric thruster to be analyzed. The flexibility of MISS has been validated for different applications where electric spacecraft have been envisioned for not only transportation mission but also for disposal and EOR of telecommunication satellites from LEO up to the operational GEO. Further details can be found in Appendix A.

The design phase focuses on the selected propulsive technology both in terms of selection of the proper operative points and the definition of the corresponding PROP architecture. Thus, each LST design corresponds to a different combination of thruster performance and subsystem configuration. As shown in Figure 3.1, MISS is organized in several layers, connected each other, and allows to define the LST optimal design among the configurations analyzed. In particular, five main areas can be identified: (i) mission scenario definition (purple block), which represents the interface with the mission analysis presented in Chapter 2; (ii) delta-v estimation (light-blue block); (iii) spacecraft design (green block), incorporating the analytical models to obtain the LST sizing; (iv) scenario selection (red block), in order to

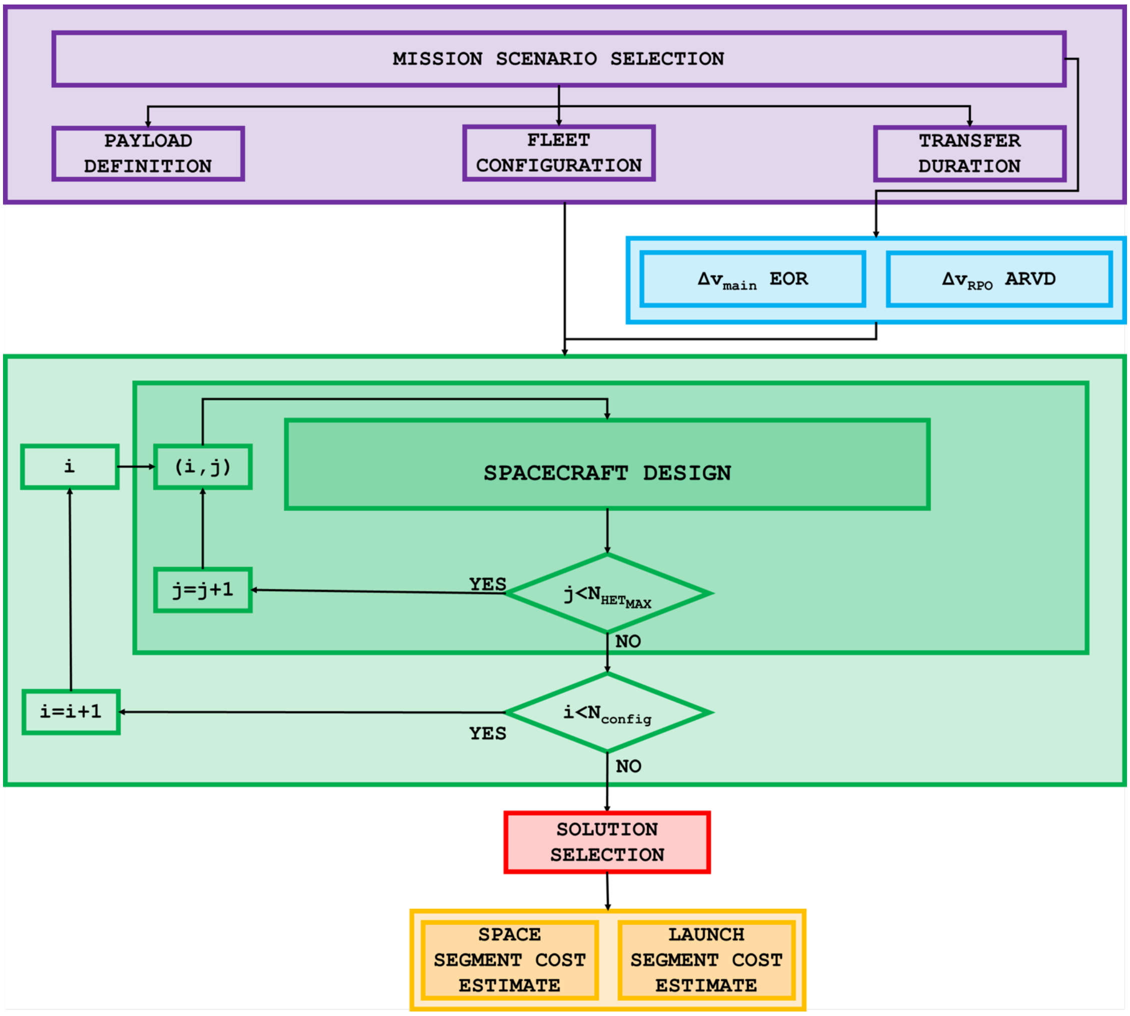

Figure 3.1: MISS high-level algorithm block diagram.

identify the optimal solution among all those analyzed; and (v) cost analysis, to preliminarily estimate the space and launch segments cost exploiting a multi-level parametric cost model developed ad-hoc developed per high-mass high-power SEP spacecraft. Further details are provided in the follows.

3.1.1 Mission Scenario Definition

The mission scenario definition provides the initialization data functional to the design phase. A shown in Figure 3.1, it consists of five main tasks: (i) implementation of mission and system requirements and constraints, directly coming from Functional Analysis and ConOps; (ii) payload definition, which in the LST case it is a function of the period spent by the crew on-board the LOP-G; (iii) definition of the fleet configuration, in terms of number of LST exploited to support the Gateway; (iv) definition of the operational timeline, obtaining the additional constraints for the design phase; and last (v) selection of the proper polynomial function to evaluate the transfer duration with respect to the thrust-over-mass ratio.

Payload Definition

The LST mission is significantly influenced by the needs of the LOP-G crew in terms of goods resupply. In this task, the cargo mass to transfer is defined as a function of the number of crew members N_{cm}, their mission duration on board the Gateway Δt_{cm} and the number of mission per year $N_{miss_{cm}}$. In this way, the total refurbishment can be evaluated once defined the minimum daily demand per crewmember is defined. In particular, MISS allows to either insert a tailored amount of kg/day/person or use a default value, which has been evaluated according to the guidelines provided in [33], as shown in Figure 3.2.

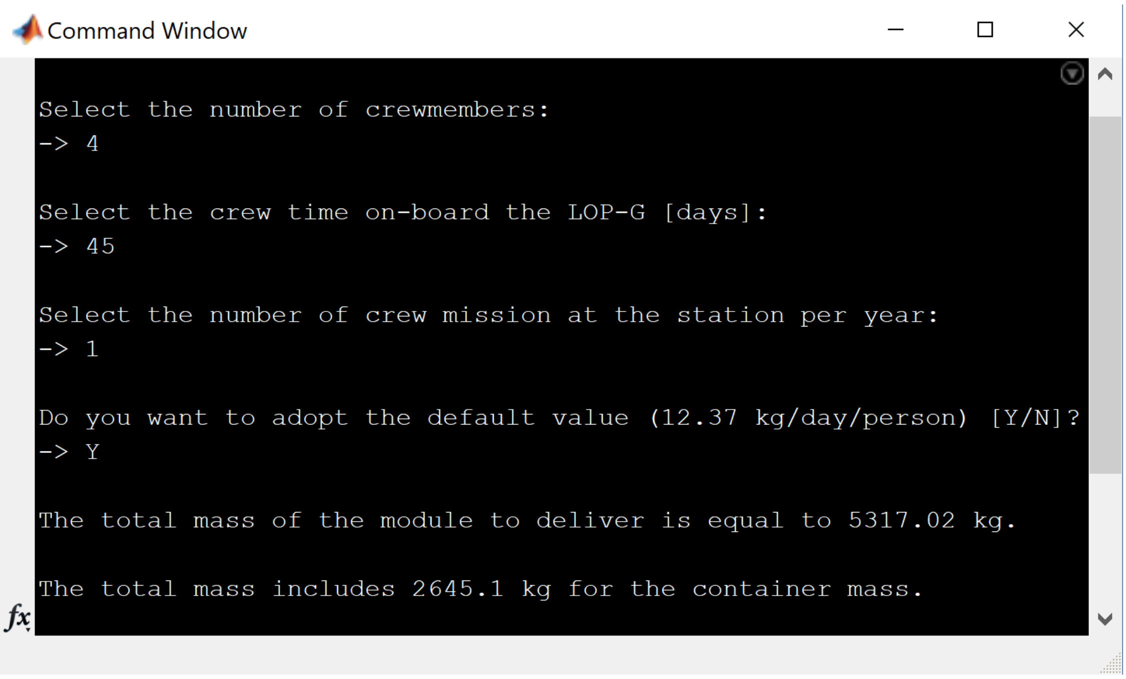

```
Select the number of crewmembers:
-> 4

Select the crew time on-board the LOP-G [days]:
-> 45

Select the number of crew mission at the station per year:
-> 1

Do you want to adopt the default value (12.37 kg/day/person) [Y/N]?
-> Y

The total mass of the module to deliver is equal to 5317.02 kg.

The total mass includes 2645.1 kg for the container mass.
```

Figure 3.2: Example of payload setup during the MISS algorithm initialization phase.

For the default daily need, which has been set to 12.37 kg/d/p, the following items and corresponding amount have been considered: (i) 1.02 kg/p/d of oxygen; (ii) 1.5 kg/p/d for dried and fresh canned food and beverage powder; (iii) 2.8 kg/p/d of drinking and food hydrating water; (iv) 5.05 kg/p/d of water for urinal flush, hygiene and shower; and (v) 2 kg/p/d for food packaging, dry and impregnate towel packaging, hygienic products, hygienic wipes and clothing.

Thus, the total cargo mass m_{cargo} is evaluated as

$$m_{cargo} = N_{cm} \cdot \Delta t_{cm} \cdot N_{miss_{cm}} \cdot m_{daily}, \tag{3.1}$$

where m_{daily} is the daily amount of goods. Once, obtained the resupply need, MISS estimates the mass of the cargo container in which the refurbishment will be stored for the transfer up to the Gateway. As stated in Chapter 2, the MPLM has been taken as reference to define the geometry as well as to estimate mass and volume of the cargo module. In particular, considering a cylinder with a radius of $r_{cyl}2.3$ m, the length of the cargo module h_{cyl} is defined such that 1 m of length corresponds to about 1 ton of goods. Hence, the height of the cylinder is obtained from the following proportion

$$1m : 1ton = h_{cyl} : m_{cargo}, \tag{3.2}$$

Defined the geometry, the mass of the cargo container results a function of the available volume $V_{cyl} = \pi r_{cyl}^2 h_{cyl}$ and the average density of the material considered for the structure, i.e. $\rho_{cargo} = 49.64$ kg/m^3, i.e. the MPLMs density plus a 20% of margin to include additional layers of MLI and MMOD to sustain the deep space environment.

Fleet Configuration

As anticipated in Chapter 2, the fleet strategy has been conceived to further relax the transfer time exploiting multiple LST in sequence, sharing the same design and performance to resupply the Gateway. MISS allows to define different fleet configuration and consequently defines the maximum transfer duration in compliance with Eq. (2.1). The outcome of the fleet configuration represents the mission constraint to be exploited during the selection process described in the follows.

Transfer Duration

The transfer duration task consists in updating the proper polynomial coefficient to build up the function that will be exploited for preliminarily evaluating the Δt required to the LST to transfer first the cargo module from its GTO injection orbit to the LOP-G and then to go back from the Gateway to the waiting orbit. As anticipated before, the transfer duration is a 5-th order polynomial function, in which the variable is represented by the ratio between the total thrust available, i.e. the single HET thrust times the number of thrusters operated contemporary, and the LST total wet mass. Following the guidelines provided in [67], the transfer duration for a trajectory from GTO to the LOP-G has been approximated by the following polynomial function

$$\Delta t = -5.46 \cdot 10^{18} x^5 + 1.87 \cdot 10^{16} x^4 - 2.52 \cdot 10^{13} x^3 + 1.67 \cdot 10^{10} x^2 - 5.57 \cdot 10^6 x + 983.93, \tag{3.3}$$

which trend is shown in Figure 3.3 where it is highlighted that for a thrust-over-mass ratio of about $2 \cdot 10^{-4}$ N/kg, the transfer time is close to one year.

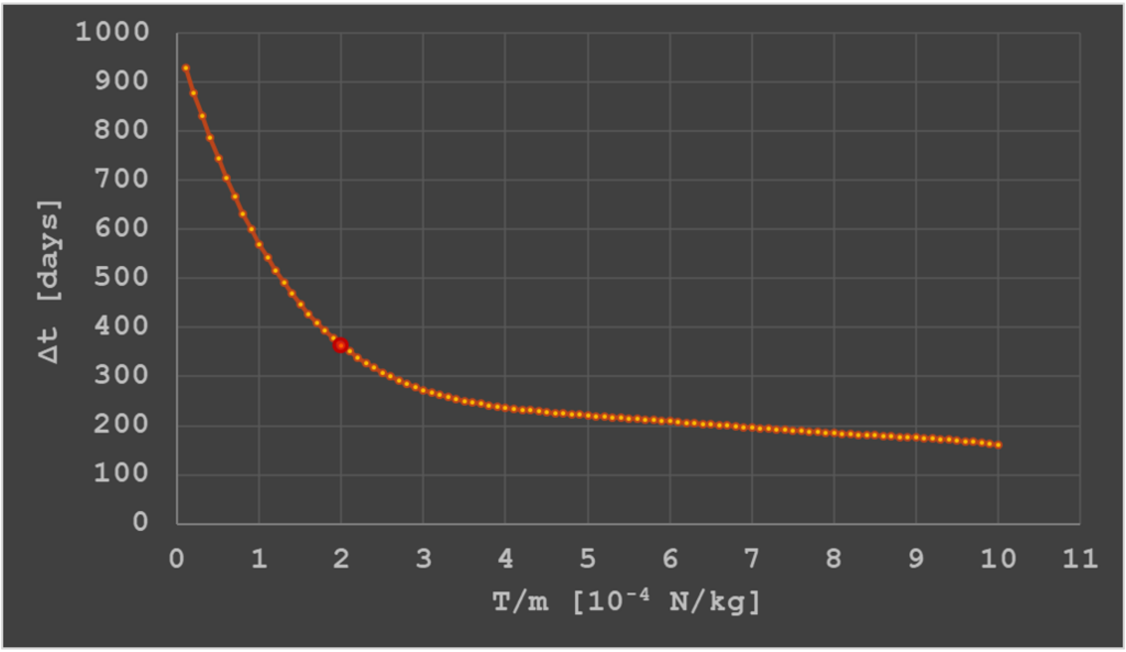

Figure 3.3: Transfer duration as a function of the thrust-over-mass ratio. The red dot highlights the T/m value, i.e. $2 \cdot 10^{-4}$ N/kg, corresponding to one year transfer.

3.1.2 Delta-v Budget

The second step consists in the evaluation of the delta-v budgets, both for EOR and close-range rendezvous phases. Considering the adoption of electric propulsion for the whole transfer except for those phases in which monopropellant thrusters are exploited, the LST will perform a low-thrust transfer characterized by spiraling trajectories, which shape is defined according to the chosen thrust profile. In first approximation, the delta-v for the EOR phases can be evaluated as the difference among the circular velocities of the starting and target orbits, i.e. v_{in} and v_{fin} respectively, following the guidelines provided in SMAD when a constant low-thrust burn is considered. On the other hand, the reference orbits are both highly-elliptical and the periastrum and apoastrum velocities are quite different. Moreover, an orbit plane change shall be considered since the inclination of the cargo injection orbit in GTO and the LOP-G reference orbit have different inclinations. Thus, first the delta-v budget has been evaluated for all four different periastrum-apoastrum combinations and considering that $\Delta i = 0$ as

$$\Delta v = |v_{fin} - v_{in}|, \quad \text{with} \quad v_{in} = \sqrt{\frac{\mu_{pl}}{r_{in}}} \quad \text{and} \quad v_{fin} = \sqrt{\frac{\mu_{pl}}{r_{fin}}}, \tag{3.4}$$

where μ_{pl} is the planetary gravitational parameter, i.e., $\mu_{\oplus} = 398600\ km^3/s^2$ for Earth and $\mu_M = 4904\ km^3/s^2$ for the Moon, and r_{in} and r_{fin} represent the initial and final radius of the reference orbits, respectively. Once defined the optimal strategy, i.e. the combination corresponding to the lowest delta-v, the term related to the inclination change Δi is included and it has been evaluated as

$$\Delta v_{incl} = v\cos\beta_0 - \frac{v\sin\beta_0}{\tan\left(\Delta i\frac{\pi}{2} + \beta 0\right)}, \text{ with } \beta_0 = \text{atan}\left(\frac{sin(\Delta i\frac{\pi}{2})}{1 - \cos(\Delta i\frac{\pi}{2})}\right) \tag{3.5}$$

finally obtaining the preliminary total delta-v budget as $\Delta v_{EOR} = \Delta v + \Delta v_{incl}$. Moreover a 5% of margin has been added for covering uncertainties in mission design and system performance plus another 5% since electric propulsion is exploited and this margin takes into account trajectory inaccuracies compensation, as regulated in [68].

On the other hand, for the ARVD maneuvers, the delta-v budget has been evaluated assuming the circular approximation of the reference orbits, both GTO and NRHO in correspondence of their apoastrum, i.e. lower angular velocity. As introduced in Chapter 2, the close-range rendezvous maneuver is split in two parts and, as a consequence, the delta-v devoted to this phase is given by the sum of two contributions. For the radial boost maneuver, the delta-v is a function of the orbit angular velocity ω_{orb} and the chaser-target relative distance to be covered Δx, considering a continuous thrust transfer along V-bar strategy, where V-bar is the axis along the target velocity direction with respect to a LVLH reference frame. Considering a transfer time equal to the orbital one, i.e. $T = 2\pi\sqrt{a_{orb}^3/\mu_{pl}}$ with a_{orb} the semi-major axis, the delta-v for the closing phase Δv_{RB} is given by

$$\Delta v_{RB} = \frac{\omega_{orb}}{2}\Delta x, \tag{3.6}$$

where Δx represents the difference among the chaser V-bar coordinates at the beginning and at the end of this phase, as defined in [66]. It is important to highlight that Δx is regulated according to the target features and safety and collision avoidance guidelines. Further details can be found in Chapter 5 whereas the mission constraints adopted for the design phase are stated at the beginning of Chapter 6. On the other hand, for the final approach phase, the delta-v is significantly influenced by the orbital control strategy adopted. In first approximation, considering a straight line V-bar approach, the delta-v for this phase, i.e. Δv_{FA}, can be evaluated as a function of the force per mass unit $\gamma_z = 2\omega_{orb}V_x$ along R-bar, the approaching velocity V_x at the beginning of the maneuver, which is assumed constant, and the relative distance chaser-target to be covered Δx_{FA}

$$\Delta v_{FA} = |\Delta V_x|_1 + |\gamma_z \Delta t| + |\Delta V_x|_2, \tag{3.7}$$

where $\Delta t = \Delta x_{FA}/V_x$, ΔV_{x_1} is the starting impulse producing the velocity V_x and ΔV_{x_2} is the stopping impulse of the same magnitude of ΔV_{x_1} but opposite direction. Hence, for the close-range rendezvous, the total delta-v budget is given by $\Delta v_{ARVD} = \Delta v_{RB} + \Delta v_{FA}$. Further details about the estimation of delta-v budget for proximity operations can be found in [66].

3.1.3 Spacecraft Design

The spacecraft design layer represents the core of the MISS tool since it is in charge of defining the mass and power budgets at subsystem and components level for the different LST solutions envisioned. Moreover, the preliminary transfer duration is evaluated according to the polynomial function selected during the mission scenario definition phase.

As highlighted in Figure 3.1, the external layer is composed by a double nested *for* loop. The outer loop is related to the i-th HET operational point identified over the reference performance map, for a total of $N_{config} = 125$ (see Figure 2.15 in Section 2.2.1). The inner loop, instead, defines the e-PROP architecture in terms of number of HET j considered in the cluster, varying from 1 up to $N_{HET_{MAX}} = 4$. This constraint has been set in compliance with the current HET cluster roadmap, which envisions a limited number of thruster contemporary operated to limit the plume interaction and the complexity of the subsystem itself, in terms of both design and operative and management requirements. Thus, the total number of LST solutions analyzed is equal to 500.

The internal layer is the real design core, as shown in Figure 3.4 and it involves two convergence cycles, one for the thrust-over-mass ratio and the other for the Hydrazine and Xenon tanks as a function of the propellant mass. The former is initialized at each (i, j)-th cycle with a default value, i.e. $(T/m)_0 = 2 \cdot 10^{-4}$, and MISS goes to the next $(i, j+1)$-th step if and only if the difference among the latest $(T/m)_{NEW}$ ratio and the previous one $(T/m)_j$ is less than 10^{-5}. On the other hand, the convergence loop within the *FUEL* block is described in Section 3.2.2.

Table 3.1: Mass breakdown exploited for LST design.

Subsystem	**Relative Percentage (RP) [%]**	**Safety Margin (SM) [%]**
AOCS	9	–
PROP	24	–
EPS	36	–
TCS	13	–
TTC	1	20
CDH	1	20
StrMech	16	10

For the design process, first the mass and power demand of the AOCS are obtained according to the models presented in Section 3.2.1. Then, the PROP subsystem is sized (mass, power and thrust T_{PROP}) in compliance with the cluster architecture, the transfer duration corresponding to $(T/m)_j$, the mission constraint and the thruster performance. A thorough overview of the design process exploited for the e-PROP is presented in Section 3.2.2. The power demand of AOCS and

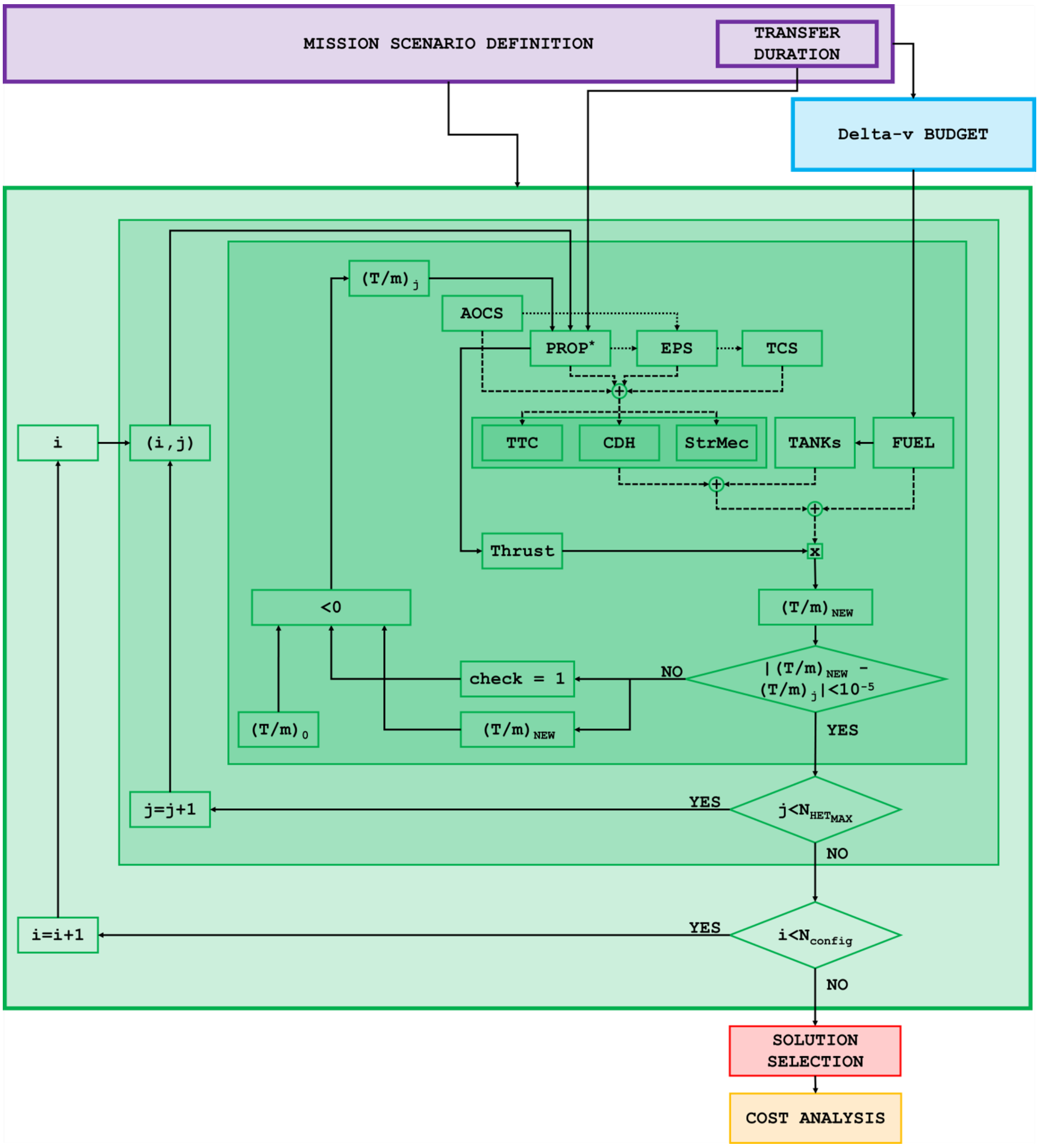

Figure 3.4: MISS detailed architecture and algorithm logic. The mass budget links are represented with dashed lines whereas the power budget links are in dotted lines.

e-PROP contribute to the design of the EPS subsystem, considering that the sizing power corresponds to the mission phases in which all the active HETs are operated at the maximum power. Then, the thermal loads are evaluated and the TCS subsystem sized, obtaining the mass budget at components level, as explained in

Section 3.2.4. For the mass budget of the other subsystems, i.e. TTC, CDH and StrMech, a tailored mass breakdown has been defined in which each subsystem mass is expressed as relative percentage over the total spacecraft dry mass. Table 3.1 provides the mass percentage considered and the corresponding safety margins applied at subsystem level (instead of components level as regulated in [68] for pre-Phase A studies). The percentages for AOCS, e-PROP, EPS and TCS are here reported only for completeness since they are not exploited to obtain the corresponding mass budget. Further details are provided in Section 3.2.5. As shown in Figure 3.4, to complete the evaluation of the LST dry mass, the tanks for both Hydrazine and Xenon shall be sized according to the corresponding propellant mass, function of the related delta-v. Furthermore, an additional 20% of safety margin is considered as ESA system level mass margin above the nominal dry mas at launch, as stated in [68]. Last, once obtained the LST wet mass $m_{LST_{wet}}$, the total wet mass $m_{LST_{wet_{tot}}}$ is derived as $m_{LST_{wet_{tot}}} = m_{LST_{wet}} + m_{cargo}$ and then, the new thrust-over-mass ratio is evaluated as

$$(T/m)_{NEW} = \frac{T_{PROP}}{m_{LST_{wet_{tot}}}}. \tag{3.8}$$

3.1.4 Optimal Solution Selection

Once the design phase is completed, all the 500 solutions obtained are filtered, deleting those that are not compliant with both the transfer duration and e-PROP cluster constraints. Then, the remaining feasible solutions are further analyzed to identify the optimal solution, which maximizes the spacecraft performance while minimizing its power demand, dry mass, propellant consumption, and transfer duration. Indeed, these latter four parameters have been identified as figure of merits for the trade-off analysis performed to obtain the chosen LST design. For this analysis, a weighting factor range has been set for each figure of merit, ranging between 1 and 10 and representing the relevance of each parameter with respect to the others. Then, a Monte Carlo simulation is exploited to perform the sensitivity analysis of the effect of different weights with respect to the overall process, sampling over 10000 time random weighting factors for each figure of merit. The next step consists in summing all these scores and normalizing them to 1. In this way, the normal weigh for each figure of merit is obtained and it can be further exploited to evaluate the impact of figure with respect to the i-th LST configuration analyzed. Once obtained the weighted sum of all the figure scores, they are used to define the final ranks among the feasible LST solutions, highlighting the optimal one. The weighting ranges for the different figures of merit and Monte Carlo results are provide in Table 3.2.

Table 3.2: Figures of Merit for LST trade-off analysis.

Figure of Merit	MIN	MAX	Monte Carlo weight
Power Demand	7	9	0.2821
LST Dry Mass	6	8	0.2448
Propellant Consumption	8	9	0.29961
Transfer Duration	4	6	0.1735

3.1.5 Mission Cost Estimate

The last layer of MISS is represented by the preliminary esteem of the LST design and development cost, exploiting the cost model developed as external interface to MISS and presented in [69]. The so-called Lunar Space Tug Cost Model (LSTCM) is a multi-layer parametric cost model developed to estimate the space and launch segment cost of mission in which high-mass high-power electric spacecraft are envisioned. Considering a bottom-up approach for e-PROP and a top-down for all the other subsystems, this cost model is based on a pre-Phase A level of fidelity and a protoflight development approach is assumed. Each subsystem cost model is built with respect to critical design parameters and technologies involved. In particular, the major innovation is introduced in the cost estimate of e-PROP in which, starting from the NASA JPL cost model proposed in [70], the LSTCM extends it to the concept of cluster, in which some components are shared among multiple thrusters, to obtain an esteem of the e-PROP cost as a function of the power provided to each thruster. Further details can be found in [69].[1]

3.2 Spacecraft Design Analytical Models

In this Section, the analytical models exploited to size the LST subsystems up to component level are presented.

3.2.1 Attitude and Orbit Control Subsystem

The AOCS subsystem design is driven by the mission needs in terms of guidance, navigation and control requirements to be fulfilled. Considering a 3-axis stabilization strategy, reaction wheels are envisioned to control LST attitude and, in particular, the Rockwell Collins RDR 68-3 as anticipated in Section 2.2.3. However, this design choice has to be confirmed comparing the angular momentum capacity

---

[1] It is important to highlight that the LSTCM tool is not part of this work but it has been only exploited to preliminary define the cost of the new transportation concept represented by the LST.

provided by these wheels and the mission demand, which is related to the external and internal torque disturbances affecting the spacecraft during its lifetime. First, the main environmental disturbance sources are estimated together with the torque required for the slew maneuvers. For the AOCS sizing, four main sources have been considered and implemented in MISS: (i) aerodynamic drag τ_{aero}, which contribution is limited to Earth proximity; (ii) spacecraft residual dipole τ_{mag}, due to its interaction with the planetary magnetic field; (iii) solar radiation pressure τ_{SRP}, affecting the spacecraft motion when it is not in the planet shadow; and (iv) gravity-gradient τ_{GG}, given by the interaction among a non-symmetrical spacecraft and the planetary gravity field. Further detail are provided in Section 4.2.5. The sizing torque considered for the evaluation of the RW angular momentum capacity is defined as the maximum contribution among the total external torque, i.e. $\tau_{ext} = (1 + SM_\tau) \cdot (\tau_{aero} + \tau_{mag} + \tau_{SRP} + \tau_{GG})$, and the torque demand for the slew maneuvers, i.e. τ_{slew}. According to the guidelines provided in [17], τ_{slew} is evaluated as

$$\tau_{slew} = 4 J_{SC_{max}} \frac{\theta_{slew}}{t_{slew}^2}, \tag{3.9}$$

where $J_{SC_{max}}$ is the maximum moment of inertia of the LST, θ_{slew} is the slew requirement and t_{slew} is the time allocated to complete the maneuver. In MISS, the following requirements and assumptions are implemented: (i) $SM_\tau = 0.2$; (ii) $\theta_{slew} = 20$ deg; (iii) $t_{slew} = 20$ min.

Once obtained the sizing torque as

$$\tau_{RW_{req}} = \max(\tau_{ext}, \tau_{slew}), \tag{3.10}$$

the RW angular momentum capacity $h_{RW_{req}}$ is evaluated as

$$h_{RW_{req}} = \frac{\tau_{RW_{req}} \cdot T_{orb}}{n_{dump}}, \tag{3.11}$$

where T_{orb} is the orbital period. The minimum storage requirement is defined considering at most n_{dump} wheels dumping maneuvers over one orbit, which has been set to 2. If $h_{RW_{req}} \leq h_{RW_{nom}}$, where $h_{RW_{nom}}$ is the nominal angular momentum capacity of the Rockwell Collins RDR 68-3, MISS provides the mass budget following the information provided in the actuators database. On the other hand, if $h_{RW_{req}} > h_{RW_{nom}}$, the mass of the n_{RW} RWs is obtained as

$$m_{RW} = n_{RW} \cdot (-2 \cdot 10^{-7} h_{RW_{req}}^4 + 6 \cdot 10^{-5} h_{RW_{req}}^3 - 0.0076 h_{RW_{req}}^2 + 0.4039 h_{RW_{req}} + 0.5609). \tag{3.12}$$

The wheels desaturation is provided by the chemical thrusters equipped on the LST, as presented in Section 2.2.3, which define the propellant demand for this maneuver as

$$m_{fuel_{dest}} = \frac{F_{thr} \cdot t_{desat}}{g_0 \cdot I_{sp_{thr}}} \tag{3.13}$$

where F_{thr} is nominal thrust provided by each thruster. Moreover, t_{pulse} is the total burn time given by

$$t_{pulse} = n_{pulse} \cdot n_{RW} \frac{365}{T_{orb_{day}}} \cdot n_{miss} \tag{3.14}$$

considering $n_{pulse} = 1$ dumping maneuver per orbit per wheel and n_{miss} missions performed by the LST during its entire lifetime.

Last, the mass and power budgets for the navigation sensors, $m_{sensors}$ and $P_{sensors}$ respectively, are defined according to the suite features described in Section 2.2.3 and the sensor performance reported in Table 3.3. Thus, the sensors budgets are defined as

Table 3.3: AOCS sensors main features.

Sensor	n_{sensor_i}	m_{sensor_i} [kg]	P_{sensor_i} [W]
Star sensor	$3+3$	30	20
Sun sensor	$3+3$	2	3
IMU	$1+1$	15	200
Magnetometer	$3+3$	1.5	1

$$m_{sensors} = (1 + \mathrm{SM}_{sensor}) \cdot \sum_i n_{sensor_i} \cdot m_{sensor_i}, \tag{3.15}$$

$$P_{sensors} = (1 + \mathrm{SM}_{sensor}) \cdot \sum_i n_{sensor_i} \cdot P_{sensor_i}, \tag{3.16}$$

with SM_{sensor} set to 0.2. Last, the mass and power budgets for the AOCS subsystem are obtained as

$$m_{AOCS} = n_{thr} \cdot m_{thr} + n_{RW} \cdot m_{RW} + m_{sensors}, \tag{3.17}$$

$$P_{AOCS} = n_{thr} \cdot P_{thr} + n_{RW} \cdot P_{RW} + P_{sensors}. \tag{3.18}$$

3.2.2 Propulsion Subsystem

The design process adopted to define the e-PROP architecture is represented in Figure 3.5, where it is shown that the cluster configuration is a function of the total number of HETs, in turn function of the number of operative thrusters $N_{HET_{op}} = j$, the thrust-over-mass ration $(T/m)_j$ and the maximum transfer duration t_{max}.

First, the total number of thrusters required for the entire LST operational lifetime is defined as

$$N_{HET} = j \cdot n_{clust} + N_{red}, \;\text{ with }\; n_{clust} = \mathrm{ceil}\frac{\Delta t((T/m)_j)}{Life_{thr}} \tag{3.19}$$

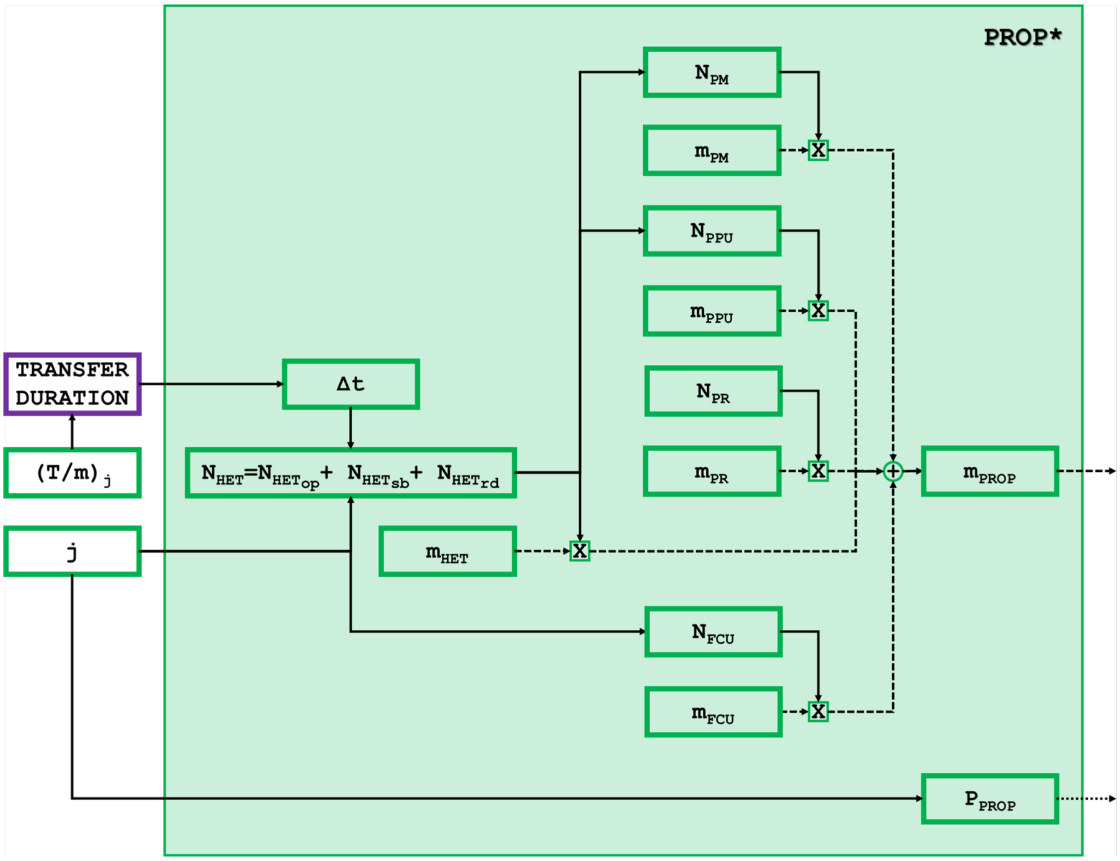

Figure 3.5: MISS PROP algorithm block diagram. The mass budget links are represented with dashed lines whereas the power budget links are in dotted lines.

where $\Delta t((T/m)_j)$ is the transfer time corresponding to $(T/m)_j$ applying the proper polynomial function, $Life_{thr}$ is the HET operational lifetime and $N_{red} = n_{clust}$ is the number of redundant thrusters. Then, the number of PPU is obtained considering a power distribution architecture that allows to connect 4 HETs to the same PPU, only one provided with power whereas the other 3 are stand-by thrusters, connected through a thruster switching unit to the PPU. Thus, N_{PPU} is defined starting from a first attempt value, i.e. $N_{PPU_{FA}} = j + 1$, and then

- if $N_{HET} - 4 \cdot N_{PPU_{FA}} \leq 0$, then $N_{PPU} = N_{PPU_{FA}}$.
- $N_{HET} - 4 \cdot N_{PPU_{FA}} > 0$, then $N_{PPU} = N_{PPU_{FA}} + N_{PPU_{add}}$, where

$$N_{PPU_{add}} = \text{ceil}(\frac{N_{HET} - 4 \cdot N_{PPU_{FA}}}{4}). \tag{3.20}$$

Moreover, according to the assumption introduced in Section 2.2.1, the number of the other components of e-PROP is defined as follows: (i) pointing mechanism:

$N_{PM} = N_{HET}$; (ii) pressure regulator: $N_{PR} = 2$; and (iii) flow control unit: $N_{FCU} = N_{HET}$. Thus, the e-PROP mass budget is obtained as

$$\begin{aligned} m_{e-PROP} = {} & N_{HET}((1+SM_{HET})m_{HET} + (1+SM_{PM})m_{PM} + (1+SM_{FCU})m_{FCU}) \\ & + N_{PPU}(1+SM_{PPU})m_{PPU} + N_{PR}(1+SM_{PR})m_{PR} + (1+SM_{tank})m_{tank}. \end{aligned} \tag{3.21}$$

with the mass of Xenon tank is preliminarily evaluated as 10% of $m_{fuel_{Xe}}$. The other safety margins adopted in MISS and the mass of the single components are reported in Table 3.4. Furthermore, the e-PROP power budget is given by $P_{e-PROP} = (1 + SM_{HET_P}) \cdot jP_{HET}$, where $SM_{HET_P} = 0.2$.

Table 3.4: e-PROP components main features. The mass of the PR is a function of the HET propellant flow rate $\dot{m}_{flow}$.

Component	**Safety Margin [-]**	$m_{component}$ [kg]
Thruster	0.1	45
Pointing Mechanism	0.05	0.2
Power Processing Unit	0.2	40
Pressure Regulator	0.1	$0.1366\log(\dot{m}_{flow}) + 0.1599$
Flow Control Unit	0.1	6

3.2.3 Electrical Power Subsystem

The design of the EPS subsystem is thoroughly related to the LST total power demand, which main contribution is provided by the e-PROP subsystem. As anticipated in Section 2.2.2, EPS is composed by solar arrays, which design is defined by the area of deployable panels, and secondary batteries, characterized by their storage capacity.

First, the LST total power demand is evaluated starting from the power budget of AOCS and e-PROP considering that, in first approximation, $P_{e-PROP} + P_{AOCS}$ represents the 70% of the total power budget

$$P_{LST_{tot}} = (1 + SM_{SRR} + SM_{harn}) \cdot \frac{P_{e-PROP} + P_{AOCS}}{0.7} \tag{3.22}$$

where $SM_{SRR} = 0.25$ is the system margin at the SRR and includes the contribution of the other subsystems and $SM_{harn} = 0.05$ corresponds to the harness loss. The power to generate by solar arrays is evaluated following the guidelines provided in SMAD and considering that the same amount of power shall be provided during both sunlight and eclipse

$$P_{SA} = \frac{P_{LST_{tot}}(\frac{T_{ecl}}{\chi_{ecl}} + \frac{T_{day}}{\chi_{day}})}{T_{day}}, \tag{3.23}$$

where T_{ecl} and T_{day} represent the length of eclipse and daylight periods per orbit, respectively, and $\chi_{ecl} = 0.65$ and $\chi_{day} = 0.9$ represent the efficiency of the paths from the solar arrays through the batteries to the individual loads and the path directly from the arrays to the loads, respectively. To size the solar array area, it is necessary first to define the ideal power requirement at BOL per unit area as

$$P_{BOL} = \eta_{cell} \cdot I_{solar} \cdot I_d \cdot \cos\theta, \tag{3.24}$$

where $\eta_{cell} = 0.45$ is the solar cells efficiency and I_d is their inherent degradation, given by the product of three contributions: (i) the inherent degradation due to design and assembly inefficiencies $I_{ass} = 0.9$; (ii) the inherent degradation due to temperature inefficiencies $I_t = 0.944$; and (iii) the inherent degradation due to shadowing of cells $I_s = 1$. Then, considering 15 years of operative lifetime $t_{sa_{year}}$ for the solar arrays and a annual performance degradation l_d of about 2.75%, the lifetime degradation L_d is given by $L_d = (1 - l_d)^{t_{sa_{year}}}$ and finally the total power demand at End Of Life (EOL) is obtained as $P_{EOL} = P_{BOL} \cdot L_d$, thus obtaining the solar array area as

$$A_{SA} = P_{SA}/P_{BOL}. \tag{3.25}$$

The corresponding mass is then evaluated as $m_{SA} = (1 - SM_{SA}) \cdot (P_{SA}/P_{SA_{sp}})$, where $SM_{SA} = 0.1$ in compliance with the ESA guidelines for off-the-shelves components requiring minor modifications, and $P_{SA_{sp}}$ is the solar array specific power, which for the Northrop Ultraflex is set to $P_{SA_{sp}} = 200$ W/m^2. Then, the secondary batteries are sized as a function of the specific performance in terms of Depth of Discharge (DoD), i.e. $DoD = 0.5$, and specific energy density, eclipse length, transmission efficiency $\eta_{trans} = 0.9$. The total battery capacity, according to [17], is defined as

$$C_{batt} = \frac{P_{LST_{tot}} \cdot T_{ecl}}{\eta_{trans} \cdot DoD}. \tag{3.26}$$

Then, preliminarily assuming that all the batteries are arranged in series, the number of batteries N_{batt} is obtained as $N_{batt} = \text{floor}(C_{batt}/C_{batt_{GY}})$, where the specific capacity of each GS-Yuasa LSE134-101 is $C_{batt_{GY}} = 548$ Wh. Then, the mass of the batteries is evaluated as $m_{batt} = (1 + SM_{batt}) \cdot N_{batt} \cdot m_{batt_{GY}}$, where $SM_{batt} = 0.1$. Last, the total EPS mass budget is obtained as

$$m_{EPS} = m_{SA} + m_{batt} + m_{EPS_{add}}, \tag{3.27}$$

where $m_{EPS_{add}} = (1 + SM_{EPS_{add}}) \cdot 0.05 \cdot (m_{SA} + m_{batt})$ takes into account all the other components not explicitly sized within this sizing block.

3.2.4 Thermal Control Subsystem

The TCS subsystem sizing is a function of the thermal control strategy as well as the temperature ranges of the critical components, such as solar arrays, secondary batteries, and AOCS sensors. As described in [17], considering the exploitation of an active control strategy, the design logic can be split in two main phases: (i) first the HOT worst case from a thermal point-of-view is used to size the radiators area; then, (ii) the heaters power required to keep the electronics above their minimum non-operating temperature limit the COLD worst case ic considered. The first step consists in the definition of the temperature operative range, which lower and upper bounds are set as $T_{MIN} = -10°\text{C}$ and $T_{MAX} =30°\text{C}$, respectively. Then, the environmental heat absorbed $Q_{external}$ is evaluated as $Q_{external} = q_{external} A_{rad}$, with A_{rad} the radiators area and $q_{external}$ the external heat absorbed per unit area evaluated as the sum of four different heat loads

$$q_{external} = q_{solar} + q_{albedo} + q_{IR_{pl}} + q_{backload}, \tag{3.28}$$

where:

- q_{solar} is the heat load due to the Sun, which is estimated as

  $$q_{solar} = (1 - \beta_{ecl}) \cdot \alpha_{EOL} \cdot I_{solar} \cdot \cos\theta \tag{3.29}$$

  where β_{ecl} is the percentage of orbital period where the spacecraft is in the planet shadow, α_{EOL} is the radiators absorptivity at the EOL, $I_{solar_{HOT}}$ is the Solar constant and θ represents the angle among the Sun direction and the normal to the radiator panel.

- q_{albedo} is the heat load given by the sunlight reflected off a planet, i.e. albedo, and is evaluated as

  $$q_{albedo} = \alpha_{EOL} \cdot I_{solar_{HOT}} \cdot \rho_{albedo} \cdot F_{albedo}, \tag{3.30}$$

  where ρ_{albedo} and F_{albedo} are the planet albedo and the albedo geometrical factor accounting for the direction of the radiator relative to the planet and Sun, respectively. In particular, the geometrical factor F_{albedo} is defined as

  $$F_{albedo} = \left(\frac{R_{pl}}{R_{pl} + h_{orb}}\right)^2 \tag{3.31}$$

  with R_{pl} the planet radius and h_{orb} the orbit altitude.

- $q_{IR_{pl}}$ is the heat load due to all incident sunlight not reflected as albedo and absorbed by the planet, and eventually re-emitted as IR energy. The planet IR load per unit area is obtained as

  $$q_{IR_{pl}} = \epsilon \cdot I_{IR_{pl}} \cdot F_{IR_{pl}}, \tag{3.32}$$

  where ϵ is the emissivity of the radiator panels, $I_{IR_{pl}}$ is the planet IR flux and $F_{IR_{pl}} = F_{albedo}$ is the IR geometrical factor accounting for the direction of the radiator relative to the planet and Sun.

- $q_{backload}$ is the radiative backload from other spacecraft surfaces, which contribution has been neglected in MISS.

Thus, starting from the generalized heat balance equation

$$Q_{external} + Q_{internal} = Q_{radiator}, \tag{3.33}$$

where $Q_{internal}$ is the power dissipation load and $Q_{radiator}$ is the heat rejected from the radiators. Assuming that $Q_{internal} = P_{LST_{tot}}$ and $Q_{radiator} = \epsilon \cdot \sigma \cdot A_{rad} \cdot T^4_{MAX}$, where $\sigma = 5.67051 \cdot 10^{-8}$ W/m^2/K^4 is the Stefan Boltzmann constant, the radiator area is obtained as

$$A_{rad} = \frac{Q_{internal}}{q_{radiator} - q_{solar} - q_{albedo} - q_{IR_{pl}}}. \tag{3.34}$$

The corresponding mass is estimated considering that the mass per unit area has been set to 3.3 kg/m^2. Table 3.5 summarizes the thermal parameters exploited in MISS.

Table 3.5: TCS thermal parameters for HOT and COLD assessment in Earth and Lunar orbits.

Parameter	**Safety Margin [-]**
$I_{solar_{HOT}}$ [W/m^2]	1418
$I_{solar_{COLD}}$ [W/m^2]	1360
$\rho_{HOT_\oplus}$ [-]	0.37
$\rho_{HOT_{Moon}}$ [-]	0.07
$\rho_{COLD_\oplus}$ [-]	0.23
$\rho_{COLD_{Moon}}$ [-]	0.03
$I_{IR_{HOT_\oplus}}$ [W/m^2]	244
$I_{IR_{HOT_{Moon}}}$ [W/m^2]	430
$I_{IR_{COLD_\oplus}}$ [W/m^2]	218
$I_{IR_{COLD_{Moon}}}$ [W/m^2]	410
α_{HOT} [-]	0.15
α_{COLD} [-]	0.05
ϵ [-]	0.85

Next, the heaters power requirement is obtained evaluating again all the heat loads per unit area but considering the COLD worst case thermal parameters to define the corresponding radiators temperature

$$T_{rad} = \left(\frac{Q_{external_{COLD}} + Q_{internal_{COLD}}}{\epsilon \cdot \sigma \cdot A_{rad}} \right)^{0.25}, \tag{3.35}$$

with $Q_{internal_{COLD}} = 0.9 \cdot Q_{internal}$. Then, applying an uncertainty margin of -10°C to the minimum non-operating temperature T_{MIN}, the COLD heat load rejected by the radiators is defined as $Q_{radiator_{COLD}} = \epsilon \cdot \sigma \cdot A_{rad} \cdot (T_{MIN} - 10°)^4$ and the difference $Q_{radiator_{COLD}} - Q_{extermal_{COLD}}$ provides the heaters power requirement.

3.2.5 Other Subsystems

As anticipated in Section 3.1.3, the mass budgets for TTC, CDH and StrMech are defined as relative percentage of the LST dry mass, which is estimated starting from the mass budget for the other four subsystems as

$$m_{LST_{dry}} = \frac{m_{AOCS} + (m_{e-PROP} + m_{tank}) + m_{EPS} + m_{TCS}}{RP_{AOCS} + RP_{PROP} + RP_{EPS} + RP_{TCS}}. \tag{3.36}$$

Thus, the mass of the i-th subsystem is obtained as

$$m_{S/S_i} = \left(1 + \frac{SM_{S/S_i}}{100}\right) \cdot (RP_{S/S_i} \cdot m_{LST_{dry}}). \tag{3.37}$$

3.2.6 Propellant Consumption and Tank Design

As anticipated in Section 3.2.2, the e-PROP is completed with the design of the Xenon tanks whereas from a physical point of view the PROP subsystem includes also the mass of the chemical thrusters as well as the Hydrazing tanks. To properly estimate the propellant consumption, for both Xenon and Hydrazine, the Tsiolkovsky's equation is exploited as follows

$$m_{fuel_{Xe}} = m_{LST_{dry_{tot}}} \left(\exp\left(\frac{\Delta v_{EOR}}{g_0 I_{sp_{HET}}}\right) - 1\right), \tag{3.38a}$$

$$m_{fuel_{Hyd}} = m_{LST_{dry_{tot}}} \left(\exp\left(\frac{\Delta v_{ARVD}}{g_0 I_{sp_{thr}}}\right) - 1\right), \tag{3.38b}$$

where $I_{sp_{HET}}$ and $I_{sp_{thr}}$ are the HET and chemical thruster Isp, respectively. In both cases, the tank mass can be preliminarily estimated as $m_{tank_{Xe}} = 0.1 \cdot m_{fuel_{Xe}}$ and $m_{tank_{Hyd}} = 0.1 \cdot m_{fuel_{Hyd}}$, where $m_{fuel_{Hyd}} = m_{fuel_{ARVD}} + m_{fuel_{desat}}$. Moreover, since the propellant mass is a function of the current LST total dry mass, the propellant consumption is given by the sum of contribution for each mission phase, characterized by a different delta-v budget and LST masses as well as the presence or absence of the cargo module.

Once obtained the preliminary tank masses, a convergence loop allows to estimate the real values starting from the first-attempt ones, i.e. $m_{tank_{HET_{FA}}}$ and $m_{tank_{thr_{FA}}}$. The convergence loop logic can be described as follows:

1. Estimate $m_{tank_{FA}} = 0.1 m_{fuel_{FA}}$;

2. Obtain the e-PROP first-attempt mass budget following Eq. (3.21) with $m_{tank} = m_{tank_{FA}}$;
3. Evaluate the preliminary LST dry mass budget as $m_{LST_{dry_{FA}}} = \sum_i m_{S/S_i}$;
4. Calculate the new propellant consumption $m_{fuel_{new}}$ applying Eq. (3.38);
5. Run the following:

```
begin
if $m_{fuel_{new}} \leq m_{fuel_{FA}}$ then
    $m_{tank} = m_{tank_{new}}$
    $m_{fuel} = m_{fuel_{new}}$
else
    $\Delta m_{fuel} = 0.05$
    $m_{tank_{FA}} = m_{tank_{new}}$
    $m_{fuel_{FA}} = (1 + \Delta m_{fuel}) m_{fuel_{new}}$
    go back to step 2
end if
end
```

Chapter 4

Simulated Trajectories for Automated Rendezvous Tool

4.1 Automated Rendezvous Maneuver

1963. Cambridge. A young Edwin Eugene "Buzz" Aldrin defended his PhD thesis entitled *Line-Of-Sight Guidance Techniques For Manned Orbital Rendezvous* [71] at the Massachusetts Institute of Technology, where he proposed an innovative rendezvous guidance algorithm to extend human control capabilities. And he had somehow prophetically enscribed the following thesis dedication:

> *"In the hopes that this work may in some way contribute to their exploration of space, this is dedicated to the crew members of this country's present and future manned space programs. If only I could join them in their exciting endeavors!"*

Two years later, June 1965, the first American attempt, turned out to be a failure, with the US astronaut Jim McDivitt trying to maneuver the Gemini IV spacecraft to rendezvous with its Titan II launch vehicle's upper stage. Only six months later, on December 15 1965, Gemini VI and Gemini VII successfully accomplished the first manned rendezvous maneuver, maintaining station-keeping for more than 20 minutes within 30 cm each other thanks to the ability of the US astronaut Wally Schirra (see Figure 4.1a). On March 1966, Gemini VIII (Figure 4.1b) was able to rendezvous and dock with an unmanned Agena target vehicle under the command of US astronaut Neil Armstrong. No more than 15 months after, the Soviets realized the first *automated, unmanned rendezvous and docking* in the history of space exploration on October 20, 1967 (see Figure 4.2). The Kosmos 186 spacecraft, thank to its IGLA-system equipped on board, approached, docked and jointly flighted for 3.5 hours with the Kosmos 188, paving the way for the future ARVD era.

Rendezvous represented a key technology in the settlement and refurbishment of orbiting space stations, such as the Russian Salyut 1 (1971) and Mir (1986-2001), the American Skylab (1973-1979) and the ISS (1998-). However, at the

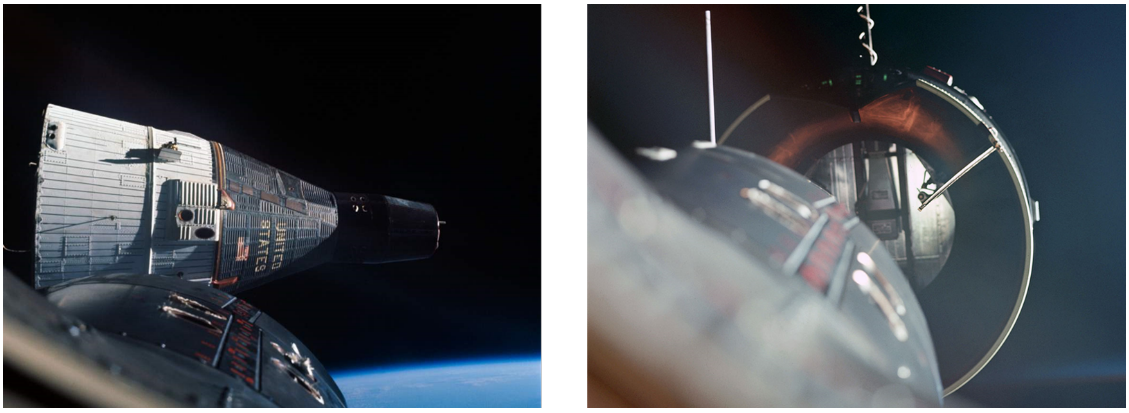

Figure 4.1: Gemini VII photographed by Gemini VI during the first manned rendezvous maneuver, December 15, 1965 (left) and view from Gemini VIII just 0.6 m from an Agena target vehicle before achieving the first docking, March 16, 1966 (right) (credit: NASA).

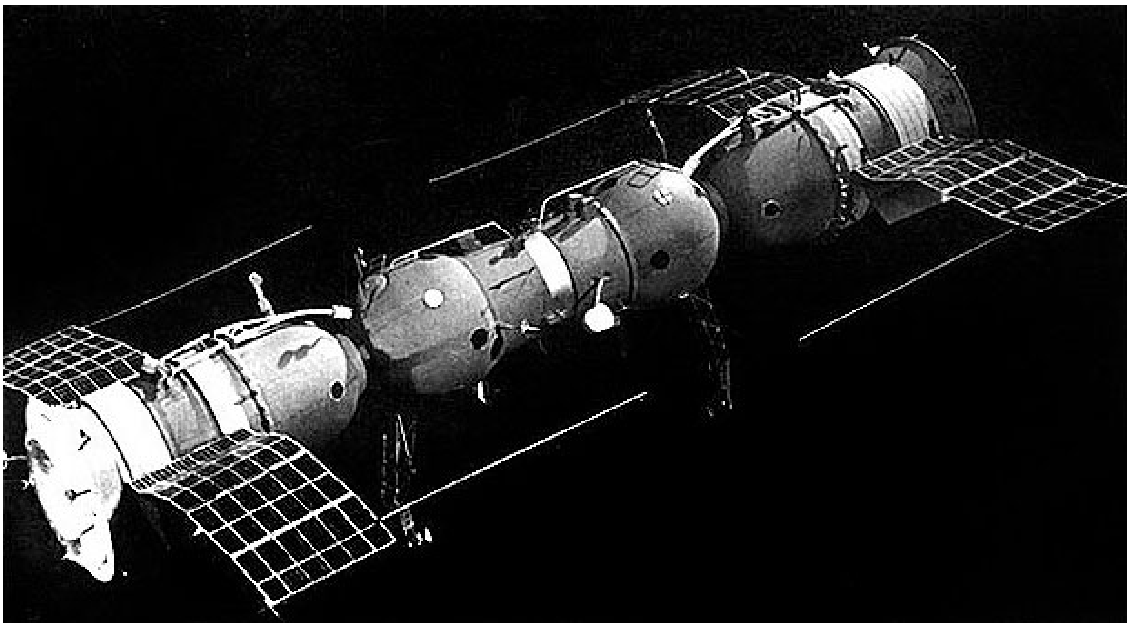

Figure 4.2: Kosmos 186 and Kosmos 188 performing the first automatic docking in space. (credit: collectSPACE).

beginning of the new millennium only Russians have already developed ARVD capability and extensively use it in several missions, as described in [72] and [73]. In the meantime, US, Europe and Japan have started several independent, ongoing technology programs for developing analogous ARVD capabilities to primarily level off the disparity with the Russians into resupply the ISS. The NASA Space Shuttle, the European ATV [74] and the Japanese H-II Transfer Vehicle [75] are the main outcomes of their progress in ARVD. With the successful docking among the Shenzhou-8 and Shenzhou-9 spacecraft with the Tiangong-1 space lab on 2011 and 2012, respectively, also the Chinese marked the breakthrough in the rendezvous and docking technology [76]. Further historical data about the development of the rendezvous technology over the past 50 years can be found in [77]. Moreover, on-orbit servicing has been recognized as a crucial asset in several applications such as mission life extension, refueling repair and upgrading. A relevant example is represented by the five NASA Space Shuttle missions dedicated to rendezvous and intercept in orbit the Hubble telescope to perform either repair and replacement of dated, degraded or failed components and then redeploy Hubble to a higher orbit to address the orbital decay caused by atmospheric drag, as described in [78]. Other missions that could benefit from on-orbit servicing are related to *observation*, i.e. remote inspection, *motion*, i.e. station keeping, relocation and disposal, and *manipulation*, e.g. refueling, maintenance and repair. All of them have at least one commonality: rendezvous and mating maneuvers are involved to ensure the successful accomplishment of the mission.

With the begin of the new space exploration era, ARVD stepped back in the public spotlight as one of the crucial enabling technology. Indeed, as anticipated in Chapter 1, *automated rendezvous and docking* has been identified as one of the top ten technical challenges for extending and sustaining the human presence beyond LEO, i.e. TA04 "*Robotics, TeleRobotics, and Autonomous Systems*". In particular, the ability to perform autonomous rendezvous and safe docking/berthing has been declared as central to the future of diverse mission concepts. Indeed, there is an increasing interest in on-orbit assembly of space infrastructures, such as the LOP-G, inspection, maintenance and repair missions, servicing and refueling, as well as orbital debris removal [11]. Indeed, all the scenarios that space agencies have defined for the future exploration program have one thing in common. Each mission architecture heavily relies on the ability to rendezvous and mate multiple elements in space. As these missions become more and more popular, the number of rendezvous and docking class operations will increase dramatically. Longer term concepts also include the assembly of human outposts or supply depots. Major challenges linked to ARVD include improving their robustness to ensure mating and avoid collision with the target itself, in different operational conditions, environment and with diverse space systems. Moreover, Pierro Miotto from Draper Laboratory highlighted that the next-generation ARVD technologies shall rely on common standards, open architectures, and non-proprietary solutions. The advancements of robotics and autonomous systems will be central to the transition of space mission from current ground-in-the-loop (geocentric) architectures to self-sustainable, independent systems. This represents a key step, necessary for outer-planet exploration and for overcoming the many difficulties of interplanetary travel. In order to meet the exploration enterprise goals of affordability, safety and sustainability, the critical capabilities of rendezvous, capture and in-space assembly must become routine and autonomous. For these critical capabilities to become routine, a much more reliable and autonomous rendezvous, capture and in-space assembly capability must be employed [12].

The LST, being a fully-automated transfer vehicle, shall significantly rely on ARVD technology not only for motion/relocation purpose, i.e. rendezvous with both cargo module and LOP-G, but also for manipulation tasks, i.e. on-orbit refueling via ORS. Moreover, being a reusable space transportation system and conceiving the possibility to use multiple tugs in the same fleet, the ARVD reliability representes a must of the mission. All the LST shall be able to safely perform all the ARVD maneuvers multiple times with different targets and in different environments, exploiting the same resources. Thus, robustness to mission uncertainty and environmental changes is *fundamental*. Despite the classical rendezvous mission profile involves multiple phases, from the launch up to the mating operation as presented in [66], the LST rendezvous maneuver stars when the tug acquires the target orbit when the electric thrusters are turned of and the AOCS actuators are exploited for navigation and propulsion purposes (see Figure 4.3). A constraint on the location of this first aim point may come from operational requirements imposed either by the target system and the main stakeholders. For instance, for the ISS, the so-called close-range rendezvous shall begin outside an approach ellipsoid.

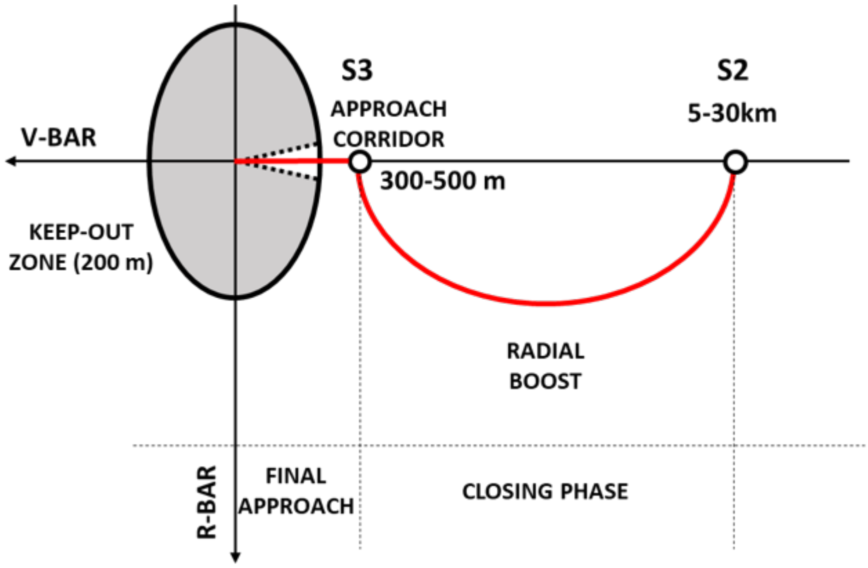

Figure 4.3: LST rendezvous mission profile including closing phase and final approach.

In particular, the radial boost maneuver allows to reduce the range to the target vehicle as preparatory phase leading to the final approach corridor and results in an eccentric orbit trajectory without changing the average orbital altitude, as described in [66], considering a continuous thrust transfer along V-bar, i.e., the target orbital velocity direction as represented in Figure 4.4a. For the final approach, instead, the objective is to drive the chaser to achieve the docking or berthing capture conditions, in terms of velocities and relative attitude and angular rates, and while remaining in the LOS cone corridor (feasible region in Figure 4.4b), following a minus V-bar approach as the ATV.

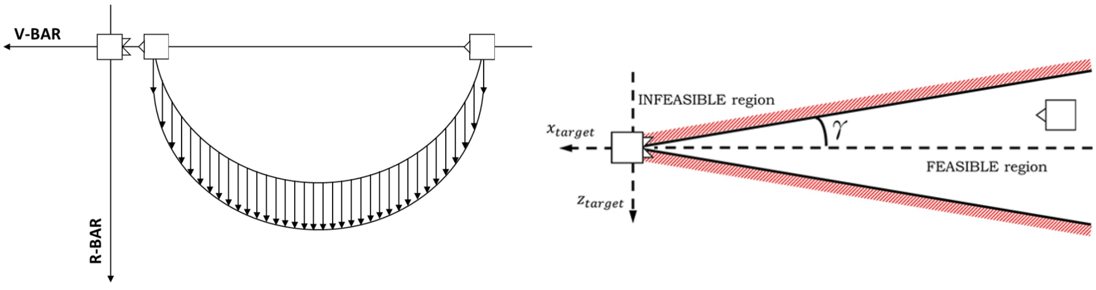

(a)

(b)

Figure 4.4: LST close-range rendezvous: (a) closing phase and (b) final approach ([79]).

The closing phase and the final approach are the most critical ARVD phases since in these phases, the bodies involved in the maneuver are relatively close together and they have to perform a controlled "collision", as defined in [66]. The complexity of the rendezvous maneuver mainly results from the multitude of safety and operational *constraints* which must be fulfilled, defined accordingly to the mission profile considered. In terms of safety, the close-range rendezvous phases are the most critical, especially when the on-ground supervision could be compromised due to the large distances, i.e. beyond LEO towards the deep space, and a higher level of autonomy shall be ensured. Moreover, during close-range rendezvous maneuvers the trajectory of the chaser vehicle, by definition, leads toward the target one and the two space systems are relatively close together so that any deviation from the planned trajectory can potentially lead to a collision. For sensing purposes (see [80]), it is required that the chaser vehicle during the final approach remains inside a LOS from the docking point. The LOS constraint is usually defined in terms of an approaching corridor within the keep-out zone, as represented in Figure 4.3. During the rendezvous hovering phase at the end of the final approach, to allow either berthing or docking, the chaser is required to remain in the interior of a certain limited region of the space, which can be modeled as a polytope, i.e. a rectangular parallelepiped, without any generality loss. Moreover, soft docking constraints can be enforced, reducing the approach velocity in line with distance to the target, as well as limiting the maximum approach velocity, during the whole close-range rendezvous maneuver. Additional constraints are not mission-related but are inherent to the specific space system configuration. In particular, when using thrusters for spacecraft trajectory control, not only there are constraints on the maximum force that can be applied at any given instant, i.e. saturation of the actuators, but there is also the physical constraint of a thrust *dead-zone* between the thruster being fully off, and delivering its minimum non-zero thrust, often referred to as the Minimum Impulse Bit (MIB), and the total number of firings available. Indeed, constraints on the maximum deliverable Δv are placed on each element of the input vector. Analogously, momentum wheels as well as reaction wheels performance are constrained in terms of maximum angular velocity and momentum, requiring dedicated maneuvers to desaturate the wheel when the maximum saturation limit is reached. Last but not least, other constraints can be set on both fuel consumption (or on the amount of fuel dedicated to the maneuver) and on the maneuver duration, as described in [81].

Nowadays, no official regulations for fully ARVD have been established whereas there are current guidelines in force for the LOP-G, which have been preliminarily summarized in [82] by the ISS membership to establish interoperable interfaces, techniques, and environments to facilitate collaborative endeavors of future space exploration missions. Within the first draft of this document, released on February 2018, the *International Rendezvous System Interoperability Standards* Chapter provides the basic common design parameters to allow developers to independently design compatible rendezvous operations. while trying to lower development cost, decrease operational complexity, and improve safety and mission success. In particular, each phase has been defined in terms of operational region where the chaser vehicle shall not enter prior to a predefined maneuver that takes the vehicle inside the specific region. Considering those that are of interest to the LST, the following regions have been identified:

1. **Approach Sphere**: 2 km radius sphere centered at the LOP-G center of mass.
2. **Keep-out Sphere**: 200 m radius sphere centered at the LOP-G center of mass.
3. **Approach Corridor**: ±10° centered to the docking port axis within the keep-out sphere.

Hence, for this work two different approaches have been followed to define the initial relative distance to start the ARVD maneuver: (i) for cargo module and ORS, i.e. unmanned systems, the LST radial boost maneuver starts when the vehicles are 6 km far, i.e. outside the approach sphere; (ii) for the LOP-G, the presence of crewmembers represents a severe safety-criticality and the minimum distance set among the LST and the Gateway has been set to 30 km, far outside the approach sphere. The latter setting has been considered also because no regulations have been defined yet for electric propelled spacecraft, which do not follow the classical mission profile and are subject to major issue due to plume impingement. On the other hand, both final approach phases begin when the chaser is to a relative distance equal to 500 m far from the target, i.e. slightly outside the keep-out zone.

Safety regions are critical to contributing to mission safety and success, together with the previous introduced mission and system constraints, and all of them have a significant impact on expected GNC performance. On the other hand, the limited resources available for aerospace systems significantly affect related mission planning and operability, especially for systems with high levels of autonomy as the LST. The resources constraints can come from either physical limitations/actuation capacity and encapsulate limited onboard computational power. Thus, GNC algorithms development requires a rather complex process from the conceptual design to actual implementation. In particular, as highlighted in [8] and in [83], to meet the GNC challenges of next-generation space missions, on-board algorithms shall meet the following specifications: (i) *real-time implementability*; (ii) *optimality*; (iii) *verifiability*. Hence, new GNC algorithms need to be implemented and executed on real-time processors, in a compatible amount of time, providing a feasible and (approximately) optimal solution, verifying the design metrics identified to describe their performance. Moreover, flight software development shall undergo an additional constraint raising from the computational cost to comply with available memory usability. Thus, the ARVD cruciality enforces design of customized, highly reliable AOCS subsystems either in terms of hardware, e.g. flight computer and actuators, and GNC software.

Hence, for design purposes, it is imperative to have a reliable and realistic simulation environment, able to reproduce the chaser and target vehicles attitude and orbital dynamics during the close-range rendezvous maneuver. At this end, the STAR 6 DoF orbital simulator has been developed with the purpose to create a highly reliable and flexible environment where it is possible to preliminarily validate the effectiveness of several combination of GNC algorithms in different scenarios, as those characterizing the LST mission, combining the features of the AOCS subsystem with the requirements and constraints coming from the mission and the system itself. The main goal was to build up a software suite in a MATLAB/Simulink environment, interfaced with the MISS design tool, to properly propagate the LST and target vehicles dynamics in both GTO and cislunar proximity and to validate the control strategies proposed (further details are provided in Chapter 5) whereas the guidance algorithm provides the reference according to the rendezvous profile selected, i.e. ATV-like minus V-bar approach (see [66]). For navigation purpose, on the other hand, it is assumed that all the chaser and target status, position, velocity and attitude are always available whereas the measurement errors that could arise from sensors malfunctioning are introduced as parametric uncertainty and additive disturbance. Moreover, in compliance with the on-board algorithm specifications required for the next-generation GNC architecture, STAR allows to verify the compliance with the design metrics, in terms of fuel consumption and maneuver duration, while preliminarily verifying the real-time implementability running over an Intel Core i7 – 7500U CPU @2.70 GHz with 16 GB of RAM and 512 GB solid-state drive, which performance are similar to state-of-the-art space-qualified hardware. Furthermore, to guarantee feasibility and optimality of the solution provided by the control algorithm, optimal control strategies have been considered and implemented which are able to deal with uncertainty, either additive and parametric, while guaranteeing constraint satisfaction. In particular, three different MPC schemes, i.e. a classical, a robust and a stochastic MPC algorithm, have been designed for both attitude and orbital control during the ARVD maneuvers in GTO as well as in NRHO, while perturbations arising from model uncertainty and environmental disturbances affect the LST dynamics during the proximity operations. Further details are provided in Chapter 5. In the following Section a thorough presentation of the STAR tool is provided, highlighting the main features included in the simulation environment to cope with the peculiar needs of the LST mission, e.g. highly elliptic orbits, whereas the theoretical properties of the control strategies adopted are described in Chapter 5. Last, to complete the validation of the control strategy, three different experimental campaigns have been performed, two of them to test the real-time implementability on space-qualified hardware running the multirate GNC directly on board mock up of spacecraft (Chapter 6). On the other hand, the third experimental campaign was focused on analyzing the extension of control strategies operational envelope, implementing the same algorithms for a system characterized by much faster dynamics than spacecraft and typically equipping less performing hardware from a computational point-of-view, i.e. fixed wing UAV. Further details on the latter test campaign can be found in Appendix B.

4.2 STAR Orbital Simulator

In this Section, a thorough description of the main elements composing the 6DoF orbital simulator STAR is provided starting from the definition of the coordinate reference frames considered. Then, the STAR architecture is presented. The simulation tool is primarily composed by an initialization environment representing the main interface with the MISS design tool and by a Simulink environment where the chaser and target dynamics are simulated during the different ARVD maneuvers in GTO and NRHO.

4.2.1 Coordinate Reference Frames

In this Section, the coordinate reference frames exploited for later describing the attitude and translational dynamics of both LST and target vehicles are recalled, together with the corresponding coordinate transformation matrices.

Inertial Frame

Two different inertial frames (see Figure 4.5) have been adopted to describe the orientation of the orbit as well as the chaser and target vehicles relative to inertial space. The ECI has its origin in the center-of-mass of Earth, has the x-axis x_{ECI} on the equatorial plane, inclined by an angle of 23.4° with respect to the ecliptic, and oriented towards the mean vernal equinox at J2000 epoch, the z-axis z_{ECI} is aligned with the Earth spin axis (celestial North Pole) whereas the y-axis y_{ECI} completes the right-handed triad. For the lunar space, an analogous inertial frame, i.e., the Moon-Centered Inertial Frame (MCI), has been exploited, where the x-axis x_{MCI}, lying in the Lunar equatorial plane, is parallel to the ECI x-axis, the z-axis z_{MCI} is along the Moon spin axis, which is inclined by 6.68° with respect to the normal to the Moon orbital plane. The third axis, i.e., y-axis y_{MCI}, is in the lunar equatorial plan and completes the triad.

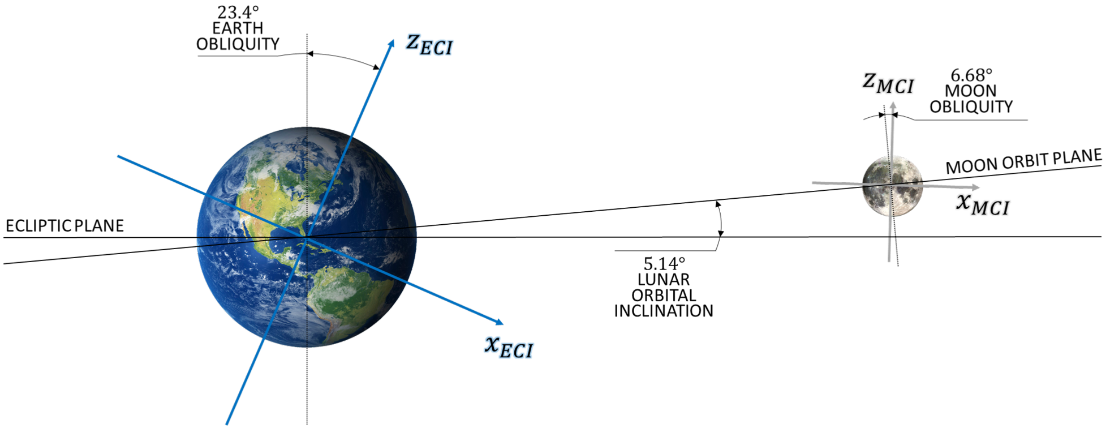

Figure 4.5: ECI and MCI inertial reference frames.

Perifocal Reference Frame

The Perifocal reference frame is a non-rotating frame, fixed with respect to the orbit, with the origin in one of the ellipse focal points, coinciding with the main body center-of-mass. Indeed, the x-axis p_{PQW} is along the eccentricity vector $\mathbf{e}$, which results constant for Keplerian trajectories, whereas the z-axis w_{PQW} is aligned with the orbit angular momentum $\mathbf{h}$, which represents a constant of the motion as well. The third axis, i.e., q_{PQW}, lies in the orbit plane and it is parallel to ellipse semi-minor axis, making the triad right-handed. The coordinate transformation from ECI to perifocal is obtained by three rotations: (i) first, a rotation about $z_{ECI/MCI}$ by the right ascension of the ascending node angle Ω; (ii) then, by a second rotation about $x_{ECI/MCI}$ equal to the orbit inclination i; (iii) last, a further rotation about z-axis by the argument of perigee angle ω. Thus, to convert a ECI vector to perifocal, the L_{E2P} rotation matrix shall be exploited, defined as

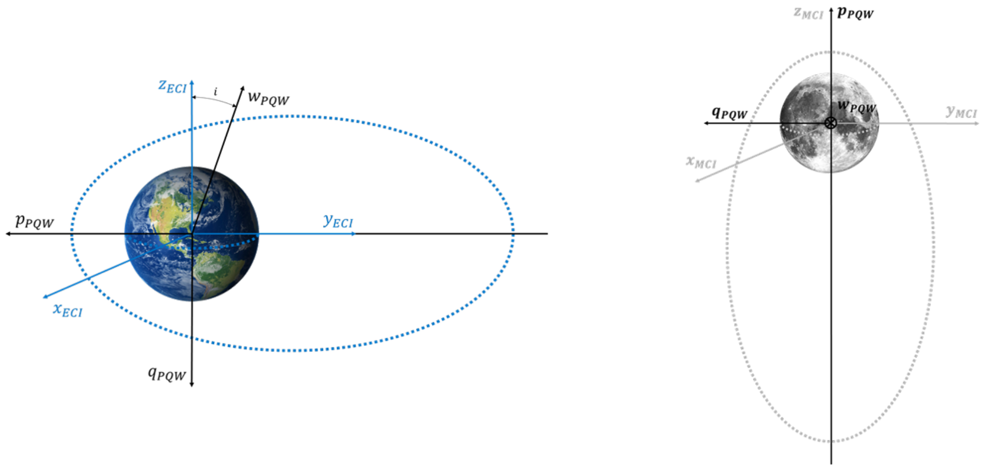

(a) (b)

Figure 4.6: Perifocal reference frames for (a) GTO and (b) NRHO.

$$L_{E2P} = \begin{bmatrix} \cos\omega & \sin\omega & 0 \\ -\sin\omega & \cos\omega & 0 \\ 0 & 0 & 1 \end{bmatrix} \begin{bmatrix} 1 & 0 & 0 \\ 0 & \cos i & \sin i \\ 0 & -\sin i & \cos i \end{bmatrix} \begin{bmatrix} \cos\Omega & \sin\Omega & 0 \\ -\sin\Omega & \cos\Omega & 0 \\ 0 & 0 & 1 \end{bmatrix}.$$

Local-Vertical/Local-Horizontal Frame

The rendezvous and proximity operations are typically treated as relative trajectories of the active vehicle, the chaser, with respect to the passive one, i.e., the target, and its local orbital frame, i.e. the LVLH frame. This frame is conveniently centered in the target center-of-mass and its z-axis z_{lvlh}, also called R-bar in rendezvous literature, points along the nadir vector, directed towards the center of the planet, i.e., either Earth or Moon, as defined in [65] and [66]. The x-axis x_{lvlh}, i.e., V-bar, is in the direction of the orbital velocity but not necessarily aligned with it whereas the y-axis y_{lvlh}, i.e., H-bar, is aligned with the orbit angular momentum, but in the opposite direction. Given the target position in ECI, $\mathbf{r}_I$, and the orbit angular momentum $\mathbf{h}_I = \mathbf{r}_I \times \mathbf{v}_I$, where $\mathbf{v}_I$ is the spacecraft velocity in ECI, the

LVLH unit vectors are given by

$$\hat{z}_{lvlh} = -\frac{\mathbf{r}_I}{\|\mathbf{r}_I\|}, \qquad \hat{y}_{lvlh} = -\frac{\mathbf{h}_I}{\|\mathbf{h}_I\|}, \qquad \hat{x}_{lvlh} = \hat{y}_{lvlh} \times \hat{z}_{lvlh}.$$

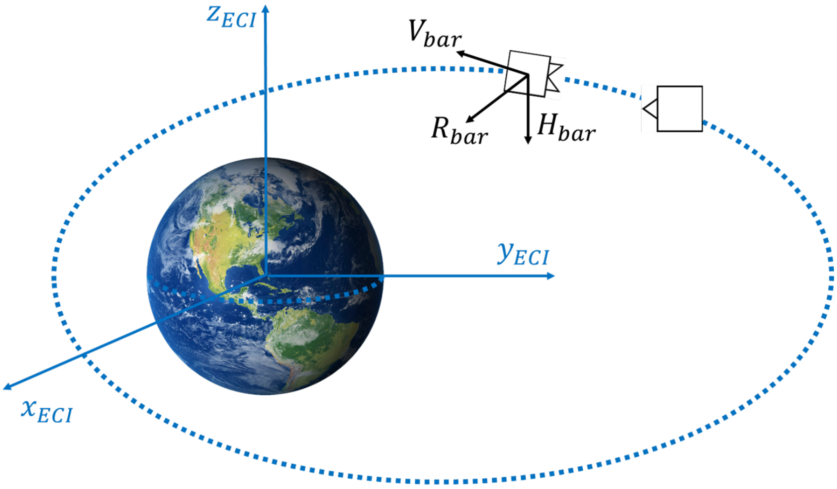

Figure 4.7: LVLH reference frame with respect to the target vehicle.

Body Reference Frame

The last reference frame, the body frame (see Figure 4.8), has been adopted to describe the attitude dynamic and kinematic of the LST relative to its center of mass and with respect to the LVLH frame, looking for the proper alignment of the docking mechanisms equipped on both the spacecraft. The body frame axes orientation for the LST is represented in Figure 4.8. The transformation from LVLH to body frame is obtained by a classical 3-2-1 rotation sequence.

Moreover, a second body frame has been defined with respect to the center-of-mass of the solar arrays as represented in Figure 4.8 to evaluate the overall tensor of inertia and center-of-mass of the LST as described in the follows.

4.2.2 STAR Initialization

As anticipated before, the initialization environment can be seen as the major interface among the two software suite, i.e. MISS and STAR. Indeed, on one side it allows to upload the mission data as well as requirements and constraints coming from the ConOps analysis, such as maximum ARVD maneuver duration and fuel consumption. On the other side, the AOCS architecture represents a fundamental output of the design phase as well as a crucial input for the ARVD maneuver

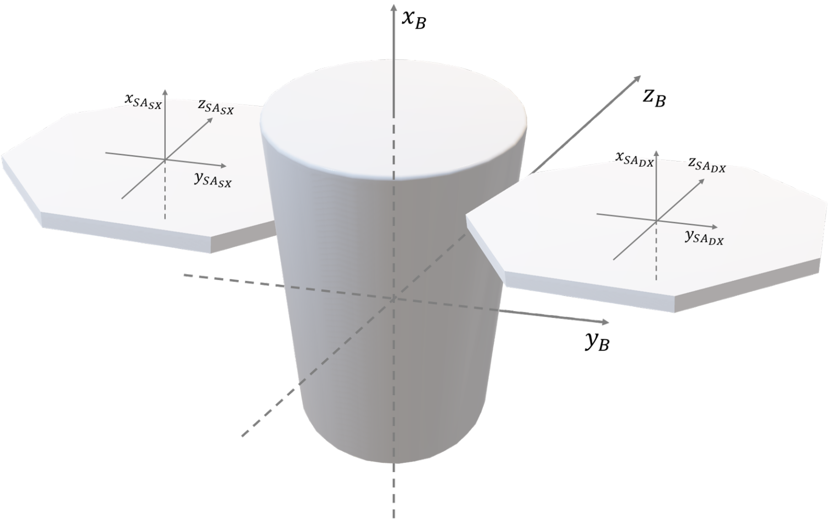

Figure 4.8: LST body reference frame.

analysis. In fact, the control performance of the spacecraft during proximity operations are significantly influenced by the actuation capabilities available and their compliance with the controllability effort required. Thus, a collection of MATLAB files has been realized to collect the mission and system analysis outputs useful to initialize the ARVD maneuver simulation while enforcing the identified constraints.

The first step consists into defining for each target vehicle, i.e. cargo module, LOP-G and ORS, the main physical features in terms of mass m_{TV}, volume V_{TV}, geometry, e.g. height, diameter, solar array size and orientation, and tensor of inertia J_{TV}. Analogously, the corresponding data for the chaser spacecraft are uploaded recalling the output of the MISS solution selection process. In particular, beside the geometrical features of the optimal LST configuration, the AOCS architecture is initialized according to the design phase outcome in terms of:

- Number, orientation and peculiar specifications of the RWs equipped on board the spacecraft, e.g. maximum angular speed, momentum, nominal torque and RW moment of inertia.
- Number, orientation, location and specific performance of the chemical thrusters used for orbital control and wheel desaturation, e.g. maximum thrust, MIB and Isp.

The next step consists in setting the initial conditions for the different ARVD maneuvers in compliance with the selected strategy and mission constraints, as anticipated in Section 4.1, in terms of: (i) chaser-target initial relative distance at the begin of the close-range phase along the V-bar axis; (ii) chaser-target relative distance at the end of the radial boost phase, again along the V-bar axis, coinciding with the starting point of the final approach phase; (iii) ending point of the final approach maneuver along the V-bar axis; and (iv) terminal V-bar velocities at the end of each rendezvous phase. Then, the reference orbit parameters, inherited from the mission analysis, are uploaded first in terms of orbit inclination i, right ascension of the ascending node Ω and argument of periapsis ω in order to define the L_{E2P} rotation matrix and later as semi-major axis a and eccentricity e for the purpose of initializing the initial location of the target vehicle on the reference orbit. Thus, assuming that the target is initially located at the orbit periastrum, i.e. target initial true anomaly $\nu_T = 0$, and that

$$\mathbf{r}_{CV_{PQW}} = \mathbf{r}_{TV_{PQW}} - L_{P2L}\mathbf{R} \tag{4.1}$$

where $\mathbf{r}_{CV_{PQW}}$ and $\mathbf{r}_{TV_{PQW}}$ are the initial position vectors of chaser and target vehicles in the perifocal frame, respectively, $\mathbf{R}$ is the initial relative distance among the two spacecraft and L_{P2L} is the rotation matrix from perifocal to LVLH, it is possible to estimate the true anomaly of the chaser vehicle ν_C at the beginning of the closing phase solving a simple second-order polynomial equation of the form $\alpha x^2 + \beta x + \gamma = 0$ where $x = \cos\nu_C$ and

- $\alpha = (\|\mathbf{R}\|^2 - \|\mathbf{r}_{TV_{PQW}}\|^2)e^2 + 2\|\mathbf{r}_{TV_{PQW}}\|ae(1-e^2)$;
- $\beta = 2(\|\mathbf{R}\|^2 - \|\mathbf{r}_{TV_{PQW}}\|^2)e + 2\|\mathbf{r}_{TV_{PQW}}\|a(1-e^2)$;
- $\gamma = \|\mathbf{R}\|^2 - \|\mathbf{r}_{TV_{PQW}}\|^2 - a^2(1-e^2)^2$.

from which it is possible to obtain also the initial position of the chaser vehicle in the perifocal frame as

$$\mathbf{r}_{CV_{PQW}} = \frac{a(1-e^2)}{1+e\cos\nu_C}\begin{bmatrix}\cos\nu_C\\ \sin\nu_C\\ 0\end{bmatrix}. \tag{4.2}$$

To complete the chaser and target dynamics initialization, their velocity in the perifocal frame has to be defined, first evaluating the orbital angular momentum as

$$\mathbf{h}_{orb} = \sqrt{\mu_{pl}a(1-e^2)}, \tag{4.3}$$

and then obtaining the radial v_r and tangential v_θ components of the velocity vector as

$$v_r = \frac{\mu_{pl}}{\|\mathbf{h}_{orb}\|}e\sin\nu \tag{4.4a}$$

$$v_\theta = \frac{\mu_{pl}}{\|\mathbf{h}_{orb}\|}(1+e\cos\nu). \tag{4.4b}$$

The last step consists in setting the MPC parameters for both attitude and orbital control. It is important to remark that, as anticipated before, the same weight matrices, prediction horizon and sample time shall be used for both GTO and NRHO ARVD maneuvers and for all the MPC strategies envisioned.

4.2.3 STAR Simulation Environment

Figure 4.9 provides an overview of the high-level architecture of the STAR simulator, including all the main elements included in the Simulink model to obtain a realistic, reliable as well as flexible simulation environment where validate different GNC strategies for controlling a spacecraft, i.e. the LST in this specific context, during ARVD maneuvers. Analogously to MISS, the STAR simulator can be split in four areas:

- **environmental disturbance** (green blocks): includes five different sources of either orbital and attitude perturbations affecting the chaser spacecraft dynamics during the maneuver, among which: (i) aerodynamic drag; (ii) planetary magnetic field; (iii) SRP; (iv) gravity gradient; and (v) third-body.
- **chaser rotational dynamics and kinematics** (light blue blocks): reproduces the chaser attitude dynamics and kinematics whereas the control strategy is included in the chaser attitude control block.
- **chaser orbital dynamics** (red blocks): simulates the chaser orbital dynamics in the LVLH frame while the control action is provided by the orbital control block.
- **target and chaser propagators** (orange blocks): propagate the orbital dynamics of both chaser and target vehicle in highly-elliptic orbits, such GTO and NRHO, with respect to perifocal frame first and then ECI frame.

A thorough description of each mathematical model implemented in either the STAR initialization and Simulink environment is provided in the following Sections.

Attitude Dynamics

The classical formulation of the spacecraft attitude dynamics is obtained starting from the definition of the rigid-body angular momentum in a non-rotating frame, i.e. H_I, as described in [65]. This leads to the Euler's equation $\dot{H}_I = M_I$, where $\dot{H}_I$ is the spacecraft time-derivative of the angular momentum and M_I is the external torque acting on the spacecraft itself. This proves that, if no torque acts on the body, the angular momentum is constant. First, let define the tensor of inertia of the LST J_SC about its center-of-mass, considering that the spacecraft is composed by three elements:

- a cylinder representing the main body which center-of-mass is located at $h_{cyl}/2$ and $d_{cyl}/2$, i.e. $(0,0,0)_B$, with a mass defined as $m_{cyl} = m_{LST} - m_{SA}$

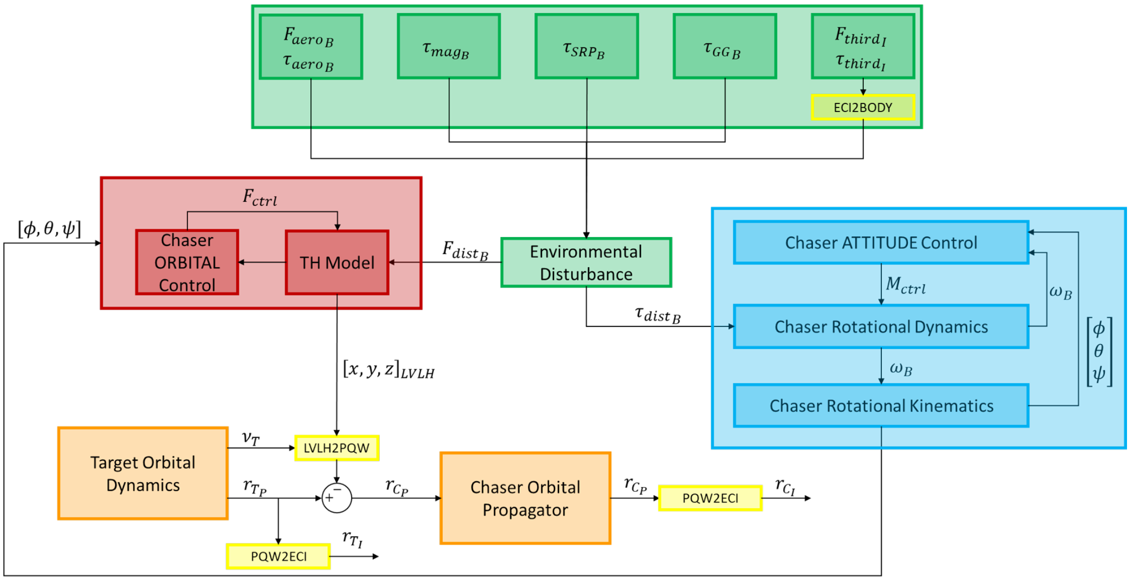

Figure 4.9: STAR simulation environment high-level architecture.

and moments of inertia defined by

$$\begin{aligned} J_{x_{cyl}} &= \frac{1}{2} m_{cyl} \left(\frac{d_{cyl}}{2}\right)^2, \\ J_{y_{cyl}} &= \frac{1}{4} m_{cyl} \left(\frac{d_{cyl}}{2}\right)^2 + \frac{1}{12} m_{cyl} \left(h_{cyl}\right)^2, \\ J_{z_{cyl}} &= \frac{1}{4} m_{cyl} \left(\frac{d_{cyl}}{2}\right)^2 + \frac{1}{12} m_{cyl} \left(h_{cyl}\right)^2. \end{aligned}$$

- two polyhedrons with octagonal basis for the solar arrays with the center-of-mass centered in the polygonal basis whereas the moments of inertia are obtained preliminarily considering a parallelepiped with same area, i.e. $A_{SA} = l_{y_{SA}} \cdot l_{z_{SA}}$ and width, i.e. $l_{x_{SA}}$ as

$$\begin{aligned} J_{x_{SA}} &= \frac{1}{24} m_{cyl} \left(l_{z_{SA}}^2 + l_{y_{SA}}^2\right)^2, \\ J_{y_{SA}} &= \frac{1}{24} m_{cyl} \left(l_{x_{SA}}^2 + l_{z_{SA}}^2\right)^2, \\ J_{z_{SA}} &= \frac{1}{24} m_{cyl} \left(l_{y_{SA}}^2 + l_{x_{SA}}^2\right)^2. \end{aligned}$$

Then, obtained the overall center-of-gravity of the LST as

$$\begin{aligned}
x_{G_{LST}} &= \frac{x_{G_{cyl}} \cdot V_{cyl} + x_{G_{SA_{sx}}} \cdot V_{SA_{sx}} + x_{G_{SA_{dx}}} \cdot V_{SA_{dx}}}{V_{LST}} \\
y_{G_{LST}} &= \frac{y_{G_{cyl}} \cdot V_{cyl} + y_{G_{SA_{sx}}} \cdot V_{SA_{sx}} + y_{G_{SA_{dx}}} \cdot V_{SA_{dx}}}{V_{LST}} \\
z_{G_{LST}} &= \frac{z_{G_{cyl}} \cdot V_{cyl} + z_{G_{SA_{sx}}} \cdot V_{SA_{sx}} + z_{G_{SA_{dx}}} \cdot V_{SA_{dx}}}{V_{LST}}
\end{aligned}$$

the diagonal of the LST tensor of inertia J_{SC} is given by

$$\begin{aligned}
J_x = {} & (J_{x_{cyl}} + m_{cyl}(x_{G_{cyl}} - x_{G_{LST}})^2) + (J_{x_{SA_{sx}}} + \frac{m_{SA}}{2}(x_{G_{SA_{sx}}} - x_{G_{LST}})^2) \\
& + (J_{x_{SA_{dx}}} + \frac{m_{SA}}{2}(x_{G_{SA_{dx}}} - x_{G_{LST}})^2) \\
J_y = {} & (J_{y_{cyl}} + m_{cyl}(y_{G_{cyl}} - y_{G_{LST}})^2) + (J_{y_{SA_{sx}}} + \frac{m_{SA}}{2}(y_{G_{SA_{sx}}} - y_{G_{LST}})^2) + (J_{y_{SA_{dx}}} \\
& + \frac{m_{SA}}{2}(y_{G_{SA_{dx}}} - y_{G_{LST}})^2) \\
J_z = {} & (J_{z_{cyl}} + m_{cyl}(z_{G_{cyl}} - z_{G_{LST}})^2) + (J_{z_{SA_{sx}}} + \frac{m_{SA}}{2}(z_{G_{SA_{sx}}} - z_{G_{LST}})^2) \\
& + (J_{z_{SA_{dx}}} + \frac{m_{SA}}{2}(z_{G_{SA_{dx}}} - z_{G_{LST}})^2).
\end{aligned}$$

Given A_{E2B} the rotational matrix from ECI to body-fixed reference frame, the angular momentum in the body frame can be reformulated as

$$H_B = A_{E2B} H_I = A_{E2B}(J_{SC}\omega_I) = J_{SC}\omega_B, \tag{4.9}$$

where $\omega_I = (\omega_{x_I}, \omega_{y_I}, \omega_{z_I})$ and $\omega_B = (\omega_{x_B}, \omega_{y_B}, \omega_{z_B})$ are the spacecraft angular velocity in ECI and body reference frame, respectively. Deriving Eq. (4.9) in time, the Euler's rotational equation is obtained

$$\dot{\omega}_B = J_{SC}^{-1}[M_B - \omega_B \times (J_{SC}\omega_B)], \tag{4.10}$$

in which M_B is the total external torque acting on the rigid-body expressed in the body frame. When the spacecraft is equipped with reaction wheels, like in this work, the rotational dynamics equation shall include also the wheels dynamics and Eq. (4.10) becomes

$$\dot{\omega}_B = J_{SC}^{-1}[M_B - M_{RW_B} - \omega_B \times (J_{SC}\omega_B + H_{RW})], \tag{4.11}$$

with M_{RW_B} the reaction wheel torque in the body frame, i.e., the control action applied, and $H_{RW} = J_{RW}\omega_{RW}$ is the wheel angular momentum applied to the spacecraft, where J_{RW} is the reaction wheels tensor of inertia and ω_{RW} is their angular velocity with respect to the relative spin axes.

On the other hand, the quaternion kinematics equation, exploited to define the spacecraft orientation in terms of quaternion $q = (q_1, q_2, q_3, q_S)$ with respect to the inertial frame, can be expressed in two different forms, as highlighted in [84]

$$\dot{q} = \frac{1}{2}\Sigma(q)\omega_B \quad \text{or} \quad \dot{q} = \frac{1}{2}\Sigma(\omega_B)q, \tag{4.12}$$

where $\Sigma(q)$ and $\Sigma(\omega_B)$ are given by

$$\Sigma(q) = \begin{bmatrix} q_S & -q_3 & q_2 \\ q_3 & q_S & -q_1 \\ -q_2 & q_1 & q_S \\ -q_1 & -q_2 & -q_3 \end{bmatrix}, \quad \Sigma(\omega_B) = \begin{bmatrix} 0 & \omega_{z_B} & -\omega_{y_B} & \omega_{x_B} \\ -\omega_{z_B} & 0 & \omega_{x_B} & \omega_{y_B} \\ \omega_{y_B} & -\omega_{x_B} & 0 & \omega_{z_B} \\ -\omega_{x_B} & -\omega_{y_B} & \omega_{z_B} & 0 \end{bmatrix}. \tag{4.13}$$

Integrating Eq. (4.13), the spacecraft attitude in terms of quaternion is obtained and then it can be expressed also in terms of Euler angles, for a more intuitive interpretation, as follows

$$\phi = \text{atan}\left(\frac{2(q_S q_1 + q_2 q_3)}{1 - 2(q_1^2 + q_2^2)}\right) \tag{4.14a}$$

$$\theta = \text{asin}\Big(2(q_S q_2 - q_1 q_3)\Big) \tag{4.14b}$$

$$\psi = \text{atan}\left(\frac{2(q_1 q_2 + q_3 q_S)}{1 - 2(q_2^2 + q_3^2)}\right) \tag{4.14c}$$

with ϕ, θ ψ the roll, pitch and yaw angles, respectively, giving the orientation of the spacecraft.

Orbital Dynamics

The chaser and target vehicle orbital dynamics in an inertial frame can be described as the relative motion of these spacecraft with respect to the main body around which they are orbiting, as thoroughly described in [85], by the two-body equation of motion

$$\ddot{r}_I = -\frac{\mu_{pl}}{\|r_I\|^3} r_I + a_d, \tag{4.15}$$

where $a_d = (a_{d_x}, a_{d_y}, a_{d_z})$ is the sum of external disturbance and control action acting on the spacecraft, r_I is the distance of the spacecraft from the planet corresponding center-of-mass expressed in the inertial frame, either ECI or MCI, and μ_{pl} is the planetary gravitational parameter, i.e., $\mu_\oplus = 398600\ km^3/s^2$ for the Earth and $\mu_M = 4904\ km^3/s^2$ for the Moon. If disturbance term is neglected, integrating Eq. (4.15) the trajectory equation is derived and it corresponds to a conic of the form

$$\|r\| = \frac{a(1 - e^2)}{1 + e\cos\nu}. \tag{4.16}$$

If the orbit eccentricity e is between 0 and 1, the conic is an ellipse with semi-major axis a. ν represents the true anomaly, defining the position of the spacecraft on the reference elliptic orbit with respect to the perifocal reference frame.

The rendezvous problem is typically analyzed and solved considering the relative orbital dynamics of the chaser vehicle with respect to the target one, expressed in the target LVLH frame. In most cases, the assumption of (near) circular Keplerian orbit allows to exploit the well-known CW model, proposed in 1960 as simplified strategy to describe the relative motion of the chaser vehicle during a rendezvous maneuver [86]. The equations of motion have been derived starting form the starting from the nonlinear equations for the restricted three-body problem previously introduced in (4.15). Considering both spacecraft on a circular orbit around a master body (reference planet) and with a mass infinitesimal with respect to the mass of the main body, the chaser vehicle dynamics can be rewritten as

$$\frac{d^2\mathrm{\rho}}{dt^2} + 2\omega \times \frac{d\mathrm{\rho}}{dt} + \omega \times [\omega \times (\mathrm{\rho} + \mathrm{r}_1)] = -\frac{\omega^2 r_1^3}{r^3}\mathrm{r}, \tag{4.17}$$

where ω is the orbital angular rate, $\mathrm{\rho} = \rho \mathrm{i}_\rho$ and $\mathrm{r}_1 = r_1\, \mathrm{i}_\xi$ are the position vectors of the chaser and the target spacecraft from the main body, respectively, and $\mathrm{r} = r\, \mathrm{i}_\xi = \mathrm{\rho} + \mathrm{r}_1$ is the vectorial sum of the two distances. First using a Taylor series expansion and later neglecting several high-order dynamics terms, e.g. $\mathrm{O}(\rho^2)$, $\mathrm{O}(\rho^2/r_1^2)$ and $\mathrm{O}(\rho^2)$, the CW's equations can be obtained as

$$\begin{aligned}
\frac{d^2x}{dt^2} &= 2\omega\frac{dz}{dt} + \frac{F_x}{m_{CV}},\\
\frac{d^2y}{dt^2} &= -\omega^2 y + \frac{F_y}{m_{CV}},\\
\frac{d^2z}{dt^2} &= -2\omega\frac{dx}{dt} + 3\omega^2 z + \frac{F_z}{m_{CV}}.
\end{aligned} \tag{4.18}$$

where m_{CV} is the chaser vehicle mass and (F_x, F_y, F_z) are the correction actions including either external disturbance forces and thrust contributions.

On the other hand, in this work dealing with highly elliptical orbits, the linear time-invariant CW model cannot be adopted in this work. On the other hand, the Tschauner–Hempel (TH) model [87], first developed in 1965, provides a linear time-varying description of the relative position and velocity of the chaser spacecraft if the target is orbiting in an elliptical orbit. Moreover, in [88], the TH model has been extended to orbits with eccentricity $0 \leq e < 1$, removing the singularities related to zero-eccentricity, i.e. circular orbits. The TH model is receiving considerable interest in the last years, and several researches have been proposed in literature. A geometric interpretation of the TH solution is proposed in [89] whereas an approximate solution that explicitly includes time and is valid also for non-coplanar orbit is provided in [90]. In all these approaches, the target true anomaly, i.e. ν_T, becomes an independent variable. The nonlinear equations obtained from the definition of the relative chaser-target dynamics in the inertial frame first, and then in the target LVLH, can be linearized with respect to the local frame origin, i.e. corresponding to the target center-of-mass, such that the

$$\ddot{x} = (\omega_T^2 - n^2)x + 2\omega_T \dot{z} - \dot{\omega}_T z + a_{d_x} \tag{4.19a}$$

$$\ddot{y} = -n^2 y + a_{d_y} \tag{4.19b}$$

$$\ddot{z} = (\omega_T^2 + 2n^2)z - 2\omega_T \dot{x} + \dot{\omega}_T x + a_{d_z}, \tag{4.19c}$$

where $r_{C_L} = (x, y, z)$ is the chaser position relative to the target LVLH frame, ω_T and $\dot{\omega}_T$ are the time-derivative and second-order time-derivative of the target true anomaly ν_T, respectively, and n is the orbital angular velocity. In particular,

$$\omega_T = \dot{\nu}_T = \frac{\sqrt{\mu_{pl} a(1-e^2)}}{r_T^2}, \quad \dot{\omega}_T = -\frac{2\mu_{pl} e \sin\nu_T}{r_T^3}, \quad n = \sqrt{\frac{\mu_{pl}}{r_T^3}} \tag{4.20}$$

where $r_T = \frac{a(1-e^2)}{1+e\cos\nu_T}$ (see [91] and [92] for further details). Integrating this system of equation, the relative position and velocity of the chaser vehicle in the target LVLH frame are obtained. Then, the spacecraft relative dynamics can be represented in a linear-time variant state-space formulation, i.e., $\dot{x} = A_{orb}(t)x + B_{orb}(t)u$, where the state and input matrices, $A(t)$ and $B(t)$ respectively, can be rewritten as

$$A_{orb}(t) = \begin{bmatrix} 0 & 0 & 0 & 1 & 0 & 0 \\ 0 & 0 & 0 & 0 & 1 & 0 \\ 0 & 0 & 0 & 0 & 0 & 1 \\ n^2 e\cos\nu_T & 0 & \dot{\omega}_T & 0 & 0 & 2\omega_T \\ 0 & -n^2 & 0 & 0 & 0 & 0 \\ -\dot{\omega}_T & 0 & n^2(3+e\cos\nu_T) & -2\omega_T & 0 & 0 \end{bmatrix}, \tag{4.21a}$$

$$B_{orb}(t) = \begin{bmatrix} 0 & 0 & 0 \\ 0 & 0 & 0 \\ 0 & 0 & 0 \\ \frac{1}{m_{LST}} & 0 & 0 \\ 0 & \frac{1}{m_{LST}} & 0 \\ 0 & 0 & \frac{1}{m_{LST}}. \end{bmatrix} \tag{4.21b}$$

Last, the chaser vehicle position is propagated first in the perifocal frame, i.e., r_{C_P}

$$r_{C_P} = r_T \begin{bmatrix} \cos\nu_T \\ \sin\nu_T \\ 0 \end{bmatrix} - \begin{bmatrix} 1 & 0 & 0 \\ 0 & 0 & -1 \\ 0 & 1 & 0 \end{bmatrix} \begin{bmatrix} 0 & -1 & 0 \\ 1 & 0 & 0 \\ 0 & 0 & 1 \end{bmatrix} \begin{bmatrix} \cos\nu_T & \sin\nu_T & 0 \\ -\sin\nu_T & \cos\nu_T & 0 \\ 0 & 0 & 1 \end{bmatrix} \begin{bmatrix} x \\ y \\ z \end{bmatrix} \tag{4.22}$$

and then in the inertial frame, i.e., $r_{C_I} = L_{E2P}^T r_{C_P}$.

The linearized time-varying TH's equations have been exploited in this work for both closing and final approach phases. The difference among these phases is given by the term a_d, in which both disturbances and control force are included. Further details are provided in Section 4.2.7.

4.2.4 Model Parametric Uncertainty

Describing an observable phenomenon in terms of some underlying structure identifies the discipline of system dynamic model development, which is not a simple task in most cases. Such models are rarely a perfect representation of the observables. Typically, high-frequency dynamics are unmodeled, exploiting reduced-order models deliberately thus introducing the first sources of discrepancies among the real system and the modeled one. Moreover, when a nonlinearities are neglected, for instance via linearization process, further modeling errors are included. Additional source of discrepancy could be related to system-parameter variations due to either environmental changes, manufacturing process and measurement inaccuracy. Hence, uncertainties are unavoidable in a representing the actual dynamics of the system in operation through a mathematical model.

On the other hand, these modeling errors may adversely affect the stability and performance of control systems. To ensure the expected level of reliability of the controller, it is important to include these parametric uncertainties in the system modeling as well as into the controller design, following a three-step procedure: (i) identify the possible source of uncertainty which may affect the system model under analysis; (ii) provide a preliminary estimation and eventually a statistical description of these modeling errors; and (iii) design the control law such that, in the presence of these modeling errors affecting the system dynamics, stability and expected performance can still be guaranteed.

In this Section, the main sources of parametric uncertainty affecting the LST attitude and orbital dynamics are first identified and then preliminarily evaluated whereas possible solutions to include them in the controller design are provided in Chapter 5.

Attitude Dynamics Parametric Uncertainty

The spacecraft attitude dynamics is typically described by the nonlinear equation in (4.10). On the other hand, the corresponding linear model, i.e. linearized with respect to steady-state conditions of reference frames alignment and zero-angular velocity, can be represented in a classical continuous time state-space formulation $\dot{x} = A_{att}x + B_{att}u$ where the state x includes Euler angles and angular velocity whereas the state and input matrices, A_{att} and B_{att} respectively, have the following form

$$A_{att} = \begin{bmatrix} 0 & 0 & \omega_0 & 1 & 0 & 0 \\ 0 & 0 & 0 & 0 & 1 & 0 \\ -\omega_0 & 0 & 0 & 0 & 0 & 1 \\ 0 & 0 & 0 & 0 & 0 & \frac{J_z-J_y}{J_x}\omega_0 \\ 0 & 0 & 0 & 0 & 0 & 0 \\ 0 & 0 & 0 & \frac{J_y-J_x}{J_z}\omega_0 & 0 & 0 \end{bmatrix}, \quad B_{att} = \begin{bmatrix} 0 & 0 & 0 \\ 0 & 0 & 0 \\ 0 & 0 & 0 \\ \frac{1}{J_x} & 0 & 0 \\ 0 & \frac{1}{J_y} & 0 \\ 0 & 0 & \frac{1}{J_z} \end{bmatrix}. \tag{4.23}$$

Since the LST is operating on highly elliptic orbits, the value of the orbital angular velocity ω_0 is subject to slight changes over the orbit itself. In particular, considering as nominal values the average value over the reference orbit, the corresponding uncertainty introduced varies from $q_\omega^- = -2 \cdot 10^{-3}$ to $q_\omega^+ = 4 \cdot 10^{-5}$. Moreover, due to slight changes in the center-of-mass as a consequence of fuel consumption, the moment of inertia could be affected by errors and for the LST spacecraft a ±1% variation has been considered, i.e. $q_J = [-0.01,0.01]$. Thus, introducing those uncertainties in the system matrices, the corresponding uncertain one assume the following form

$$A_{att}(q) = \begin{bmatrix} 0 & 0 & (\omega_0 + q_\omega) & 1 & 0 & 0 \\ 0 & 0 & 0 & 0 & 1 & 0 \\ -(\omega_0 + q_\omega) & 0 & 0 & 0 & 0 & 1 \\ 0 & 0 & 0 & 0 & 0 & \frac{J_z-J_y}{(1+q_J)J_x}(\omega_0 + q_\omega) \\ 0 & 0 & 0 & 0 & 0 & 0 \\ 0 & 0 & 0 & \frac{J_y-J_x}{J_z(1+q_J)}(\omega_0 + q_\omega) & 0 & 0 \end{bmatrix},$$

$$B_{att}(q) = \begin{bmatrix} 0 & 0 & 0 \\ 0 & 0 & 0 \\ 0 & 0 & 0 \\ \frac{1}{(1+q_J)J_x} & 0 & 0 \\ 0 & \frac{1}{(1+q_J)J_y} & 0 \\ 0 & 0 & \frac{1}{(1+q_J)J_z} \end{bmatrix}.$$

Furthermore, let consider the term

$$\begin{aligned} & \frac{J_z - J_y}{(1+q_J)J_x}(\omega_0 + q_\omega) \\ &= \frac{1}{1+q_J}\frac{J_z - J_y}{J_x}(\omega_0 + q_\omega) \\ &= \frac{1}{1+q_J}\frac{J_z - J_y}{J_x}\omega_0 + \frac{q_\omega}{1+q_J}\frac{J_z - J_y}{J_x} \end{aligned}$$

and it results that a third uncertainty $q_{\omega/J} = \frac{q_\omega}{1+q_J}$ can be identified. Moreover, $q_J = [q_J^-, q_J^+] = [-0.01, 0.01]$ corresponds to

$$q_{\hat{J}} = [\frac{1}{1+q_J^+}, \frac{1}{1+q_J^-}] \approx [1+q_J^-, 1+q_J^+],$$

thus obtaining

$$A_{att}(q) = \begin{bmatrix} 0 & 0 & (\omega_0 + q_\omega) & 1 & 0 & 0 \\ 0 & 0 & 0 & 0 & 1 & 0 \\ -(\omega_0 + q_\omega) & 0 & 0 & 0 & 0 & 1 \\ 0 & 0 & 0 & 0 & 0 & \Big((1+q_J)\omega_0 + q_{\omega/J}\Big)\frac{J_z - J_y}{J_x} \\ 0 & 0 & 0 & 0 & 0 & 0 \\ 0 & 0 & 0 & \Big((1+q_J)\omega_0 + q_{\omega/J}\Big)\frac{J_y - J_x}{J_z} & 0 & 0 \end{bmatrix},$$

$$B_{att}(q) = \begin{bmatrix} 0 & 0 & 0 \\ 0 & 0 & 0 \\ 0 & 0 & 0 \\ \frac{(1+q_J)}{J_x} & 0 & 0 \\ 0 & \frac{(1+q_J)}{J_y} & 0 \\ 0 & 0 & \frac{(1+q_J)}{J_z} \end{bmatrix}.$$

Hence, the LST linearized, uncertain attitude dynamics can be represented by the following state matrices

$$A_{att}(q) = A_{0_{att}} + A_{1_{att}} q_\omega + A_{2_{att}} q_J + A_{3_{att}} q_{\omega/J},$$
$$B_{att}(q) = B_{0_{att}} + B_{1_{att}} q_\omega + B_{2_{att}} q_J + B_{3_{att}} q_{\omega/J},$$

where

$$A_{0_{att}} = \begin{bmatrix} 0 & 0 & \omega_0 & 1 & 0 & 0 \\ 0 & 0 & 0 & 0 & 1 & 0 \\ -\omega_0 & 0 & 0 & 0 & 0 & 1 \\ 0 & 0 & 0 & 0 & 0 & \frac{J_z - J_y}{J_x}\omega_0 \\ 0 & 0 & 0 & 0 & 0 & 0 \\ 0 & 0 & 0 & \frac{J_y - J_x}{J_z}\omega_0 & 0 & 0 \end{bmatrix}, \quad A_{1_{att}} = \begin{bmatrix} 0 & 0 & 1 & 0 & 0 & 0 \\ 0 & 0 & 0 & 0 & 0 & 0 \\ -1 & 0 & 0 & 0 & 0 & 0 \\ 0 & 0 & 0 & 0 & 0 & 0 \\ 0 & 0 & 0 & 0 & 0 & 0 \\ 0 & 0 & 0 & 0 & 0 & 0 \end{bmatrix},$$

$$A_{2_{att}} = \begin{bmatrix} 0 & 0 & 0 & 0 & 0 & 0 \\ 0 & 0 & 0 & 0 & 0 & 0 \\ 0 & 0 & 0 & 0 & 0 & 0 \\ 0 & 0 & 0 & 0 & 0 & \frac{J_z - J_y}{J_x}\omega_0 \\ 0 & 0 & 0 & 0 & 0 & 0 \\ 0 & 0 & 0 & \frac{J_y - J_x}{J_z}\omega_0 & 0 & 0 \end{bmatrix}, \quad A_{3_{att}} = \begin{bmatrix} 0 & 0 & 0 & 0 & 0 & 0 \\ 0 & 0 & 0 & 0 & 0 & 0 \\ 0 & 0 & 0 & 0 & 0 & 0 \\ 0 & 0 & 0 & 0 & 0 & \frac{J_z - J_y}{J_x} \\ 0 & 0 & 0 & 0 & 0 & 0 \\ 0 & 0 & 0 & \frac{J_y - J_x}{J_z} & 0 & 0 \end{bmatrix},$$

whereas $B_{0_{att}} = B_{2_{att}} = B_{att}$ in (4.23) and $B_{1_{att}} = B_{3_{att}} = zeros(6,3)$.

Orbital Dynamics Parametric Uncertainty

As described in Section 4.2.3, the chaser vehicle relative dynamics can be described exploiting either the CW model, when circular orbits are considered or the reference orbit can be approximated as circular, or the TH model for highly-elliptic orbits such those involved in the LST ARVD maneuvers. Recalling the time-varying state-space formulation of the TH's equation (4.21), the terms ω_0, $\dot{\omega_0}$ and n are all source of uncertainties in the sense that they do not remain constant along the orbit. Moreover, the LST wet mass slightly changes during the maneuver due to propellant consumption and it also affected by discrepancies with respect to the budget coming from the design analysis due to measurement and modeling inaccuracy. Thus, a mass variation of ±5% over the nominal one has been envisioned. As a consequence, the following uncertainties have been included in the LST uncertain orbital dynamics:

- Analogously to the attitude dynamics, the uncertainty over the term ω_T, representing the time-derivative of the true anomaly, has been set as $q_\omega = [-2 \cdot 10^{-3}, 4 \cdot 10^{-5}]$.

- for the double derivative of the true anomaly $\dot{\omega_T}$, let start from its definition given in (4.20). If $\nu_T = 0°$, then $\dot{\omega_T} = 0$ whereas if $\nu_T = 90°$, the numerator is maximized. Moreover, $\dot{\omega_T}$ varies with $1/r_T^3$, which ranges from the periastrum radius up to the apoastrum radius and it is different in GTO and NRHO. Thus, the $q_{\dot{\omega}} = [q_{\dot{\omega}}^-, q_{\dot{\omega}}^+]$ uncertainty affects the orbital dynamics with different contributions according to the orbit considered.

- An additional source of modeling error is related to the term n, representing the orbital angular velocity in the sense of circular orbits, which is present in the dynamics at the power of two and it results a function of $1/r_T^{\frac{3}{2}}$, which depends on the target orbit. Moreover, it appears in (4.21) that the two terms involving the parameter n^2 multiply $e \cos \nu_T$, which again can vary from 0 (when $\nu_T = 90°$) to e (for $\nu_T = 0°$). Thus, the uncertainty considered in the model has been defined with respect to the term $n^2 e$ obtaining $q_{n/e_\oplus} = [3.88 \cdot 10^{-9}, 1.05 \cdot 10^{-6}]$ for the GTO orbit and $q_{n/e_{Moon}} = [1.56 \cdot 10^{-11}, 1.31 \cdot 10^{-7}]$ in NRHO.

- The last uncertainty involves the LST mass, which in analogy to te moment of the inertia can be first defined as $q_m = [q_m^-, q_m^+] = [-0.05, 0.05]$ and then redefined as
$$\frac{1}{(1+q_m)m_{LST}} = \frac{1+q_{\hat{m}}}{m_{LST}},$$
where $q_{\hat{m}} = [q_{\hat{m}}^-, q_{\hat{m}}^+] = [-0.0476, 0.0526]$.

Hence, the uncertain orbital dynamics state and input matrices, $A_{orb}(q)$ and $B_{orb}(q)$ can be defined as follows

$$A_{orb}(t) = \begin{bmatrix} 0 & 0 & 0 & 1 & 0 & 0 \\ 0 & 0 & 0 & 0 & 1 & 0 \\ 0 & 0 & 0 & 0 & 0 & 1 \\ q_{n/e}n^2 & 0 & q_{\dot{\omega}}\dot{\omega}_T & 0 & 0 & 2(\omega_T + q_\omega) \\ 0 & -n^2 & 0 & 0 & 0 & 0 \\ -q_{\dot{\omega}}\dot{\omega}_T & 0 & 3n^2 + q_{n/e} & -2(\omega_T + q_\omega) & 0 & 0 \end{bmatrix},$$

$$B_{orb}(t) = \begin{bmatrix} 0 & 0 & 0 \\ 0 & 0 & 0 \\ 0 & 0 & 0 \\ \frac{(1+q_m)}{m_{LST}} & 0 & 0 \\ 0 & \frac{(1+q_m)}{m_{LST}} & 0 \\ 0 & 0 & \frac{(1+q_m)}{m_{LST}}. \end{bmatrix}$$

from which it is possible to define

$$A_{0orb} = \begin{bmatrix} 0 & 0 & 0 & 1 & 0 & 0 \\ 0 & 0 & 0 & 0 & 1 & 0 \\ 0 & 0 & 0 & 0 & 0 & 1 \\ 0 & 0 & 0 & 0 & 0 & 2\omega_T \\ 0 & -n^2 & 0 & 0 & 0 & 0 \\ 0 & 0 & 3n^2 & -2\omega_T & 0 & 0 \end{bmatrix}, \quad A_{1_{orb}} = \begin{bmatrix} 0 & 0 & 0 & 0 & 0 & 0 \\ 0 & 0 & 0 & 0 & 0 & 0 \\ 0 & 0 & 0 & 0 & 0 & 0 \\ 0 & 0 & 0 & 0 & 0 & 2 \\ 0 & 0 & 0 & 0 & 0 & 0 \\ 0 & 0 & 0 & -2 & 0 & 0 \end{bmatrix},$$

$$A_{2_{orb}} = \begin{bmatrix} 0 & 0 & 0 & 0 & 0 & 0 \\ 0 & 0 & 0 & 0 & 0 & 0 \\ 0 & 0 & 0 & 0 & 0 & 0 \\ 0 & 0 & 1 & 0 & 0 & 0 \\ 0 & 0 & 0 & 0 & 0 & 0 \\ -1 & 0 & 0 & 0 & 0 & 0 \end{bmatrix}, \quad A_{3_{orb}} = \begin{bmatrix} 0 & 0 & 0 & 0 & 0 & 0 \\ 0 & 0 & 0 & 0 & 0 & 0 \\ 0 & 0 & 0 & 0 & 0 & 0 \\ 1 & 0 & 0 & 0 & 0 & 0 \\ 0 & 0 & 0 & 0 & 0 & 0 \\ 0 & 0 & 1 & 0 & 0 & 0 \end{bmatrix},$$

whereas $A_{4_{orb}} = zeros(6)$, $B_{0_{orb}} = B_{4_{orb}} = B_{orb}(t)$ and $B_{1_{orb}} = B_{2_{orb}} = B_{3_{orb}} = zeros(6,3)$.

4.2.5 Internal and External Additive Disturbances

The space environment is the primary source of disturbances acting on the spacecraft, which can jeopardize its dynamics. Additionally, internal sources, such as uneven mass distribution as well as actuators activation errors, can potentially affect the spacecraft mission (see [65] for further details). Dealing with safety-critical maneuvers such as ARVD requires a particular attention regards the attitude and trajectory deviations with respect to the planned one, mainly when manned systems are involved. In this Section, the internal and external disturbance sources taken into account in this work are here briefly introduced and their relative analytical models are presented, to provide a thorough overview of the scenario setup considered for the simulations.

External Disturbances

For the GTO environment, four different sources of external disturbances have been included, which have been modeled according to the guidelines provided in [65] and [93]: (i) aerodynamic drag; (ii) Earth gravity field; (iii) solar radiation pressure; (iv) spacecraft residual magnetic dipole. Instead, in lunar proximity, only the Moon gravity field and the solar pressure have been considered since their is no (real) lunar atmosphere (hence no drag) and the lunar magnetic field is quite small and generates negligible disturbance torque when combined with the LST residual dipole. Moreover, the effects on the LST orbit of third bodies, i.e. Sun and Earth, have been considered since they cannot be neglected for the NRHO orbit.

- Aerodynamic drag represents a significant source of perturbing force and torque, mainly for objects orbiting in LEO. Even if the LST orbit in Earth proximity is not a LEO but a GTO, the perturbation due to the drag is still considerable, especially at the orbit perigee. Moreover, the LST large solar arrays notable increase the spacecraft exposed area.

  To evaluate the disturbance contribution due to the Earth atmosphere, the LST has been modeled as a collection of N (quasi-)flat plates of known area A_i, characterized by a well defined center of pressure, at a non-null distance $\mathbf{r}_{i_B}$ from the LST center-of-mass, and a normal unit vector $\mathbf{n}_{i_B}$, defined in the body-fixed reference frame. Given the spacecraft relative velocity in the body frame $\mathbf{v}_{rel_B}$, obtained rotating the corresponding $\mathbf{v}_{rel_I}$ in ECI through the attitude matrix, and defining the inclination of the i-th plate θ_{aero_i} with respect to $\mathbf{v}_{rel_B}$ direction as

  $$\theta_{aero_i} = \text{acos}\left(\frac{\mathbf{n_{i_B}} \cdot \mathbf{v}_{rel_B}}{\|\mathbf{v}_{rel_B}\|_2}\right), \tag{4.30}$$

  the aerodynamic force acting on the i-th spacecraft plate is given by

  $$F_{aero_{i_B}} = -\frac{1}{2}\rho C_D \|v_{rel_B}\|_2^2 A_i \max(\cos\theta_{aero_i}, 0), \tag{4.31}$$

  where ρ is the atmospheric density, evaluated following the Harris-Priester model atmosphere [94], and C_D is the drag coefficient, typically set to 2.2 [66].

Last, the disturbance torque due to the atmospheric drag τ_{aero_B}, resulting from the non-coincidence of center-of-mass and centers of pressure, is obtained as

$$\tau_{aero_B} = \sum_{i=1}^{N} (\mathbf{r}_{i_B} \times F_{aero_{i_B}}). \tag{4.32}$$

- The magnetic torque is generated by the interaction of the spacecraft residual magnetic dipole m_{SC_B}, due to electric currents and magnetic material within itself, and the planetary magnetic field B_{pl}. In this work, only the Earth magnetic field $B_{\oplus_B}$, which is in the range of 20-50 μT, has been considered whereas the Moon magnetic field and its interaction with the LST residual dipole have been neglected. The disturbance torque due to the residual dipole τ_{mag_B} can be evaluated as

$$\tau_{mag_B} = m_{SC_B} \times B_{\oplus_B}. \tag{4.33}$$

- Solar radiation pressure generates a disturbance torque on the spacecraft when this is not in the shadow of the Earth or the Moon. To evaluate this torque, first the spacecraft is modeled again as composed by N flat plates, each one with given unit normal vector $\mathbf{n}_{i_B}$ and distance between center of pressure and center-of-mass equal to $\mathbf{r}_{i_B}$. Then, the inclination of each i-th plate with respect to the direction spacecraft-to-Sun $\mathbf{s}_B$, obtained rotating the corresponding spacecraft-to-Sun vector in ECI $\mathbf{e}_{sat\odot}$[1], is defined as

$$\theta_{SRP_i} = \mathrm{acos}(\mathbf{n}_{i_B} \cdot \mathbf{s}_B) \tag{4.34}$$

and the corresponding solar pressure disturbance force acting on the i-th plate is evaluated as

$$F_{SRP_{i_B}} = -P_\odot A_i \left[2\left(\frac{R_{diff_i}}{3} + R_{spec_i} \cos\theta_{SRP_i} \right) \mathbf{n}_{i_B} + (1 - R_{spec_i}) \mathbf{s}_B \right] \max(\cos\theta_{SRP_i}, 0), \tag{4.35}$$

where R_{diff_i} and R_{spec_i} represent the diffuse and specular reflection coefficients respectively, and $P_\odot$ is the solar radiation pressure, function of the solar constant, the speed of light and spacecraft-to-Sun distance $\mathbf{r}_{sat\odot_I}$ equal. Again, the total disturbance torque due to the solar radiation pressure τ_{SRP_B} acting on the spacecraft is given as the sum over the N plates of the cross product among $\mathbf{r}_{i_B}$ and $F_{SRP_{i_B}}$

---

[1] The unit vector $\mathbf{e}_{sat\odot}$ represents the direction of the spacecraft-to-Sun vector $\mathbf{r}_{sat\odot_I}$, which can be calculated as the vectorial difference between the Earth-to-Sun distance in ECI $\mathbf{r}_{\oplus\odot_I}$ and the spacecraft position in ECI $\mathbf{r}_I$. Further details can be found in [65].

- A non-symmetrical spacecraft in a planetary gravity field is subject to a so-called gravity-gradient torque. Simplifying the gravity field shape as a sphere, the gravitational acceleration g results a function of the spacecraft position in ECI $\mathbf{r}_I$

  $$g(\mathbf{r}_I) = -\frac{\mu}{\|\mathbf{r}_I\|^3}\mathbf{r}_I \tag{4.36}$$

  and, as presented in the NASA report [95], the gravity-gradient torque τ_{GG_B} can be approximated as

  $$\tau_{GG_B} = \frac{3\mu}{\|\mathbf{r}_I\|^3}\mathbf{n} \times (J_{SC}\mathbf{n}) \tag{4.37}$$

  where μ is the gravitational parameter of the central body, J_{SC} is the spacecraft tensor of inertia, and $\mathbf{n}$ is the nadir-pointing unit vector in the body-fixed reference frame.

- An extensive research branch is dedicated to the modeling and estimation of the perturbation due to a third-body on the trajectory of a spacecraft, mainly within the low-thrust trajectory framework. For example, in [96] a semi-analytical and numerical study of the perturbation due to a third-body on a spacecraft is provided for elliptic orbit. Moreover, it has been demonstrate in [97] that this perturbation is a function of the distance between the primary and secondary body s_{pl}, calculated exploiting the NASA JPL Ephemeris models DE 421 [98] for both Moon-Earth and Moon-Sun positions in Moon-Centered Inertial frame, and the distance from the secondary body to the spacecraft d_{pl}. However, it has been shown in [99] that the calculation proposed in [97] is prone to cancellation due to the significant differences in the terms involved. Instead, it provides an alternative formulation in which the third-body acceleration perturbation in ECI τ_{third_I} is given by

  $$\tau_{third_I} = -\frac{\mu_{pl}}{d_{pl}^3}[\mathbf{r}_I + F(q_{pl})s_{pl}] \tag{4.38}$$

  where μ_{pl} is the gravitational parameter of the secondary body, i.e., $\mu_{\oplus} = 398600\ km^3/s^2$ for the Earth and $\mu_{\odot} = 1.327 \cdot 10^{11}\ km^3/s^2$ for the Sun, and q_{pl} and $F(q_{pl})$ are defined as

  $$q_{pl} = \frac{\mathbf{r}_I^T(\mathbf{r}_I - 2s_{pl})}{s_{pl}^T s_{pl}}, \qquad F(q_{pl}) = q_{pl}\left[\frac{3 + 3q_{pl} + q_{pl}^2}{1 + (1 + q_{pl})^{\frac{3}{2}}}\right]. \tag{4.39}$$

Internal Disturbances

In this work, no disturbances related to either LST asymmetry and unbalanced mass have been included unlike thruster errors, due to both thrust deviations in magnitude and direction with respect to the required one. In particular, following the approach proposed in [100], a bias thrust error has been introduced for each thruster to take into account fixed-magnitude error during burns due to manufacturing process, set to 1% of the maximum thrust available. Moreover, a uniform random zero-mean noise has been considered affecting the thrusters performance, both in direction, i.e., bounded between ±1% of the maximum thrust as well, and magnitude, i.e., ±0.1° of deviation. Hence, for the k-th thruster, the actuated thrust is $F_{k_{act}}$ evaluated as

$$F_{k_{act}} = \|F_{k_{cmd}}\|_1 \cdot f_k, \tag{4.40}$$

where $F_{k_{cmd}}$ is the commanded control and $f_k = R_{k_{rand}} f_{k_{nom}}$ is the thrust unit vector of the k-th thruster affected by random error, evaluated rotating the nominal unit vector $f_{k_{nom}}$ by the rotation matrix $R_{k_{rand}}$, including the random deviation angles.

4.2.6 Attitude Control

Even if also the target vehicles, either the cargo module, ORS and the LOP-G, are subject to external disturbance due to the environment, they have been considered stabilized and their attitude control was not analyzed. Hence, their body axes have been considered as perfectly aligned with the target LVLH ones all the time, i.e. $(\phi_T, \theta_T, \psi_T) = (0,0,0)$. On the other hand, the LST attitude control represented a crucial task to include in STAR in order to ensure the proper alignment of the chaser docking interface with the target one at the end of the rendezvous maneuver despite the presence of disturbance torques, as those described in Section 4.2.5. Two different control strategies have been envisioned: (i) one for to ensure the fulfillment of the pointing accuracy constraint while satisfying the hard constraint due to the technology exploited; (ii) a second one to properly distribute the torque control action among the 4 RWs in order to avoid the wheels saturation. In particular, three different MPC control strategies have been implemented (see Chapter 5 for further details) and separately validated to control the LST attitude along the three ARVD maneuver in the presence of both parametric uncertainty, introduced in Section 4.2.4, and torque disturbance.

Once the optimal control torque is obtained solving the MPC problem, it is necessary to properly allocate the required control action among the available RWs to avoid their saturation. The selected control strategy is based on the concept of Moore-Penrose generalized inverse, or pseudoinverse, starting from the transformation matrix built up according to the selected architecture, i.e. a NASA Standard four-wheel configuration in which the fourth wheel is equally tilted of 54.7° with respect to the body axes. Thus, following the guidelines provided in [65], first the transformation matrix corresponding to the NASA Standard configuration has been designed as

$$W_{RW} = \begin{bmatrix} 1 & 0 & 0 & \alpha \\ 0 & 1 & 0 & \beta \\ 0 & 0 & 1 & \gamma \end{bmatrix}, \tag{4.41}$$

where $\alpha^2 + \beta^2 + \gamma^2 = 1$, and $\alpha = \beta = \gamma = 1/\sqrt{3}$. Then, the pseudoinverse of the transformation matrix W_{RW}, i.e. $W_{RW}^{\dagger}$, can be evaluated as

$$W_{RW}^{\dagger} = \frac{1}{1+\alpha^2+\beta^2+\gamma^2} \begin{bmatrix} 1+\beta^2+\gamma^2 & -\alpha\beta & -\alpha\gamma \\ -\alpha\beta & 1+\alpha^2+\gamma^2 & -\beta\gamma \\ -\alpha\gamma & -\beta\gamma & 1+\alpha^2+\beta^2 \\ \alpha & \beta & \gamma \end{bmatrix} \tag{4.42}$$

Then, the pseudoinverse distribution law is defined as

$$M_{RW} = W_{RW}^{\dagger} M_{ctrl}, \tag{4.43}$$

where M_{ctrl} is the control torque defined by the controller and M_{RW} is the vector of torques distributed over the 4 RWs.

4.2.7 Orbital Control

Analogously to the attitude, the LST orbital control during both close-range and final approach is demanded to MPC control algorithms, which are in charge to ensure that:

- At the end of the radial boost maneuver, the chaser shall reach the prescribed terminal velocity along the V-bar direction in order to ensure the proper residual velocity at the begin of the final approach.

- For the final approach phase, constraints on both position and velocity have been considered. In particular, a LOS corridor limits the entry region within the keep-out zone and it is defined in terms of entry radius r_i and final radius r_f, as represented in Figure 4.10, where θ represents the half-aperture of the entry corridor. Moreover, soft docking constraint has been enforced in order to limit the maximum approach velocity at the end of this phase along the docking axis.

- Moreover, hard constraints are imposed on the thrust available during each phase, which are related to the technology equipped on board the LST and the actuation strategy selected. Furthermore, an additional constraint arises from the monopropellant thruster performance in terms of MIB [63].

- Last, fuel consumption as well as maneuver duration shall be compliant with the preliminary budgets obtained with MISS and the time constraints defined in Section 2.3.3 within the LST traffic plane analysis.

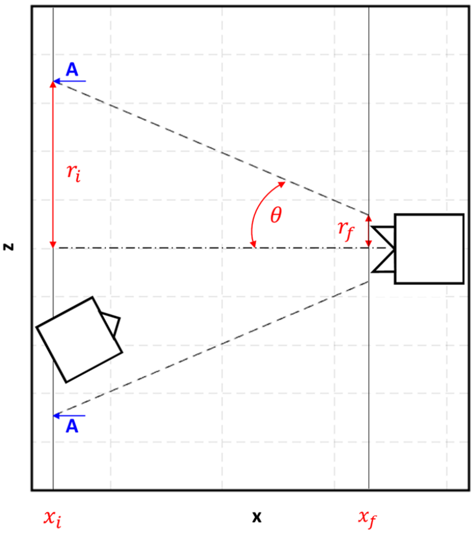

Figure 4.10: LOS approach corridor with entry radius r_i and final radius r_f corresponding respectively at -500 m and -2 m along V-bar.

Additional constraints arise from the mission profile related to the selected rendezvous strategy. In particular, as anticipated in Section 4.1, an ATV-like rendezvous approach has been selected for the LST, envisioning a continuous thrust transfer for the close-range phase as represented in Figure 4.4a and the target vehicle docking port located along the minus V-bar axis. According to the guidelines reported in [66], the continuous acceleration along the R-bar axis required over an orbital period T to achieve the desired Δx, i.e. the relative chaser-target distance to cover with the radial boost maneuver, is defined as

$$\gamma_z = \frac{\omega_T^2}{4\pi}\Delta x, \tag{4.44}$$

which correspond to a thrust vector $[0,\ 0,\ m_{LST} \cdot \gamma_z]$. On the other hand, this "control" strategy does not allow to enforce the velocity constraint at the end of the maneuver. For this reason, the radial boost maneuver has been split into two sub-phases:

1. during the first sub-phase, for $t \in [0, T/2]$, the thrust profile is constant and given by (4.44). The corresponding trajectory bring the chaser to

   $$z\left(\frac{\Delta x}{2}, \frac{T}{2}\right) = \frac{2}{\omega_T^2}\gamma_z$$

   along R-bar.

2. during the second sub-phase, the LST orbital control is demanded to a dedicated MPC strategy where terminal constraints are enforced together with saturation constraints on the actuation system, as anticipated before.

Once the controller provides the desired control action to be actuated by the AOCS thrusters, a TMF has been designed to properly allocate the control action over the 30 monopropellant thrusters, selecting the optimal thrusters to operate according to their physical location while minimizing their firing time in order to reduce the fuel consumption as well. Moreover, the TMF design includes the MIB constraint arising from the thruster technology, resetting the control action if it's lower than the MIB margin. This task has been modeled as a classic Linear Programming, a convex optimization problem characterized by linear objective function and equality and inequality constraints, in analogy to the approach proposed in [101] for the ATV TMF, which numerical validation and effectiveness is described in [102]. For the LST TMF algorithm, let consider the following Linear Programming problem

$$\min_{x} \quad x \tag{4.45a}$$

$$\begin{aligned} \text{s.t.} \quad & Ax = b \\ & lb \leq x \leq ub \end{aligned} \tag{4.45b}$$

where $b = [F_{x_{ctrl}}, F_{y_{ctrl}}, F_{z_{ctrl}}]^T$ is the control vector provided by the controller, and $x \in \mathbb{R}^{30\times 1}$ is the normalized thruster firing duration vector, representing the objective function to be optimized, and lb and ub are the minimum and maximum firing durations, i.e. lb =MIB and $ub = 1$. Last, the matrix $A \in \mathbb{R}^{3\times 30}$ is the so-called force response matrix of the LST AOCS thrusters and for the LST it has the following form.

$$A = F_{max}\begin{bmatrix} 0 & 1 & 0 \\ 0 & 0 & 1 \\ 1 & 0 & 0 \\ 0 & \cos(-\pi/3) & \sin(-\pi/3) \\ 0 & \cos(-\pi/3+\pi/2) & \sin(-\pi/3+\pi/2) \\ -1 & 0 & 0 \\ 0 & \cos(-2\pi/3) & \sin(-2\pi/3) \\ 0 & \cos(-2\pi/3+\pi/2) & \sin(-2\pi/3+\pi/2) \\ 1 & 0 & 0 \\ -1 & 0 & 0 \\ 0 & -1 & 0 \\ -1 & 0 & 0 \\ 0 & \cos(2\pi/3) & \sin(2\pi/3) \\ 0 & \cos(2\pi/3+\pi/2) & \sin(2\pi/3+\pi/2) \\ 1 & 0 & 0 \\ 0 & \cos(\pi/3) & \sin(\pi/3) \\ 0 & \cos(\pi/3+\pi/2) & \sin(\pi/3+\pi/2) \\ -1 & 0 & 0 \\ 0 & \cos(-7\pi/8) & \sin(-7\pi/8) \\ 0 & \cos(-7\pi/8+\pi/2) & \sin(-7\pi/8+\pi/2) \\ -1 & 0 & 0 \\ 0 & \cos(-\pi/8) & \sin(-\pi/8) \\ 0 & \cos(-\pi/8+\pi/2) & \sin(-\pi/8+\pi/2) \\ 1 & 0 & 0 \\ 0 & \cos(\pi/8) & \sin(\pi/8) \\ 0 & \cos(\pi/8+\pi/2) & \sin(\pi/8+\pi/2) \\ -1 & 0 & 0 \\ 0 & \cos(7\pi/8) & \sin(7\pi/8) \\ 0 & \cos(7\pi/8+\pi/2) & \sin(7\pi/8+\pi/2) \\ 1 & 0 & 0 \end{bmatrix} \tag{4.46}$$

Indeed, it identifies each thruster with a 3 × 1-vector that provides the maximum thrust contribution along each of body axes according to their orientation and location (see Figure 2.19b).

Chapter 5

Control Strategies for Automated Rendezvous Maneuver

5.1 Controllers for Rendezvous Maneuver

As extensively described in Chapter 4, ARVD is one of the cornerstone technologies enabling the future of space exploration. The crucial element behind this technology is represented by the software suite for the exploitation of GNC functionalities. In the past 50 years, rendezvous orbital dynamics and control has represented a thrilling topic around which several handbook, papers and monographs have been published, as highlighted in [103]. The reliability and safety of the ARVD maneuvers can be achieved thanks to the proper design of guidance and control algorithms that ensure the compliance with mission requirements and fulfillment of operational and system constraints while providing the yearned performance.

The rendezvous maneuver can be seen as a planned collision among two space system driving the active vehicle, i.e. the chaser, to approach and reach the passive one, i.e. the target, allowing very small trajectory deviations with respect to the planned one and with a minimum residual velocity to guarantee the safe accomplishment of the entire operation with the proper alignment and connection of the mating interfaces on the two vehicle. Thus, while the guidance algorithm is in charge of computing the optimal rendezvous trajectory with respect to pre-defined design variables (burn time and maneuver impulse) and optimization objectives (propellant cost, total velocity increment, total time of flight), the controller shall guarantee the proper actuation profile to be fed to the AOCS actuators in order to allow the chaser to follow the specified trajectory and velocity profile while tracking and eventually maintaining the desired attitude, as highlighted in [104].

Typically, the rendezvous control problem refers only to orbital control, while the attitude control is not involved. Indeed, focusing on the ARVD maneuver, the chaser attitude is either neglected, e.g. [105], or considered fixed and equal to the desired one, i.e. perfect alignment of the docking interfaces, as proposed in [106] where the attitude is assumed to be stabilized in the LVLH coordinate system. In some other cases, both attitude and orbit controls are considered, either exploiting the same control strategy or different controllers. For example, in [107] the main focus was given to the orbital control, exploiting an improved optimal guidance law, while a classical Linear-Quadratic Regulator (LQR) has been adopted for the attitude control. Instead, in [108] a classical back-stepping technique with a simple norm-estimation adaptive method has been exploited to control the coupled translational and rotational dynamics of spacecraft during proximity operations. Another example is provided in [100] where the combination of an Artificial Potential Field (APF) guidance law with a double Sliding Mode Control (SMC) scheme for orbital and attitude control is proposed, also envisioning the presence of obstacles. For the rotational dynamics control, the major effort can be found in two different fields of application, where tracking or following a desired attitude is crucial: (i) station keeping of GEO telecommunication and navigation satellites [109] and [110]; (ii) nadir-pointing tracking for LEO satellites involved in Earth observation missions, including also CubeSat and small spacecraft, as described in [111], [112] and [113].

For the orbital control, numerous approaches have been proposed in the last 50 years, from the most simple controllers, such as Proportional Integral Derivative (PID) and feedback-based schemes, to those requiring higher computational effort and improved mathematical and control techniques, as closed-loop feedback algorithms to achieve high precision and ideal robustness. However, developing and designing improved control techniques for ARVD missions remains an open issue and still achieves resounding success in the space control community. Indeed, completely automated rendezvous maneuvers have been accomplished only in few missions. The first successful attempt dates back to 1967 when the Kosmos 186 and Kosmos 188 docked fully automated after 3.5 h of joint flight. Later on, the Russian Progress and Soyuz inherited the capability to perform rendezvous and dock fully autonomously dock with the ISS during unmanned cargo missions. Until now, no other spacecraft rely on ARVD while the need of reaching a much higher level of autonomy is mandatory for future on-orbit servicing, intercept, and rendezvous mission in the deep space. In the following Section, a thorough overview of the most reliable and exploited control techniques for ARVD is provided.

5.1.1 Control Techniques for Orbital Control

Different theoretical approaches have been explored to solve the orbital control problem aiming at achieving autonomous rendezvous among spacecraft and they can be categorized into three main groups: (i) analytical methods, such as PID, representing the control approaches with the lowest computational complexity; (ii) hybrid methods, either involving convex and unconstrained optimization approaches, e.g. LQR and H_∞, or trajectory tracking/path-planning control optimization methods, e.g. SMC; and (iii) optimization methods, exploiting either direct or indirect and online or offline schemes, among which MPC. The latter category provides the highest level of optimality at the cost of increased computational effort and complexity. Moreover, it is important to highlight that the wide range of control techniques proposed in the last decades is driven by the specific ARVD maneuver envisioned, e.g. tumbling target, obstacle avoidance, elliptical orbit, and the performance indexes, e.g. fuel consumption, time-to-dock, robustness to uncertainty.

In [114] a simple feedback tracking control scheme has been proposed to address the autonomous chasing and close proximity maneuver problem, in combination with a guidance algorithm that provides the reference trajectory to follow. Instead, a Lyapunov-based control strategy has been presented in [115], where differential drag forces are exploited to obtain a quasi propellant-free control of the relative orbital dynamics. In [108], a back-stepping controller is proposed in combination with a simple norm-estimation adaptive method to obtain the desired control capabilities during the rendezvous maneuver while reducing the computational load, making this approach appealing for real-time spacecraft proximity missions. All the previous strategies do not rely on optimization techniques and are not robust by definition, even if some inherent robustness is provided by the feedback-based control structure. Moreover, state ad input constraints, typically characterizing the rendezvous maneuver cannot be directly enforced into the control design. However, some low-complexity and reliable solutions have been proposed in literature to overcome both the robustness to uncertainty and the limited-thrust constraint, as described in [116]. Indeed, in that work a feedback controller has been developed by a Lyapunov approach, casting the control problem into a convex feasibility problem subject to Linear Matrix Inequality (LMI) constraints to address both actuator saturation and parametric uncertainty, inherent to the system model.

Another control approach proposed for the ARVD problem, relying on the minimization of a pre-defined cost function properly built to address the desired performance, is the LQR control scheme for linear/linearized systems. In [117] a LQR has been exploited to provide the control functionalities for the continuous thrust rendezvous maneuver of a microsatellite combined with an image-based processing algorithm and a correction batch filter for navigation purpose and a waypoint logic for the guidance. Another example of LQR is proposed in [118], where the authors attempted to enforce safety constraint satisfaction by properly choosing the cost matrices Q and R to normalize each of the state and input variables. The previous approach has been extended in [119] where a hybrid solution is presented for spacecraft rendezvous where a piecewise continuous feedback control law is periodically updated by recomputing a quadratic optimization problem. This optimization problem implicitly enforces system constraints, taking the form of an infinite-horizon LQR problem, where, at every periodic update, the cost functional evolves according to a function of the current state. On one side the computation effort as well as the fuel consumption are reduced, while on the other side the constraint fulfillment cannot be guaranteed, as remarked in [119]. A suboptimal LQR-based motion control is proposed in [120], in which the control gains are re-computed at each time step using dynamically sized weighting matrices, and the real-time implementability has been demonstrated via experimental tests on a hardware-in-the-loop six-degree-of-freedom spacecraft simulator with an increase of control effort of approximately 15% with respect to time-invariant LQR control schemes. Moreover, in [121] a LQR control algorithm has been combined with an APF guidance law to improve the chaser vehicle performance during a rendezvous maneuver. In particular, the LQR is in charge of driving the spacecraft towards the target position while the APF algorithm provides the repulsive effect for collision avoidance. The effectiveness of the control strategy proposed has been experimentally validated highlighting the improvements obtained. In particular, the local minima issues is overcome introducing a decisional logic that takes over when the local minima is maintained for a time longer than a predefined tolerance. These combinations of guidance and control strategies have been also experimentally tested with the Synchronized Position Hold Engage and Reorient Experimental Satellites (SPHERES) facility on-board the ISS in 2009. During flight testing, a chaser satellite successfully approached a virtual target satellite while avoiding collision with a virtual obstacle satellite, as described in [122].

In realistic applications, uncertainty and disturbance shall be included in the system modeling to improve the adherence among the model and the reality. In these cases, robustness to uncertainty becomes a fundamental task to guarantee and robust control laws have been developed to overcome the effects of uncertainty and external noise over the controller performance. Among all the robust controllers, the H_∞ controller represents the most widespread solution for spacecraft rendezvous. The theoretical formulation of the controller dates back to 1980s whereas the first application to the space field is presented in [123] where a multi-objective robust H_∞ control scheme for the rendezvous problem in which both parametric uncertainties and external perturbations. The controller design has been tailored to guarantee robustness to parametric uncertainty and disturbance simultaneously while enforcing input constraints and pole assignment. In the same period, another H_∞ approach has been proposed in [124] where the controller was designed to guarantee robustness to neglected dynamics of the system. For the first time, the efficacy of this control strategy has been experimentally validated on board the ISS during a rendezvous and docking maneuver among two SPHERES mini-satellites. Later on, the problem of rendezvous with a non-cooperative target has been investigated in [125], where a H_∞ scheme has been proposed to achieve rendezvous in the presence of sensor measurement and thrust errors, control input saturation and orbital parametric uncertainty in the system dynamics and geometrical uncertainty on the spacecraft mass. In [126], the applicability of the H_∞

controller has been further extended to spacecraft terminal rendezvous on highly-elliptical orbits. In particular, the robustness to environmental disturbances, such as J_2 perturbation and atmospheric drag, and parametric uncertainty, for instance introduced with the linearization process, is ensured thanks to a H_∞ algorithm. Its control law is developed using the *zero-sum two-player differential game*, inherited from the differential game theory.

Another robust control technique able to handle uncertainty is the SMC, used either for orbital and attitude control, as described in [127]. In particular, a first-order SMC was designed for position tracking, whereas a supertwisting second-order SMC was exploited for attitude stability in the presence of external additive disturbance. In [128], a simplex SMC algorithm has been proposed for the orbital control to reduce the control effort, i.e. propellant consumption, with respect to the previous first-order SMC scheme. Moreover, in [129] an APF-based SMC control strategy is proposed to guarantee the convergence of relative position and attitude errors during the rendezvous maneuver while avoiding any accidental collision between the two spacecraft, even in the presence of known and bounded external disturbances. Due to the increasing interest on rendezvous maneuvers involving highly-elliptic orbits, in [130] two robust control schemes based on SMC theory have been proposed to guarantee robustness and to reduce tracking errors and fuel cost. Two fault tolerant scenarios, i.e. thruster degradation and short thruster failure, have been considered to validate the effectiveness and robustness of the proposed control approaches.

Model Predictive Control

In the last decades, the advancement in computing hardware as well as the significant improvements in developing numerical solvers for convex optimization problems have gradually increased the interest of the space control community towards the applications of MPC. MPC uses an explicitly dynamic plant model to predict the effect of future reaction of the manipulated variables on the output and the control signal obtained by minimizing a pre-defined cost function. The disruptive success of MPC controllers in the aerospace field is mainly ascribable to their peculiarity of providing optimized performance while guaranteeing mission and system constraints satisfaction via repetitive online optimization. This *unique* ability represents an appealing quality for space missions in which autonomy, safety, reliability, cost-saving and flexibility are crucial requirements.

The concept of model-based predictive control was first introduced in early 1970's when the so-called Dynamic Matrix Control algorithm was proposed in the oil refinery industries by Cutler and Ramaker to use a dynamic model of the process to predict the effect of the future control action while enforcing system and process constraints. Then, MPC became very famous in industrial process applications, e.g. chemical plants (see [131]), involving slow processes operating in the neighborhood of the steady-state operational points and requiring low computational power. These restrictive factors have limited for a long time the spread of MPC until the tremendous progress in computing hardware at the beginning of the new millennium, expanding the field of application to electronic, automotive and aerospace systems. In 1999, MPC-based approach has been exploited for spacecraft formation keeping and attitude control ([132]) where the first evidence of MPC for trajectory control during rendezvous maneuver was first proposed in 2003 [133]. A classical Linear-Quadratic Model Predictive Control (LQMPC) was exploited to guarantee finite-completion of vehicle maneuvers and modifications to the constraints definition allowed to obtain an inherent robust feasibility. Moreover, the same authors have shown in [134] that slightly modifying the control input constraint definition and introducing a variable-horizon approach, the improved MPC scheme allows to save fuel compared to a glideslope algorithm when unmodeled disturbances are included. In the last decade, several works have been proposed in which the orbital control during rendezvous maneuvers was based on a LQMPC algorithm, in which the problem and constraint formulations could be treated by Quadratic Programming solvers. Some examples can be found in: (i) [135] where the target has been considered tumbling and non-cooperative; (ii) [136] where the previous approach was extended to include debris avoidance constraint; (iii) [137] and [138] for rendezvous in elliptic orbits; (iv) [139] where the MPC application is addressed within the Mars Sample Return scenario; (v) [140] where the computational efficiency of MPC was enhanced by using low-thrust propulsion; and (vi) [141] where a 3-D LOS cone constraints was enforced instead the classical in-plane dynamics and trajectory constraint.

All these approaches do represent appealing solutions to the trajectory control during rendezvous and proximity operations. On the other hand, none of them takes explicitly into account in the controller design either parametric uncertainties, in terms of model discrepancies with respect to the actual dynamics, nonlinearities neglected and imprecise knowledge of spacecraft geometrical parameters, and additive disturbance, e.g. orbital perturbations and aerodynamic drag, that could affect the spacecraft dynamics and compromise the constraint satisfaction. To overcome these issues, in the last decade several robust MPC approaches have been proposed, in which the uncertainties, either additive and multiplicative, are directly included in the control algorithm design, guaranteeing the required performance, constraint satisfaction, and robustness to uncertainty and disturbance. A thorough overview of the Robust Model Predictive Control (RMPC) approaches can be found in [142]. The underlying idea of RMPC is to define upper and lower bounds for the perturbations, when no statistical information are available on the uncertainty nature, and include them in designing the cost function and the (new) constraint sets as well. Hence, a worst-case scenario approach is envisioned in the majority of RMPC schemes. For example, in the framework of ARVD, a robust MPC algorithm has been proposed in [143] for spacecraft rendezvous in the presence of additive disturbance and LOS constraint. The robustness to external disturbances due to thruster errors and unmodelled dynamics, e.g. eccentricity perturbations, is guaranteed directly including the additive disturbance, which disturbance bounds are predicted online, into the cost function and constraints definition. In the same paper, the reliability of the robust control scheme with respect to a classical one is provided, highlighting how a standard MPC approach is not able to cope with disturbance guaranteeing constraint fulfillment.

On the other hand, uncertainty bounds are not always known a priori or easily identifiable, especially when the system has to operate in highly uncertain environments. Deep space missions could be easily subject to both parametric and additive uncertainty due to incomplete or non-reliable information for both system dynamics modeling, navigation sensor degradation and external environment, e.g. radiations and solar events. Because the model involves uncertainty, process output predictions could be uncertain as well, possibly resulting in adverse constraints violation. Moreover, robustness implies an inherent conservativeness, which in some cases is unnecessary and at the same time has relevant consequences over the mission success and cost, e.g. increased propellant consumption due to the higher control effort required to robustly satisfy the constraints. A reliable solution is represented by RMPC algorithms in which chance (probabilistic) constraints are enforced. These schemes rely on the idea to ensure that the constraints are satisfied with a prescribed probability according to the statistical properties of the uncertainty itself, still resulting in a convex optimization problem as proposed in [144]. Following this approach, the spacecraft rendezvous problem under unmodelled dynamics uncertainty and environmental disturbance has been analyzed in [145]. In particular, an on-line estimator has been employed to evaluate the statistical properties of the uncertainties, inferred for the past realizations. A Gaussian model has been considered to obtain an explicit solution of the probabilistic constraints and a convex optimization problem and the predicted uncertainty. Starting from the approach proposed in [145], an improved version of RMPC algorithm subject to chance constraints has been recently proposed in [146] where, to reduce the conservativeness of the previous robust scheme, the uncertainty coming from the navigation sensors has been separated from those arising from the process, explicitly incorporating the former, which statistical properties are usually known. Still, a certain level of inherent conservativeness shall be paid to guarantee robustness to uncertainty.

More recently, to overcome these limitations a new field of research has emerged, focused on the development and design of innovative MPC approach, the so-called SMPC algorithms. These control strategies can be applied to processes where a stochastic model can be formulated to represent the uncertainty and disturbance and constraints violation does not correspond to compromise the application or lose the mission, as thoroughly described in [147]. Indeed, the exploitation of a probabilistic model allows to optimize average performance or appropriate risk measures, and the adoption of chance constraints provides a higher cost-effectiveness of the application itself. Moreover, this innovative MPC framework allows to tackle those applications in which unbounded uncertainty and disturbance are involved. SMPC schemes have been considered as a promising solution in a numerous number of application domains such as water networks [148], river flood control [149], chemical processes [150], energy management [151], and path planning for aeronautical application [152]. Most of the proposed methods share some critical commonalities, regardless the system modeling (linear or nonlinear), the uncertainty (additive, multiplicative or parametric), and the type of chance constraint (polytopic and quadratic). In particular, according to the categorization suggested in [147], the current SMPC methods can be divided in two main groups, depending on the approach followed to solve the chance-constrained optimization problem: (i) analytic approximation methods; and (ii) randomized [153] and scenario-based methods. For the analytic approximation methods, the probabilistic properties of the uncertainty are exploited to reformulate the chance constraints is a deterministic form. On the other hand, for the second class of methods, the craved control performance and constraint satisfaction are guaranteed properly generating a sufficient number of uncertainty realizations, and on the solution of a suitable constrained optimization problem, as proposed in [154, 155]. The main advantage of this class of SMPC algorithms is given by the inherent flexibility to be applied to (almost) every class of systems, including any type of uncertainty and both state and input constraints, as long as the optimization problem is *convex*. However, as highlighted in [83] and [147], these approaches are still very demanding for real-time implementations due to their computational load since different samples need to be drawn at each step, especially when computability limitations are inherent to the application resources available. Thus, no SMPC approach has been never proposed for space applications, nor even for the attitude or orbital control of spacecraft during rendezvous maneuvers.

Nonetheless the numerous benefits related to the MPC schemes, the classical criticism, especially in their robust/stochastic instantiations, is their *slowness*. Indeed, typically this widely recognized shortcoming is mainly due to the computational effort required in the online solution of the ensuing optimization problem, and to the difficulty of embedding a real-time solver for MPC implementation. In general, the implementation of classical MPC on low-cost hardware, such as microcontrollers, is already quite demanding and in particular, in space applications, the available processors provide limited on-board computational power since the on-board computers typically used in the space field are not the state of the art of the current technology due to radiation hardening requirements. This constrains the level of spacecraft autonomy because even relatively simple autonomous operations require complex computations to be performed in near real time. In this framework, the requirement of real-time implementability for new GNC algorithms gains the highest priority, while guarantee the minimum safety requirements. The space community is currently working towards new regulations to define the safety constraints for ARVD maneuvers. These rules should be defined with respect to collision avoidance requirements and keep-out-zones driven by the mission as well as by the stakeholders. Until now, rendezvous maneuvers have mainly involved the ISS and the rigid safety requirements are due to the presence of a crew on board, which requires the highest level of failure tolerance. On the other hand, as anticipated in the previous Chapters, numerous missions will involve *fully-automated* rendezvous maneuvers between unmanned systems: hence it is expected that the safety requirements could be relaxed, by introducing a maximum level of constraints violation probability allowance, always in compliance with the protection of the investment made in the space systems involved.

Motivated by all these limitations inherent to the selected application, i.e. ARVD maneuvers with both manned and unmanned systems, three different MPC algorithms have been designed to control either the attitude and the trajectory of a completely autonomous spacecraft, i.e. LST, during close-range rendezvous: (i) a classical LQMPC (see Section 5.2); (ii) a Tube-Based Robust Model Predictive Control (TRMPC); and (iii) a new offline-sampling based SMPC. In particular, over the several RMPC approaches available in literature, the so-called TRMPC [156, 157, 158] has been selected thanks to its highly desirable efficient computability as highlighted also in [83]. Indeed, TRMPC envisages the additive disturbance acting on the system dynamics directly in the control algorithm, computing *offline* the stabilizing feedback gain matrix exploited in the time-varying control law, significantly reducing the computational load with respect to other RMPC approaches. In particular, the approach proposed in [159] has been followed to properly design the *tightened* constraint sets to guarantee robustness to additive disturbance, as recalled in Section 5.3.

On the other hand, a promising approach proposed in literature [160] to overcome the significant computational load required by scenario-based SMPC methods due to the high number of samples and the corresponding size of the problem, is to draw the required samples *offline* and then only *necessary* samples are kept for online optimization. In particular, [161] and [162] provide a nonconservative SMPC based on offline sampling for linear system subject to chance constraints and affected by parametric uncertainty, guaranteeing recursive feasibility. On the other hand, in [163] and [164] the tube-based MPC approach has been extended to systems subject to chance constraints and in the presence of additive disturbance. However, neither of them allows to contemporary consider the presence of *both* additive disturbance and parametric uncertainty, which is more representative and attractive for real-world applications. The OS-SMPC scheme here proposed solves the nontrivial problem of extending the previous results proposed in [162] and [164] into a comprehensive framework, able to tackle situations in which *both* additive disturbances and parametric uncertainties are simultaneously present. The main contribution to the theory of SMPC is the introduction of an SMPC scheme, less conservative than most analytical approaches based on Chebyschev's inequality (see [165] and [166] for further details), that is computationally tractable and guarantees recursive feasibility. As in [164], the computational load is reduced by generating scenarios offline and keeping only selected, *necessary* samples for the online optimization. The algorithm guarantees robust satisfaction of the input constraints and bounds on the confidence that the chance constraints are satisfied can be chosen by the designer. Due to the additive disturbance, the state does not converge to the origin. Instead, an asymptotic performance bound is provided.

In the following Section, the main theoretical features of LQMPC and TRMPC schemes are recalled and the proposed OS-SMPC is described in detail, including the derived theoretical guarantees in terms of recursive feasibility and convergence of the asymptotic average stage cost to a finite, steady-state value. Last, it is important to highlight that the development of the previously introduced robust and stochastic MPC schemes mainly targeted real-time implementability while maximizing the system control performance and fulfilling the mission and system constraints. Thus, the validation campaign has been split into three main phases: (i) first, implementation of the control schemes into the STAR simulator and SIL simulations to validate their effectiveness within the selected scenario (see Section 6.2); (ii) experimental validation implementing the MPC algorithms on a space-qualified micro-controller running on-board a spacecraft engineering model (see Section 6.3); (iii) SIL and HIL validation of both TRMPC and OS-SMPC schemes for trajectory and attitude tracking of a fixed-wing UAV, in which the much faster dynamics and the limited on-board computational capabilities represent an additional challenge for the real-time feasibility of these controllers (see Appendix B for a thorough overview of the aeronautical application and corresponding preliminary results).

5.2 Linear-Quadratic MPC

The LQMPC belongs to the class of MPC control problem typically referred as *classical* MPC in which systems whose dynamics are described by either linear or linearized discrete time models are involved. Thus, neither parametric uncertainty nor additive disturbance are included and the system dynamics can be described by the following linear time invariant state-space model

$$x_{k+1} = Ax_k + Bu_k, \tag{5.1a}$$

$$y_k = Cx_k + Du_k, \tag{5.1b}$$

where $x_k \in \mathbb{R}^n$ is the system state, $u_k \in \mathbb{R}^m$ the control input, $y_k \in \mathbb{R}^{n_y}$ the system output, and k is the discrete time index.

Assumption 1. *The state x_k of the system* (5.1a) *is assumed to be fully measurable and available to the controller at each sampling time $k \in \mathbb{N}_{\geq 0}$.*

Assumption 1 allows to set the output y_k as coincident to the state x_k. Thus, the output matrix $C \in \mathbb{R}^{n_y \times n}$ is the identity matrix $\mathbb{I}_n$, i.e. $n_y = n$, whereas $D \in \mathbb{R}^{n_y \times m}$ is set to $0_{n \times m}$.

The controlled system is also assumed to be subject to hard constraints on both the state x_k and the control input u_k. Hence, they are constrained into convex polytopic constraint sets $\mathbb{X} \subseteq \mathbb{R}^n$ and $\mathbb{U} \subseteq \mathbb{R}^m$, respectively. The same constraints can be expressed in terms of linear inequalities as follows

$$\mathbb{X} = \left\{ x_k \in \mathbb{R}^n \mid H_x x_k \leq h_x, \ \forall k \in \mathbb{N}_{\geq 0} \right\}, \tag{5.2a}$$

$$\mathbb{U} = \left\{ u_k \in \mathbb{R}^m \mid H_u u_k \leq h_u, \ \forall k \in \mathbb{N}_{\geq 0} \right\}, \tag{5.2b}$$

with $H_x \in \mathbb{R}^{n \times n}$, $h_x \in \mathbb{R}^n$, $H_u \in \mathbb{R}^{m \times m}$, and $h_u \in \mathbb{R}^m$. Furthermore, as typical in stabilizing MPC, a suitable terminal set $\mathbb{X}_T$ can be included, which shall satisfy the following Assumption.

Assumption 2. *There exist a control gain K, which is asymptotically stabilizing for the system* (5.1a)*, and a terminal set $\mathbb{X}_T \subseteq \mathbb{R}^n$ with $\mathbb{X}_T = \{x_k \in \mathbb{R}^n \mid H_T x_k \leq h_T\}$, which is robustly forward invariant for the system* (5.1a) *under given control law $u_k = K x_k$. Given any $x_k \in \mathbb{X}_T$, the state and input constraints* (5.2) *are satisfied and there exist a matrix $P \in \mathbb{R}^{n \times n}$ that satisfy the following Lyapunov function*

$$Q + K^T R K + (A + BK)^T P (A + BK) - P \preceq 0, \tag{5.3}$$

with $Q \in \mathbb{R}^{n \times n}$ and $R \in \mathbb{R}^{m \times m}$ symmetric positive-definite matrices.

The control objective consists in the minimization of a quadratic cost function J_T at time k for a given (measured) x_k guaranteeing the constraint satisfaction. The finite horizon cost function J_T is defined as

$$J_T(x_k, \mathbf{u}_k) = \sum_{\ell=0}^{T-1} (\|x_{\ell|k}\|_Q^2 + \|u_{\ell|k}\|_R^2) + \|x_{T|k}\|_P^2, \tag{5.4}$$

where T is the prediction horizon, $\mathbf{u}_k = [u_{0|k}, \ldots, u_{T-1|k}]$ the control sequence, and $x_{\ell|k}$ representes the system state predicted ℓ steps ahead at time k.[1] The LQMPC control problem seeks a control sequence $\mathbf{u}_k$, with knowledge of the current input x_k, that minimize the objective function J_T subject to both state and input constraints. Of the T-move control sequence that minimizes the objective in 5.4, only the first one is implemented. Then, when another measurement becomes available, the parameters of the problem are updated and a new optimization problem is formulated whose solution provides the next control. The so-called finite horizon optimal control problem can be formally stated as follows.

---

[1] Here $\|v\|_S^2$ denotes the quadratic form $v^T S v$.

Definition 1 (Finite Horizon Optimal Control Problem)**.** *Given the system dynamics* (5.1a)*, the constraint sets* $\mathbb{X}$ *and* $\mathbb{U}$ *in* (5.2)*, and the cost* J_T *in* (5.4)*, the LQMPC finite horizon optimization problem is*

$$\min_{\boldsymbol{u}_k} \quad J_T(x_k, \boldsymbol{u}_k) \tag{5.5a}$$

$$\begin{aligned} s.t. \quad & x_{\ell+1|k} = Ax_{\ell|k} + Bu_{\ell|k}, \quad x_{0|k} = x_k, \\ & x_{\ell|k} \in \mathbb{X}, \quad i \in [0, T-1], \\ & u_{\ell|k} \in \mathbb{U}, \quad i \in [0, T-1], \\ & x_{T|k} \in \mathbb{X}_T. \end{aligned} \tag{5.5b}$$

5.3 Tube-based Robust MPC

The essential components of robust MPC control schemes are similar to those that underpin the classical approach described in the previous Section. On the other hand, in the presence of additive disturbance acting on the system dynamics, properties as invariance, recursive feasibility and monotonicity of the predicted cost cannot be guaranteed anymore for all possible uncertainty realizations, as stated in [142]. Moreover, stability and convergence of the closed-loop as well as constraints fulfillment are compromised. Robust MPC approaches allows to preserve certain properties despite the presence of uncertainty, either additive and multiplicative/parametric, i.e. result of an imprecise knowledge of the model parameters. Within the range of approaches that have been proposed in literature for robust MPC, the one selected in this work envisages optimization performed over an open-loop prediction strategy, simpler to design and characterized by a lower computational complexity, comparable with the one of classical MPC schemes.

The TRMPC rotates around the concept of *tube* of trajectories, each one corresponding to a particular realization of the additive uncertainty itself. Indeed, starting from the same initial condition, the system dynamics evolves differently according to the peculiar disturbance sequence acting on the system. The use of tubes in the control field dates back to 1970s, as witnessed by [167] and [168], whereas this concept has been transferred in MPC leading to specialized technique such as TRMPC. Because of the model uncertainty, the predicted states can be described by a tube constituted by a sequence of sets $\mathcal{X}_{0|k}, \ldots, \mathcal{X}_{T|k}$, each of which contains the state at a given time instant for all realizations of future uncertainty, as described in [159].

The underlying idea for the TRMPC scheme involves the control of the associated nominal (undisturbed) system dynamics subject to *tightened* constraint sets such that the designated system dynamics will evolve within the initial constraint sets lying in the tube of trajectories, properly designed. In particular, the optimization problem is based on an open-loop strategy in which the sequence of nominal control inputs $\mathbf{v}_k = \left\{v_{0|k}, \ldots, v_{T-1|k}\right\}$, predicted at time k, is independent of the realization of the disturbance sequence and defined the nominal trajectory z_k, representing the center of the tube (see Figure 5.1). On the other hand, the final time-varying control law takes into account the discrepancies among the actual state and the undisturbed one.

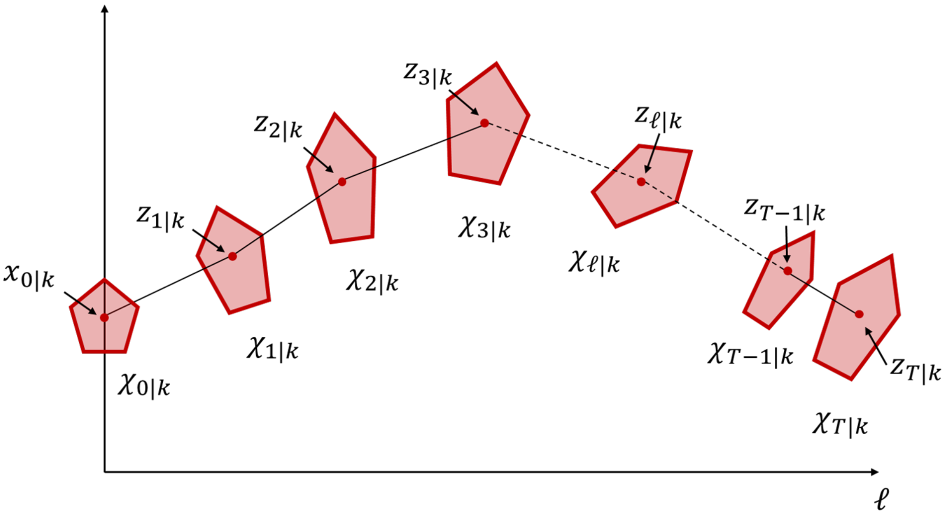

Figure 5.1: An illustration of the state tube, the sequence of constraint set and the nominal trajectory.

Let consider the following linear time invariant state-space model

$$x_{k+1} = Ax_k + Bu_k + w_k, \tag{5.6}$$

with w_k the additive model uncertainty at time k, which is assumed to be a realization of a stochastic process W_k for $k \in \mathbb{N}_{\geq 0}$, introduced into the linear dynamics of (5.1a).

Assumption 3 (Bounded random Disturbance)**.** *The disturbances W_k, for $k =$ 0,1,2..., are independent and identically distributed (iid), zero-mean random variables with support $\mathbb{W}$, which is a bounded and convex set, containing the origin in its interior.*

Still, the state x_k and u_k are subject to hard constraints of the form (5.2) and the finite horizon cost $J_T(x_k, \mathbf{u}_k)$ to be minimized at time k is defined as (5.4).

On the other hand, due to the presence of a persistent disturbance w_k, the predicted system state $x_{\ell|k}$

$$x_{\ell|k} = z_{\ell|k} + e_{\ell|k}, \tag{5.7}$$

can be split into a nominal part $z_{\ell|k}$ and an error part $e_{\ell|k}$, representing the deviation of the actual state from the nominal one, as typical in robust and stochastic MPC, e.g. [164].

As anticipated before, a time-varying feedback control law is envisioned such that

$$u_{\ell|k} = v_{\ell|k} + K(x_{\ell|k} - z_{\ell|k}), \tag{5.8}$$

where $v_{\ell|k}$ is the control input of the nominal system dynamics and K is the quadratically stabilizing feedback gain matrix for the system (5.6).

To estimate the gain matrix K such that the closed-loop is quadratically stable, a LMI approach applied to the well-known Edge Theorem [169] has been envisioned for the stability analysis of the system (5.6) under parametric uncertainties, which can include: (i) discrepancies between the mathematical model and the actual dynamics, in terms of neglected nonlinearities, unmodeled high-frequency dynamics, and deliberate reduced-order models; (ii) geometrical uncertainties of the system itself. As explained in [169], the Edge Theorem is an extension of the Karitonov's theorem (see [170]) and states that the stability of a polytope of polynomials can be guaranteed by the stability of its exposed edge polynomials. Thus, it takes into account the dependence of the polynomial coefficients on the uncertain parameters $q = [q_1, ..., q_l]$, which are defined in a convex and compact hyper-rectangle such that each i-th uncertainty $q_i \in [q_i^-, q_i^+]$ for $i = 1, \dots, l$. Analogously, it is possible to define a system of Lyapunov function of the form (5.3), where each function involves a couple $(A(q), B(q))$ built with respect to the identified vertexes of the uncertain matrices $A(q^{\pm})$ and $B(q^{\pm})$ such that the solution of the system

$$\begin{cases} Q + K^T R K + (A^+ + B^+ K)^T P (A^+ + B^+ K) - P \preceq 0, \\ Q + K^T R K + (A^+ + B^- K)^T P (A^+ + B^- K) - P \preceq 0, \\ Q + K^T R K + (A^- + B^+ K)^T P (A^- + B^+ K) - P \preceq 0, \\ Q + K^T R K + (A^- + B^- K)^T P (A^- + B^- K) - P \preceq 0, \end{cases} \tag{5.9}$$

is the quadratically stabilizing feedback gain matrix K. Each Lyapunov function can be rewritten as a LMI of the form

$$\begin{bmatrix} P & * & * & * \\ AP + BY & P & * & * \\ \sqrt{Q}P & 0 & 0 & * \\ \sqrt{R}Y & 0 & 0 & 0 \end{bmatrix} \tag{5.10}$$

where $Y = KP$. Hence, the solution of the system provides the value of the matrices P and Y from which $K = YP^{-1}$ can be obtained, ensuring the stability of the system for all the uncertain matrices $A(q)$ and $B(q)$ which values are within the stable edges. It is important to highlight that the evaluation of the feedback gain matrix can be performed *offline* thus reducing the computational cost of the online optimization process, as highlighted in [159].

Then, substituting (5.7) and (5.8) in (5.6), it results

$$z_{\ell+1|k} + e_{\ell+1|k} = A(z_{\ell|k} + e_{\ell|k}) + B(v_{\ell|k} + Ke_{\ell|k}) + w_k, \tag{5.11}$$

from which it is possible to obtain the following composite system

$$z_{\ell+1|k} = Az_{\ell|k} + Bv_{\ell|k}, \tag{5.12a}$$

$$e_{\ell+1|k} = A_{cl}e_{\ell|k} + w_{\ell|k}, \tag{5.12b}$$

with $A_{cl} = A + BK$ quadratically stable and so that

$$e_{\ell|k} = A^{\ell}e_{0|k} + \sum_{j=0}^{\ell-1} A_{cl}^{j} w_{\ell|k}, \quad e_{\ell|k} \in S_K(\ell|k). \tag{5.13}$$

In order to robustly satisfy the state and input constraints (5.2), they shall be *tightened* to allow the trajectories of the uncertain system, affected by additive disturbance w_k, to lie in a tube centered on the nominal trajectory, as represented in Figure 5.1. Since A_{cl} is stable by design, then the uncertainty sets $S_K(\ell|k)$ is defined by

$$S_K(\ell|k) = \sum_{j=0}^{\ell-1} A_{cl}^{j}\mathbb{W} = \mathbb{W} \oplus A_{cl}\mathbb{W} \oplus \ldots \oplus A_{cl}^{\ell-1}\mathbb{W}, \tag{5.14}$$

where $\oplus$ denotes the *Minkovsky sum* of a pair of sets.

Definition 2 (Minkovsky Sum). *Given a pair of sets $\mathbb{X}, \mathbb{Y} \subseteq \mathbb{R}^{n_x}$, their Minkovsky sum, denoted as $\mathbb{X} \oplus \mathbb{Y}$, is defined by the set*

$$\mathbb{X} \oplus \mathbb{Y} \doteq \{z \in \mathbb{R}^{n_x} \mid z = x + y, \ \forall x \in \mathbb{X}, \ y \in \mathbb{Y}\}.$$

Starting from the tube definition as sequence of sets $\left\{\mathcal{X}_{0|k}, \ldots, \mathcal{X}_{\ell|k}, \ldots, \mathcal{X}_{T|k}\right\}$, where $x_\ell = z_{\ell|k} + e_{\ell|k} \in \mathcal{X}_{\ell|k}$, and using the decomposition (5.12) yields

$$\mathcal{X}_\ell = \left\{z_{\ell|k}\right\} \oplus S_K(\ell|k), \tag{5.15}$$

which implies a tube for the predicted control input $\left\{\mathcal{U}_{0|k}, \ldots, \mathcal{U}_{\ell|k}, \ldots, \mathcal{U}_{T-1|k}\right\}$, where $u_\ell \in \mathcal{U}_{\ell|k}$. In accordance with the predicted control law in (5.8), $\mathcal{U}_{\ell|k}$ is given by

$$\mathcal{U}_{\ell|k} = \left\{v_{\ell|k}\right\} \oplus KS_K(\ell|k). \tag{5.16}$$

Moreover, according to the definition of $S_K(\ell|k)$ in (5.14),

$$S_K(\ell+1|k) = S_K(\ell|k) \oplus A_{cl}^{\ell}\mathbb{W}$$

implying that $S_K(\ell|k)$ results a subset of $S_K(\ell+1|k)$. Thus, for $\ell \to \infty$, its has been proved in [159] that $S_K(\infty)$ exists, contains the origin in its interior, given the definition of $\mathbb{W}$ in (3) and can be exploited to obtain an outer-bounding approximation of the tube (see Figure 5.2). In particular, $S_K(\infty)$ is the *minimal Robust Positive Invariant* set for (5.12b) for $\forall w_{\ell|k} \in \mathbb{W}$. Let recall the following well–known definition as provided in [171].

Definition 3. *(Robust Positive Invariant Set) The set* $\Omega \subset \mathbb{R}^{n_\Omega}$ *is a Robust Positive Invariant (RPI) set for the system* $x_{k+1} = Ax_k + w_k$ *with* $w_k \in \mathbb{W}$ *if* $\Omega \subseteq \mathbb{X}$ *and* $Ax_k + w_k \in \Omega$ *for* $\forall x_k \in \Omega$ *and* $w_k \in \mathbb{W}$*, i.e. if and only if* $\Omega \subseteq \mathbb{X}$ *and* $A\Omega \oplus \mathbb{W} \subseteq \Omega$

Definition 4. *(Minimal Robust Positive Invariant Set) The minimal Robust Positive Invariant Set* R_∞ *for the system* $x_{k+1} = Ax_k + w_k$*,* $w_k \in \mathbb{W}$ *is the closed RPI set in* $\mathbb{R}^{n_\Omega}$ *that is contained in every closed RPI set for the system* $x_{k+1} = Ax_k + w_k$ *with* $w_k \in \mathbb{W}$*.*

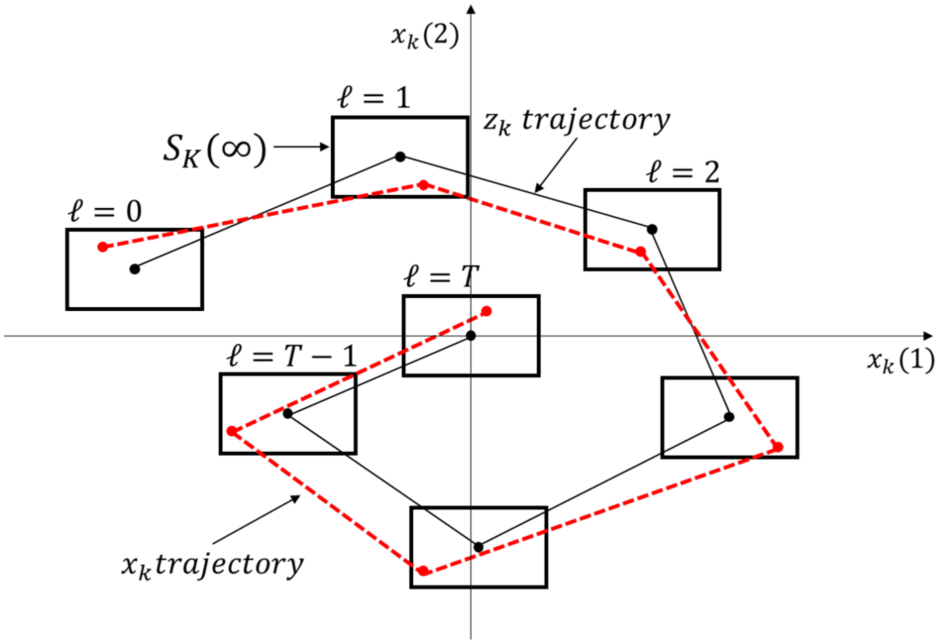

Figure 5.2: Example of outer-bounding tube representation at the k-th time step over a prediction horizon of T for $x \in \mathbb{R}^2$.

As stated in [159], the fact that the state and control input trajectories $\left\{x_{\ell|k}\right\}$ and $\left\{u_{\ell|k}\right\}$ lie in known neighborhoods of the corresponding nominal ones, is the basic concept for the TRMPC control scheme. Indeed, $\left\{z_{\ell|k}\right\}$ and $\left\{v_{\ell|k}\right\}$ should be chosen to satisfy the *tighter* constraint sets $z_{\ell|k} \in \mathbb{Z}$ and $v_{\ell|k} \in \mathbb{V}$, properly designed to ensure that for each realization of the disturbance sequence defined in $\mathbb{W}$, the initial state and input constraints in (5.2) are robustly satisfied. In particular, $\mathbb{Z}$ and $\mathbb{V}$ shall satisfy $\mathbb{Z} \doteq \mathbb{X} \ominus S$ and $\mathbb{V} \ominus KS$, respectively, where S is either equal to $S_K(\infty)$ or its outer approximation and $\ominus$ recall the Pontryagin difference, as defined in the follows.

Definition 5 (Pontryagin Difference)**.** *Given a pair of sets* $\mathbb{X}, \mathbb{Y} \subseteq \mathbb{R}^{n_x}$*, their Pontryagin difference, denoted as* $\mathbb{X} \ominus \mathbb{Y}$*, is defined by the set*

$$\mathbb{X} \ominus \mathbb{Y} \doteq \{z \in \mathbb{R}^{n_x} \mid z + x \in \mathbb{X}, \ \ \forall y \in \mathbb{Y}\}\,.$$

Given the correlation among S and the disturbance set $\mathbb{W}$, it is important to highlight that $\mathbb{W}$ shall be sufficiently small to ensure that $S \subset \mathbb{X}$ and $KS \subset \mathbb{U}$. To easily compute the tightened constraint sets starting from the initial ones in (5.2), the approach proposed in [159] has been followed and here described in detail.

Starting from the definition of the state control set given in (5.2a) and since for $\forall \ell \in \mathbb{N}_{\geq 0}$ $x_{\ell|k} = z_{\ell|k} + e_{\ell|k}$ where $e_{\ell|k} \in S_K(\infty)$, it follows that $H_x x_{\ell|k} \leq h_x$ if

$$H_x z_{\ell|k} \leq h_x - \Phi_\infty,$$

with $\Phi_\infty = \max_{e_{\ell|k}} \Big\{ H_x e_{\ell|k} \mid e_{\ell|k} \in S_K(\infty) \Big\}$. Thus,

$$\hat{\mathbb{Z}} = \Big\{ z_{\ell|k} \in \mathbb{R}^n \mid H_x \leq h_x - \Phi_\infty \Big\}$$

represents a suitable constraint set for the nominal state $z_{\ell|k}$. To compute Φ_∞ an infinite dimensional optimization problem shall be solved whereas it is possible to compute and exploit an upper bound of Φ_∞ to obtain an inner approximation of $\hat{\mathbb{Z}}$ following the approach proposed in [172]. For each $\ell \in \mathbb{N}_{\geq 0}$:

- $\Phi_\ell = \max_{e_{\ell|k}} \Big\{ H_x e_{\ell|k} \mid e_{\ell|k} \in S_K(\ell|k) \Big\}$,
- $\Phi_T = \max_{w_{\ell|k}} \Big\{ H_x \sum_{j=0}^{T-1} A_{cl}^j \mathbb{W}, w_{\ell|k} \in \mathbb{W} \Big\}$,
- $\Phi_\infty = \max_{w_{\ell|k}} \Big\{ H_x \sum_{j=0}^{\infty} A_{cl}^j \mathbb{W}, w_{\ell|k} \in \mathbb{W} \Big\}$.

Assumption 4. *Let define the feedback matrix K and the prediction horizon T such that*

$$A_{cl}^T w_k \in \alpha \mathbb{W} \; \forall w_k \in \mathbb{W},$$

with $\alpha \in (0,1)$.

If Assumption 4 holds, then it follows from the definition of Φ_T and Φ_∞ that

$$\begin{aligned}
\Phi_\infty &= \Phi_T + \max_{w_{\ell|k}} \left\{ H_x \sum_{j=0}^{T} A_{cl}^j \mathbb{W}, w_{\ell|k} \in \mathbb{W} \right\} \\
&= \Phi_T + \max_{w_{\ell|k}} \left\{ H_x \sum_{j=0}^{T-1} (A_{cl}^T w_{0|k} + A_{cl} A_{cl}^T w_{0|k} + \ldots) \mathbb{W}, w_{\ell|k} \in \mathbb{W} \right\} \\
&\leq \Phi_T + \max_{w_{\ell|k}} \left\{ H_x \sum_{j=0}^{T-1} (\alpha w_{0|k} + \alpha A_{cl} w_{0|k} + \ldots) \mathbb{W}, w_{\ell|k} \in \mathbb{W} \right\} \\
&= \Phi_T + \alpha \max_{w_{\ell|k}} \left\{ H_x \sum_{j=0}^{T} A_{cl}^j \mathbb{W}, w_{\ell|k} \in \mathbb{W} \right\} \\
&= \Phi_T + \alpha \Phi_\infty.
\end{aligned}$$

Hence, $\Phi_\infty \leq (1-\alpha)^{-1}\Phi_T$ where Φ_T is the solution of a Linear Programming problem and it is possible to obtain an upper bound of Φ_∞ properly selecting α as close as desired to 1. Then, the constraint set $\mathbb{Z}$ can be defined by

$$\mathbb{Z} \doteq \left\{ z_{\ell|k} \in \mathbb{R}^n \mid H_x z_{\ell|k} \leq h_x - (1-\alpha)^{-1}\Phi_T \right\} \subseteq \hat{\mathbb{Z}}. \tag{5.18}$$

Analogously, the constraint set on the control input $\mathbb{V}$ can be approximated as

$$\mathbb{V} \doteq \left\{ v_{\ell|k} \in \mathbb{R}^m \mid H_u v_{\ell|k} \leq h_u - (1-\alpha)^{-1}K\Phi_T \right\}, \tag{5.19}$$

starting from the initial control input constraint set $\mathbb{U}$ in (5.2b).

Thus, the TRMPC approach first envisages an *offline* part, in which the quadratically stabilizing feedback matrix K is designed together with the tightened constraint sets related to the nominal state and control input. Then, the *online* optimization problem revolves around the minimization of the following nominal finite horizon cost function

$$J_T(x_k, \mathbf{v}_k) = \sum_{\ell=0}^{T-1} (\|z_{\ell|k}\|_Q^2 + \|v_{\ell|k}\|_R^2) + \|z_{T|k}\|_P^2, \tag{5.20}$$

subject to the nominal dynamics in (5.12a) and the tightened constraint sets $\mathbb{Z}$, $\mathbb{V}$ and $\mathbb{Z}_T$. Hence, the nominal finite horizon optimal control problem can be stated as follows.

Definition 6 (Nominal Finite Horizon Optimal Control Problem)**.** *Given the system dynamics* (5.6)*, the constraint sets* $\mathbb{Z}$ *and* $\mathbb{V}$*, and the cost* J_T *in* (5.20)*, the TRMPC nominal finite horizon optimization problem can be written as follows*

$$\underset{\boldsymbol{v}_k}{min} \quad J_T(z_k, \boldsymbol{v}_k) \tag{5.21a}$$

$$\begin{aligned} s.t. \quad & z_{\ell+1|k} = Az_{\ell|k} + Bv_{\ell|k}, \quad z_{0|k} = x_k, \\ & z_{\ell|k} \in \mathbb{Z}, \quad i \in [0, T-1], \\ & v_{\ell|k} \in \mathbb{V}, \quad i \in [0, T-1], \\ & z_{T|k} \in \mathbb{Z}_T. \end{aligned} \tag{5.21b}$$

The solution of (5.21) is the optimal control sequence $\mathbf{v}_k^* = [v_{0|k}^*, \ldots, v_{T-1|k}^*]$ and the first control action $v_{0|k}^*$ represents the optimal nominal control input to be applied on the uncertain system (5.6) such that

$$x_{k+1} = (A+BK)x_k + Bv_{0|k}^* + w_k. \tag{5.22}$$

5.4 Offline Sampling-based Stochastic MPC

Let consider the following uncertain discrete-time system to be controlled

$$x_{k+1} = A(q_k)x_k + B(q_k)u_k + Bww_k \tag{5.23}$$

with additive disturbance $w_k \in \mathbb{R}^{m_w}$ and parametric uncertainty $q_k \in \mathbb{R}^{n_q}$. The disturbance sequence $(w_k)_{k\in\mathbb{N}_{\geq 0}}$ is assumed to be a realization of a stochastic process $(W_k)_{k\in\mathbb{N}_{\geq 0}}$ satisfying the Assumption 3. The system matrices $A(q_k) \in \mathbb{R}^{n\times n}$ and $B(q_k) \in \mathbb{R}^{n\times m}$ are subject to stochastic parametric disturbance $q_k \in \mathbb{Q}$, which can enter nonlinearly under the following assumption on $A(q_k)$ and $B(q_k)$.

Assumption 5 (Stochastic Uncertainty)**.** *The uncertainties q_k, which belong to a compact polytope $\mathbb{Q} \subseteq \mathbb{R}^{n_q}$ for $k \in \mathbb{N}_{\geq 0}$, are realizations of iid multivariate real-valued, random variables Q_k. Let $\mathbb{G} = \{(A(q_k), B(q_k))\}_{q_k\in\mathbb{Q}}$, a polytopic outer approximation with N_c vertexes $\bar{\mathbb{G}} = co\{A^j, B^j\}_{j\in\mathbb{N}_1^{N_c}} \supseteq \mathbb{G}$ exists and is known.*

Unlike LQMPC and TRMPC schemes, the system state is subject to n individual chance-constraints of the form

$$\mathbb{P}\left\{[H_x]_\alpha x_{\ell|k} \leq [h_x]_\alpha\right\} \geq 1 - \varepsilon_\alpha, \ \ \forall\, \ell \in \mathbb{N}_{\geq 0},\, \alpha \in \mathbb{N}_1^n \tag{5.24}$$

with $\varepsilon_\alpha \in [0{,}1)$ representing the maximum probability of constraint violation allowed for each α-th state constraint. Moreover, $\mathbb{P}$ denotes the joint probability with respect to both uncertainty and disturbance sequences $\mathbf{q}_k$ and $\mathbf{w}_k$, where $\mathbf{q}_k \doteq \left\{q_{\ell|k}\right\}_{\ell\in\mathbb{N}_0^{T-1}}$ and $\mathbf{w}_k \doteq \left\{w_{\ell|k}\right\}_{\ell\in\mathbb{N}_0^{T-1}}$.

On the other hand, the control input u_k is subject to m hard constraints, given the typical nature of this constraint related to physical limitations of actuators. Thus,

$$H_u u_{\ell|k} \leq h_u, \ \ \forall\, \ell \in \mathbb{N}_{\geq 0}. \tag{5.25}$$

Then, let assume that a suitable terminal constraint set $\mathbb{X}_T$ and an asymptotically stabilizing control gain for the system (5.23) exist, partially retracing Assumption 2 exploited for both LQMPC and TRMPC.

Assumption 6 (Terminal set)**.** *There exists a terminal set $\mathbb{X}_T = \{x_k\, |H_T x_k \leq h_T\}$, which is robustly forward invariant for (5.23) under the (given) control law $u_k = Kx_k$. Given any $x_k \in \mathbb{X}_T$, the state and input constraints* (5.24) *and* (5.25)*, respectively, are satisfied and there exists $P \in \mathbb{R}^{n\times n}$ such that*

$$Q + K^T RK + \mathbb{E}[A_{cl}(q_k)^T PA_{cl}(q_k)] - P \preceq 0 \tag{5.26}$$

for all $q \in \mathbb{Q}$, with $A_{cl}(q_k) \doteq A(q_k) + B(q_k)K$.[2]

---

[2] $\mathbb{E}$ denotes the expected value of a random variable.

The control objective is to design a stabilizing receding horizon control, which guarantees constraint satisfaction and minimizes J_∞, the *expected* value of the following infinite horizon quadratic cost function

$$J_\infty = \sum_{\ell=0}^{\infty} \mathbb{E}\left\{ \|x_{\ell|k}\|_Q^2 + \|u_{\ell|k}\|_R^2 \right\}. \tag{5.27}$$

Following a dual-mode prediction scheme, based on a closed-loop paradigm as presented in [142], the design of the parametrized feedback policy is of the form

$$u_{\ell|k} = Kx_{\ell|k} + v_{\ell|k}, \tag{5.28}$$

where, for a given $x_{0|k} = x_k$, the sequence of correction terms $\mathbf{v}_k \doteq \left\{ v_{\ell|k} \right\}_{\ell \in \mathbb{N}_0^{T-1}}$ is determined by the OS-SMPC algorithm as the minimizer of the *expected* finite-horizon cost function

$$J_T(x_k, \mathbf{v}_k) = \mathbb{E}\left\{ \sum_{\ell=0}^{T-1} (x_{\ell|k}^T Q x_{\ell|k} + u_{\ell|k}^T R u_{\ell|k}) + x_{T|k}^T P x_{T|k} \right\}, \tag{5.29}$$

subject to the system dynamics (5.23) and state and input constraints, i.e. (5.24) and (5.25) respectively. Thus, for the following analysis, first equation (5.23) is explicitly solved with the pre-stabilizing input (5.28) for the predicted state $x_{1|k}, \ldots, x_{T|k}$ and predicted inputs $u_{0|k}, \ldots, u_{T-1|k}$. Thus, substituting (5.28) in (5.23)

$$x_{\ell+1|k} = A_{cl}(\mathbf{q}_k)x_{\ell|k} + B(\mathbf{q}_k)v_{\ell|k} + B_w w_{\ell|k}$$

- For $l = 0$,

$$x_{0|k} = x_k, \quad u_{0|k} = Kx_k + v_{0|k}.$$

- For $l = 1$,

$$x_{1|k} = A_{cl}(q_{0|k})x_k + B(q_{0|k})v_{0|k} + B_w w_{0|k}$$

$$u_{1|k} = Kx_{1|k} + v_{1|k} = K(A_{cl}(q_{0|k})x_k + B(q_{0|k})v_{0|k} + B_w w_{0|k}) + v_{1|k}$$

$$= KA_{cl}(q_{0|k})x_k + [KB(q_{0|k}) \ 1] \begin{bmatrix} v_{0|k} \\ v_{1|k} \end{bmatrix} + KB_w w_{0|k}.$$

- For $l = 2$,

$$\begin{aligned}
x_{2|k} &= A_{cl}(q_{1|k})x_{1|k} + B_{1|k}(q_{1|k})v_{1|k} + B_w w_{1|k} \\
&= A_{cl}(q_{1|k})A_{cl}(q_{0|k})x_k + [A_{cl}(q_{1|k})B(q_{0|k})\ \ B(q_{1|k})] \begin{bmatrix} v_{0|k} \\ v_{1|k} \end{bmatrix} + \\
&+ [A_{cl}(q_{1|k})B_w\ \ B_w] \begin{bmatrix} w_{0|k} \\ w_{1|k} \end{bmatrix} \\
u_{2|k} &= Kx_{2|k} + v_{2|k} = K(A_{cl}(q_{1|k})x_{1|k} + B_{1|k}(q_{1|k})v_{1|k} + B_w w_{1|k}) + v_{2|k} \\
&= KA_{cl}(q_{1|k})A_{cl}(q_{0|k})x_k + [KA_{cl}(q_{1|k})B(q_{0|k})\ \ KB(q_1|k)\ \ 1] \begin{bmatrix} v_{0|k} \\ v_{1|k} \\ v_{2|k} \end{bmatrix} + \\
&+ [KA_{cl}(q_{1|k})B_w\ \ KB_w] \begin{bmatrix} w_{0|k} \\ w_{1|k} \end{bmatrix}.
\end{aligned}$$

- $\dots$.

Thus, iterating the formulation, it results

$$x_{l|k}(\mathbf{q}_k, \mathbf{w}_k) = \Phi^0_{l|k}(\mathbf{q}_k)x_k + \Phi^v_{l|k}(\mathbf{q}_k)\mathbf{v}_k + \Phi^w_{l|k}(\mathbf{q}_k)\mathbf{w}_k \tag{5.33a}$$

$$u_{l|k}(\mathbf{q}_k, \mathbf{w}_k) = K\Phi^0_{l|k}(\mathbf{q}_k)x_k + [K\Phi^v_{l|k}(\mathbf{q}_k) + \Gamma_l]\mathbf{v}_k + K\Phi^w_{l|k}(\mathbf{q}_k)\mathbf{w}_k, \tag{5.33b}$$

where for $\ell = 0$ $\Phi^0_{0|k} = \mathbb{I}_n$, $\Phi^v_{0|k} = 0_{n\times mT}$ and $\Phi^w_{0|k} = 0_{n\times m_w T}$, whereas for $\ell \geq 1$

$$\Phi^0_{\ell|k}(\mathbf{q}_k) = A^{cl}(q_{\ell-1|k})A^{cl}(q_{\ell-2|k})\cdots A^{cl}(q_{0|k})$$

$$\Phi^v_{\ell|k}(\mathbf{q}_k) = \begin{bmatrix} A^{cl}(q_{\ell-1|k})\cdots A^{cl}(q_{1|k})B(q_{0|k}) \\ \vdots \\ B(q_{\ell-1|k}) \\ 0_{n\times(T-\ell)m} \end{bmatrix}^T$$

$$\Phi^w_{\ell|k}(\mathbf{q}_k) = \begin{bmatrix} A^{cl}(q_{\ell-1|k})\cdots A^{cl}(q_{1|k})B_w(q_{0|k}) \\ \vdots \\ B_w(q_{\ell-1|k}) \\ 0_{n\times(T-\ell)m_w} \end{bmatrix}^T,$$

while the matrix Γ_l

$$\Gamma_\ell = [0_{m\times \ell m}\ \ I_m\ \ 0_{m\times(T-\ell-1)m}],$$

allows to select the ℓ-th entry in the stack vector $\mathbf{v}_k$. Last, it is possible to combine all the previous transfer matrices as

$$\Phi_T(\mathbf{q}_k) \ \doteq\ \begin{bmatrix} \Phi^0_{0|k}(\mathbf{q}_k) & \Phi^v_{0|k}(\mathbf{q}_k) & \Phi^w_{0|k}(\mathbf{q}_k) \\ \vdots & \vdots & \vdots \\ \Phi^0_{T|k}(\mathbf{q}_k) & \Phi^v_{T|k}(\mathbf{q}_k) & \Phi^w_{T|k}(\mathbf{q}_k) \end{bmatrix}.$$

Given the solution (5.33), the expected value of the finite-horizon cost function (5.29) can be evaluated *offline*, leading to a quadratic cost function of the form

$$J_T(x_k, \mathbf{v}_k) = [x_k^T\ \mathbf{v}_k^T\ \mathbf{1}^T_{m_w}]\tilde{S}\begin{bmatrix} x_k \\ \mathbf{v}_k \\ \mathbf{1}_{m_w}\end{bmatrix} \tag{5.34}$$

in the deterministic variables x_k and $\mathbf{v}_k$. The evaluation of $\tilde{S}$ requires the computation of an expected value, which can be explicitly evaluated or sufficiently exact approximated taking random samples of the sequences $\mathbf{q}_k$ and $\mathbf{w}_k$. In particular, considering $\bar{Q} = \mathbb{I}_T \otimes Q$, $\bar{R} = \mathbb{I}_T \otimes R$, $\bar{K} = \mathbb{I}_T \otimes K$, and defining $\Gamma = [0_{mT\times n}\ \mathbb{I}_{mT}\ 0_{mT\times m_w T}]$, the two terms, Q_E and R_E of the explicit cost matrix $\tilde{S}$

$$\tilde{S} = \mathbb{E}\left\{(Q_E + R_E)\right\}, \tag{5.35}$$

can be derived as follows. First, for $\ell \in [0, T-1]$

$$\begin{aligned}
\|x_{\ell|k}\|^2_{barQ} &= (\Phi^0_{\ell|k}x_k + \Phi^v_{\ell|k}v_{\ell|k} + \Phi^w_{\ell|k}w_{\ell|k})^T Q (\Phi^0_{\ell|k}x_k + \Phi^v_{\ell|k}v_{\ell|k} + \Phi^w_{\ell|k}w_{\ell|k}) \\
&= \left(\Phi_T(\mathbf{q}_k)\begin{bmatrix} x_k \\ \mathbf{v}_k \\ \mathbf{w}_k\end{bmatrix}\right)^T \bar{Q}\left(\Phi_T(\mathbf{q}_k)\begin{bmatrix} x_k \\ \mathbf{v}_k \\ \mathbf{w}_k\end{bmatrix}\right) \\
&= \left(\Phi_T(\mathbf{q}_k)\begin{bmatrix} \mathbb{I}_n & 0 & 0 \\ * & \mathbb{I}_{mT} & 0 \\ * & * & \mathbf{w}_k\end{bmatrix}\begin{bmatrix} x_k \\ \mathbf{v}_k \\ \mathbf{1}_{m_w}\end{bmatrix}\right)^T \bar{Q}\left(\Phi_T(\mathbf{q}_k)\begin{bmatrix} \mathbb{I}_n & 0 & 0 \\ * & \mathbb{I}_{mT} & 0 \\ * & * & \mathbf{w}_k\end{bmatrix}\begin{bmatrix} x_k \\ \mathbf{v}_k \\ \mathbf{1}_{m_w}\end{bmatrix}\right) \\
&= \left(\Phi_T(\mathbf{q}_k)M\begin{bmatrix} x_k \\ \mathbf{v}_k \\ \mathbf{1}_{m_w}\end{bmatrix}\right)^T \bar{Q}\left(\Phi_T(\mathbf{q}_k)M\begin{bmatrix} x_k \\ \mathbf{v}_k \\ \mathbf{1}_{m_w}\end{bmatrix}\right) \\
&= \left(\begin{bmatrix} x_k & \mathbf{v}_k & \mathbf{1}_{m_w}\end{bmatrix} M^T\Phi_T^T(\mathbf{q}_k)\right)\bar{Q}\left(\Phi_T(\mathbf{q}_k)M\begin{bmatrix} x_k \\ \mathbf{v}_k \\ \mathbf{1}_{m_w}\end{bmatrix}\right) \\
&= \begin{bmatrix} x_k & \mathbf{v}_k & \mathbf{1}_{m_w}\end{bmatrix}\tilde{Q}\begin{bmatrix} x_k \\ \mathbf{v}_k \\ \mathbf{1}_{m_w}\end{bmatrix}.
\end{aligned}$$

Then, for $\ell = T$, $\|x_{T|k}\|_P$ and

$$
\begin{aligned}
&\Big(\begin{bmatrix} x_k & \mathbf{v}_k & \mathbf{1}_{m_w} \end{bmatrix} M^T \Phi_T^T(\mathbf{q}_k) \Big) \begin{bmatrix} \bar{Q} & 0_{nT\times n} \\ 0_{n\times nT} & P \end{bmatrix} \left(\Phi_T(\mathbf{q}_k) M \begin{bmatrix} x_k \\ \mathbf{v}_k \\ \mathbf{1}_{m_w} \end{bmatrix} \right) \\
&= \begin{bmatrix} x_k & \mathbf{v}_k & \mathbf{1}_{m_w} \end{bmatrix} Q_E \begin{bmatrix} x_k \\ \mathbf{v}_k \\ \mathbf{1}_{m_w} \end{bmatrix}.
\end{aligned}
$$

Last,

$$
\begin{aligned}
\|u_{\ell|k}\|_R^2 &= \Big(\bar{K}\Phi^0_{\ell|k} x_k + [\bar{K}\Phi^v_{\ell|k} + \Gamma_l]\mathbf{v}_k + \bar{K}\Phi^w_{\ell|k}\mathbf{w}_k \Big)^T \bar{R} \Big(* \Big) \\
&= \left([\bar{K}\Phi_T(\mathbf{q}_k) + \Gamma] M \begin{bmatrix} x_k \\ \mathbf{v}_k \\ \mathbf{1}_{m_w} \end{bmatrix} \right)^T \bar{R} \left([\bar{K}\Phi_T(\mathbf{q}_k) + \Gamma] M \begin{bmatrix} x_k \\ \mathbf{v}_k \\ \mathbf{1}_{m_w} \end{bmatrix} \right) \\
&= \begin{bmatrix} x_k & \mathbf{v}_k & \mathbf{1}_{m_w} \end{bmatrix} M^T [\bar{K}\Phi_T(\mathbf{q}_k) + \Gamma]^T \bar{R} \left([\bar{K}\Phi_T(\mathbf{q}_k) + \Gamma] M \begin{bmatrix} x_k \\ \mathbf{v}_k \\ \mathbf{1}_{m_w} \end{bmatrix} \right) \\
&= \begin{bmatrix} x_k & \mathbf{v}_k & \mathbf{1}_{m_w} \end{bmatrix} R_E \begin{bmatrix} x_k \\ \mathbf{v}_k \\ \mathbf{1}_{m_w} \end{bmatrix}.
\end{aligned}
$$

Thus,

$$
\begin{aligned}
Q_E &= M^T \Phi_T^T(\mathbf{q}_k) \begin{bmatrix} \bar{Q} & 0_{nT\times n} \\ 0_{n\times nT} & P \end{bmatrix} \Phi_T(\mathbf{q}_k) M \\
\\
R_E &= M^T [\bar{K}\Phi_T(\mathbf{q}_k) + \Gamma]^T \bar{R} [\bar{K}\Phi_T(\mathbf{q}_k) + \Gamma] M,
\end{aligned}
$$

where the matrix M is

$$
M = \begin{bmatrix} \mathbb{I}_n & 0_{n\times mT} & 0_{n\times nT} \\ 0_{mT\times n} & \mathbb{I}_{mT} & 0_{mT\times nT} \\ 0_{m_w T\times n} & 0_{m_w T\times mT} & \mathbf{w}_k \mathbb{I}_{m_w T} \end{bmatrix}.
$$

It is important to highlight that, as discussed in [164], matrix $\tilde{S}$ may be approximated via random sampling by exploiting classical Monte Carlo or Quasi Monte Carlo tools, as those presented in e.g. [173].

For the constraints design, instead of directly evaluating the chance constraints in (5.24), the sampling-based approach proposed by [174] and [155] has been exploited, which basic idea is to compute a finite-horizon optimal input trajectory

$v_{0|k}, \ldots, v_{T-1|k}$ that results feasible under a pre-defined number of sampled scenarios of the uncertainty, properly selected in order to attain the desired properties of the controller, as firstly proposed in [175]. In particular, properly choosing the number of samples it is possible to design an inner approximation of the chance constraints with confidence $1-\delta$ such that each *feasible* solution to the finite horizon scenario program satisfies the initial chance constraints.

Thus, following the approach presented in [162], an inner approximation for the chance constraints in (5.24) can be derived in the form of linear constraints on x_k, $\mathbf{v}_k$ and $\mathbf{w}_k$. Indeed, for each α-th probabilistic state constraint and for each time step $\ell \in \mathbb{N}_0^{T-1}$, the corresponding chance-constrained set can be defined as follows

$$\mathbb{X}_\ell^{P,\alpha} = \Big\{x_k, \mathbf{v}_k \mid \mathbb{P}\Big\{[H_x]_\alpha x_{\ell|k}(\mathbf{q}_k, \mathbf{w}_k) \leq [h_x]_\alpha\Big\} \geq 1 - \varepsilon_\alpha\Big\}, \tag{5.37}$$

where the apex P indicates the probabilistic nature of the set. Then, exploiting the results inherited from the statistical learning theory, as thoroughly described in [176], an estimate of $\mathbb{X}_\ell^{P,\alpha}$ may be constructed extracting N_ℓ^x iid sample sequences $\mathbf{q}^{(i_\ell^x)}$ and $\mathbf{w}^{(i_\ell^x)}$, with $i_\ell^x \in \mathbb{N}_1^{N_\ell^x}$, and building the corresponding *sampled* state constraint set

$$\mathbb{X}_\ell^{S,\alpha} = \Big\{x_k, \mathbf{v}_k \mid [H_x]_\alpha x_{\ell|k}(\mathbf{q}^{(i_\ell^x)}, \mathbf{w}^{(i_\ell^x)}) \leq [h_x]_\alpha, i_\ell^x \in \mathbb{N}_1^{N_\ell^x}\Big\}, \tag{5.38}$$

for $\ell \in \mathbb{N}_0^{T-1}$. In this case, the apex S is used to indicate that the set is obtained as outcome of a sampling process.

To provide the controller with the desired properties in terms of maximum constraint violation allowed, i.e. ε_α, and confidence level δ, the minimum number of samples to draw $\tilde{N}(n,\varepsilon,\delta)$ shall be properly defined. Indeed, it has been proved in [162] that for any $\varepsilon \in (0,0.14)$ and $\delta \in (0,1)$ if the number of drawn samples N_s is selected such that

$$N_s \geq \tilde{N}(n,\varepsilon,\delta) = \frac{4.1}{\varepsilon}\Big(\ln\frac{21.64}{\delta} + 4.39n\log_2\Big(\frac{8\mathrm{e}}{\varepsilon}\Big)\Big) \tag{5.39}$$

than it holds

$$\mathbb{P}^{N_s}\Big\{\mathbb{C}^S \subseteq \mathbb{C}^P\Big\} \geq 1 - \delta, \tag{5.40}$$

where $\mathbb{C}^P$ is a generic chance constraint set and $\mathbb{C}^S$ is the corresponding sample constraint set.

Hence, the choice $N_\ell^x \geq \tilde{N}(n + \ell m, \varepsilon_\alpha, \delta)$ guarantees that $\mathbb{X}_\ell^{S,\alpha} \subseteq \mathbb{X}_\ell^{P,\alpha}$ with probability greater than $1-\delta$. Hence, we obtain that $x_{\ell|k} \in \mathbb{X}_\ell^{S,\alpha}$ is guaranteed with high probability whenever $x_{\ell|k}$ satisfies the following set of linear constraints

$$H_x x_{\ell|k}(\mathbf{q}^{(i_\ell^x)}, \mathbf{w}^{(i_\ell^x)}) \leq h_x, \quad \text{for } i_\ell^x \in \mathbb{N}_1^{N_\ell^x}. \tag{5.41}$$

Moreover, substituting (5.33a) in (5.41), it results

$$H_x\Phi^0_{l|k}(\mathbf{q}^{(i^x_\ell)})x_k + \Phi^v_{l|k}(\mathbf{q}^{(i^x_\ell)})\mathbf{v}_k + \Phi^w_{l|k}(\mathbf{q}^{(i^x_\ell)})\mathbf{w}_k^{(i^x_\ell)} \le h_x$$

$$H_x\Phi^0_{l|k}(\mathbf{q}^{(i^x_\ell)})x_k + H_x\Phi^v_{l|k}(\mathbf{q}^{(i^x_\ell)})\mathbf{v}_k + H_x\Phi^w_{l|k}(\mathbf{q}^{(i^x_\ell)})\mathbf{w}_k^{(i^x_\ell)} \le h_x$$

$$[H_x\Phi^0_{l|k}(\mathbf{q}^{(i^x_\ell)})\ H_x\Phi^v_{l|k}(\mathbf{q}^{(i^x_\ell)})] \begin{bmatrix} x_k \\ \mathbf{v}_k \end{bmatrix} \le h_x - H_x\Phi^w_{l|k}(\mathbf{q}^{(i^x_\ell)})\mathbf{w}_k^{(i^x_\ell)}.$$

Note that, from (5.33a), the above equations rewrite as the following linear constraint in x_k, $\mathbf{v}_k$

$$\begin{bmatrix} \tilde{H}^x_x & \tilde{H}^u_x \end{bmatrix} \begin{bmatrix} x_k \\ \mathbf{v}_k \end{bmatrix} \le \tilde{h}_x \tag{5.43}$$

where

$$[\tilde{H}^x_x\ \tilde{H}^u_x] = \begin{bmatrix} H_x\Phi^0_{0|k}(\mathbf{q}^{(1)}) & H_x\Phi^v_{0|k}(\mathbf{q}^{(1)}) \\ \vdots & \vdots \\ H_x\Phi^0_{0|k}(\mathbf{q}^{(N^x_0)}) & H_x\Phi^v_{0|k}(\mathbf{q}^{(N^x_0)}) \\ \vdots & \vdots \\ H_x\Phi^0_{T-1|k}(\mathbf{q}^{(1)}) & H_x\Phi^v_{T-1|k}(q^{(1)}) \\ \vdots & \vdots \\ H_x\Phi^0_{T-1|k}(\mathbf{q}^{(N^x_{T-1})}) & H_x\Phi^v_{T-1|k}(\mathbf{q}^{(N^x_{T-1})}) \end{bmatrix}, \tag{5.44a}$$

$$\tilde{h}_x = \begin{bmatrix} h_x - H_x\Phi^w_{0|k}(\mathbf{q}^{(1)})\mathbf{w}_k^{(1)} \\ \vdots \\ h_x - H_x\Phi^w_{0|k}(\mathbf{q}^{(N^x_0)})\mathbf{w}_k^{(N^x_0)} \\ \vdots \\ h_x - H_x\Phi^w_{T-1|k}(\mathbf{q}^{(1)})\mathbf{w}_k^{(1)} \\ \vdots \\ h_x - H_x\Phi^w_{T-1|k}(\mathbf{q}^{(N^x_{T-1})})\mathbf{w}_k^{(N^x_{T-1})} \end{bmatrix}. \tag{5.44b}$$

Note that the total number of samples to be drawn to construct the sampled constraint sets (5.43) is equal to $N^x \doteq \sum_{\ell=0}^{T-1} N^x_\ell$, and thus the total number of linear inequalities will be nN^x. On the other hand, these sets can be be computed *offline*.

In a similar way, the hard input constraints can be approximated by introducing a suitable sampled approximation. To this end, for given probabilistic level $\varepsilon_\beta \in (0,0.14)$ for each $\beta \in \mathbb{N}^m_1$, $N^u_\ell \ge \tilde{N}(n + \ell m, \varepsilon_\beta, \delta)$ random samples are drawn and the following sampled input constraint set is built as

$$\mathbb{U}_\ell^{S,\beta} = \left\{ x_k, \mathbf{v}_k \mid [H_u]_\beta u_{\ell|k}(\mathbf{q}^{i_u}, \mathbf{w}^{(i_u)}) \le h_u, \quad i_u \in \mathbb{N}_1^{N_\ell^u} \right\} \tag{5.45}$$

for $\ell \in \mathbb{N}_0^{T-1}$, thus obtaining the N_ℓ^u linear constraints

$$H_u u_{l|k}(\mathbf{q}^{(i_u)}, \mathbf{w}^{(i_u)}) \le h_u$$

$$H_u(K\Phi_{l|k}^0(\mathbf{q}^{(i_j)})x_k + (K\Phi_{l|k}^v(\mathbf{q}^{(i_j)}) + \Gamma_l)\mathbf{v}_k + K\Phi_{l|k}^w(\mathbf{q}^{(i_j)})\mathbf{w}_k^{(i_u)}) \le h_u$$

$$H_u K\Phi_{l|k}^0(\mathbf{q}^{(i_j)})x_k + H_u(K\Phi_{l|k}^v(\mathbf{q}^{(i_j)}) + \Gamma_l)\mathbf{v}_k + H_u K\Phi_{l|k}^w(\mathbf{q}^{(i_j)})\mathbf{w}_k^{(i_u)} \le h_u$$

$$[H_u K\Phi_{l|k}^0(\mathbf{q}^{(i_j)}) \; H_u(K\Phi_{l|k}^v(\mathbf{q}^{(i_j)}) + \Gamma_l)] \begin{bmatrix} x_k \\ \mathbf{v}_k \end{bmatrix} \le h_u - H_u K\Phi_{l|k}^w(\mathbf{q}^{(i_j)})\mathbf{w}_k^{(i_u)}$$

$$H_u(K\Phi_{l|k}^v(\mathbf{q}^{(i_j)}) + \Gamma_l)\mathbf{v}_k \le h_u - H_u K\Phi_{l|k}^w(\mathbf{q}^{(i_j)})\mathbf{w}_k^{(i_u)} - H_u K\Phi_{l|k}^0(\mathbf{q}^{(i_j)})x_k$$

which, from (5.33b), rewrites as the following linear constraint in x_k, $\mathbf{v}_k$

$$\begin{bmatrix} \tilde{H}_u^x & \tilde{H}_u^u \end{bmatrix} \begin{bmatrix} x_k \\ \mathbf{v}_k \end{bmatrix} \le \tilde{h}_u. \tag{5.47}$$

where $\tilde{H}_u^x$ and $\tilde{H}_u^u$ are defined analogously to (5.44), and involve $N^u \doteq \sum_{\ell=1}^{T-1} N_\ell^u$ samples.

Finally, for each $\gamma \in \mathbb{N}_1^n$, $\varepsilon_\gamma \in (0,0.14)$, the terminal constraints can also be approximated by drawing $N_T \ge \tilde{N}(n+Tm, \varepsilon_\gamma, \delta)$ random samples and constructing the sets

$$\mathbb{X}_T^{S,\gamma} = \left\{ x_k, \mathbf{v}_k \mid [H_T]_\gamma x_{T|k}(\mathbf{q}^{i_T}, \mathbf{w}^{(i_T)}) \le h_T, \quad i_T \in \mathbb{N}_1^{N_T} \right\} \tag{5.48}$$

for $i_T \in \mathbb{N}_1^{N_T}$, which lead to

$$H_T x_{T|k}(\mathbf{q}^{(i_T)}, \mathbf{w}^{(i_T)}) \le h_T$$

$$H_T(\Phi_{T|k}^0(\mathbf{q}^{(i_T)})x_k + \Phi_{T|k}^v(\mathbf{q}^{(i_T)})\mathbf{v}_k + \Phi_{T|k}^w(\mathbf{q}^{(i_T)})\mathbf{w}_k^{(i_T)}) \le h_T$$

$$H_T\Phi_{T|k}^0(\mathbf{q}^{(i_T)})x_k + H_T\Phi_{T|k}^v(\mathbf{q}^{(i_T)})\mathbf{v}_k + H_T\Phi_{T|k}^w(\mathbf{q}^{(i_T)})\mathbf{w}_k^{(i_T)} \le h_T$$

$$[H_T\Phi_{T|k}^0(\mathbf{q}^{(i_T)}) \; H_T\Phi_{T|k}^v(\mathbf{q}^{(i_T)})] \begin{bmatrix} x_k \\ \mathbf{v}_k \end{bmatrix} \le h_T - H_T\Phi_{T|k}^w(\mathbf{q}^{(i_T)})\mathbf{w}_k^{(i_T)}$$

$$H_T\Phi_{T|k}^v(\mathbf{q}^{(i_j)})\mathbf{v}_k \le h_T - H_T\Phi_{T|k}^w(\mathbf{q}^{(i_j)})\mathbf{w}_k^{(i_j)} - H_T\Phi_{T|k}^0(\mathbf{q}^{(i_j)})x_k$$

that through (5.33a),

$$\begin{bmatrix} \tilde{H}_T^x & \tilde{H}_T^u \end{bmatrix} \begin{bmatrix} x_k \\ \mathbf{v}_k \end{bmatrix} \leq \tilde{h}_T \tag{5.50}$$

where $\tilde{H}_T^x$ and $\tilde{H}_T^u$ involve N^T samples.

The linear constraints (5.43), (5.47), (5.50) can be summarized in the following linear constraint set

$$\begin{aligned} \mathbb{D} &= \left\{ x_k, \mathbf{v}_k \ \mid \ \begin{bmatrix} \tilde{H}_x^x & \tilde{H}_x^u \\ \tilde{H}_T^x & \tilde{H}_T^u \\ \tilde{H}_u^x & \tilde{H}_u^u \end{bmatrix} \begin{bmatrix} x_k \\ \mathbf{v}_k \end{bmatrix} \leq \begin{bmatrix} \tilde{h}_x \\ \tilde{h}_T \\ \tilde{h}_u \end{bmatrix} \right\} \\ &= \left\{ x_k, \mathbf{v}_k \ \mid \ \tilde{H} \begin{bmatrix} x_k \\ \mathbf{v}_k \end{bmatrix} \leq \tilde{h} \right\}. \end{aligned} \tag{5.51}$$

It is also possible to notice that, due to the sampling procedure, these linear constraints are in general highly redundant. To cope with this issue, a suitable algorithm for redundant constraints removal is proposed hereafter following the guidelines provided in [164], which can be applied to further simplify the sampled constraint sets.

```
begin
$Hx \leq h$ with $H \in \mathbb{R}^{n_c \times n}$ and $h \in \mathbb{R}^{n_c}$
while $i \leq n_c$ do
    solve
        $h_i^* = \max_x [H]_i x$
        $\text{s.t.} [H]_k x \leq [h]_k, \quad \forall k \in \mathbb{N}_1^{n_c}\ i$
    if $h_i^* \leq [h]_i$ then
        $H \leftarrow H\ [H]_i$
        $h \leftarrow h\ [h]_i$
        $n_c = n_c - 1$
    else
        $i = i + 1$
    end if
end while
return $H$, $h$.
end
```

Moreover, in accordance with the the results shown in [164], a first step constraint is added to (5.51), defined starting from the set

$$\mathbb{C}_T = \left\{ \begin{bmatrix} x_k \\ v_{0|k} \end{bmatrix} \in \mathbb{R}^{n+m} \ \middle| \begin{matrix} \exists v_{1|k}, \cdots, v_{T-1|k} \in \mathbb{R}^n, \\ s.t. \ (x_k, \mathbf{v}_k) \in \mathbb{D} \end{matrix} \right\} \tag{5.53}$$

which defines the set of feasible states and first inputs of the scenario program with given fixed samples. Therefore, it is possible to define $\mathbb{C}^{\infty}_{T,x} = \{x_k \mid H_\infty x_k \leq h_\infty\}$ as the (maximal) robust control invariant set for the system (5.23) with $(x_k, u_k) \in \mathbb{C}_T$. Finally, in order to ensure robust recursive feasibility, a constraint on the first input is added to (5.51) and the additional constraint set is given by

$$\mathbb{D}_R = \left\{x_k, \mathbf{v}_k \mid H_\infty A^j_{cl} x_k + H_\infty B^j v_{0|k} \leq h_\infty - H_\infty B^j_w w_{0|k}\right\} \tag{5.54}$$

with A^j, B^j, B^j_w from Assumption 5 and $A^j_{cl} = A^j + B^j K$. The final set of linear constraints to be employed in online implementation is thus given by the intersection of the sets $\mathbb{D}$ and $\mathbb{D}_R$, defined in (5.51) and (5.54) respectively. It is important to highlight that the final set of constraints can also benefit from a further redundant constraint reduction process.

5.4.1 SMPC Algorithm Based on Offline Sampling

As anticipated in the previous Sections, the complete OS-SMPC algorithm can be split into two parts: (i) an *offline* step, which comprises the samples generation and the computation of the ensuing sets, properly reduced to sale down the size of the final problem removing the redundant constraints, and (ii) a repeated *online* optimization. While the first step may be rather costly, the online implementation only involves the solution of quadratic programs, which may be carried out in a very efficient way. A detailed description of the OS-SMPC scheme is reported next.

OS-SMPC Algorithm

OFFLINE. *Before running the online control* algorithm:

1. *Compute the finite-horizon cost matrix* $\tilde{S}$ *in* (5.34).
2. *Draw a sufficiently large number of samples to determine the sampled constraints* $\mathbb{X}^{S,\alpha}_\ell$, $\mathbb{U}^{S,\beta}_\ell$, *and* $\mathbb{X}^{S,\gamma}_T$, *defined respectively in (5.43), (5.47), (5.50).*
3. *Get* $\mathbb{D}$ *in* (5.51) *and remove redundant constraints.*
4. *Determine the first step constraint set* $\mathbb{D}_\mathbb{R}$ *in* (5.54).
5. Intersect $\mathbb{D}$ and $\mathbb{D}_\mathbb{R}$ and possibly remove additional redundant constraints.

ONLINE. *At each time step k:*

1. *Measure the current state* x_k;

2. *Determine the minimizer* $\mathbf{v}_k^*$ *of the finite-horizon quadratic cost function (5.34) subject to the pre-computed linear constraints* $\mathbb{D}$ *and* $\mathbb{D}_{\mathbb{R}}$

$$\mathbf{v}_k^* = \arg \min_{\mathbf{v}_k} [x_k \ \mathbf{v}_k \ \mathbf{1}_{m_w}]\tilde{S} \begin{bmatrix} x_k \\ \mathbf{v}_k \\ \mathbf{1}_{m_w} \end{bmatrix} \tag{5.55a}$$

$$\text{s.t. } (x_k, \mathbf{v}_k) \in \mathbb{D} \cap \mathbb{D}_R; \tag{5.55b}$$

3. *Apply the control input*

$$u_k = Kx_k + v_{0|k}^*,$$

where $v_{0|k}^*$ *is the first control action of the optimal sequence* $\mathbf{v}_k^*$.

5.4.2 Theoretical Guarantees of OS-SMPC

First, it is shown that the introduction of the first step constraint $\mathbb{D}_R$ allows to prove recursive feasibility of the OS-SMPC scheme.

Proposition 1 (Recursive Feasibility)**.** *The closed loop renders the set* $\mathbb{D} \cap \mathbb{D}_R$ *forward invariant. In particular, let* $\mathbb{V}(x_k) = \left\{ \boldsymbol{v}_k \in \mathbb{R}^{mT} \mid (x_k, \boldsymbol{v}_k) \in \mathbb{D} \cap \mathbb{D}_R \right\}$*. If* $\boldsymbol{v}_k \in \mathbb{V}(x_k)$*, then, for every realization* q_k *and* w_k*, and* $x_{k+1} = A_{cl}(q_k)x_k + B(q_k)v_{0|k} + B_w(q_k)w_{0|k}$*, the OS-SMPC guarantees*

$$\mathbb{V}(x_{k+1}) \neq \emptyset.$$

Proof The proof follows similar lines to the one provided in [164], and is briefly recalled hereafter. From $(x_k, \mathbf{v}_k) \in \mathbb{D}_R$ it follows $x_{k+1} \in \mathbb{C}_{T,x}^{\infty}$ robustly. Then, $\mathbb{C}_{T,x}^{\infty} \subset \{x \,|\, \mathbb{V}(x) \neq \emptyset\}$, by construction, which proves the claim. □

The previous proposition, besides showing how the OS-SMPC algorithm guarantees recursive feasibility, it is also instrumental in proving that the control input returned by the algorithm guarantees satisfaction of the chance-constraints on the state and hard constraints on the input defined in (5.24) and (5.25).

Proposition 2 (Constraint Satisfaction)**.** *If* $x_0 \in \mathbb{C}_{T,x}^{\infty}$*, then the closed-loop system under the OS-SMPC control law, for all* $k \geq 1$*, satisfies each probabilistic state constraint (5.24) with confidence* $(1-\delta)$*, and the hard input constraint (5.25) robustly.*

Proof Since the OS-SMPC algorithm is robustly recursively feasible (Proposition 1), hard input constraint satisfaction is guaranteed, because of $H_u u_{0|k} \leq h_u$, which does not rely on sampling. On the other hand, for all $j = 1, \ldots, p$, we have $\mathbb{D} \subseteq \mathbb{X}_1^{S,j}$. Hence, by Proposition 1, for all feasible $(x_k, \mathbf{v}_k) \in \mathbb{D}$, we can ensure with confidence $(1-\delta)$ that the chance constraint (5.24) is satisfied. $\square$

Finally, the convergence properties of the proposed scheme are analyzed but first it is important to remark that, since additive disturbances affect the system at every time instant, the closed-loop system cannot be asymptotically stable at the origin. On the other hand, it is possible to show that, under persistent noise excitation, the closed-loop state at time $k+1$ does remain bounded even if the candidate solution, i.e. the previously planned trajectory, may not remain feasible with given probability. First, let formally define the candidate solution as follows.

Definition 7 (Candidate Solution)**.** *Given the OS-SMPC optimization problem in* (5.55) *and a feasible solution* $v_{T|k}$ *at time k, the candidate solution* $\tilde{v}_{\ell|k+1}$ *at time k+1 is defined as*

$$\tilde{v}_{\ell|k+1} = \begin{cases} v_{\ell+1|k} + KA_{cl}^{\ell}B_w w_k, & \ell = 0,\dots,T-2 \\ KA_{cl}^{\ell}B_w w_k, & \ell = T-1 \end{cases}.$$

Then, under the following assumption, it is possible to prove that the cost increase is bounded if the candidate solution does not remain feasible for a given probability.

Assumption 7 (Bounded Optimal Value Function)**.** *Let* $V_T(x_k)$ *be the optimal value function of the quadratic program (5.55), and let* P_ℓ, $P_u \in \mathbb{R}^{n\times n}$, $P_\ell \succ 0$, $P_u \succ 0$, $c \in \mathbb{R}$ *be such that* $x_k^T P_\ell x_k \le V_T(x_k) - c \le x_k^T P_u x_k$ *holds for all* $x_k \in \mathbb{C}_{T,x}^{\infty}$.

Then it is possible to state the main result of this section, i.e. the asymptotic average stage cost converges to a steady-state value, which is finite. Indeed, due to the presence of additive disturbance, the system does not asymptotically converge to the origin but it remain in its neighborhood, "oscillating" with a bounded variance, as proved in the following Proposition.

Proposition 3 (Asymptotic Bound)**.** *Let* $\varepsilon_f = [0,1)$ *be the maximum probability that the previously planned trajectory is not feasible. Then, there exists a constant* $C = C(\varepsilon_f)$ *such that*

$$\lim_{t\to\infty} \frac{1}{t}\sum_{k=0}^{t} \mathbb{E}\left\{\|x_k\|_2^2\right\} \le C. \tag{5.56}$$

Remark 1. *The probability* ϵ_f *is a problem-dependent parameter related to the maximum probability that the previously planned trajectory does not remain feasible. In this approach,* ϵ_f *can only be evaluated a posteriori and depends on the application and indirectly on the chosen allowed probability of constraint violation. However, similar to the approach discussed in [164], the constraint tightening could be modified to guarantee an user-chosen bound on* ϵ_f.

Proof If the candidate solution does not remain feasible, the cost increase can be bounded through the matrices in Assumption 7. Let $V_T(x_k) = J_T(x_k, \mathbf{v}_k^*)$ be the optimal value of (5.55) at time k and consider the optimal value function of the online optimization program as stochastic Lyapunov function. Hence, if the candidate solution $\tilde{\mathbf{v}}$ remains feasible, it results

$$\mathbb{E}\left\{V_T(x_{k+1}) \mid x_k,\ \tilde{\mathbf{v}}_{k+1} \text{ feasible}\right\} - V_T(x_k) \le \mathbb{E}\left\{J_T(x_{k+1}, \tilde{\mathbf{v}}_{k+1}) \mid x_k\ \right\} - V_T(x_k)$$

$$\le \mathbb{E}\left\{\sum_{l=0}^{T-1}(\|\tilde{x}_{\ell|k+1}\|_Q^2 + \|\tilde{u}_{\ell|k+1}\|_R^2) + \|\tilde{x}_{T|k+1}\|_P^2\right\} - \mathbb{E}\left\{\sum_{l=0}^{T-1}(\|x^*_{\ell|k}\|_Q^2 + \|u^*_{\ell|k}\|_R^2) + \|x^*_{T|k}\|_P^2\right\}$$

$$= \mathbb{E}\left\{\|x^*_{T|k}\|_Q^2 + \|u^*_{T|k}\|_R^2 + \|x^*_{T+1|k}\|_P^2 - \|x^*_{0|k}\|_Q^2 - \|u^*_{0|k}\|_R^2 - \|x^*_{T|k}\|_P^2\right\}$$

$$= \mathbb{E}\left\{\|x^*_{T|k}\|_Q^2 + \|u^*_{T|k}\|_R^2 + \|A(q_k)x^*_{T|k} + B(q_k)u^*_{T|k} + B_w w^*_{T|k}\|_P^2\right.$$

$$\left.- \|x^*_{0|k}\|_Q^2 - \|u^*_{0|k}\|_R^2 - \|x^*_{T|k}\|_P^2\ \right\}$$

$$= \mathbb{E}\left\{\|x^*_{T|k}\|^2_{Q+K^TRK-P} + \|A_{cl}(q_k)x^*_{T|k} + B_w(q_k)w_{T|k}\|_P^2 - \|x^*_{0|k}\|_Q^2 - \|u^*_{0|k}\|_R^2\right\}$$

$$\le \mathbb{E}\left\{\|x^*_{T|k}\|^2_{Q+K^TRK-P} + \|A_{cl}(q_k)x^*_{T|k}\|_P^2 + \|B_w(q_k)w_{T|k}\|_P^2 + \right.$$

$$\left.+\ 2(A_{cl}(q_k)x^*_{T|k})^T P(B_w(q_k)w_{T|k}) - \|x^*_{0|k}\|_Q^2 - \|u^*_{0|k}\|_R^2\ \right\}$$

$$\le \mathbb{E}\left\{\|x^*_{T|k}\|^2_{Q+K^TRK-P} + \|A_{cl}(q_k)x^*_{T|k}\|_P^2 + \|B_w w^*_{T|k}\|_P^2\right.$$

$$\left.+\ 2(A_{cl}(q_k)x^*_{T|k})^T P(B_w w^*_{T|k}) - \|x^*_{0|k}\|_Q^2 - \|u^*_{0|k}\|_R^2\ \right\}$$

$$= \mathbb{E}\left\{\|x^*_{T|k}\|^2_{Q+K^TRK-P} + \|A_{cl}(q_k)x^*_{T|k}\|_P^2 + \|B_w w^*_{T|k}\|_P^2 - \|x^*_{0|k}\|_Q^2 - \|u^*_{0|k}\|_R^2\right\}.$$

According to the definition of the terminal set (Assumption 6), one obtains

$$\mathbb{E}\left\{\|x^*_{T|k}\|^2_{Q+K^TRK-P+A_{cl}(q_k)^TPA_{cl}(q_k)} + \|B_w(q_k)w_{T|k}\|_P^2 - \|x^*_{0|k}\|_Q^2 - \|u^*_{0|k}\|_R^2\right\}$$

$$\le \mathbb{E}\left\{\|B_w(q_k)w_{T|k}\|_P^2 - \|x^*_{0|k}\|_Q^2 - \|u^*_{0|k}\|_R^2\right\} \le \mathbb{E}\left\{\|B_w(q_k)w_{T|k}\|_P^2\right\} - \|x_k\|_Q^2 - \|u_k\|_R^2.$$

On the other hand, if the candidate solution is not feasible, it follows that

$$\mathbb{E}\Big\{V_T(x_{k+1})\,|\,x_k, \tilde{\mathbf{v}}_{T|k+1} \text{ not feasible}\Big\} - V_T(x_k)$$

$$= \max_{(A(q_k),B(q_k))\in\mathbb{G},\, w\in\mathbb{W}} \|A_{cl}(q_k)x_k + B(q_k)v_k + B_w w_k\|^2_{P_u} - \|x_k\|^2_{P_l}$$

$$\leq \max_{\substack{w\in\mathbb{W}\\(A(q_k),B(q_k))\in\mathbb{G}}} \|A(q_k)x_k + B(q_k)u_k + B_w(q_k)w_k\|^2_{P_u} - \|x_k\|^2_{P_\ell}$$

$$\leq \max_{(A(q_k),B(q_k))\in\mathbb{G},\, w\in\mathbb{W}} \Big(\|A_{cl}(q_k)x_k + B(q_k)v_k\|^2_{P_u} + \|B_w w_k\|^2_{P_u}$$

$$+\ 2\|(P_u^{1/2}(A_{cl}(q_k)x_k + B(q_k)v_k))^T(P_u^{1/2}B_w w_k)\|\Big) - \|x_k\|^2_{P_l}$$

$$\leq \max_{\substack{w\in\mathbb{W}\\(A(q_k),B(q_k))\in\mathbb{G}}} \Big(\|A_{cl}(q_k)x_k + B(q_k)v_k\|^2_{P_u} + \|B_w(q_k)w_k\|^2_{P_u} + 2\|(A_{cl}(q_k)x_k$$

$$+\ B(q_k)v_k)^T P_u B_w(q_k)w_k)\|\Big) - \|x_k\|^2_{P_\ell}.$$

Applying Cauchy-Schwarz Inequality first, and then Young Inequality

$$\max_{\substack{w\in\mathbb{W}\\(A(q_k),B(q_k))\in\mathbb{G}}} \Big(\|A_{cl}(q_k)x_k + B(q_k)v_k\|^2_{P_u} + \|B_w(q_k)w_k\|^2_{P_u} + 2\|(P_u^{1/2}(A_{cl}(q_k)x_k$$

$$+\ B(q_k)v_k))^T(P_u^{1/2}B_w(q_k)w_k)\|\Big)\|x_k\|^2_{P_\ell}$$

$$\leq \max_{(A(q_k),B(q_k))\in\mathbb{G},\, w\in\mathbb{W}} \Big(\|A_{cl}(q_k)x_k + B(q_k)v_k\|^2_{P_u} + \|B_w w_k\|^2_{P_u}$$

$$+ \, 2\|(P_u^{1/2}(A_{cl}(q_k)x_k + B(q_k)v_k)\| \; \|P_u^{1/2}(B_w w_k)\|\Big) - \|x_k\|^2_{P_l}$$

$$\leq \max_{(A(q_k),B(q_k))\in\mathbb{G},\, w\in\mathbb{W}} \Big(\|A_{cl}(q_k)x_k + B(q_k)v_k\|^2_{P_u} + \|B_w w_k\|^2_{P_u}$$

$$+ \, 2\Big(\frac{\|(P_u^{1/2}(A_{cl}(q_k)x_k + B(q_k)v_k)\|^2}{2} + \frac{\|(\|P_u^{1/2}(B_w w_k)\|^2}{2}\Big)\Big) - \|x_k\|^2_{P_l}$$

$$= \max_{(A(q_k),B(q_k))\in\mathbb{G},\, w\in\mathbb{W}} \Big(\|A_{cl}(q_k)x_k + B(q_k)v_k\|^2_{P_u} + \|B_w w_k\|^2_{P_u}$$

$$+ \, \Big(\|P_u^{1/2}(A_{cl}(q_k)x_k + B(q_k)v_k)\|^2 + \|P_u^{1/2}(B_w w_k)\|^2\Big)\Big) - \|x_k\|^2_{P_l}$$

$$= \max_{(A(q_k),B(q_k))\in\mathbb{G},\, w\in\mathbb{W}} \Big(\|A_{cl}(q_k)x_k + B(q_k)v_k\|^2_{P_u} + \|B_w w_k\|^2_{P_u}$$

$$+ \, \Big(\|A_{cl}(q_k)x_k + B(q_k)v_k\|^2_{P_u} + \|B_w w_k)\|^2_{P_u}\Big)\Big) - \|x_k\|^2_{P_l}$$

$$\leq \max_{\substack{w\in\mathbb{W} \\ (A(q_k),B(q_k))\in\mathbb{G}}} \Big(2\|A_{cl}(q_k)x_k + B(q_k)v_k\|^2_{P_u} + 2\|B_w(q_k)w_k\|^2_{P_u}\Big) - \|x_k\|^2_{P_\ell}$$

$$\leq 2 \max_{(A(q_k),B(q_k))\in\mathbb{G}} \Big(\|A_{cl}(q_k)x_k + B(q_k)v_k\|^2_{P_u} + 2\max_{w\in\mathbb{W}}\|B_w(q_k)w_k\|^2_{P_u} - \|x_k\|^2_{P_\ell}\Big).$$

Hence, applying the law of total probability

$$\mathbb{E}\left\{V_T(x_{k+1}) \,|\, x_x,\, \tilde{\mathbf{v}}_{T|k+1}\right\} - V(x_k) \leq (1-\epsilon_f)\Big(\mathbb{E}\left\{\|B_w w^*_{T|k}\|^2_P\right\} - \|x_k\|^2_Q - \|u_k\|^2_R\Big)$$

$$+ \, \epsilon_f\Big(2 \max_{(A(q_k),B(q_k))\in\mathbb{G}}\|A_{cl}(q_k)x_k + B(q_k)v_k\|^2_{P_u} + 2\max_{w\in\mathbb{W}}\|B_w w_k\|^2_{P_u} - \|x_k\|^2_{P_l}\Big)$$

$$= \, -(1-\epsilon_f)\|x_k\|^2_Q - (1-\epsilon_f)\|u_k\|^2_R + \; 2\epsilon_f \max_{(A(q_k),B(q_k))\in\mathbb{G}}\|A_{cl}x_k + Bv_k\|^2_{P_u} - \epsilon_f\|x_k\|^2_{P_l}$$

$$+(1-\epsilon_f)\mathbb{E}\left\{\|B_w w^*_{T|k}\|^2_P\right\} + 2\epsilon_f \max_{w\in\mathbb{W}}\|B_w w_k\|^2_{P_u}.$$

Let $\lambda_{min}(q_k)$ be a lower bound on the smallest eigenvalue of

$$U(q_k) = \begin{bmatrix} Q - \frac{2\varepsilon_f}{1-\varepsilon_f}(A(q_k)^T P_u A(q_k) - \frac{1}{2}P_\ell) & -\frac{2\varepsilon_f}{1-\varepsilon_f}A(q_k)^T P_u B(q_k) \\ \\ -\frac{2\varepsilon_f}{1-\varepsilon_f}B(q_k)^T P_u A(q_k) & R - \frac{2\varepsilon_f}{1-\varepsilon_f}B(q_k)^T P_u B(q_k) \end{bmatrix}, \tag{5.63}$$

that is $\lambda_{min} \le \min_{q_k \in \mathbb{Q}} \left(\min_{i=1,\dots,n+m} \lambda_i(U(q_k))\right)$. Hence, applying the law of total probability

$$\mathbb{E}\left\{V_T(x_{k+1})\,|\,x_x,\,\tilde{\mathbf{v}}_{T|k+1}\right\} - V(x_k) \le (1-\varepsilon_f)\Big(\mathbb{E}\left\{\|B_w(q_k)w^*_{T|k}\|^2_P\right\} - \|x_k\|^2_Q - \|u_k\|^2_R\Big)$$

$$+\,\varepsilon_f\Big(2\max_{(A(q_k),B(q_k))\in\mathbb{G}}\|A_{cl}(q_k)x_k + B(q_k)v_k\|^2_{P_u} + 2\max_{w\in\mathbb{W}}\|B_w(q_k)w_k\|^2_{P_u} - \|x_k\|^2_{P_\ell}\Big)$$

$$\le\; -(1-\varepsilon_f)\lambda_{min}\|x_k\|^2_2 + (1-\varepsilon_f)\mathbb{E}\left\{\|B_w(q_k)w^*_{T|k}\|^2_P\right\} + 2\varepsilon_f\max_{w\in\mathbb{W}}\|B_w(q_k)w_k\|^2_{P_u}$$

$$\le\; -\|x_k\|^2_2 + \frac{1}{\lambda_{min}}\mathbb{E}\left\{\|B_w w\|^2_P\right\} + \frac{2\varepsilon_f}{\lambda_{min}(1-\varepsilon_f)}\max_{w\in\mathbb{W}}\|B_w(q_k)w_k\|^2_{P_u}$$

$$\le\; -(1-\varepsilon_f)\lambda_{min}\|x_k\|^2_2 + \tilde{C}.$$

Thus, noting that $V(x_k) < \infty$ and $\mathbb{E}\left\{V_T(x_{k+1})\,|\,x_x,\,\tilde{\mathbf{v}}_{T|k+1}\right\} - V(x_k) \ge 0$

$$(1-\varepsilon_f)\lambda_{min}\|x_k\|^2_2 \le \tilde{C}$$

$$\|x_k\|^2_2 \le \frac{\tilde{C}}{(1-\varepsilon_f)\lambda_{min}}$$

$$\|x_k\|^2_2 \le C.$$

The final statement follows taking iterated expectations. ☐

The results of this section guarantee that the proposed OS-SMPC scheme enjoys important theoretical properties. These, combined with the efficiency of the scheme, which confines all costly computations in an offline step, and the generality of the considered setup, addressing both additive noise and parametric uncertainty, render the scheme suitable for efficient real-time and safety-critical applications.

Chapter 6

MISS STAR Results

This Chapter focuses on the main results obtained exploiting the design and simulation tools, i.e. MISS and STAR respectively, and applying the innovative propulsive and ARVD technologies. The first step consisted into analyzing all the different LST designs for the three fleet configurations introduced in Chapter 2 and Chapter 3 in order to identify those compliant with the mission and system constraints. The second step was the identification of the optimal LST architecture which results flexible enough to be exploited in different missions with evolving demands in terms of refurbishment to transfer up to the LOP-G. Thus, the design phase allowed to recognize the underlying propulsive technology and corresponding operational performance and cluster architecture that could be exploited for all three case studies selected, each one corresponding to a different crew mission duration on board the Gateway (see Section 6.1 for further details). For the optimal LST design, the ARVD maneuvers have been simulated in both GTO and Cislunar NRHO exploiting three different enhanced control strategies, presented in Chapter 5, to guarantee the fulfillment of the operational constraints that typically characterized these maneuvers, as widely described in Chapter 4. Last, as anticipated before, to properly validate the proposed control strategies in terms of real-time implementability and reliability, an extensive experimental campaign has been carried out where all three MPC schemes have been implemented and run on-board a spacecraft mock-up on a space-qualified micro-controller.

6.1 MISS Results

As explained in Chapter 3, the first step in initializing the MISS design tool consisted in uploading the mission scenario features in terms of initial and final orbits parameters, which are recalled in Table 6.2. Then, it is required to define the mission constraints coming from the ConOps and traffic plan analysis identifying the Gateway crew needs to provide in terms of their mission duration on board the LOP-G. As anticipated in Section 2.1.3, initially the LOP-G shall host a crew of 4 astronauts for up 30 days but its habitable volume allows to extend the crew permanence up to 12 months, i.e. it could become a permanent outpost as the current ISS. On the other hand, the Gateway has been conceived only as a manned outpost temporarily inhabited. Thus, three case studies have been selected for this project where the crew mission duration can be extended up to three months: (i) case A: 30 days; (ii) case B: 60 days; and (iii) case C: 90 days. To each case study corresponds a different replenishment need and corresponding cargo module geometry, both defined according to the guidelines presented in Section 2.1.4 and reported in Table 6.1. For all case studies, several fleet configurations have been envisioned varying the number of LST from 1 up to 3, consequently defining the mission constraint related to the maximum transfer duration $\Delta t_{MAX_{EOR}}$ according to (2.1), i.e. 4.5 months for case A, 10.5 for case B and 16.5 for case C.

Table 6.1: LST case studies and related resupply need and cargo module geometry.

Case Study	**Resupply Need [kg]**	r_{cyl} **[m]**	h_{cyl} **[m]**	m_{cyl} **[kg]**
30-days	1484.4	2.3	1.48	2060.28
60-days	2968.8	2.3	2.97	4120.56
90-days	4453.2	2.3	4.45	6180.84

Table 6.2: LST operational orbits parameters.

Orbit	h_P **[km]**	h_A **[km]**	i **[deg]**	Ω **[deg]**	ω **[deg]**	T **[days]**
GTO	250	35943	6	0	178	0.44
NRHO	1496	63263	90	0	0	6.66

Once identified the reference orbits and the nine subcases to analyze, the Δv budgets for each mission phase has been evaluated, according to the guidelines introduced in Section 3.1.2. The main results are reported in Table 6.3 both for EOR and ARVD closing phases.

6.1.1 Lunar Space Tug Design

As anticipated in Section 2.2.1 and recalled in Chapter 3, the propulsive technology envisioned for the LST spacecraft is based on high-power HET, which performance envelope is represented in Figure 2.15 and on which 25 different nominal operational points have been identified, which performance are detailed in Table 6.4. Each of them has been further characterized assigning five peculiar lifetime

Table 6.3: LST preliminary Δv budgets.

Δv_{phase}	**From**	**To**	Δv **[m/s]**
Δv_{EOR}	GTO	NRHO	1837.6
Δv_{incl}	GTO	NRHO	1287.3
Δv_{RB}	GTO	GTO	3.2176
Δv_{FA}	GTO	GTO	1.27
Δv_{RB}	NRHO	NRHO	1.0474
Δv_{FA}	NRHO	NRHO	0.4809

Table 6.4: HET reference operational points.

$\mathbf{HET}_i$	**T [mN]**	$\mathbf{I}_{sp}$ **[s]**	**P [W]**	$\dot{\mathbf{m}}_f$ **[mg/s]**
HET_1	889.90	2300	16000	39
HET_2	867.30	2400	16000	36.5
HET_3	844.70	2500	16000	34
HET_4	822.10	2600	16000	32
HET_5	799.50	2700	16000	30
HET_6	1000.00	2300	18000	44
HET_7	975.00	2400	18000	41
HET_8	950.00	2500	18000	38
HET_9	925.00	2600	18000	36
HET_{10}	900.00	2700	18000	33.5
HET_{11}	1107.40	2300	20000	49
HET_{12}	1080.00	2400	20000	46
HET_{13}	1052.60	2500	20000	42.5
HET_{14}	1025.20	2600	20000	40
HET_{15}	997.80	2700	20000	37.5
HET_{16}	1215.61	2300	22000	54
HET_{17}	1187.78	2400	22000	50
HET_{18}	1159.95	2500	22000	47
HET_{19}	1132.12	2600	22000	44
HET_{20}	1104.29	2700	22000	41
HET_{21}	1316.56	2300	24000	59
HET_{22}	1287.68	2400	24000	55
HET_{23}	1258.8	2500	24000	52
HET_{24}	1229.92	2600	24000	48
HET_{25}	1201.04	2700	24000	45

level, varying from 20000 up to 40000 h. Thus, the number of possible HET configurations raised up to $N_{config} = 125$. Then, considering that the maximum number of HET operated at the same time has been limited to $N_{HET_{MAX}} = 4$, for each of the 9 subcases, $N_{LST_{sol}} = 500$ design solutions have been obtained exploiting the MISS design tool, for an overall total of 4500 LST configurations. Once obtained all the solutions, they have been filtered in order to select only those compliant with both mission and system constraints. The former is given by the selected fleet configuration in terms of $\Delta t_{EOR_{MAX}}$ whereas a (current) technological constraint limits the maximum number of HET $N_{HET_{MAX}}$ that could be installed in the same cluster. Indeed, in order to scale down the complexity of the e-PROP architecture and the thruster firing algorithm as well as the plum impingement, N_{HET} shall be less than or equal to 10. Applying both constraints on the obtained LST solutions, it resulted that only the fleet configuration composed by 3 LST presented compliant solutions for all three case studies, as highlighted in Figure 6.1, whereas the 2-LST fleet provides solutions only for the 30-days and 60-days cases with 214 and 32 feasible design solutions, respectively. In particular, it can be observed that for the

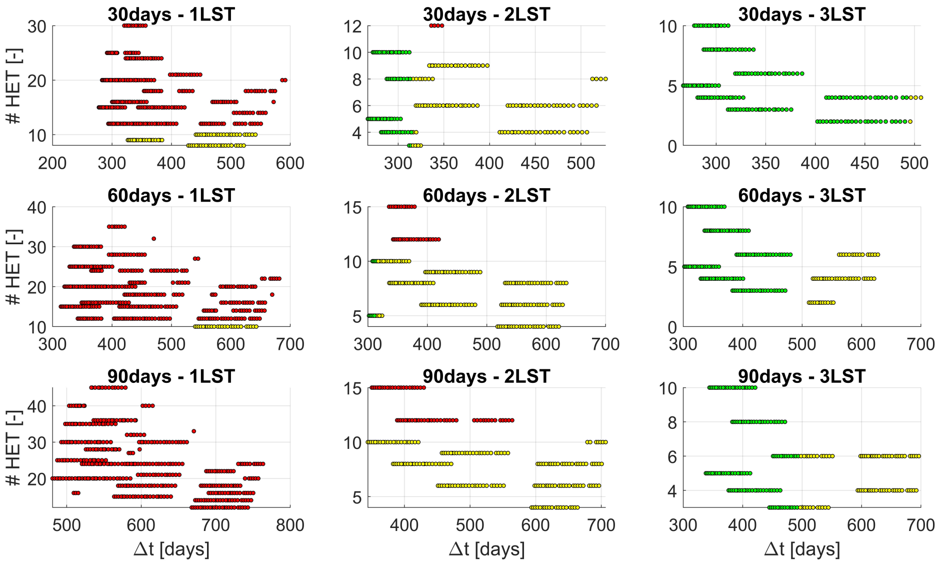

Figure 6.1: LST design solutions for all 9 subcases, highlighting in green those compliant with both system and mission constraints, in yellow those that are compliant with either one of the constraint and in red those that are not feasible.

1-LST fleet, only case A and case B presented solutions partially compliant with the constraints. Moreover, both of them includes e-PROP architecture composed by at least 10 HET whereas the transfer duration results much longer than the maximum allowed, i.e. over 400 days vs 135 days. For the 2-LST subcases, also case C presents solution compliant with the system constraints while the Δt_{EOR} is still too high with respect to the mission constraint, i.e. 315 days. Moreover, comparing all the 9 subcases it is possible to notice that increasing the number of

LST in the same fleet, the corresponding design solutions result more bundled and the transfer duration range significantly decreases whereas it increases, together with the cluster size range, when the cargo mass to transfer increases as well (as a function of the crew mission duration).

Focusing on the LST design solutions that are compliant with all the enforced mission and system constraints, their number decreases with increasing resupply demand. In particular, over the 500 solutions obtained for each case, the remaining feasible ones are: (i) 468 for case A; (ii) 343 for case B; and (iii) 268 for case C. Analyzing all the compliant LST design, it is possible to identify some common behaviors, which are thoroughly described in the follows starting from the e-PROP architecture and thruster lifetime as a function of the HET operational points, represented in Figure 6.2 and Figure 6.3, respectively. In Figure 6.2a, the smallest

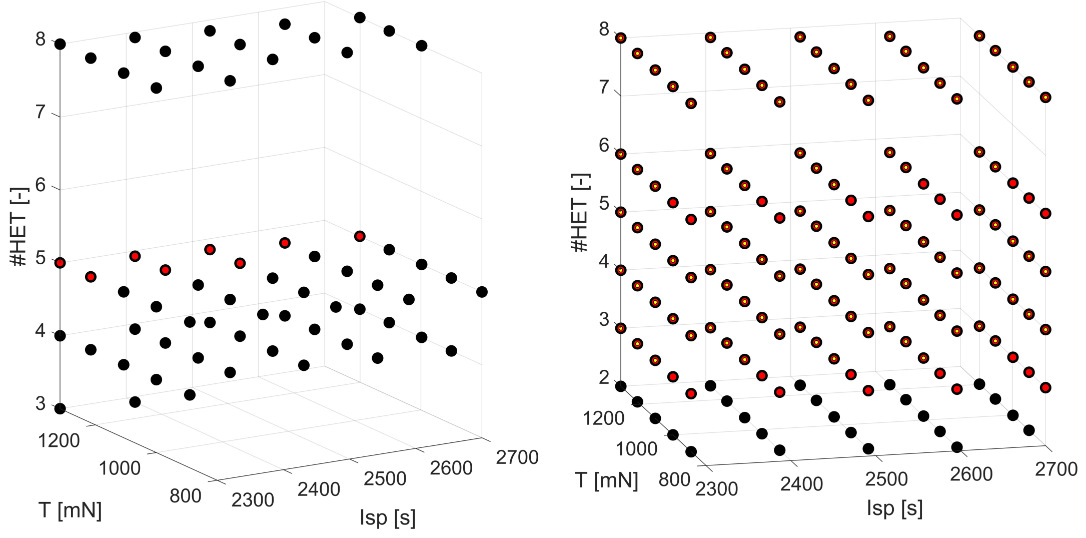

(a) 2-LST fleet

(b) 3-LST fleet

Figure 6.2: e-PROP architecture with respect to the corresponding HET operational point over the performance envelope for the three case studies: (i) 30-days (black circles); (ii) 60-days (red circles); (iii) 90-days (yellow circles).

e-PROP architecture for 2-LST fleet results composed by 3 HETs. On the other hand, for the 3-LST fleet, the minimum number of thrusters drops to 2 for the 30-days case and it is equal to 3 for the 60 and 90-days cases, as shown in Figure 6.2b. Moreover, in the same Figure, the solutions result split into two groups, the first from 2 to 5 HET while the second from 6 to 8 thrusters. It is possible to observe that within the same group, increasing the size of e-PROP architecture, the area of the performance map where feasible LST design solutions can be found increases as well. For example, for the 3HETs and 6HETs architectures, only few operational points correspond to feasible solutions for case C. On the other hand, all the operational points provide compliant design solutions when the number of thrusters increase. Figure 6.3 highlights a quite different behavior. For the 2-LST fleet configuration, from 25000 up to 40000 h, the same 8 operational points provide solution for the 60-days case whereas for the 30-days case the number of operational points increases with increasing lifetime. In particular, starting from a lifetime of 25000 h, all the performance map results feasible. On the other hand, for the 3-LST fleet configuration, all the 125 operational points correspond to at least one LST design solution compliant with all mission and system requirements for all three case studies.

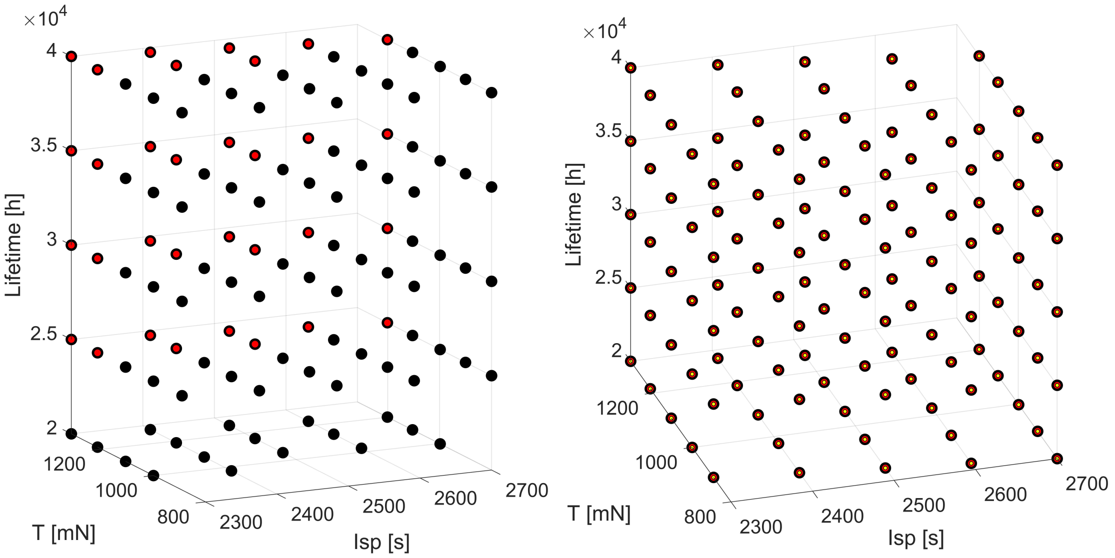

(a) 2-LST fleet

(b) 3-LST fleet

Figure 6.3: Thruster lifetime with respect to the corresponding HET operational point over the performance envelope for the three case studies: (i) 30-days (black circles); (ii) 60-days (red circles); (iii) 90-days (yellow circles).

Going into the details of the corresponding LST subsystems design, Figure 6.4 and Figure 6.5 provide an overview of the e-PROP subsystem highlighting the number of operative thrusters over the total number of HET in the cluster (Figure 6.4) and the related number of PPU required to sustaining them (Figure 6.5). First, Figure 6.4 highlights that the same number of operative thrusters can correspond to different cluster architectures, i.e. one double that the other. This is due to either the different HET operational point lifetime and transfer duration. Indeed, higher is the lifetime lower can be the number of stand-by thrusters required to cover the entire mission duration. Then, lower is the number of HET in the cluster, lower is the corresponding LST mass and, at the same amount of thrust available, faster will be the transfer, which has a significant impact on the definition of the number of stand-by thrusters as well. Moreover, it results that for the 3, 4 and 5 HETs cluster architecture, no stand-by thrusters could be required to cover the entire LST mission duration, but only one redundant thrusters is included. On the other hand, for the 6, 8 and 10 architectures, at each operative thruster corresponds one stand-by HET plus two for redundancy. These considerations are corroborated by the results presented in Figure 6.5 where at the same number of PPU equipped on-board can correspond two different cluster architectures.

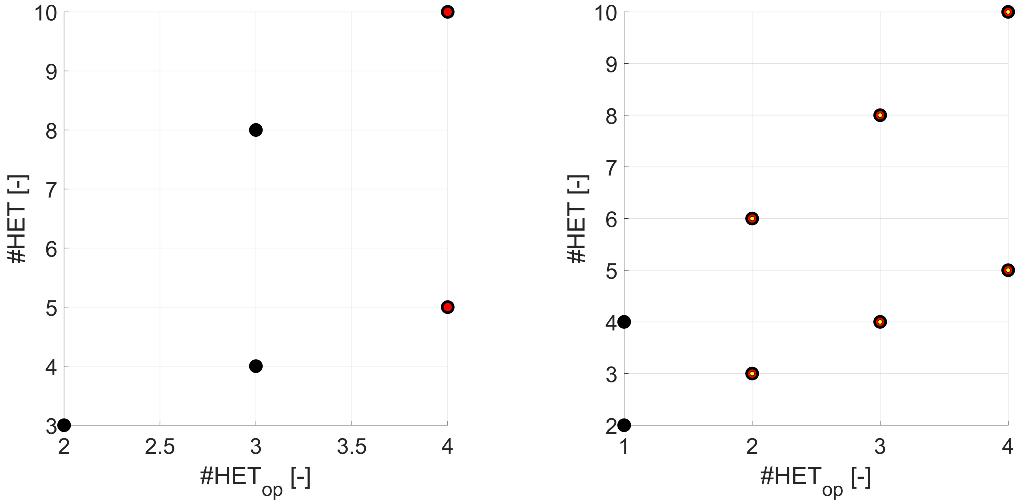

(a) 2-LST fleet (b) 3-LST fleet

Figure 6.4: e-PROP architecture in terms of $N_{HET_{op}}$ and cluster architecture for the three case studies: (i) 30-days (black circles); (ii) 60-days (red circles); (iii) 90-days (yellow circles).

Analyzing the EPS design, Figure 6.6 and Figure 6.7 represent the subsystem main features in terms of solar array area and secondary battery mass, respectively, as a function of the corresponding LST power demand and number of operative HETs. In both cases, it is possible to observe an almost linear dependence of the solar array and battery size with the total power required. This is due to the design models exploited, described in Chapter 3. Moreover, it is important to highlight other common behaviors:

1. Increasing the number of LST in the fleet (for case A and B), the power demand range broadens towards the origin, i.e. power levels lower than 100 kW, and, as a consequence, also the solar array area and battery mass ranges are widened.
2. Increasing the number of HET$_{op}$, the power demand increases as well but, on the other side, at the same $N_{HET_{op}}$ can correspond different amount of total

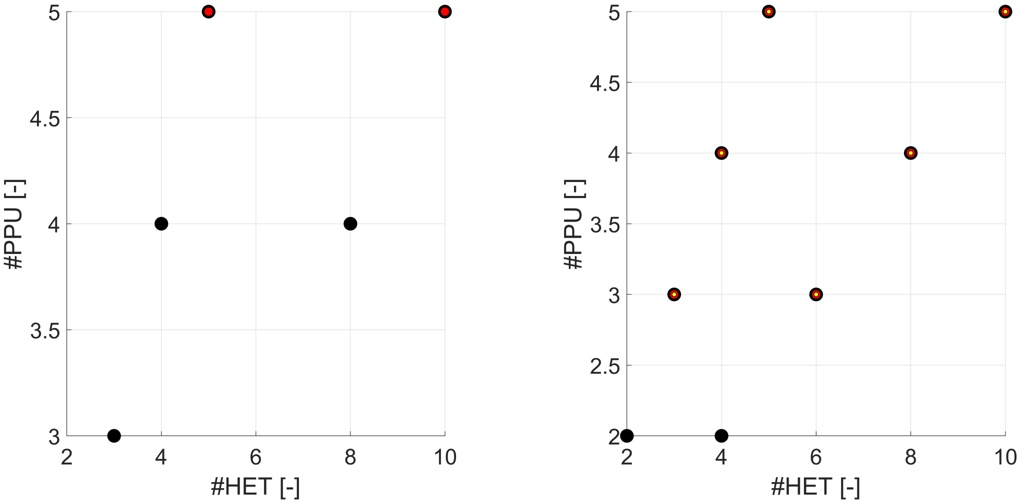

(a) 2-LST fleet

(b) 3-LST fleet

Figure 6.5: e-PROP architecture in terms of cluster architecture and number of PPU for the three case studies: (i) 30-days (black circles); (ii) 60-days (red circles); (iii) 90-days (yellow circles).

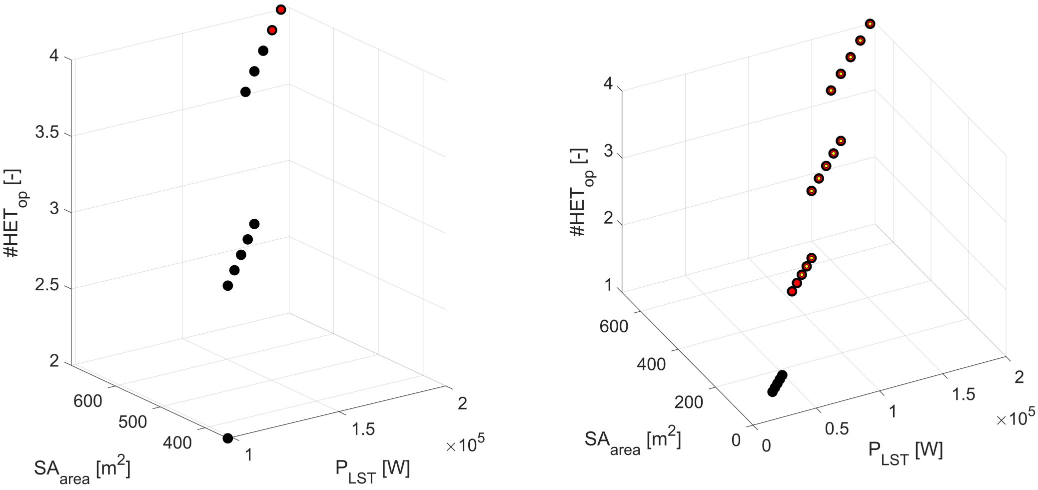

(a) 2-LST fleet

(b) 3-LST fleet

Figure 6.6: EPS design features in terms of solar array area as a function of the total power demand for the three case studies: (i) 30-days (black circles); (ii) 60-days (red circles); (iii) 90-days (yellow circles).

power request because of the peculiar power level characterizing the HET operative point.

3. Thanks to the improved technologies available for on-board power generation, to provide up to 200 kW, solar array with reasonable area, i.e. lower than 700 m^2, could be sufficient.

4. On the other hand, to always guarantee the same amount of power also during eclipses, the mass of secondary batteries could be quite significant, i.e. up to 2.5-3 tons.

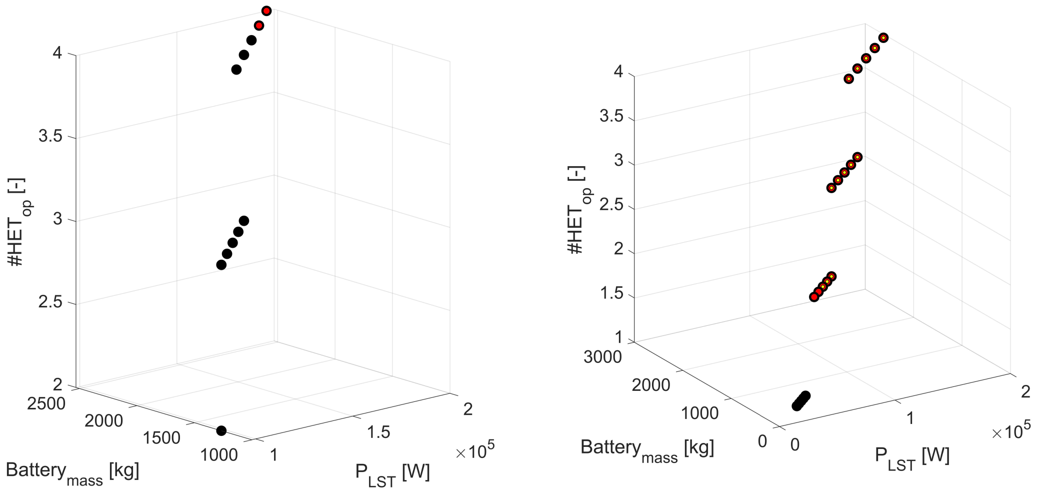

(a) 2-LST fleet

(b) 3-LST fleet

Figure 6.7: EPS design features in terms of secondary battery mass as a function of the total power demand for the three case studies: (i) 30-days (black circles); (ii) 60-days (red circles); (iii) 90-days (yellow circles).

Introducing the TCS subsystem design, Figure 6.8 highlights the linear dependence among the radiator panels area with the total power demand. For the 30-days case study, power levels similar to the ISS ones correspond to analogous radiators size, i.e. about 90 m^2, and the radiators could be installed on the external structure of the LST. On the other hand, for power levels higher than 100 kW, the heat rejection function results quite demanding, which radiator area that can exceed the 200 m^2, especially for the 60- and 90-days scenarios. In this second case, additional deployable panels could be exploited, as anticipated in Chapter 2. Thus, the radiator system can be designed as deployable and retractable wings, each one composed by multiple panels with dimensions retracing those of the ISS, i.e. 1.8 m high and 3.12 m wide [177].

Last, all the LST design solutions share the same AOCS architecture, including actuators and navigation sensors, since they are all function of the mission environment, phases and disturbance affecting the spacecraft dynamics. According to

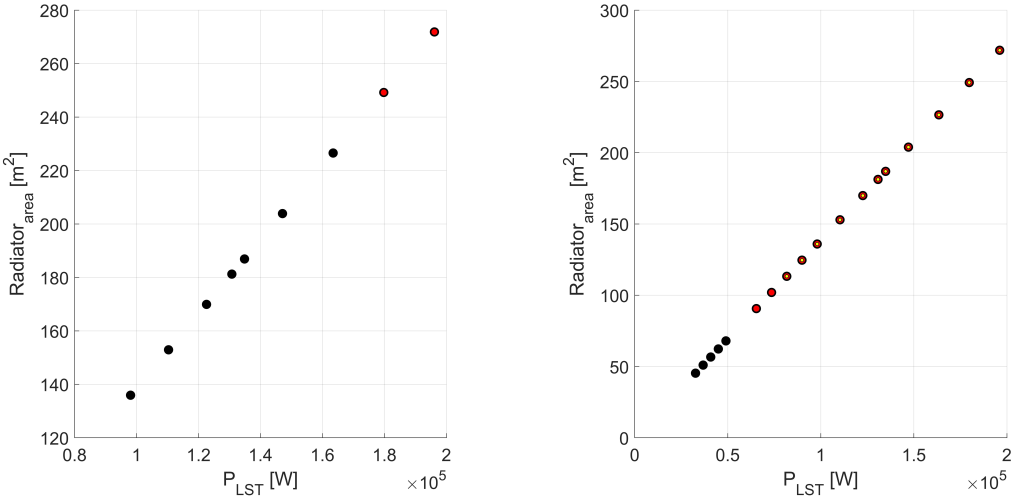

(a) 2-LST fleet (b) 3-LST fleet

Figure 6.8: TCS design features in terms of radiator panels area as a function of the total power demand for the three case studies: (i) 30-days (black circles); (ii) 60-days (red circles); (iii) 90-days (yellow circles).

Table 6.5: AOCS design feature in terms of mass and power budget at component level.

Component	**Mass [kg]**	**Power [W]**
Monopropellant thrusters	24.84	1080
Reaction Wheels	35.4	324
Star sensor	180	120
Sun sensor	12	18
IMU	30	400
Magnetometer	9	6

the assumptions made in Chapter 2 and Chapter 3, four RWs are equipped on board, arranged in the typical NASA Standard for attitude control whereas 30 arianeGROUP 20N Chemical Monopropellant Hydrazine Thrusters [63], arranged in 10 pods, shall be exploited for orbital control during ARVD maneuvers as ell as for wheels desaturation. Moreover, once evaluated the sizing torque $\tau_{RW_{req}}$ as the maximum between the disturbance torque τ_{ext} and the the torque demand for the slew maneuvers τ_{slew} and estimated the corresponding the minimum RW angular momentum capacity $h_{RW_{req}}$, the Rockwell Collins RDR 68-3 RWs have been confirmed as compliant with the system angular momentum requirement. The related mass is simply given as four times the specific mass reported in the RW database [64]. On the other hand, the same configuration presented in Section 2.2.3 for the navigation sensors has been exploited. Thus, Table 6.5 resumes the main budgets for the AOCS subsystem at components level.

Focusing the attention on the 3-LST fleet configuration, which guarantees at least one spacecraft design compliant with all the aforementioned constraints for the three case studies, the following results provide an overview of the relationship among the four high-level parameters, which are most significant from a system budget point-of-view: (i) LST total wet mass; (ii) total thrust available; (iii) LST total power demand; and (iv) two-way transfer duration.

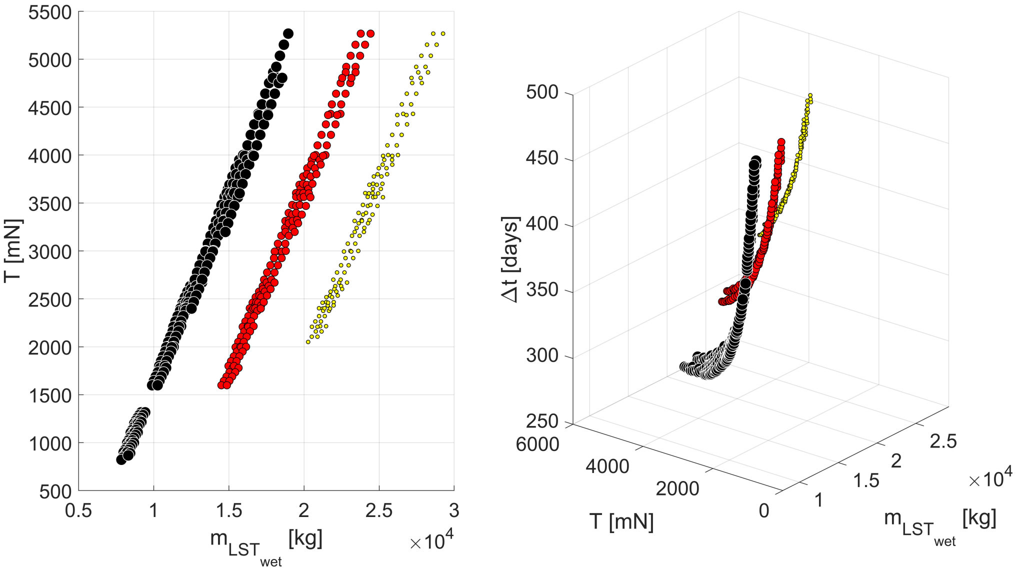

Figure 6.9: LST transfer duration as a function of its total wet mass and thrust available for the three case studies: (i) 30-days (black circles); (ii) 60-days (red circles); (iii) 90-days (yellow circles).

Figure 6.9 provides on one side the correlation among thrust available, spacecraft wet mass and transfer duration. On the left, it is shown the almost linear dependence among mass and thrust, and that for all three case studies, the mass range is about 10 tons corresponding to a 5 N thrust range, i.e. gaining 2 tons every N of thrust. Instead, on the right side it is highlighted their interrelation with the transfer time, reproducing a (quasi) hyperbolic behavior corresponding to the 5-th order polynomial function presented in Section 3.1.1.

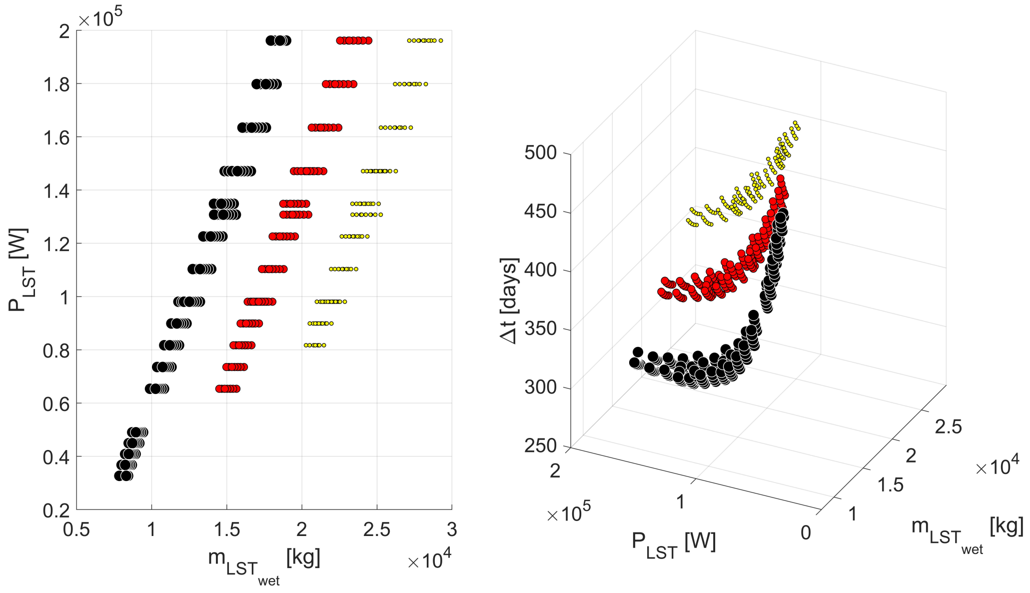

Figure 6.10: LST transfer duration as a function of its total wet mass and power demand for the three case studies: (i) 30-days (black circles); (ii) 60-days (red circles); (iii) 90-days (yellow circles).

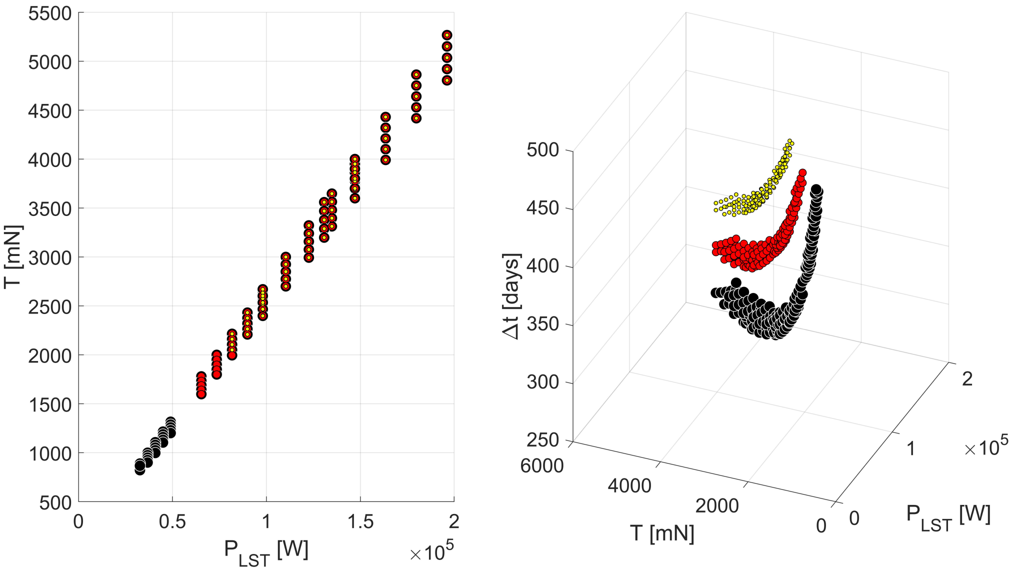

Figure 6.11: LST transfer duration as a function of its total power demand and thrust available for the three case studies: (i) 30-days (black circles); (ii) 60-days (red circles); (iii) 90-days (yellow circles).

In particular, the presence of an horizontal asymptote highlights that further increasing the thrust available, contemporary operating more than 4 HETs, does not imply an additional decrement of Δt, which settles around 260, 290 and 330 days for case A, B and C, respectively.

The presence of an horizontal asymptote can be observed also in both Figure 6.10 and Figure 6.11 where the transfer duration is expressed as a function of mass and power on one side and power and thrust on the other. Moreover, in Figure 6.10 the significant effect of exploiting high-power electric propulsion is emphasized highlighting the almost linear dependence among the spacecraft wet mass and the power demand. Indeed, as recalled in Section 3.1.3, PROP and EPS represent together almost the 60% of the overall LST dry mass. On the other side, at the same power demand can correspond different LST wet mass depending on the e-PROP architecture, i.e. different lifetime, thrust and Isp (see also Figure 6.11) but same $N_{HET_{op}}$ and P_{HET}, and propellant mass.

Last, Figure 6.12 and Figure 6.13 provide an overview of the Hydrazine and Xenon consumption, respectively, during the different LST mission phases as well as the corresponding tank masses, all with respect to LST dry mass. In particular, Figure 6.12 highlights how the Hydrazine required for the three different ARVD maneuvers is almost the same for all three case studies and varies linearly with the tug dry mass in a range between 15 kg up to 100 kg, i.e. the latter for the ARVD maneuver in GTO with the cargo module.

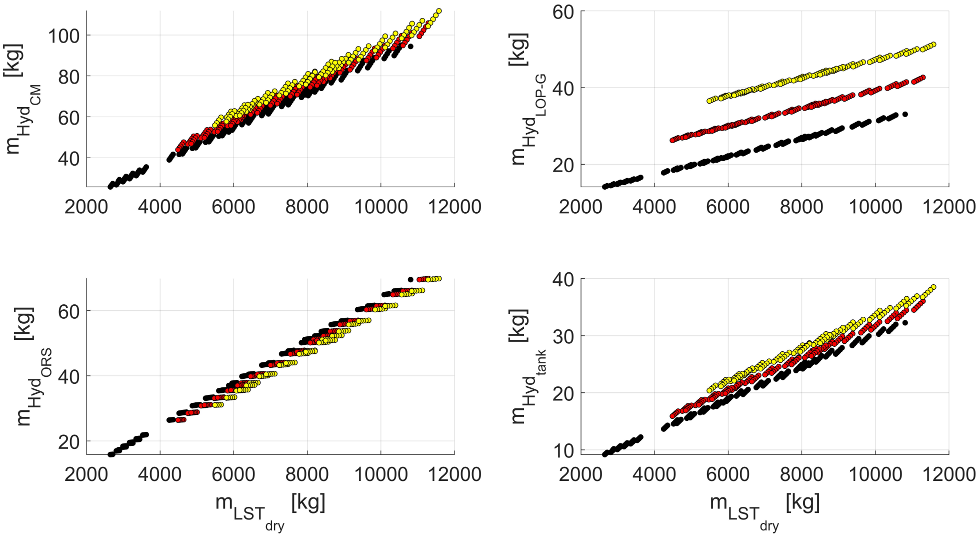

Figure 6.12: LST Hydrazine consumption during ARVD maneuvers and corresponding tanks sizing for the three case studies: (i) 30-days (black circles); (ii) 60-days (red circles); (iii) 90-days (yellow circles).

The propellant consumption results more demanding for the EOR phases, as shown in Figure 6.13, where the difference among the three case studies is about

1 ton for the GTO-NRHO phase and about 0.5 tons for the NRHO-GTO due to the lower LST total dry mass (no cargo module during the latter phase). Overall, the Xenon consumption is significant but limited, and the propellant-over-dry mass slightly decreases when the LST mass increases. For example, for the 30-days case, the smallest LST configuration has a dry mass of about 2 tons and the corresponding Xenon consumption is close to 2 tons as well. On the other hand, still for the 30-days case, the largest LST has a dry mass close to 12 tons while the propellant consumption is slightly above 4 tons, i.e. almost one third.

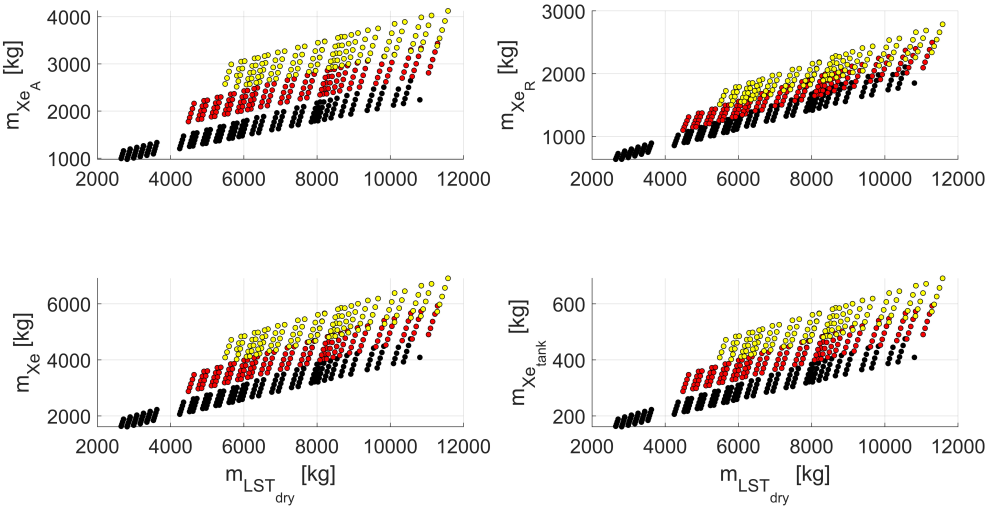

Figure 6.13: LST Xenon consumption during ARVD maneuvers and corresponding tanks sizing for the three case studies: (i) 30-days (black circles); (ii) 60-days (red circles); (iii) 90-days (yellow circles).

Once analyzed the overall behavior of the different LST design solutions and main features within the three different case studies, in the next Section the optimal configuration selection process is presented, focusing on the identification of the best LST design solution which could be exploited for all three scenarios, envisioning preliminarily a 3-LST fleet configuration.

6.1.2 Optimal Design Selection

The first step towards the selection of the optimal design solution consists in identifying the most suitable e-PROP architecture, common to all three cases and based on the same technology in terms of HET performance and features. Thus, analyzing the results reported in Figure 6.14 it is possible to observe that six over eight architectures (defined in terms of $N_{HET_{op}}$ and N_{HET}) are shared among all three scenarios. Moreover, in compliance with the need of minimizing the mass as well as the propellant consumption to reduce both the launch cost and the complexity of the spacecraft, the smallest e-PROP architecture has been selected as the most promising, which is based on 3 HETs, 2 of them operative and one for redundancy purpose, i.e. no stand-by thrusters are required. Thus, all the feasible solutions previously presented have been further filtered selecting only those compliant with the selected e-PROP architecture. Moreover, for the chosen e-PROP cluster configuration, 14 different operative points correspond to LST design solutions shared among all three case studies. Hence, the design solutions have been filtered again, collecting only those in which the cluster is based on these operational points.

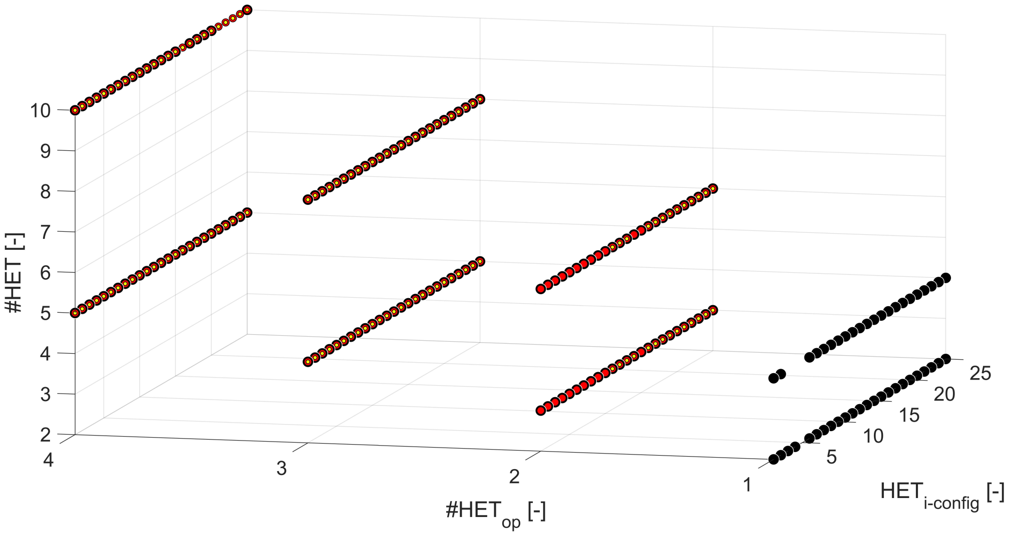

Figure 6.14: LST e-PROP architectures for all three cases design solutions compliant with mission and system constraints for the 3-LST fleet configuration.

The next step involves a trade-off analysis in which the figure of merits and the corresponding weighting factors have been previously introduced in Section 3.1.4. Applying the same rules to all three scenarios, the trade results highlight that in all three cases the ranks are always the same and the optimal solution corresponds to the HET$_{14}$ operational point, with a 40000 h lifetime, 1025.2 mN of thrust, an Isp of 2600 s and an input power of 20 kW. The corresponding LST design features can be organized in two groups: (i) the first group includes all the sizing parameters shared among all three scenarios; and (ii) the second group in which the sizing parameters are peculiar to each case study, because function of either the resupply mass and the propellant consumption. All these results are resumed in the following three tables: (i) Table 6.7 and Table 6.8 provide sizing details about the LST optimal design that belongs to the first group at subsystem and component level, respectively; and (ii) Table 6.9 highlights the differences among the three LST optimal configuration, one for each case study.

Table 6.6: LST trade-off analysis results.

Lifetime	**HET$_i$**	**30 days**	**60 days**	**90 days**	**Rank**
35000	11	-0.010859976	-0.012522642	-0.014108778	5
35000	12	-0.010713612	-0.012321546	-0.013852075	4
35000	16	-0.011467261	-0.013095866	-0.014664783	15
35000	17	-0.011310025	-0.012883559	-0.014397063	13
35000	18	-0.011170957	-0.012695176	-0.014158556	12
35000	19	-0.011047867	-0.012527758	-0.01394558	9
35000	20	-0.010938963	-0.012378864	-0.013755094	8
35000	21	-0.012091022	-0.013689957	-0.015242414	25
35000	22	-0.011924391	-0.013468026	-0.014965204	23
35000	23	-0.011776486	-0.013270614	-0.014717839	22
35000	24	-0.011645008	-0.013094653	-0.014496533	19
35000	25	-0.011528103	-0.012937648	-0.014298186	18
40000	11	-0.010859976	-0.012522642	-0.014108778	6
40000	12	-0.010713612	-0.012321546	-0.013852075	3
40000	13	-0.010584958	-0.012143852	-0.013624003	2
40000	**14**	**-0.010471961**	**-0.011986733**	**-0.01342101**	**1**
40000	16	-0.011467261	-0.013095866	-0.014664783	16
40000	17	-0.011310025	-0.012883559	-0.014397063	14
40000	18	-0.011170957	-0.012695176	-0.014158556	11
40000	19	-0.011047867	-0.012527758	-0.01394558	10
40000	20	-0.010938963	-0.012378864	-0.013755094	7
40000	21	-0.012091022	-0.013689957	-0.015242414	26
40000	22	-0.011924391	-0.013468026	-0.014965204	24
40000	23	-0.011776486	-0.013270614	-0.014717839	21
40000	24	-0.011645008	-0.013094653	-0.014496533	20
40000	25	-0.011528103	-0.012937648	-0.014298186	17

Table 6.7: Optimal LST design sizing at subsystem level.

Subsystem	AOCS	CDH	EPS	e-PROP	STRUCT	TCS	TTC
Mass [kg]	313.07	92.06	1653.35	378.16	1350.26	392.47	92.06

From the results presented in this Section, the final conclusion is: it is possible to exploit the same LST spacecraft to support the LOP-G when the resupply demand evolves together with the increase of crew permanence on-board the Gateway. The *only* modification required is related to the Hydrazine and Xenon tanks. Indeed, at the same Δv and HETs and monopropellant thrusters Isp, increasing the cargo mass to transfer implies larger propellant consumption and, as a consequence, increased

Table 6.8: Optimal LST design sizing at component level.

Parameter	**Value**
Solar array mass [kg]	505.19
Solar array area [m^2]	291.18
Secondary batteries mass [kg]	1054.58
Total power demand [W]	81714.29
Radiator panels area [m^2]	113.27
HET Mass [kg]	138.6
Pointing mechanisms mass [kg]	0.63
Number of pointing mechanisms [-]	3
PPU mass [kg]	158.4
Number of PPU [-]	3
Pressure regulators mass [kg]	1.46
Number of pressure regulators [-]	2
Xenon flow control mass [kg]	19.8
Number of Xenon flow control [-]	3
Hydrazine for RWs desaturation [kg]	31.49

tank masses. Thus, at the same thrust available, if the total dry mass as well as the wet mass increase, the corresponding transfer duration increases as well, without compromising the mission success.

Table 6.9: Optimal LST design sizing peculiar for each case study.

Parameter	**30-days**	**60-days**	**90-days**
Hydrazine mass [kg]	157.91	180.85	203.80
Hydrazine tank mass [kg]	15.79	18.09	20.38
Xenon mass GTO-NRHO [kg]	1378.59	1976.41	2574.24
Xenon mass NRHO-GTO [kg]	1000.88	1255.59	1510.30
Xenon tank mass [kg]	237.95	323.20	408.45
PROP mass [kg]	861.25	1097.76	1334.27
LST dry mass [kg]	4992.25	5240.59	5488.92
LST total dry mass [kg]	8536.93	12329.95	16122.96
LST total wet mass GTO-NRHO [kg]	10969.04	15622.24	20275.44
LST total wet mass NRHO-GTO [kg]	7782.06	10050.23	12318.40
$\Delta t_{EOR_{GTO-NRHO}}$ [days]	382.97	488.70	567.10
$\Delta t_{EOR_{NRHO-GTO}}$ [days]	297.53	358.82	416.67

6.2 STAR Results

Once obtained the optimal LST design, the STAR tool has been exploited to analyze its ARVD maneuvers in GTO and NRHO. The main goal is to validate the effectiveness and reliability of the proposed control strategies in satisfying the operational constraints characteristics of the proximity operations while complying time and fuel consumption constraints outlined during the design phase. In particular, the 60-days LST has been considered as reference spacecraft design and the interface data inherited from the previous phase are reported in Table 6.10, differentiating the chaser vehicle mass during the different maneuvers according to the absence or presence of the cargo module and the (remaining) propellant mass on board. Indeed, during the ARVD maneuver with the cargo module in GTO, the LST is full with the complete propellant load, i.e. 3444.34 kg, whereas its dry mass do not include the resupply. On the other hand, it is assumed that half of the Xenon load has been already consumed, i.e. the remaining propellant mass is about 1467.93 kg, and the LST total dry mass include the cargo, which mass is equal to 7089.36 kg. Moreover, the target vehicles physical features are initialized as anticipated in Section 4.2.2 while the tensor of inertia and center-of-gravity location for the LST have been evaluated according to the geometry reported in Table 6.10 and the guidelines given in Section 4.2.3. The corresponding data are reported in Table 6.11. The last step of the initialization process concerns the upload of the AOCS actuation system features according to the architecture choice described in Section 2.2.3 and their location and orientation as defined in (4.41) for RWs and

Table 6.10: STAR initialization data.

Parameter	**Value**
LST radius [m]	2.3
LST height [m]	10
Cargo module radius [m]	2.3
Cargo module height [m]	2.97
Solar array mass [kg]	505.19
Solar array area [m^2]	291.18
Hydrazine for RWs desaturation [kg]	31.49
Hydrazine mass [kg]	180.85
LST dry mass [kg]	5240.59
LST total dry mass [kg]	12329.95
LST total propellant mass [kg]	3444.34
LST total wet mass in GTO [kg]	8684.93
LST total wet mass at LOP-G [kg]	13797.88
$\Delta t_{ARVD_{MAX}}$ [h]	12

in (4.46).

The next phase consists in defining the initial conditions in terms of position and attitude for the different ARVD maneuvers set according to the guidelines inherited from the ISS experience, the new directive stated for the LOP-G and additional safety margins. As anticipated in Section 4.1, the starting point for the close-range phase has been set differently in GTO with respect to NRHO due to the a higher safety level typically required when humans or habitat infrastructures are involved. On the other hand, being the cargo module and the ORS unmanned systems, the safety requirements can be moderately relaxed, still in compliance with the stakeholders' expectation and demands. Thus, the radial boost maneuver with both cargo module and ORS starts when the LST is 6 km far from the target vehicles in their respective LVLH frames whereas the LST initiates the ARVD closing phase with the Gateway when the relative distance is at least 30 km. Then, the corresponding chaser position and velocity in the ECI and perifocal reference systems have been obtained, together with the chaser true anomaly, and reported in Table 6.12, considering that the target vehicles initial true anomaly has been assumed equal to zero, i.e. the target is initially at the orbital periastrum. For what concern the initial attitude of the LST in its body frame with respect to the target LVLH reference system, it has been set for all three maneuvers as $[\phi, \theta, \psi] =$ [0.57,0,1.72] [deg], which in terms of quaternion corresponds to $[q_S, q_1, q_2, q_3] \simeq$ [0.99988,0.01499,0.000075,0.004999].

Table 6.11: LST moment of inertia and center-of-mass location.

Parameter	**GTO**	**NRHO**
$J_{x_{cyl}}$ [kg·m^2]	13861	36495
$J_{y_{cyl}}$ [kg·m^2]	50602	212570
$J_{x_{cyl}}$ [kg·m^2]	50602	212570
$J_{x_{SA}}$ [kg·m^2]	13152	13152
$J_{y_{SA}}$ [kg·m^2]	763	763
$J_{z_{SA}}$ [kg·m^2]	12399	12399
$J_{x_{LST}}$ [kg·m^2]	43737	74143
$J_{y_{LST}}$ [kg·m^2]	157360	319320
$J_{z_{LST}}$ [kg·m^2]	75400	237370
$[x_{G_{LST}}, y_{G_{LST}}, z_{G_{LST}}]$ [m]	[0.7783,0,0]	[0.8723,0,0]

Another crucial point was the definition of the mission, operational and system constraints that shall be taken into account and fulfill during the ARVD maneuvers, as previously introduced in Chapter 4. Thus, hereafter the main constraints envisioned for the following analysis of the proximity operations are recalled:

- At the end of the close-range rendezvous phase both in GTO and NRHO, the

Table 6.12: LST orbital position and velocity in LVLH, ECI and perifocal frames.

Parameter	**GTO**	**NRHO**
$[x, y, z]_{LVLH}$ [km]	[-6,0,0]	[-30,0,0]
$[x, y, z]_{PQW}$ [km]	[6627.99,-5.99,0]	[3232.93,-29.99,0]
$[x, y, z]_{ECI}$ [km]	[-6623.75,237.28,-0.63]	[3232.93,0,-29.99]
$[v_x, v_y, v_z]_{PQW}$ [km/s]	[-0.004,10.19,0]	[-0.0075,1.7,0]
$[v_x, v_y, v_z]_{ECI}$ [km/s]	[-0.35,-10.14,1.07]	[-0.0075,0,1.7]
ν_{CV} [deg]	-0.052	-0.532

LST shall be at a distance of 500 m from the target vehicle along the minus V-bar axis.

- At the end of the close-range rendezvous phase both in GTO and NRHO, the LST position along the R-bar axis shall be limited to ±8.5 m, corresponding to the initial radius of the LOS entry corridor.
- At the end of the close-range rendezvous phase both in GTO and NRHO, the LST position along the H-bar axis shall be limited to ±8.5 m, corresponding to the initial radius of the LOS entry corridor.
- At the end of the close-range rendezvous phase both in GTO and NRHO, the LST shall have a residual velocity along the minus V-bar axis less than or equal to 0.25 m/s.
- During the radial boost maneuver both in GTO and NRHO, the maximum number of monopropellant thrusters than can be contemporary operated shall be 5.
- During the entire ARVD maneuver, the MIB for the monopropellant thrusters shall be set to 0.526 Ns.
- The half-aperture of the LOS approach corridor shall be set to 8°.
- At the end of the final approach phase both in NRHO, the LST shall hover at a maximum relative distance from the target vehicle of 2 m along the minus V-bar axis to allow the berthing maneuver.
- At the end of the final approach phase both in GTO and NRHO, the deviation of the LST position along the R-bar axis shall be less than or equal to 0.5 m, i.e. defined as the final radius of the LOS approach corridor in the orbital plane.

- At the end of the final approach phase both in GTO and NRHO, the deviation of the LST position along the H-bar axis shall be less than or equal to 0.5 m, i.e. defined as the final radius of the LOS approach corridor in the out-of-plane direction.
- At the end of the close-range rendezvous phase both in GTO and NRHO, the LST shall have a residual velocity along the minus V-bar axis less than or equal to 0.05 m/s.
- During the radial boost maneuver both in GTO and NRHO, the maximum number of monopropellant thrusters than can be contemporary operated shall be 2.
- At the end of the ARVD maneuver both in GTO and NRHO, the LST attitude maximum deviation in terms of Euler angles with respect to the alignment among body frame and target LVLH shall be at most 2°.

Further constraints are inherited from the mission and design analysis in terms of maneuver duration, which shall be less than or equal to 12 h, and Hydrazine consumption according to the budget reported in Table 6.10.

The next step consisted in simulating the two main automated rendezvous maneuvers with the cargo module in GTO and the LOP-G in NRHO exploiting the 6DoF orbital simulator. The goal is to control the LST attitude and orbit dynamics while enforcing the requirements previously introduced properly designing three different MPC schemes, described in Chapter 5. In particular, in Section 6.2.1 the results obtained using LQMPC and TRMPC strategies in the presence of additive, bounded disturbance are presented and compared in terms of constraints satisfaction and control effort, i.e. the Hydrazine consumption. On the other hand, the results achieved exploiting the OS-SMPC are provided in Section 6.2.2, focusing on the validation of the effectiveness, reliability and real-time implementability of this innovative control scheme for ARVD maneuvers when chance-constraints are enforced, allowing a limited probability of constraints violation.

6.2.1 LQMPC vs TRMPC

As described in Section 5.3, the TRMPC control strategy allows to robustly satisfy the state and input constraints in the presence of bounded and persistent disturbance directly controlling the associated nominal (undisturbed) system dynamics, enforcing tightened constraint sets properly designed. According to the guidelines reported in the same Section, the first step consisted in estimating the feedback gain matrix K that quadratically stabilize the closed-loop system. In particular, a system of Lyapunov functions (5.9), built with respect to the uncertain matrices starting from (5.3), has been exploited in which the symmetric positive-definite matrices Q and R are the weighting matrices used in the finite horizon cost function J_T as well. In Table 6.13, the tightened constraints obtained exploiting classical robust tools are reported. Moreover, it is important to highlight that, in order to fairly compare the results obtained exploiting LQMPC and TRMPC, the same MPC setting parameters have been exploited and their values are reported in Table 6.14. In the follows, the main results obtained exploiting both LQMPC and TRMPC running a set of 5 simulations each are provided and thoroughly described.

Table 6.13: TRMPC tightened constraints for attitude and orbital control in terms of upper and lower bounds identified as *ub* and *lb*, respectively.

Parameter	**Orbit**	**Value**
$\mathbb{Z}^{lb}_{ORB_{FA}}$	GTO	[-499.996,-8.496,-8.496,0.001,-0.149,-0.149]
$\mathbb{Z}^{lb}_{ORB_{FA}}$	NRHO	[-499.999,-8.499,-8.499,0.0002,-0.1498,-0.1498]
$\mathbb{Z}^{ub}_{ORB_{FA}}$	GTO	[1.996,8.496,8.496,0.249,0.149,0.149]
$\mathbb{Z}^{ub}_{ORB_{FA}}$	NRHO	[1.999,8.499,8.499,0.2498,0.1498,0.1498]
$\mathbb{V}^{lb}_{ORB_{FA}}$	GTO	[-43.999,-43.999,-43.999]
$\mathbb{V}^{lb}_{ORB_{FA}}$	NRHO	[-43.9998,-43.9998,-43.9998]
$\mathbb{V}^{ub}_{ORB_{FA}}$	GTO	[43.999,43.999,43.999]
$\mathbb{V}^{ub}_{ORB_{FA}}$	NRHO	[43.9998,43.9998,43.9998]
$\mathbb{V}^{lb}_{ORB_{RB}}$	GTO	[-109.997,-109.997,-109.997]
$\mathbb{V}^{lb}_{ORB_{RB}}$	NRHO	[-109.999,-109.999,-109.999]
$\mathbb{V}^{ub}_{ORB_{RB}}$	GTO	[109.997,109.997,109.997]
$\mathbb{V}^{ub}_{ORB_{RB}}$	NRHO	[109.999,109.999,109.999]
$\mathbb{Z}^{lb}_{ATT}$	GTO	[-0.0381,-0.0324,-0.0425,-0.006,-0.003,-0.006]
$\mathbb{Z}^{lb}_{ATT}$	NRHO	[-0.0786,-0.0577,-0.0783,-0.0097,-0.0095,-0.0097]
$\mathbb{Z}^{ub}_{ATT}$	GTO	[0.0381,0.0324,0.0425,0.006,0.003,0.006]
$\mathbb{Z}^{ub}_{ATT}$	NRHO	[0.0786,0.0577,0.0783,0.0097,0.0095,0.0097]
$\mathbb{V}^{lb}_{ATT}$	GTO	[-0.0736,-0.0736,-0.0736]
$\mathbb{V}^{lb}_{ATT}$	NRHO	[-0.0743,-0.0743,-0.0743]
$\mathbb{V}^{ub}_{ATT}$	GTO	[0.0736,0.0736,0.0736]
$\mathbb{V}^{ub}_{ATT}$	NRHO	[0.0743,0.0743,0.0743]

Starting from attitude control, Figure 6.15 provides an overview of the Euler angles evolution over the entire ARVD maneuvers in GTO (Figure 6.15a) and in NRHO (Figure 6.15b). The first thing to observe is that in both environments, TRMPC always allows to guarantee the attitude constraint at the end of the maneuver, (almost) perfectly aligning the LST docking mechanism with the targets one in less than 300 s. Furthermore, it is important to highlight that the results of the 5 simulations are overlapped and show similar behaviors in GTO as well as in NRHO. On the other hand, the effects of torque disturbance are quite evident when the LQMPC is used and, even if in *most* cases at the end of the maneuver the ±1° pointing constraint is satisfied, the attitude controllability is slightly compromised

Table 6.14: LQMPC and TRMPC setting parameters.

Parameter	**Value**
system sample time [s]	1
MPC sample time [s]	3
T_{ATT}	30
T_{ORB}	30
$diag(Q_{ATT})$	$[10^6,10^6,10^6,10^6,10^6,10^6]$
$diag(R_{ATT})$	$[10^0,10^0,10^0]$
$diag(Q_{ORB_{RB}})$	$[5\cdot10^{-3},5\cdot10^{-3},5\cdot10^{0},5\cdot10^{-3},5\cdot10^{-3},5\cdot10^{0}]$
$diag(R_{ORB_{RB}})$	$[[10^1,10^1,10^1]$
$diag(Q_{ORB_{FA}})$	$[10^0,10^4,10^6,10^7,10^4,10^6]$
$diag(R_{ORB_{FA}})$	$[10^3,10^1,10^3]$

and it takes longer to reach the desired attitude. But it is possible to notice that in the Cislunar environment, where the noise is lower, the Euler angles behavior, especially along the x and z axis, is characterized by dumped oscillations and the LQMPC controllability results improved.

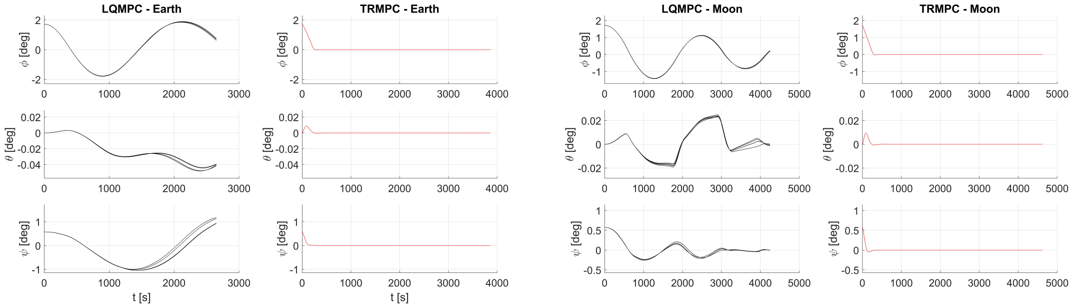

(a) GTO

(b) NRHO

Figure 6.15: LST Euler angles during the ARVD maneuver with cargo module (a) and LOP-G (b).

An analogous behavior can be spotted in Figure 6.16 where the LST angular velocity evolution is represented. Again, the LQMPC allows to satisfy the corresponding constraint with oscillations dictated from the disturbance that in the Cislunar environment are partially dumped whereas the TRMPC is able to zero the spacecraft angular velocity after a initial but limited peak. On the other hand, Figure 6.17 provides the RWs angular velocity, on one side retracing the spacecraft behavior and on the other side highlighting that TRMPC control effort is much higher than LQMPC one.

Figure 6.18a and Figure 6.18b show the LST 2D and 3D trajectories followed during the ARVD maneuvers with the cargo module and the Gateway, respectively,

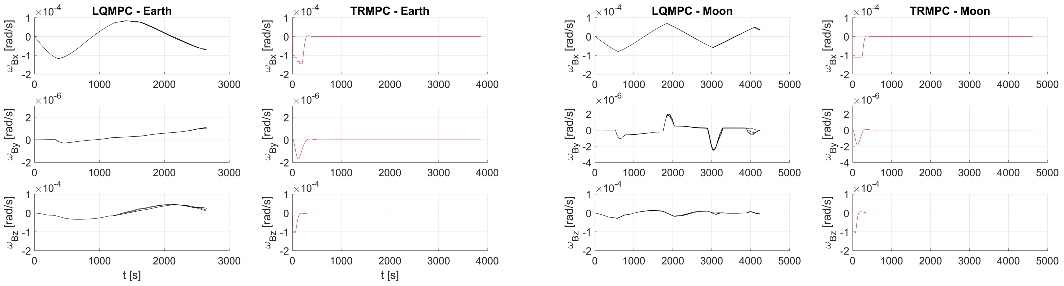

(a) GTO (b) NRHO

Figure 6.16: LST angular velocity during the ARVD maneuver with cargo module (a) and LOP-G (b).

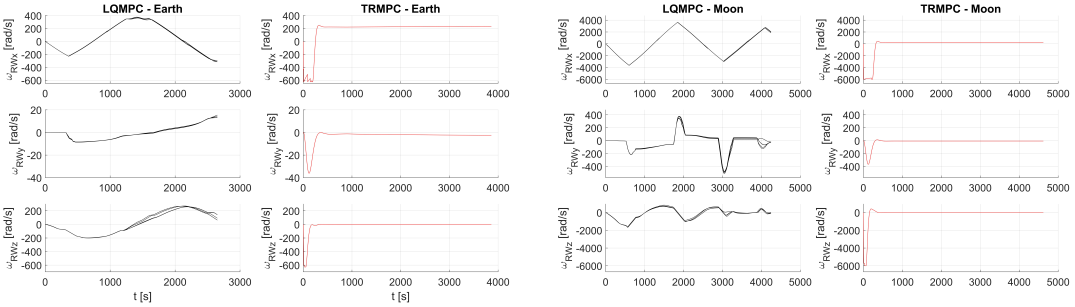

(a) GTO (b) NRHO

Figure 6.17: LST RWs angular velocity during the ARVD maneuver with cargo module (a) and LOP-G (b).

represented in the targets LVLH reference system. In the orbital plane, both controllers provide similar profile whereas significant differences can be observed in terms of the out-of-plane component. Indeed, while the TRMPC is able to reject the force disturbance effect maintaining the spacecraft close to the orbital plane, the LQMPC is not able to properly control the spacecraft and the external disturbances effect is amplified by a non perfect attitude control, as previously described.

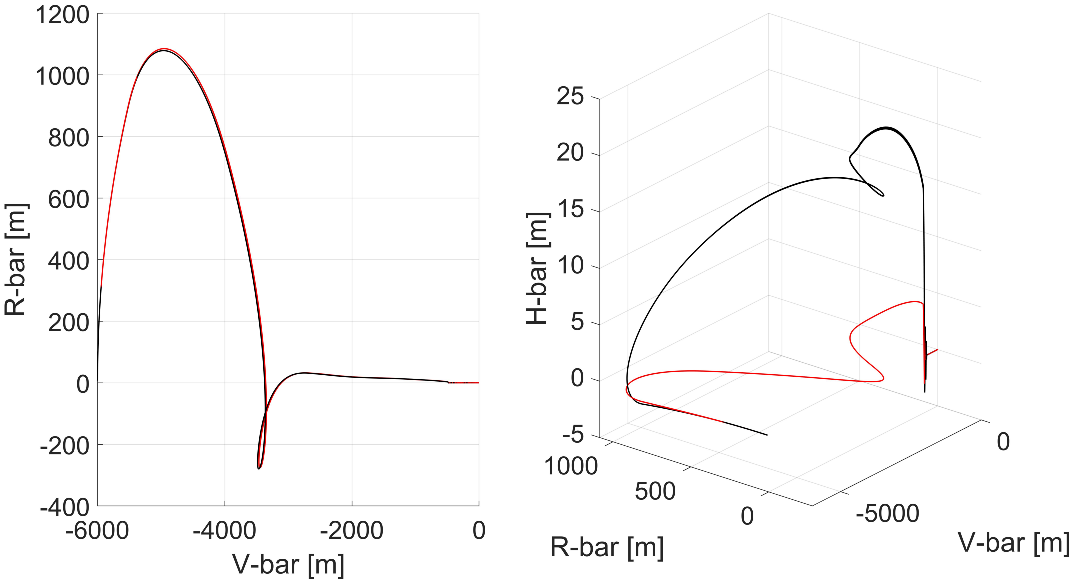

(a) GTO

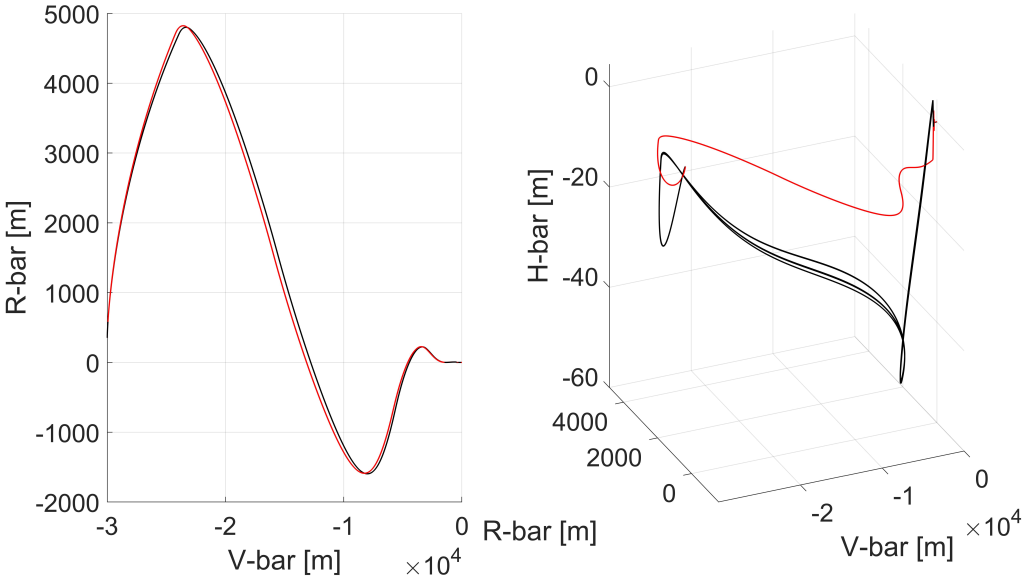

(b) NRHO

Figure 6.18: LST ARVD trajectories in the LVLH frame with cargo module (a) and the LOP-G (b) obtained exploiting LQMPC (black lines) and TRMPC (red lines) for the orbital control.

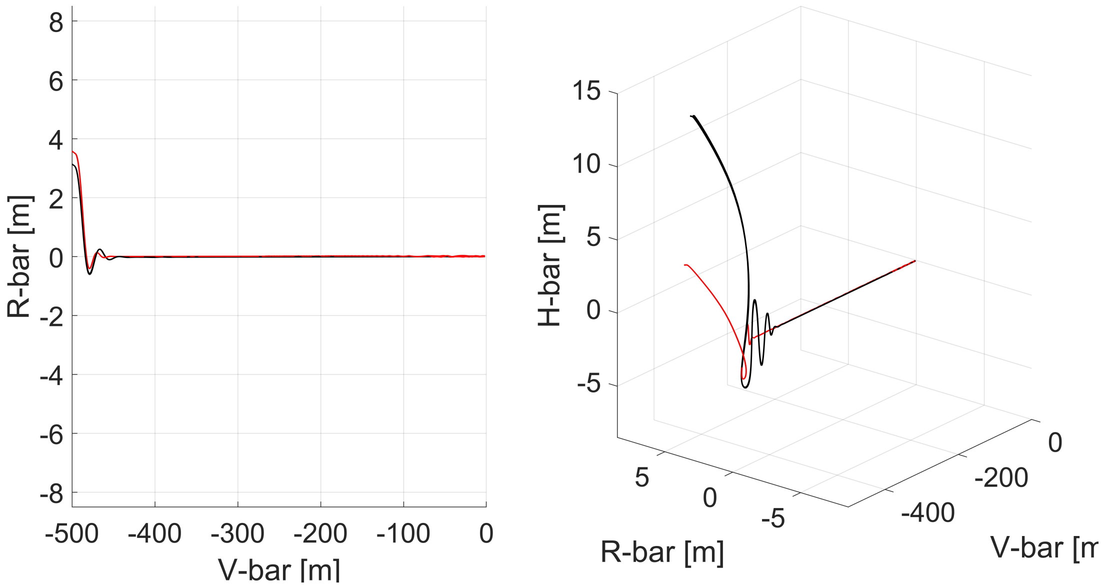

(a) GTO

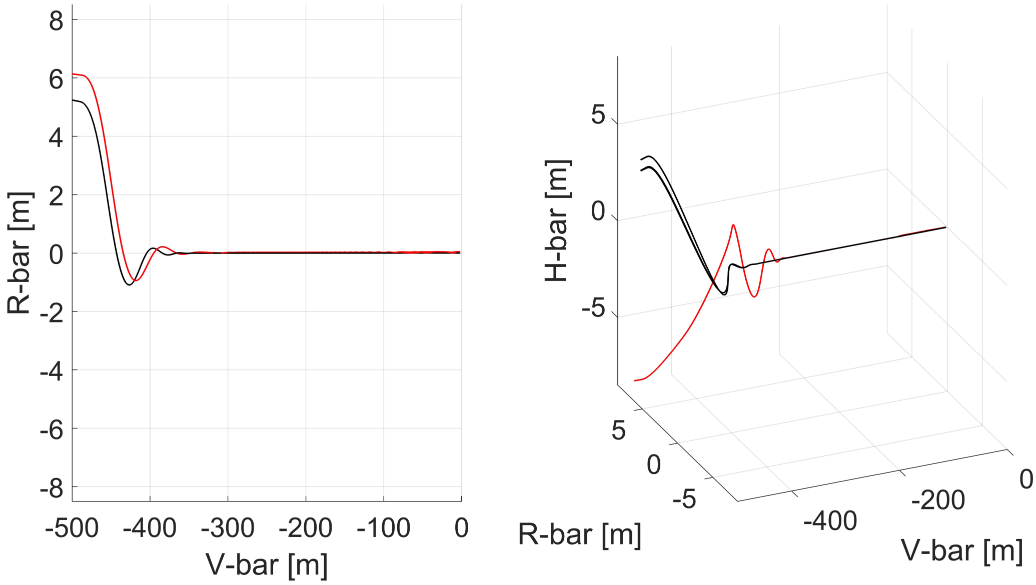

(b) NRHO

Figure 6.19: LST ARVD trajectories in the LVLH frame with cargo module (a) and the LOP-G (b) obtained exploiting LQMPC (black lines) and TRMPC (red lines) for the orbital control.

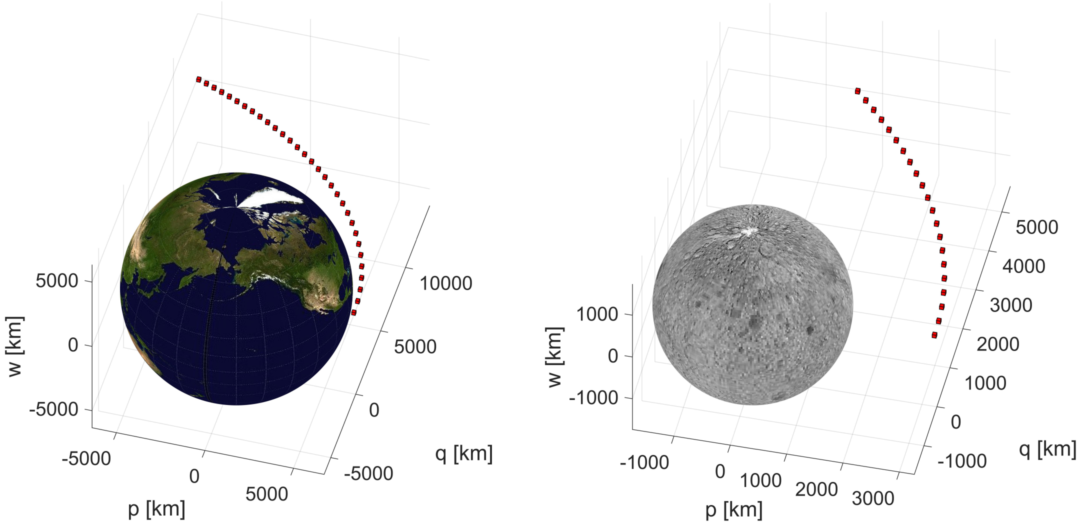

(a) GTO

(b) NRHO

Figure 6.20: LST ARVD trajectories in the perifocal frame with cargo module (a) and the LOP-G (b).

Focusing on the final approach phase, in Figure 6.19 it is possible to observe that both control schemes allows the LST to properly reach the entry corridor in the orbital plan with only slight differences and to approach the target along the V-bar axis, guaranteeing the mating operations, either docking with the cargo module or berthing with the Gateway. On the other hand, the 3D trajectories present a different scenario with respect to the H-bar direction. Indeed, in Figure 6.19a it is still relevant the effect of disturbance for the LQMPC trajectory, which it drives the chaser to initially miss the entry corridor and then, after a reasonable amount of time, to reach the approach axis, i.e. V-bar, to successfully complete the maneuver. On the other hand, TRMPC keeps the LST much closer to the orbital plane and, during the final approach phase, the spacecraft always remains within the 3D cone and properly mates the target, both in GTO and NRHO. Another overview of the LST trajectory is given in Figure 6.20a and Figure 6.20b, where the LST ARVD maneuvers in GTO and NRHO, respectively, are represented in the corresponding perifocal frames highlighting that the chaser takes less than a quarter of the orbit to reach and mate the target.

Figure 6.21 depicts the velocity profile in the target LVLH frame during both close-rang and final approach phases. In this case, no significant differences can be observed for the in-plane velocity components among LQMPC and TRMPC and in both case the velocity constraint at the end of the radial boost maneuver results satisfied. For what concern the out-of-plane component, along the H-bar axis, what it is important to highlight is the peak corresponding to the end of the radial boost maneuver at approximately 1500 s in GTO and 3000 s in NRHO, where the controller tries to reduce the corresponding position component and drives the chaser closer to the orbital plane.

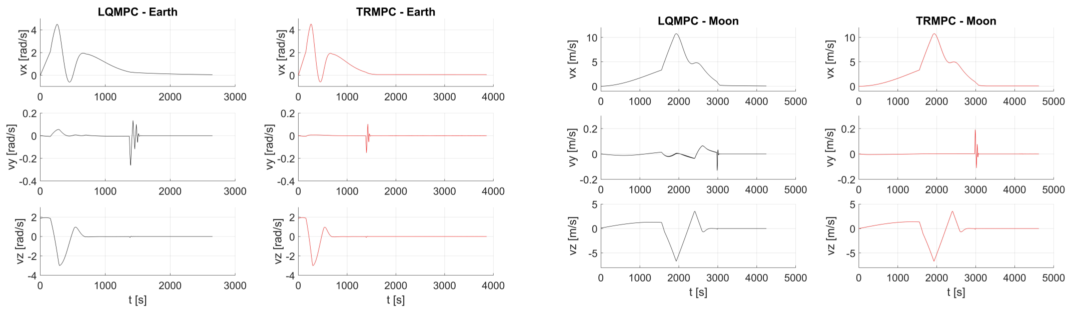

(a) GTO

(b) NRHO

Figure 6.21: LST velocity profile during the ARVD maneuver in the LVLH frame with cargo module (a) and the LOP-G (b).

This behavior is corroborated by the results shown in Figure 6.22 where the actuation profile of all 30 monopropellant thrusters is depicted. Indeed, taking into account those thrusters which thrusting direction is mainly along the y body axis, e.g. thrusters #1, #11, #16 and #26 according to the AOCS architecture represented in Figure 2.19b, it is possible to observe at $t = 1500$ s in GTO and at $t = 3000$ s in NRHO multiple close-range peaks.

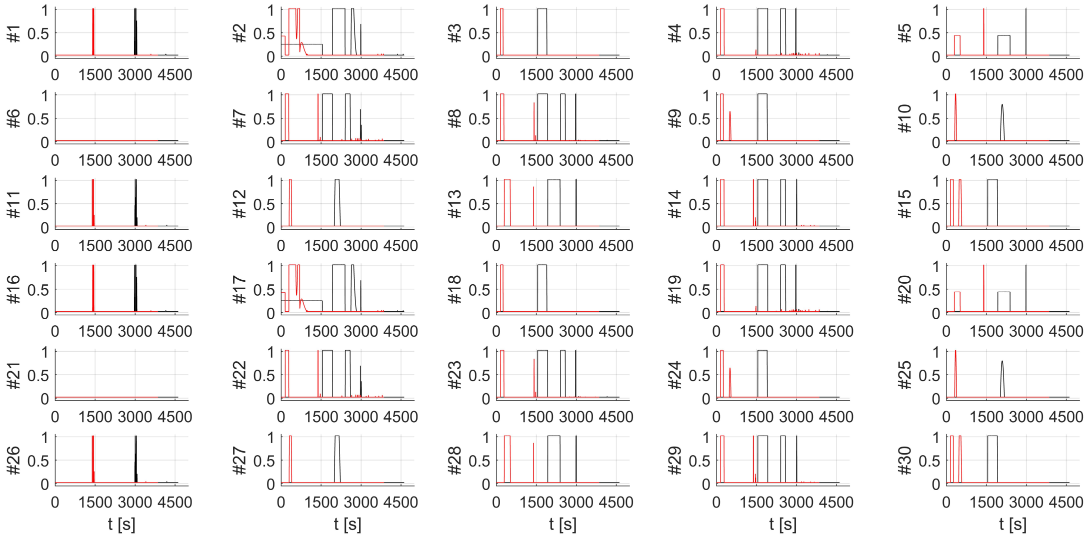

Figure 6.22: Thrusters actuation during the ARVD maneuvers with cargo module (red lines) and the LOP-G (black lines).

Last, Figure 6.23 summarizes the Hydrazine consumption during the ARVD maneuvers required when TRMPC and LQMPC are exploited. In particular, Figure 6.23a represents the total fuel consumption required for the entire maneuver and it shows a much higher fuel demand, almost 80 kg of Hydrazine, to rendezvous with the LOP-G while only 30 kg are sufficient for the ARVD maneuver in GTO with the cargo module, despite the control strategy exploited. The larger demand is mainly due to the longer distance to cover. On the other hand, a slight difference can be observed within the same environment. Indeed, comparing the fuel request for TRMPC and LQMPC, opposite behaviors can be observed. In particular, in Earth proximity, TRMPC allows to slightly save fuel keeping the chaser in the proximity of the orbital plane, whereas the LQMPC higher consumption is required to feed the out-of-plane control phase. On the other hand, in Moon proximity, the higher fuel consumption characterizes the TRMPC approach, corroborating the expectations. Indeed, typically robust constraint satisfaction implies higher control effort. However, in both cases the fuel demand is lower than the allocated amount during the design phase. On the other hand, Figure 6.23b depicts the fuel consumption trends during the different ARVD phases. The results highlight that the less demanding phase is represented by the uncontrolled radial boost, where the thrust profile is only defined according to the guidance one. On the contrary, the controlled part of the close-range phase is the most demanding, corresponding to about the 75% of the total Hydrazine consumption.

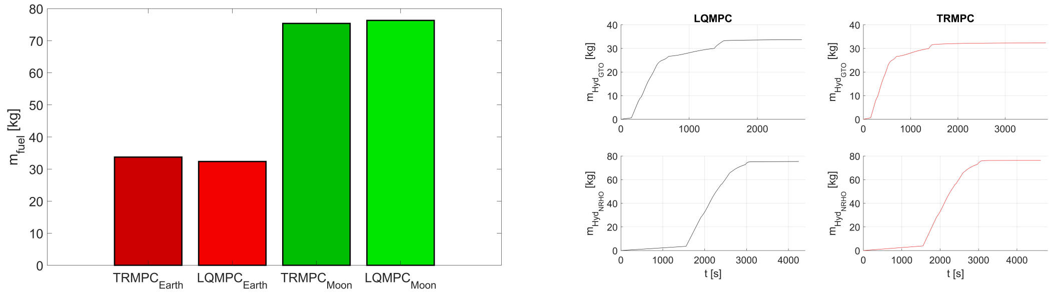

(a)

(b)

Figure 6.23: Fuel consumption during the ARVD maneuvers exploiting LQMPC and TRMPC: (a) total Hydrazine demand in GTO (red bars) and in NRHO (green bars) and (b) time evolution over the entire maneuver.

To conclude this comparison, the last performance parameter analyzed is the ARVD maneuver duration, which shall last less than 12 h according to the operational constraints introduced in Section 6.2. Figure 6.23b highlights how the drawback to robustly satisfy the operational constraints exploiting the TRMPC scheme corresponds to a quite longer maneuver. The difference results more significant in GTO, where TRMPC requires almost 4000 s to complete the maneuver whereas LQMPC less than 3000 s, i.e. about 17 minutes less. On the other hand, the TRMPC and LQMPC in NRHO are characterized by similar mission duration, 4620 s the former and 4247 s the latter. In all four cases, the mission constraint results satisfied.

These results have been validated through extensive experimental campaigns performed at the Spacecraft Robotics Laboratory of the NPS as throughly described in Section 6.3.

Table 6.15: OS-SMPC setting parameters.

Parameter	**Value**
system sample time [s]	1
MPC sample time [s]	3
T_{ATT}	10
T_{ORB}	10
ε	0.05
δ	0.01
$N_{samples}$	284,588
$N_{constraints_{in}}$	8,411,496
$N_{constraints_{red}}$	26,730
$diag(Q_{ATT})$	$[10^6,10^6,10^6,10^6,10^6,10^6]$
$diag(R_{ATT})$	$[10^0,10^0,10^0]$
$diag(Q_{ORB_{RB}})$	$[5 \cdot 10^{-}3,5 \cdot 10^{-3},5 \cdot 10^0,5 \cdot 10^{-3},5 \cdot 10^{-3},5 \cdot 10^0]$
$diag(R_{ORB_{RB}})$	$[10^1,10^1,10^1]$
$diag(Q_{ORB_{FA}})$	$[10^0,10^4,10^6,10^7,10^4,10^6]$
$diag(R_{ORB_{FA}})$	$[10^3,10^1,10^3]$

6.2.2 OS-SMPC

In this Section, the results obtained exploiting the OS-SMPC algorithm are provided and throughly described. It is important to recall that the same constraints previously introduced have been applied to all 50 simulations run. On the other hand, a 5% of probability of constraint violation is allowed, with a confidence of 99%. For what concern the main MPC parameters adopted, they are reported in Table 6.15 together with the number of samples drawn offline $N_{samples}$, the initial number of constraint inequalities $N_{constraints_{in}}$ and the final one, i.e. $N_{constraints_{red}}$, obtained applying the algorithm of redundant constraint reduction. It is important to highlight that the prediction horizon has been reduced both for attitude and orbital control in order to limit the size of the SMPC problem whereas its properties are still guaranteed properly defining the minimum number of samples to draw according to ε and δ. Moreover, the robustly stabilizing feedback gain matrix K has been evaluated offline exploiting typical robust tools, as in the TRMPC case.

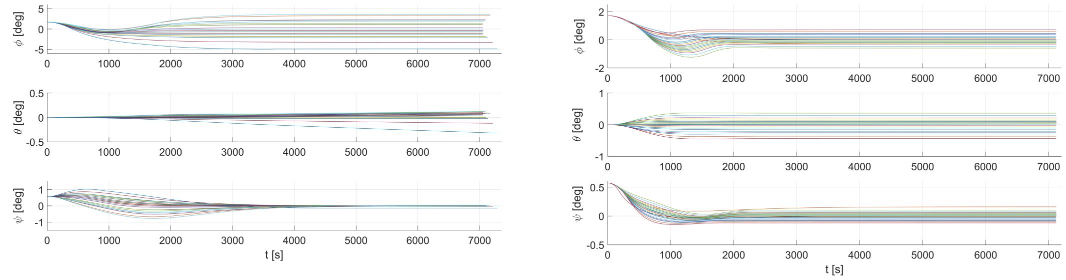

(a) GTO

(b) NRHO

Figure 6.24: LST Euler angles during the ARVD maneuver with cargo module (a) and LOP-G (b).

Starting from attitude control, Figure 6.24 shows the Euler angles evolution for all 50 simulations, highlighting the varying effects of uncertainty and disturbance over the LST orientation. The first thing to observe is that in both environments, the OS-SMPC tries to drive the LST attitude towards the desired alignment. However, only in few cases, the zero-attitude is reached at the end of the ARVD maneuvers. Indeed, in most cases the attitude reaches a stable condition close to the desired one as very clearly shown in Figure 6.24b and by the yaw angle ψ in Figure 6.24a. On the other hand, in GTO the more intense torque disturbances bring the roll angle ϕ to violate the $\pm 1^\circ$ constraint is several cases whereas the pitch angle θ shows a slightly divergent behavior in some simulations. The current results show that over the 10% of the ARVD maneuvers simulated in GTO violate the constraint related to the roll angle, whereas for all other Euler angles and the whole set of simulation in NRHO the constraints are always satisfied.

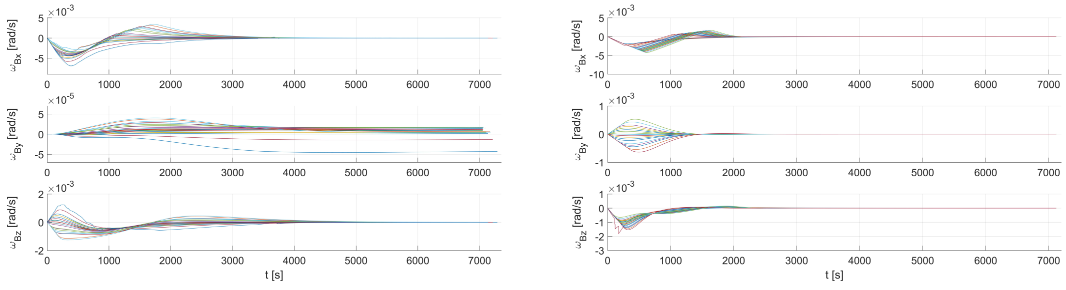

(a) GTO

(b) NRHO

Figure 6.25: LST angular velocity during the ARVD maneuver with cargo module (a) and LOP-G (b).

Figure 6.25a and Figure 6.25b provide an overview of the LST angular velocity experienced in GTO and NRHO, respectively. It is possible to notice that in both cases, all the components converge to zero even if with two different rates. In GTO, the LST takes over 4000 s to (almost) nullify the angular rate after initial deviations due to the significant torque disturbance acting on the spacecraft. For the angular rate with respect to the y body axis, the results retrace the analogous behavior of the corresponding pitch angle and very limited deviations are experience, i.e. in the order ot 10^{-5}. On the other hand, during the ARVD simulated maneuvers with the LOP-G, the effects on ω_{B_y} are of the same order of those affecting ω_{B_x} and ω_{B_z}, i.e. about 10^{-3}. However, after 2000 s the angular rate goes to zero and stays there until the end of the maneuver.

Figure 6.26 shows the ARVD trajectories in GTO (Figure 6.26a) and in NRHO (Figure 6.26b) in th corresponding perifocal frames, highlighting that exploiting the OS-SMPC scheme the maneuver duration is significantly increased with respect to the one experienced exploiting LQMPC and TRMPC.

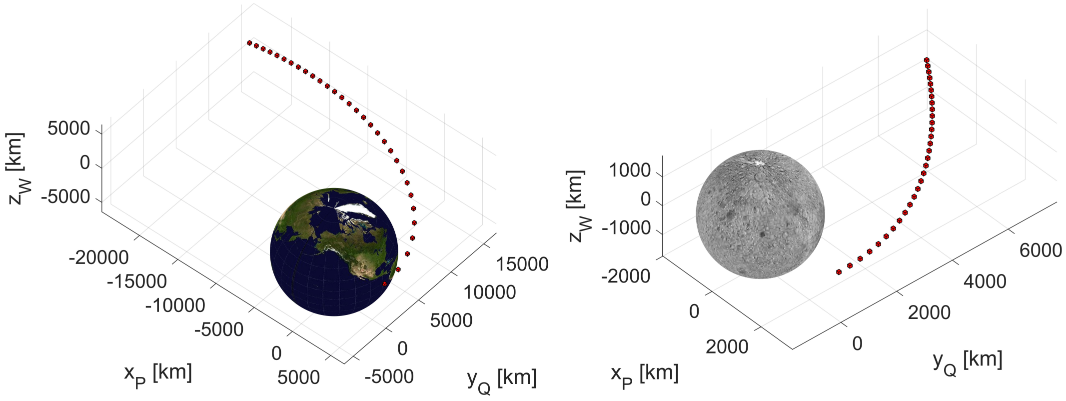

(a) GTO

(b) NRHO

Figure 6.26: LST ARVD trajectories in the perifocal frame with cargo module (a) and the LOP-G (b).

Figure 6.27a depicts the LST 2D and 3D LVLH trajectories obtained exploiting the OS-SMPC algorithm during the ARVD maneuver with the cargo module. First, it is possible to notice that in the orbital plane, all the 50 trajectories are mostly overlapped and no significant discrepancies can be observed. Moreover, the LST completes the radial boost maneuver and properly reaches the entry corridor, along the approach axis as highlighted in 6.27b.

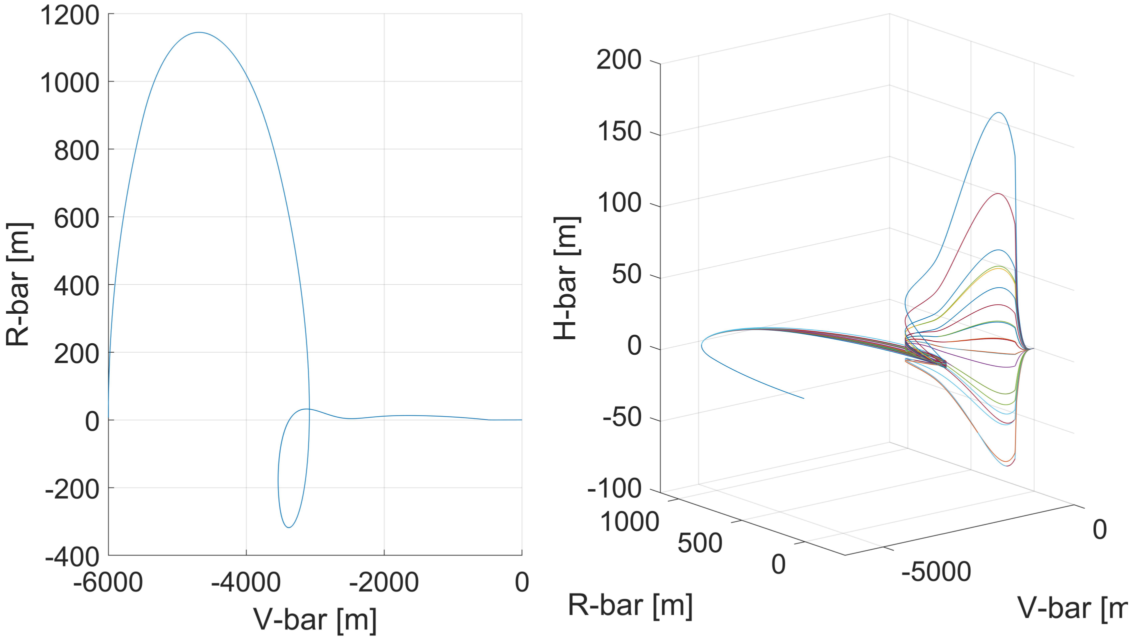

(a) GTO

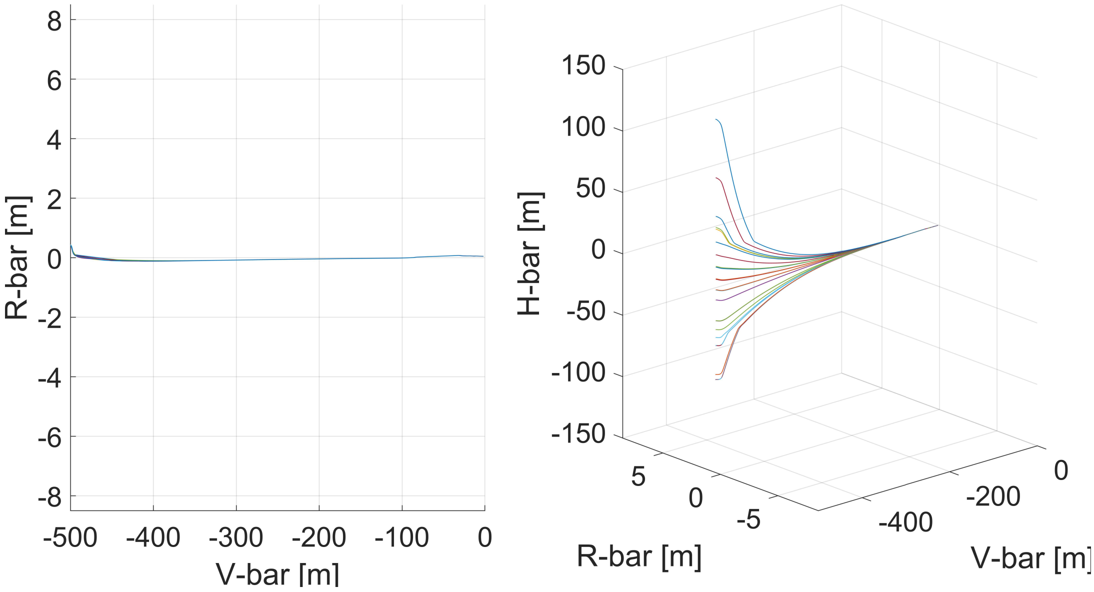

(b) NRHO

Figure 6.27: LST ARVD trajectories in the LVLH frame with the cargo module: (a) complete trajectory and (b) final approach.

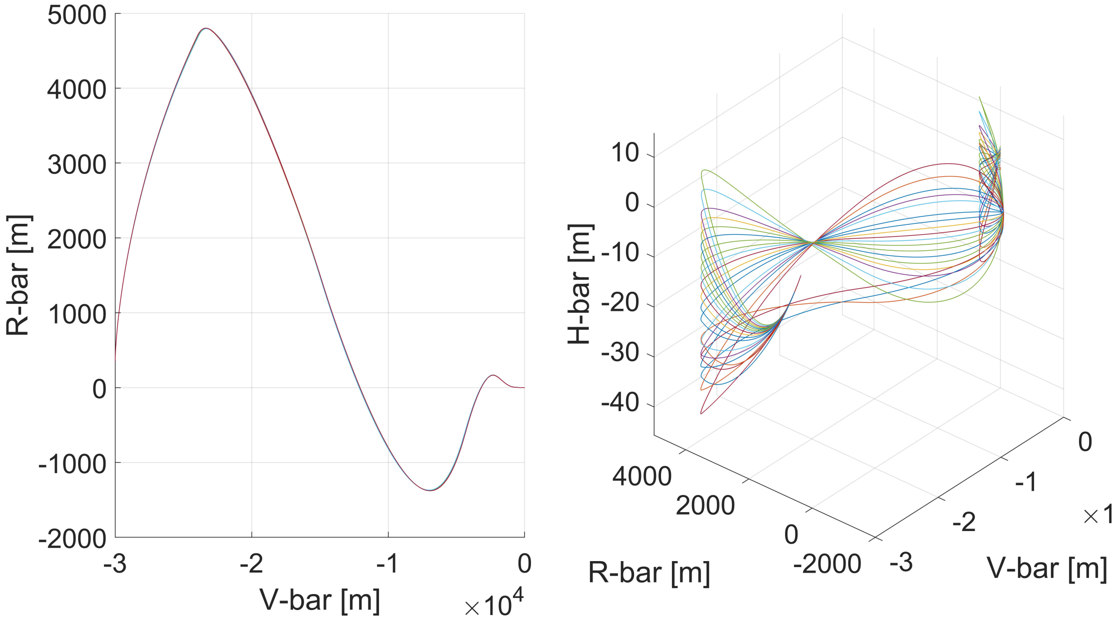

(a) GTO

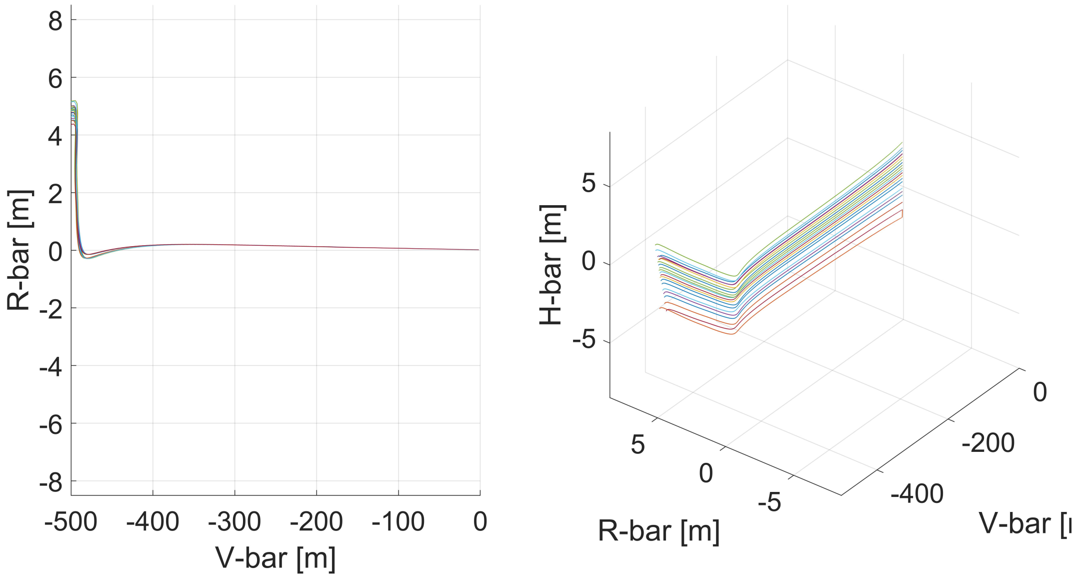

(b) NRHO

Figure 6.28: LST ARVD trajectories in the LVLH frame with the cargo module: (a) complete trajectory and (b) final approach.

On the other hand, different behavior is witnessed by the out-of-plane motion. Indeed, it is evident the effect of the divergence of the pitch angle on the trajectory that during the second part of the maneuver significantly moves away from the target up to 150 m along the H-bar axis. Furthermore, during the final approach phase, the control algorithm is able to drive the spacecraft to properly reach and dock the target, minimizing during the first 200 m along V-bar the gap with respect to the approach axis. Figure 6.28a represents the results obtained while simulating the ARVD maneuver with the LOP-G. For the orbital plane, it shows a behavior similar to the one observed in GTO, guaranteeing the LST to properly entry the approach corridor within the pre-defined constraints. Analogously, the out-of-plane component of the trajectory significantly moves away along the H-bar axis, during the entire close-range phase, but with smaller deviations, i.e. at most 40 m. Unlike the previous case, at the end of the radial boost maneuver, the LST properly enters the approach corridor in all 50 simulations, i.e. the H-bar components is within the entry radius. However, due to the convergence of the pitch angle to a neighborhood of the ideal attitude, in most cases the LST stays far from the orbital plane and in some cases does not allow to complete the rendezvous maneuver properly. On the other hand, these results can be still considered as reliable since for berthing maneuvers, less demanding constraints can be envisioned, as highlighted in [66]. Indeed, as in the case of LST mating with the LOP-G through the use of the Gateway robotic arm, the berthing box can be typically enlarged five times more with respect to the docking box, which defines the terminal constraints enforced in this study.

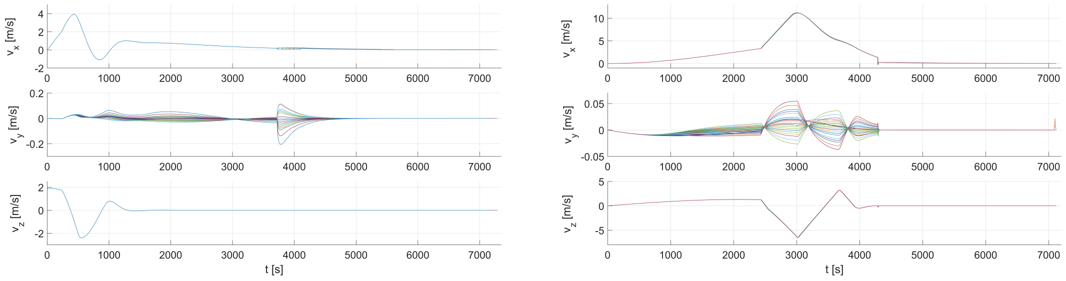

(a) GTO

(b) NRHO

Figure 6.29: LST velocity profile during the ARVD maneuver in the LVLH frame with cargo module (a) and the LOP-G (b).

Last, Figure 6.29a and Figure 6.29b provides the LST velocity behavior during the ARVD maneuver with the cargo module and the Gateway, respectively. In both cases, the velocity constraints are satisfied and the velocity profile in the orbital plane retraces the one already observed in Figure 6.21. The main difference can be noticed along the H-bar axis, where a significant effort is experience during the second part of the radial boost maneuver in GTO at about 4000 s whereas a more distributed effort can be observed in NRHO until the chaser completes the close-range phases and enters the entry cone.

As anticipated before, exploiting the OS-SMPC implies longer maneuver duration, i.e. about 2 h, and, as a consequence, the Hydrazine consumption is higher as well. Indeed, as represented in Figure 6.30, the total average cost in terms of fuel for the ARVD maneuver with the cargo module requires about 60 kg, 50% higher than the corresponding effort required exploiting LQMPC and TRMPC. Analogously in NRHO, the LST requires about 100 kg of Hydrazine, 20 kg more than the previous cases. Moreover, another difference can be observed for both ARVD maneuvers. After an initial linear trend related to the uncontrolled radial boost phase, similar to the one detected for LQMPC and TRMPC, in GTO the control close-range maneuver remains the most fuel demanding but the propellant consumption during the final approach does not settle around an (almost) fixed value but it requires about 20 kg of fuel. On the other hand, in NRHO the fuel mass has a strictly increasing behavior and the transition among the radial boost to the final approach is not evident anymore.

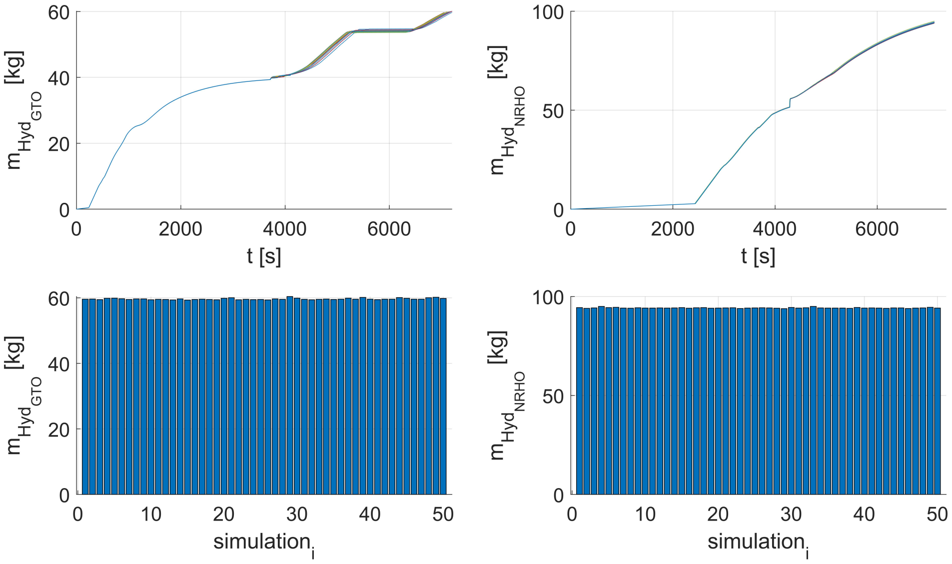

Figure 6.30: Time evolution of the fuel consumption during the ARVD maneuvers exploiting OS-SMPC over the entire maneuver and total Hydrazine demand in GTO and in NRHO.

To conclude this analysis, it is crucial to analyze the computational compliance of the OS-SMPC with the execution time constraint, i.e. 3 s for the MPC sample time. At this end, the execution time required to solve on-line the OS-SMPC problem has been registered and reported in Figure 6.31. It can be observed that, in the majority of cases, the execution time is well below 3 s, especially in NRHO both for the attitude and orbital control. On the other hand, over the entire maneuver in GTO, the OS-SMPC for attitude control requires a computational cost higher than the available in two different cases.

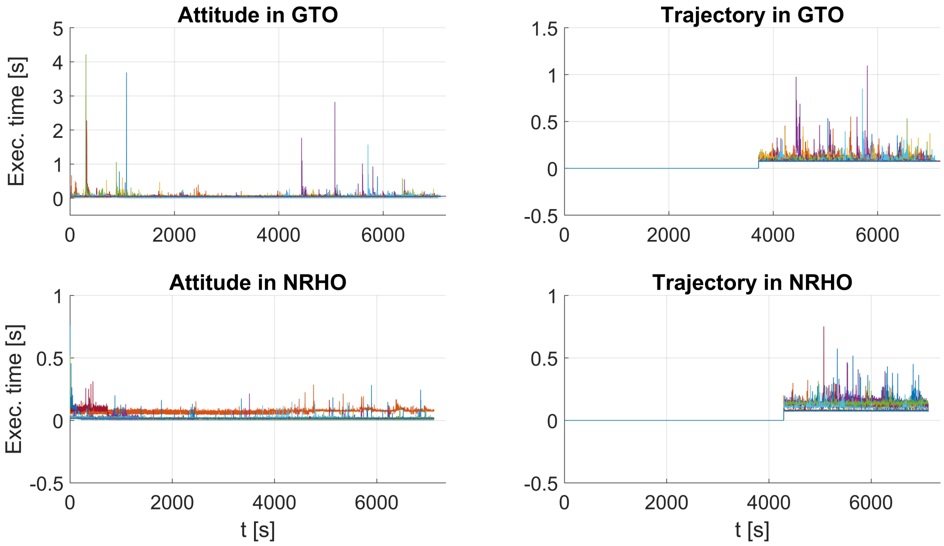

Figure 6.31: Execution time for solving on-line the OS-SMPC problem for both attitude and trajectory control in GTO and NRHO.

These results show that adopting on-board the LST a micro-controller with computational capability similar to the one of the hardware exploited for running these simulations, the proposed OS-SMPC can be solved in real-time. Thus, the real-time implementability of the OS-SMPC scheme can be considered partially verified. Further validation campaign have been performed through an experimental campaign, described in the following Section. Moreover, as anticipated before, the third phase of the validation process consisted in designing a tracking OS-SMPC for UAV path following applications, characterized by dynamics faster than the aerospace ones and less performing hardware (see Appendix B for further details).

6.3 Experimental Validation of MPC Schemes

In this Section, the experimental activities performed at the Spacecraft Robotics Laboratory of the NPS, Monterey, California, under the supervision of Professor Marcello Romano are presented and the main results are described. Thanks to the collaboration of Prof. Romano's research group, the control algorithms introduced in Chapter 5 have been validated through an extended experimental campaign exploiting the Proximity Operation of Spacecraft: Experimental hardware-In-the-loop DYNamic (POSEIDYN) simulator.

Two experimental campaigns have been performed during the six months spent at the NPS as visiting researcher. The first one was carried out between July and September 2016 and it was focused on the design, implementation and comparison of the LQMPC and TRMPC algorithms. On the other hand, from June to August 2017, the OS-SMPC scheme has been implemented and validated, comparing the results with those obtained exploiting the SMPC algorithm presented in [162] where only parametric uncertainties are taken into account. Moreover, a fuel-efficient approach has been designed for both LQMPC and TRMPC and an additional experiments have been performed to compare the new results with those obtained during the first experimental campaign, where the propellant consumption did not represent an optimization variable. The main goal of the these experiments was to test the real-time implementability of those control schemes while comparing their performance in the presence of either parametric uncertainty, due to the simplified neglected nonlinearities of the dynamics and geometric uncertainties with respect to the mass and inertia tensor of the FSS itself, and internal and environmental disturbances. The experimental campaign has been carried out implementing the algorithms on a space-qualified micro-controllers equipped on board the FSS, a robotic vehicle emulating orbital spacecraft during close proximity operations and floating over a granite table. Further details of the POSEIDYN testbed are provided in the following Section.

6.3.1 POSEIDYN Testbed and Experimental Setup

The NPS POSEIDYN simulator is an experimental testbed build up to provide a representative system-level platform upon which it is possible to design, implement and experimentally test and validate GNC algorithms.

As represented in Figure 6.32, POSEIDYN is composed by four main elements: (i) a 15 ton, 4-by-4 meter polished granite monolith, with a planar accuracy of ±0.0127 mm and a horizontal leveling accuracy at least 0.01 deg; (ii) FSSs, representing either chaser and target vehicles, according to the docking interface mounted on them (see Figure 6.33); (iii) a commercial motion capture system, composed by ten overhead Vicon cameras [178], which accurately determines the position of objects carrying passive markers (i.e. the FSS); and (iv) a ground station computer, providing the communication capabilities with both the FSS and the Vicon system via Wi-Fi and the real-time telemetry displayed for operators.

The FSS, shown in Figure 6.33, are customized robots able to emulate the 3 DoF dynamics, two translation and one rotational, of real spacecraft floating on the granite table thanks to three 25 mm air bearings, which use compressed air, stored in a small tank holding 1.87 liters of compressed air at 3000 psi (206.8 bars),

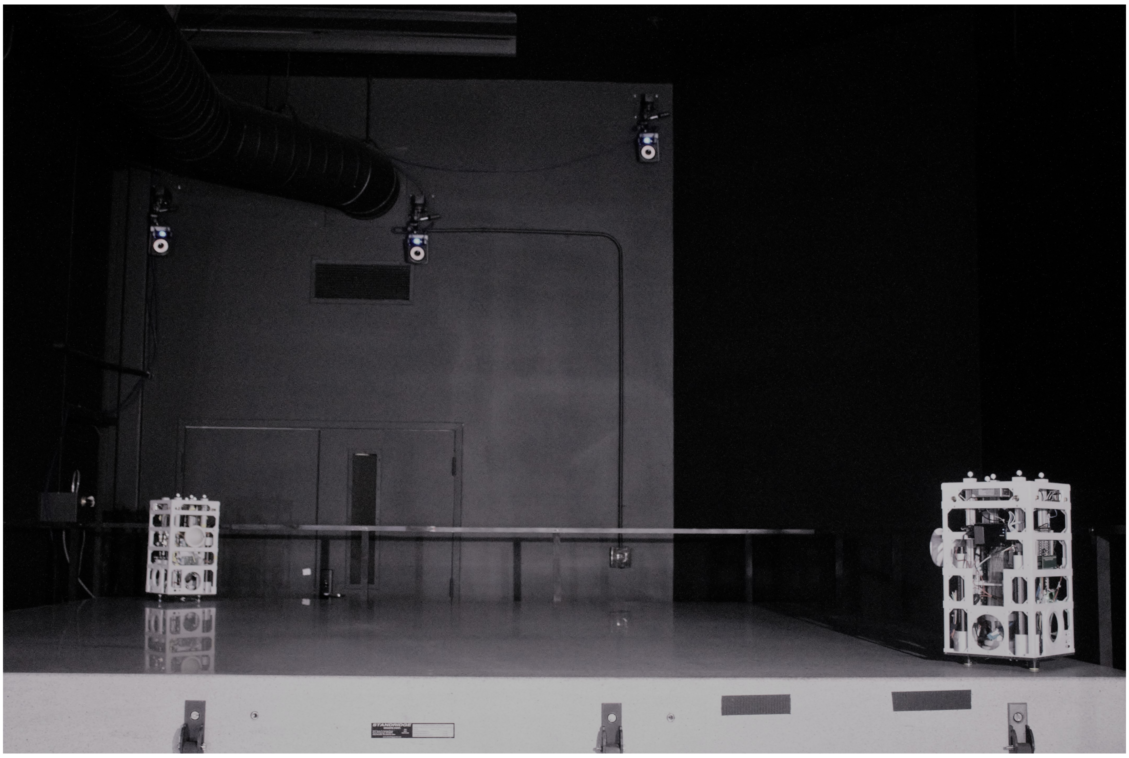

Figure 6.32: POSEIDYN testbed in the NPS Spacecraft Robotics Laboratory. On the granite table, the two FSS and, in the background, three of the Vicon cameras.

to lift the FSS approximately 5 μm. Eight cold-gas thrusters, two for each top corner of the vehicle, represent the propulsive core of the FSS, each one providing a maximum thrust of 0.15 N, and they are controlled via a Sigma-Delta Modulation method, as described in [179]. The main FSS physical properties are resumed in Table 6.16, in terms of mass, geometry, and moment of inertia.

Table 6.16: Summary of relevant FSS Physical Properties.

Parameter	Value
Dry Mass [kg]	9.465 ± 0.001
Wet Mass [kg]	9.882 ± 0.001
Dimensions [m]	$0.27 \times 0.27 \times 0.52$
Moment of Inertia [kg·m^2]	0.2527

The on-board computational capabilities of the FSS are provided by a PC-104 form-factor on-board computer, based on an Intel Atom 1.6 GHz 32-bit processor, with 2 GB of RAM and an 8 GB solid-state drive. Moreover, as described in [180],

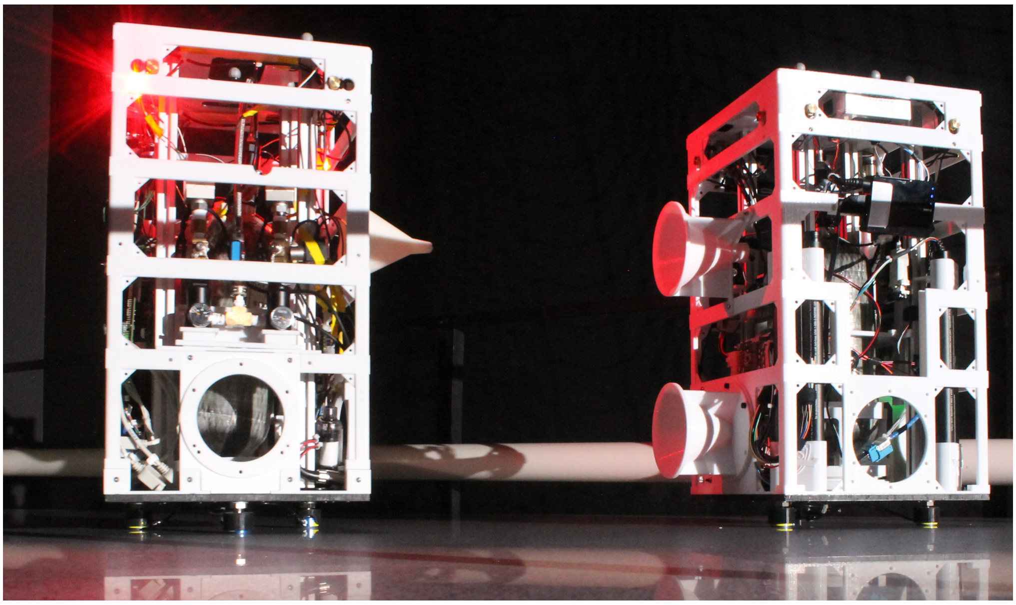

Figure 6.33: The FSS chaser vehicle (left) is equipped with a male conic docking interface while on the right the target FSS with a female funnel-like interface.

a real-time operating system represents the core of the FSS software architecture and the desired real-time requirement is ensured by the adoption of a Ubuntu 10.04, 32-bit server-edition OS and its Linux kernel 2.6.33. The multi-rate GNC software runs atop of this and the Simulink model is auto-coded into C, compiled and sent from the ground station to the FSS via Wi-Fi, loading the software on the vehicle on-board computer.

For the code generation, two different MATLAB/Simulink templates have been developed by the Prof. Romano's research Group, one for the development phase and one for the experimental tests, in order to simplify the algorithm design and implementation processes on the FSS. Both the templates are based on a custom library which contains common software for the navigation and control subsystems, on one side to simulate sensors, actuators and the plant, i.e. FSS, for the SIL validation phase and on the other side to interface the FSS with the real on-board sensors and cold-gas thrusters. The commonalities among the simulator and on-board software allow to easily implement the GNC algorithm in the simulation environment first and then, when ready, generate the FSS on-board software only copying and pasting from one template, i.e. simulator, to the other, i.e. real software, the GNC block. Additional information about the testbed are provided in [180], where the simplified procedure to develop and consequently implement the GNC algorithm on-board the FSS are exhaustively described.

Quadratic Solvers Overview for Real-Time Implementability

In this section, implementation issues related to real-time applicability of the proposed scheme are discussed, showing how it is possible to envisage the application of the LQMPC, TRMPC and OS-SMPC in an on-board implementation. In fact, MPC control schemes are well known for their inherent high computational cost, which has limited their applicability for a long time. On the other hand, the increase capabilities of the current micro-controllers exploited also in space applications and the improved optimization methods developed in the last decades allow to exploit embedded MPC algorithms. In particular, several new solvers, both commercial and public, are available to solve the optimization problem, each one characterized by peculiar features according to the principal field of applications and corresponding needs for which they have been conceived. Moreover, the size of the problem easily increases when a sampling-based SMPC scheme is envisioned, due to high number of constraints involved. Even if the offline sampling approach allows to significantly scale down the problem size and the corresponding online computational effort with respect to other sampling-based method which require online sampling, as e.g. [181, 174], a meticulous analysis of available solvers to be implemented in the embedded micro-controller is still mandatory and it's here provided.

Several solvers have been tested to evaluate their computational capabilities and limitations with respect to embedded implementation. Moreover, since hardware GNC software running on the FSS is developed in a MATLAB/Simulink environment, the selection criteria for the solver analyzed was driven by the compatibility with this environment and available MATLAB interface. The tested solvers were: (i) IBM ILOG CPLEX Optimizer [182], a decision optimization software developed by IBM which provides flexible, high-performance mathematical programming solvers also for quadratic programming problems; (ii) Mosek [183], a tool for solving mathematical optimization problems such as convex quadratic problems based on a powerful state-of-the-art interior-point optimizer; (iii) Gurobi Optimizer [184], a state-of-the-art solver for mathematical programming, designed from the ground up to exploit modern architectures and multi-core processors, using the most advanced implementations of the latest algorithms, including a quadratic programming solver; (iv) *quadprog*, the interior-point-convex algorithm provided by the MATLAB Optimization Toolbox to solve quadratic programming problem; (v) *fastmpc* exploits the structure of the quadratic programming that arise in MPC, obtaining an innovative online optimization tool, based on an interior-point method, able to evaluate the control action about 100 times faster than a method that uses a generic optimizer, as presented in [185]; (vi) *quadwright*, a quadratic programming solver developed by J. Currie at al., presented in [186], able to speed up the computational capabilities for embedded applications.

IBM CPLEX and Gurobi are commercial softwares that provide quite easy

MATLAB interfaces, enabling the user access to higher performing state-of-the-art solvers. However, both optimizers are not hardware-driven even if they provide embedding methods, and they showed bad memory leaks when calling the solver many times. Mosek is a tool for solving mathematical optimization problems, and in particular, convex quadratic problems. The software provides replacements for some MATLAB functions, including *quadprog*, and showed a rather high computational time when facing the large number of constraints involved in our setup. The MATLAB *quadprog* gives the possibility to choose between two different approaches: (i) an interior-point-convex method; and (ii) an active-set method. The first algorithm handles only convex problems whereas the second one, identified as trust-region-reflective algorithm, is able to manage problems with only bounds, or only linear equality constraints, but not both. In both cases, MATLAB *quadprog* showed slower performance than Mosek, and moreover it cannot be C-compiled. For what concerns the *fastmpc* solver, it has been developed to speed up MPC computational time and it has been proved to be able to compute in approximately 5ms the control actions for a problem with 12 states, 3 inputs, 30 as prediction horizon and about 1300 constraints. However, even if the number of states and inputs was lower for our problem, as well the prediction horizon is smaller, the much higher number of constraints resulted in a degeneration of its performance.

The final choice fell on the quadratic programming solver *quadwright*. This very fast solver, developed with a focus on efficient memory use, ease of implementation, and high speed convergence, is based on the optimization algorithm proposed in [187]. This approach has been specifically developed to handle the core problem in MPC, namely control of a linear process with quadratic objectives subject to general linear inequality constraints. In particular, the algorithm does not exploit sparsity and it has been refined by pre-factorizing where possible, using the Cholesky Decomposition factorization when required, and heuristic for warm start, as reported in [186]. The *quadwright* solver performance have been compared with other commonly used solvers, such as MATLAB *quadprog* and CVXGEN [188], which have shown uncompetitive solve times, they have in some case the drawback of being associated to large source libraries and being not compatible with hardware implementation. The chosen solver has been implemented on board two different hardware platforms, i.e. a Texas Instruments 32bit micro-controller and an ARM microprocessor, for the Processor-In-the-Loop validation and the results of the test campaign are presented in [186].

6.3.2 Model Setup

To design the control architecture, the initial point consisted in deriving a continuous-time description of the Chaser dynamics to obtain the following uncertain state-space formulation

$$\dot{x} = A(q)x + B(q)u + w, \tag{6.1}$$

in which w is the vector of iid, zero-mean, random disturbance defined in the bounded and convex set $\mathbb{W} \subset \mathbb{R}^n$ containing the origin, and q is the vector of parametric uncertainty $q \in \mathbb{Q} \subset \mathbb{R}^{n_q}$, realization of iid n_q multivariate real valued random variables.

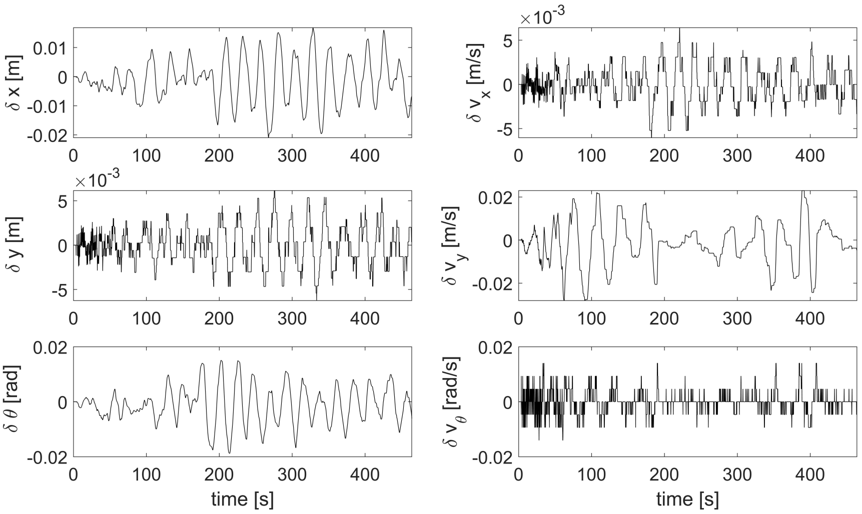

Figure 6.34: NPS-POSEIDYN testbed environmental disturbance.

For the determination of the environmental persistent disturbances acting on the POSEIDYN testbed, several preliminary experiments have been performed considering the same initial conditions and the results compared with the one obtained in the simulation environment. Indeed, the average discrepancies among the simulated states time evolution and the corresponding ones obtained during the first test campaign allowed to estimate the disturbances inherent to the experimental setup, which has been used in the definition of the disturbance polytope exploited in the controllers design phase. Figure 6.34 provides an overview of the disturbance affecting the position, i.e. $\delta\mathrm{x}$ and $\delta\mathrm{y}$, attitude, i.e. $\delta\theta$, velocity, i.e. $\delta\mathrm{v_x}$ and $\delta\mathrm{v_y}$, and angular rate, i.e. $\delta\mathrm{v}_\theta$.

On the other hand, the uncertainties in the state-space model are due to several sources: (i) discrepancies between the mathematical model and the actual dynamics of the physical system in operation, as linearization effects and neglected high-order dynamics; (ii) parametric physical uncertainties, i.e. spacecraft mass, characterized by a uniform distribution. For the latter source of uncertainties, Table 6.16 provides the references whereas for those related to the system model design, the nonlinear equations for the restricted three-body problem represented the starting point, considering both the spacecraft on a circular orbit around Earth and with masses infinitesimal with respect to the mass of the main body.

Defined $\boldsymbol{\rho} = \rho \mathrm{i}_\rho$ and $\mathrm{r}_1 = r_1\, \mathrm{i}_\xi$ as the position vectors of the chaser and the target spacecraft respectively, where i_ρ and i_ξ represent the unit vector in the direction of the main body-chaser and the main body-target, respectively. let $\mathrm{r} = r\, \mathrm{i}_\xi$ be the vectorial sum of the two positions, $\mathrm{r} = \boldsymbol{\rho} + \mathrm{r}_1$. The chaser dynamics equations can be rewritten as

$$\frac{d^2\boldsymbol{\rho}}{dt^2} + 2\omega \times \frac{d\boldsymbol{\rho}}{dt} + \omega \times [\omega \times (\boldsymbol{\rho} + \mathrm{r}_1)] = -\frac{\omega^2 r_1^3}{r^3}\mathrm{r}, \tag{6.2}$$

where ω is the orbital angular rate and the nonlinearities enters in the equation as a function of $1/r^3$. In [86], using a Taylor Series expansion, the corresponding linearized equations were obtained by ignoring the high order terms $\mathrm{O}(\rho^2/r_1^2)$, as $\frac{r_1^3}{r^3} = 1 - 3\,\mathrm{i}_\xi \cdot \mathrm{i}_\rho \frac{\rho}{r_1} + \mathrm{O}(\frac{\rho^2}{r_1^2})$. That is, Eq. (6.2) reduces to the linearized differential equation for the motion of the chaser relative to the target spacecraft as

$$\frac{d^2\boldsymbol{\rho}}{dt^2} + 2\omega \times \frac{d\boldsymbol{\rho}}{dt} = -\omega^2 \zeta \mathrm{i}_\zeta + 3\omega^2 \xi \mathrm{i}_\xi + \mathrm{O}(\rho^2). \tag{6.3}$$

Ignoring the $\mathrm{O}(\rho^2)$ and expressing the position vector in a more convenient way as

$$\boldsymbol{\rho} \equiv \mathrm{r} = x\, \mathrm{i}_\theta + z\, \mathrm{i}_r - y\, \mathrm{i}_y, \;\; \mathrm{i}_{r_1} = \mathrm{i}_r \;\; \boldsymbol{\omega} = -\omega\, \mathrm{i}_y, \tag{6.4}$$

with x in the direction of the motion i_θ, z in the radial direction i_r and $\mathrm{i}_y = \mathrm{i}_\theta \times \mathrm{i}_r$ normal to the orbital plane, the scalar form of the well-known CW equations can be obtained. Hence, the parametric uncertainty introduced in the model (Eq. (6.1)) are of the same order of $\mathrm{O}(\rho^2/r_1^2)$ and $\mathrm{O}(\rho^2)$. When external forces are acting on the system with a mass m_{CV}, in this case due to the correction actions actuated by the AOCS thrusters (F_x, F_y, F_z), Eq. (6.4) becomes

$$\begin{aligned} \frac{d^2x}{dt^2} - 2\omega\frac{dz}{dt} &= \frac{F_x}{m_{CV}}, \\ \frac{d^2y}{dt^2} + \omega^2 y &= \frac{F_y}{m_{CV}}, \\ \frac{d^2z}{dt^2} + 2\omega\frac{dx}{dt} - 3\omega^2 z &= \frac{F_z}{m_{CV}}. \end{aligned} \tag{6.5}$$

Due to the physical limitations of the POSEIDYN testbed, only the in-plane motion of the spacecraft can be emulated, combined with the rotational dynamics around the third body axis. Hence, considering the equations related to the x-z plane, and neglecting the terms $(-2\omega\dot{z})$, $(+2\omega\dot{x} - 3\omega^2 z)$ linked to the orbital angular velocity, a double integrator is obtained for the translational dynamics

$$\ddot{x} = \frac{F_x}{m_{CV}} \quad \ddot{z} = \frac{F_z}{m_{CV}}. \tag{6.6}$$

Furthermore, a double integrator is also considered for the rotational dynamics as $\ddot{\theta} = \tau/I_z$, where $\ddot{\theta}$ is the angular acceleration, τ is the control torque and I_z denotes the moment of inertia about the vertical axis of the chaser FSS. Then, starting from the definition of the FSS dynamic model, and defining the state vector as $x = \left[\mathrm{x}, \mathrm{y}, \dot{\mathrm{x}}, \dot{\mathrm{y}}\right]^T$ and the control vector $u = \left[F_x, F_y\right]^T$, a continuous-time linearized model of the form (6.1). Then, after discretization, we obtained the following discrete-time representation of the FSS uncertain dynamics as

$$x_{k+1} = A(q_k)x_k + B(q_k)u_k + w_k \tag{6.7}$$

where $x_k \in \mathbb{R}^4$ is the state vector at time k, $u_k \in \mathbb{R}^2$ is the control input, $w_k = \{\|w_{k_i}\|_\infty \leq 0.02\}$ defines the persistent disturbance, and $q_k = [q_1, q_2, q_3, q_4] \in \mathbb{R}^4$ is the parametric uncertainty vector. The corresponding continuous uncertain state and control matrices are

$$A(q) = \begin{bmatrix} q_1 & 0 & 1 & 0 \\ 0 & q_1 & 0 & 1 \\ 0 & 2q_2 & 0 & 0 \\ 0 & 3q_3 & -2q_2 & 0 \end{bmatrix}, B(q) = \begin{bmatrix} \multicolumn{2}{c}{0_{2\times 2}} \\ \frac{1}{m} + q_4 & 0 \\ 0 & \frac{1}{m} + q_4 \end{bmatrix}. \tag{6.8}$$

All the described uncertainty sources were taken into account in constructing the linearized state and control matrices defined in (6.8). In particular, the parametric uncertainties q_1, q_2, q_3 take into account linearization effects and multiplicative disturbances, and are approximated as iid random variables with uniform distribution: $q_1 \sim \mathcal{U}[5 \cdot 10^{-5}, 5 \cdot 10^{-4}]$, $q_2 \sim \mathcal{U}[0.001, 0.0014]$, $q_3 \sim \mathcal{U}[10^{-6}, 1.44 \cdot 10^{-6}]$, while q_4 refers to uncertainty in the mass, and is expressed as $q_4 \sim \mathcal{U}[-0.0091, 10^{-4}]$.

The focus of the experimental campaigns is to investigate the performance of the LQMPC, TRMPC and OS-SMPC algorithms in the control of the translational and rotational dynamics of the chaser FSS during the last part of the rendezvous maneuver. In particular, the requirement of (deterministic) robust control for the attitude was driven by the physical characteristic of the docking mechanisms, located on both the FSS, in order to align and maintain the FSS pointing at the desired attitude, with respect to the target one. On the other hand, goal of the translational control is to drive the chaser to the docking position, where the target is located, while guaranteeing the satisfaction of the typical position and velocity constraints applied to the proximity maneuver. It is important to clarify that the x-y coordinate system of the testbed “coincides" with the x-z orbital plane of (6.6).

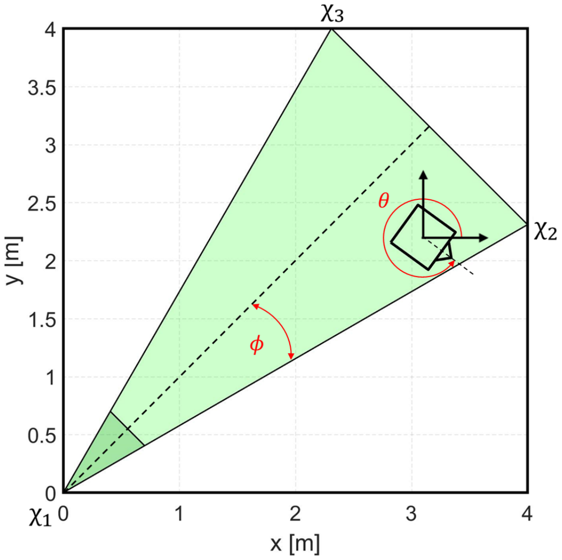

Figure 6.35: NPS-POSEIDYN testbed with the cone constraints. The chaser initial condition has to be chosen within the feasible region (light green) whereas the target spacecraft can be located within the feasible terminal region (dark green). ϕ defines the cone half-angle, whereas θ represents the chaser FSS attitude with respect to the testbed reference system.

In particular, the trajectories should lie in a desired *approach cone* (see Figure 6.35), i.e. LOS-like constraint, whose polytope vertices are defined as follows: $\chi_1 = (0{,}0), \chi_2 = (4{,}2.25), \chi_3 = (2.25{,}4)$. The target is located in the suitable terminal region, defined by a terminal set which is robustly forward invariant for Eq. (6.1) under given control law. From the state constraint polytopes, linear inequality constraints can be derived. Additionally, the approaching and terminal velocities are bounded according to soft docking constraints. Moreover, the thrusters of the chaser are limited by a saturation constraint, according to the maximum thrust available for each cold thruster equipped on the FSS. This is an hard input constraints of the form

$$u_k \in \mathbb{U} = \left\{ u \in \mathbb{R}^2 \mid \|u_i\|_\infty \leq 0.3 \right\}, \tag{6.9}$$

since at most two thrusters can be fired contemporary in the i-th direction.

6.3.3 LQMPC and TRMPC

The first test campaign has been performed in order to validate the real-time implementability of the TRMPC scheme. Moreover, TRMPC effectiveness in robustly handling the mission and system constraints under persistent disturbance has been investigated and its performance has been compared with those obtained exploiting a classical LQMPC algorithm. According to the mission scenario described in the previous Section, two different case studies have been selected for the experimental campaign, each one characterized by a different relative position of the chaser FSS with respect to the feasible region, i.e. LOS corridor:

1. Case A : $(3.50,\ 3.50,\ 0)$, representing the best-case scenario, thanks to the large margin the chaser has with respect to the cone boundaries;
2. Case B : $(3.50,\ 2.65,\ 0)$, corresponding to the worst-case scenario, where the spacecraft is close enough to one of the cone limit that, in presence of uncertainty and without a proper control, it could easily violate the LOS constraint.

Each case study has been experimentally reproduced several times for both control strategies and the results analysis was focused on the following performance parameters:

- Constraints compliance, in terms of position, velocity, attitude and actuators limitation;
- Time-to-dock t_{td}, which defines the total duration of the maneuver performed by the chaser FSS to reach the target FSS;
- Control effort f_c, an estimate of the fuel consumption required for the maneuver, which represents also the efficiency of the control approach from an application point-of-view. The control effort can be evaluated as

  $$f_c = \sum_{k=0}^{t_{td}} \|u_k\|_1 \Delta t, \tag{6.10}$$

  where Δt represents the system sample time.

The hard constraints on states and inputs envisioned in this first test campaign are reported in Table 6.17 (first column), which have been exploited for both LQMPC and TRMPC, whereas the second column provides the tightened constraints exploited for the TRMPC optimization problem and obtained following the guidelines provided in Section 5.3. For what concern the MPC parameters, the same weighting matrices, Q and R, have been exploited for both control schemes and they have been set to $Q = diag[10^4,10^4,10^0,10^8,10^8,10^0]$ and $R = diag[10^6,10^6,9 \times 10^4]$ while P was obtained as solution of the discrete Algebraic Riccati equation. Additional settings related to the MPC implementation are resumed in Table 6.18, adopted for both testbed simulations and experiments. In particular, the prediction horizon has been set to 20 to guarantee the stability of the system and, at the same time, to be compliant with the testbed constraint of maximum computation time, i.e. 5s.

Table 6.17: State and Control constraints.

Parameter	**Uncertain Value**	**Nominal Value**
F_{max} [N]	± 0.15	± 0.093
ϕ [deg]	10	8
θ [deg]	$\pm 2\pi$	± 6.2496
V_x [m/s]	± 0.2	± 0.178
V_y [m/s]	± 0.2	± 0.178
V_{x_f} [m/s]	± 0.05	± 0.048
V_{y_f} [m/s]	± 0.05	± 0.048
$\dot{\theta}$ [rad/s]	± 0.1	± 0.078

Table 6.18: MPC design parameters and model initialization settings.

Parameter	**Value**
Prediction Horizon	20
System Sample Time [s]	0.01
Navigation Sample Time [s]	0.02
MPC Sample Time [s]	3
Maximum Simulation Time [s]	450

Case A

Figure 6.36 provides an overview of both simulation and experimental results obtained exploiting LQMPC (left) and TRMPC (right). It is possible to observe that in simulation both controllers allow the chaser to reach and properly dock the target. On one side, the TRMPC confirms its robustness capability, provided by design, whereas the LQMPC shows an inherent robustness given as feedback controller. The first relevant difference is related to the divergence of the experimental trajectories with respect to the simulated one for the LQMPC mainly during the final approach. This behavior drove the chaser outside the LOS corridor, compromising the docking with the target FSS. Indeed, as shown in Figure 6.36 (a), the chaser missed the target in two over three experiments when the control capabilities are provided via LQMPC. On the other hand, the TRMPC not only guaranteed the docking accomplishment during all the experiments but also showed a quasi-perfect alignment between simulation and experimental trajectories, as depicted in Figure 6.36 (b).

On the other hand, the data reported in Table 6.19 show that the robust approach slowed down the maneuver during the experiments and, at the same time, resulted more fuel-consuming not only in simulation, i.e. the TRMPC control effort is more than double the LQMPC one. Nonetheless, the TRMPC computational cost results comparable with the LQMPC one, as highlighted by the results in terms

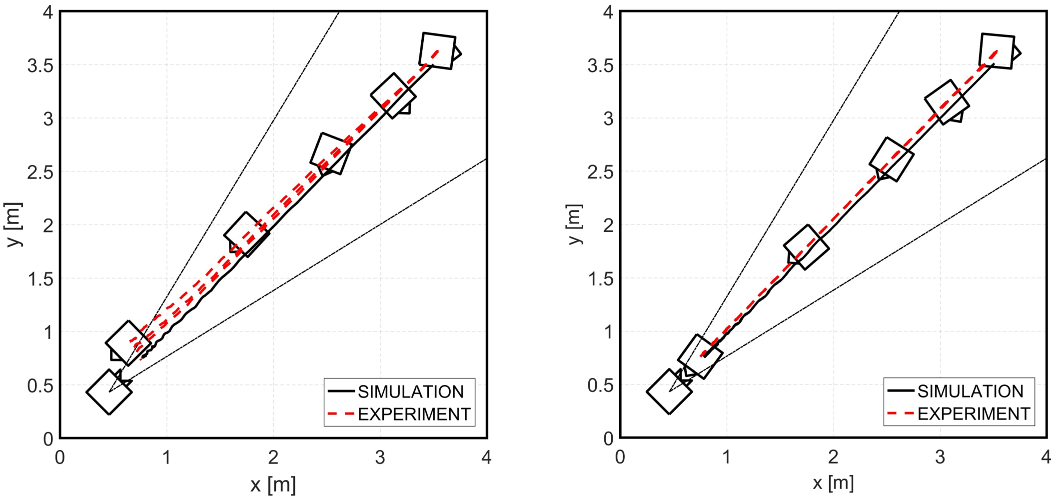

(a) LQMPC (b) TRMPC

Figure 6.36: Comparison of simulation and experimental trajectories in Case A. Three different experimental results are represented for each approach. The Chaser is represented at time $t_0 = 0s, t_1 = 20s$, $t_2 = 100s$, $t_3 = 200s$.

Table 6.19: Performance of controllers in Case A.

MPC Method	t_{td} [s]	**Control Effort** [Ns]	**Avg/Max Iter.**	**Dock** $[Y/N]$
LQMPC (sim.)	450.00	4.16	8.95/10	Y
TRMPC (sim.)	450.00	11.81	8.91/9	Y
LQMPC (exp.)	329.04	6.77	8.65/9	N
TRMPC (exp.)	337.90	17.47	9.47/10	Y

of average and maximum number of iteration required to reach the optimization method convergence.

Case B

Figure 6.37 provides the simulation and experimental results obtained when the chaser FSS initial position has been set close to one of the LOS corridor boundaries. In this second case study, the chaser was always able to reach the target with proper terminal velocity, either exploiting the LQMPC or the TRMPC control scheme. Indeed, the drifting phenomenon experienced in Case A, in this second case study has drove the chaser FSS towards the center of the of LOS corridor when the LQMPC were controlling the spacecraft dynamics. Analogously, the

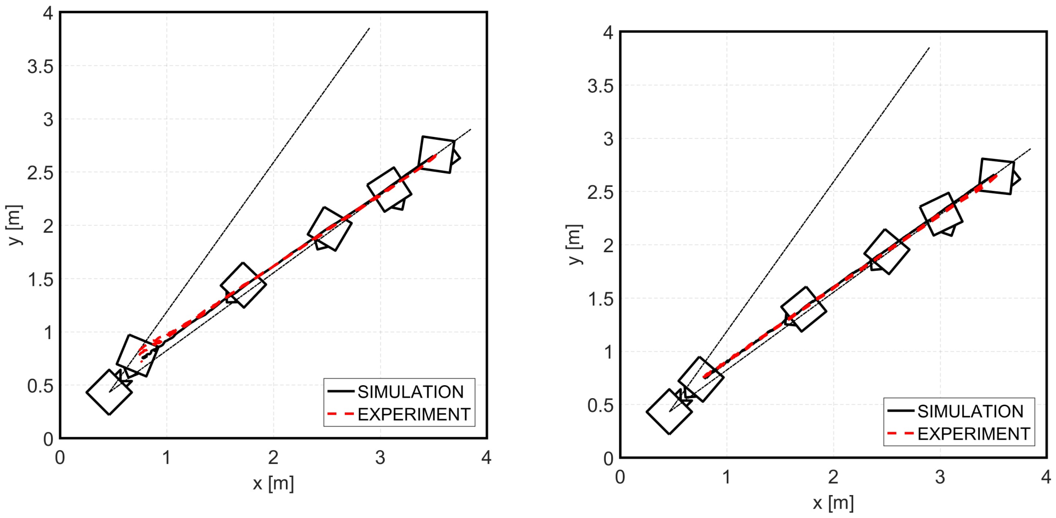

(a) LQMPC

(b) TRMPC

Figure 6.37: Comparison of simulation and experimental trajectories in Case B. Three different experimental results are represented for each approach. The Chaser is represented at time $t_0 = 0s, t_1 = 20s$, $t_2 = 100s$, $t_3 = 200s$.

TRMPC efficacy is evident also in this second scenario (see Figure 6.37b), where the robustness against external disturbance is guaranteed both in simulation and experiments, with the resulting overlapping of the trajectories.

On the other hand, Figure 6.38 shows that at the end of the maneuver, only the TRMPC allowed to properly guarantee the terminal conditions for the docking maneuver in terms of position, terminal velocity and attitude. Indeed, as highlighted in Figure 6.38a, the chaser controlled via LQMPC violated the LOS boundary during one of the experiments and moreover it did not reach the target FSS with the proper attitude guaranteeing the docking mechanisms alignment and the maneuver accomplishment. But also in this second case, the two controllers have shown pros and cons in analogy to the results discussed for Case A, as represented by the data summarized in Table 6.20. The LQMPC is still the faster control scheme and less demanding from a propellant consumption viewpoint whereas the computational cost remains similar to the TRMPC one, as expected.

6.3.4 Fuel-Efficient LQMPC and TRMPC

As shown in the previous Section, the TRMPC approach did allow to robustly satisfy the constraints in the presence of additive disturbance, at the cost of a higher

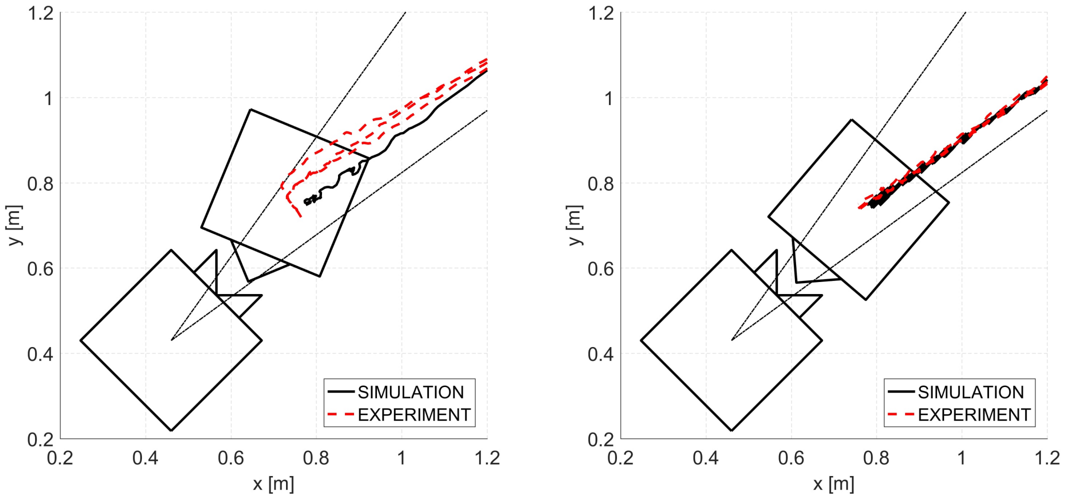

(a) LQMPC (b) TRMPC

Figure 6.38: Zoomed-in trajectory of Case B for LQMPC and TRMPC.

Table 6.20: Performance of controllers in Case B (LQ=LQMPC, TR=TRMPC).

MPC Method	t_{td} [s]	**Control Effort** [Ns]	**Avg/Max Iter.**	**Dock** [Y/N]
LQMPC (sim.)	450.00	3.82	8.94/10	Y
TRMPC (sim.)	450.00	11.60	8.90/9	Y
LQMPC (exp.)	301.13	5.22	8.58/9	N
TRMPC (exp.)	320.65	16.07	9.46/10	Y

control effort with respect to the LQMPC. Since the control effort is strictly related to the fuel consumption, the TRMPC maneuvers cannot be considered fuel-efficient, at least with respect to the ones controlled with classical approaches. Different solutions have been proposed in literature to obtain fuel-optimal controllers, as presented in [189], [190], and [191]. When the fuel-optimization is applied within the MPC scenario, the result is a l_1-regularized least square problem or Least Absolute Shrinkage and Selection Operator (LASSO) regression (see [192]), where the cost function includes both quadratic terms inherited from the classical MPC formulation and linear terms for the control effort. The LASSO problem can be formulated as follows,

$$\begin{aligned} \min_{\mathbf{u}} \quad & \|\mathrm{x}\|_Q^2 + \|\mathrm{u}\|_R^2 + \|\mathrm{u}\|_1 \\ \text{s.t.} \quad & \mathrm{x} \in \mathbb{X}, \mathrm{u} \in \mathbb{U}. \end{aligned} \tag{6.11}$$

Problem (6.11) can be cast in the form of a standard Quadratic Program by introducing a slack variable $\alpha \in \mathbb{R}^m$, obtaining

$$\begin{aligned} \min_{\mathbf{u}} \quad & \|\mathrm{x}\|_Q^2 + \|\mathrm{u}\|_R^2 + \sum_{i=1}^{m} \alpha_i \\ \text{s.t.} \quad & \mathrm{x} \in \mathbb{X}, \mathrm{u} \in \mathbb{U}, \\ & |\mathrm{u}_i| \leq \alpha_i, \quad i \in [1, m]. \end{aligned} \tag{6.12}$$

An analogous approach has been adopted to include the control effort in the cost function of both LQMPC and TRMPC. A preliminary validation campaign has been performed and the results obtained, considering the diagonal case (Case A of Section 6.3.3) both in simulation and experimentation, are reported in Figure 6.39, where the new results have been labeled with the suffix -FS, i.e. fuel saving.

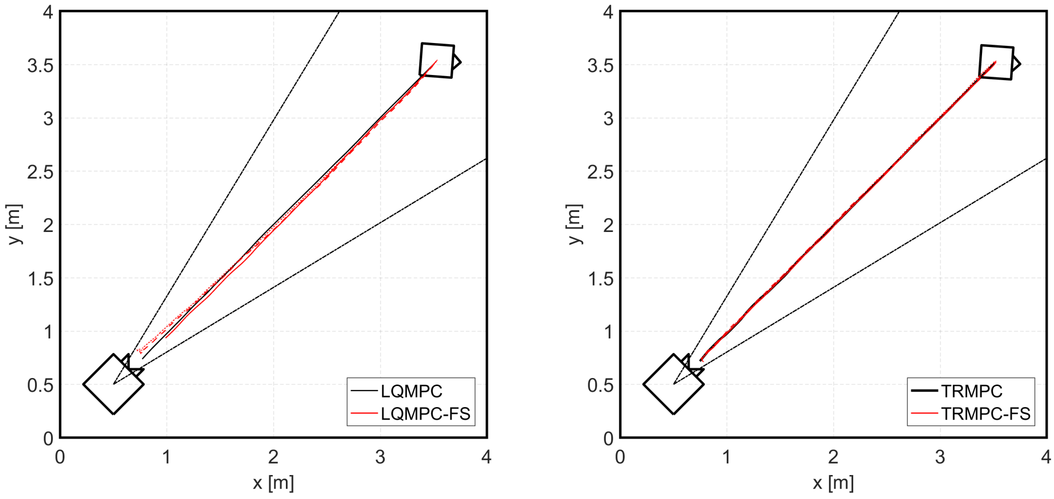

(a) LQMPC (b) TRMPC

Figure 6.39: Experimental results comparison with and without fuel saving strategy applied.

As shown in Figure 6.39, LQMPC trajectories were improved with respect to the ones represented in Figure 6.39a, thanks to an increased velocity profile. In this case, all the experiments allowed the chaser FSS to reach and dock the target FSS. On the other hand, TRMPC performances were validated also exploiting the new cost function, allowing always the accomplishment of the docking and the constraint satisfaction. For what concern the performances of both the approaches in terms of control effort and time-to-dock, the new results are reported in Table 6.21 and compared with respect to the previous cases.

Table 6.21: Performance comparison of controllers in Case A with respect to fuel saving approach, both in simulation and experiment setup.

MPC Method	t_{td} [s]	**Control Effort** [Ns]
LQMPC (sim.)	450.00	4.16
LQMPC-FS (sim.)	112.34	1.95
TRMPC (sim.)	450.00	11.81
TRMPC-FS (sim.)	112.34	5.03
LQMPC (exp.)	329.04	6.77
LQMPC-FS (exp.)	124.67	4.70
TRMPC (exp.)	337.90	17.47
TRMPC-FS (exp.)	116.73	8.83

First, it is possible to observe that the simulation results show comparable improvement among the LQMPC-FS and TRMPC-FS, with a fuel consumption reduction higher than 50% (53.1% and 57.4% respectively). In this case, the TRMPC-FS approach has a control effort closer to the LQMPC one, providing robust constraint satisfaction with reduced consumption of fuel, becoming more appealing from an application viewpoint. On the other hand, the experimental results present significant differences, both with respect to simulations and among the different approaches. The experimental fuel saving percentage for LQMPC-FS is reduced to 31%, whereas is still close to the 50% for the TRMPC-FS (49.5 %).

Hence, the results showed that the fuel-saving approach allows to efficiently reduce the fuel consumption, both for LQMPC and TRMPC approaches, aiming the robust approach to become more appealing for application with respect to the classical methods, thanks to the combination of robustness and low control effort.

6.3.5 OS-SMPC

The first step consisted in evaluating the effectiveness of the OS-SMPC approach applied to rendezvous maneuver, since it was the first time a stochastic MPC was exploited to control spacecraft during proximity operations. Hence, envisioning the further experimental testing of the OS-SMPC scheme, the preliminary validation has been performed considering the simplified translational dynamics of the FSS (Eq. (6.8)). On the other hand, the attitude control was provided exploiting the same TRMPC approach previously introduced. From a constraint viewpoint, the system is subject to chance constraints on the state which should be satisfied with high probability, defined by the LOS corridor polytope vertexes (see Figure 6.35) whereas the hard input constraints are given in Eq. (6.9). The probabilistic parameters of the state chance constraints have been set as $\varepsilon_\alpha = \varepsilon_\beta = \varepsilon_\gamma = 0.05$ and $\delta = 10^{-3}$ (they should be satisfied with probability of 95% and confidence

99.9%). The ensuing number of samples $N_{tot} = N^x + N^u + N^T$ is equal to 32,370, following the approach of [162] for $\varepsilon \in (0{,}0.14)$. Samples of the uncertainty and of the noise sequence were extracted offline and the constraint sets were derived still offline, leading to a total of 956,752 linear inequality constraints. Then, an iterative reduction procedure was applied leading to a final reduced constraint set composed by only 10,125 constraints. For what concern the MPC weight matrices, the same values exploited for both LQMPC and TRMPC have been considered, in order to eventually obtain a *fair* comparison among the three different control strategies. Hence, $Q = diag[10^4,10^4,10^8,10^8]$ and $R = diag[10^6,10^6]$ whereas the prediction horizon was set to $T = 10$. An appropriately robustly stabilizing feedback gain matrix K was designed offline using classical robust tools [193].

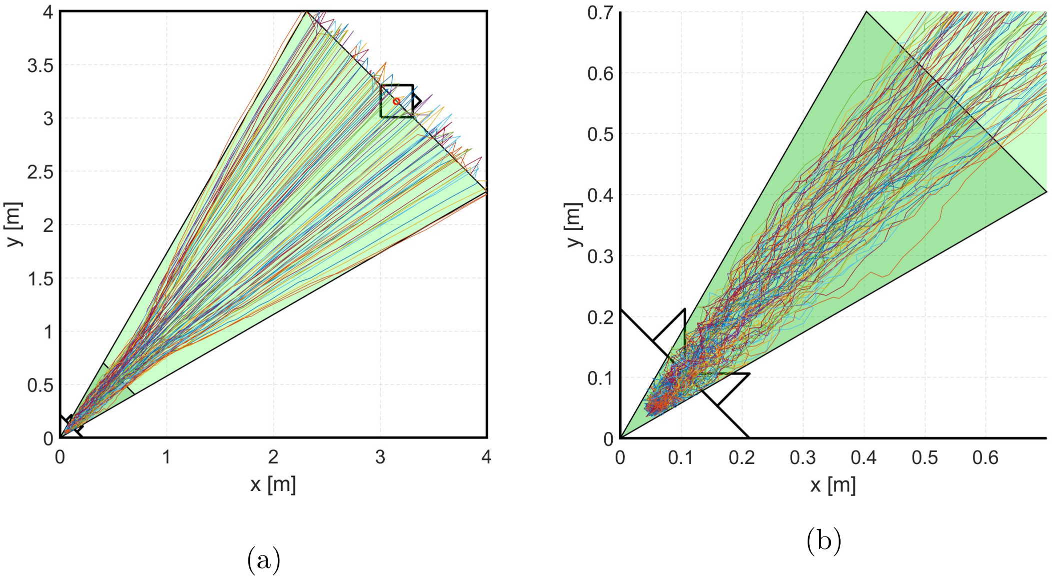

(a)

(b)

Figure 6.40: Numerical results for 100 trajectories (a) and zoom-in around the target FSS (b).

Figure 6.40a shows the results obtained for 100 runs, each one considering a feasible, random initial condition. In all the simulations, the chaser is driven towards the target position, i.e. the origin of the testbed reference system. The effect of additive disturbance and random parametric uncertainty can be observed in Figure 6.40b, where it is also highlighted how the chaser FSS converged to the origin in compliance with the OS-SMPC maximum constraint violation, i.e. 5%.

Once validated the effectiveness of this new control approach for the selected application, the second step was to verify the compliance between the OS-SMPC computational effort with the real-time implementability, considering the same MPC parameters envisioned for the preliminary validation phase. Thus, a second test campaign has been performed at the NPS Spacecraft Robotics Laboratory, in analogy to what has been previously described for LQMPC and TRMPC test campaign. On the other hand, the MPC sample time was increased to 5s, i.e. the maximum allowed, to comply with the much higher computational cost due to the relevant problem size. The initialization settings exploited for the second test campaign are the same previously introduced for the simulations, to be as conservative as possible and obtain comparable results.

For the experimental campaign, considering the symmetry of both the experimental setup and the LOS cone with respect to the table diagonal, the number of initial conditions envisioned has been reduced to three and located only in one half of the testbed plane: (i) Case A: represents the diagonal case, in which the chaser FSS is farthest from the cone constraint; (ii) Case B: the worst-case initial condition, with the FSS close to the LOS boundary; (iii) Case C: halfway condition. Each case study was simulated and subsequently experimentally reproduced 20 times and the results obtained are represented in Figure 6.41. Comparing the simulation trajectories (Figure 6.41a) with the experimental ones in Figure 6.41b), it is possible to observe a rather good adherence of the results. In particular, in all experiments the chaser FSS is always driven from the initial position to the terminal region, where the target FSS is located.

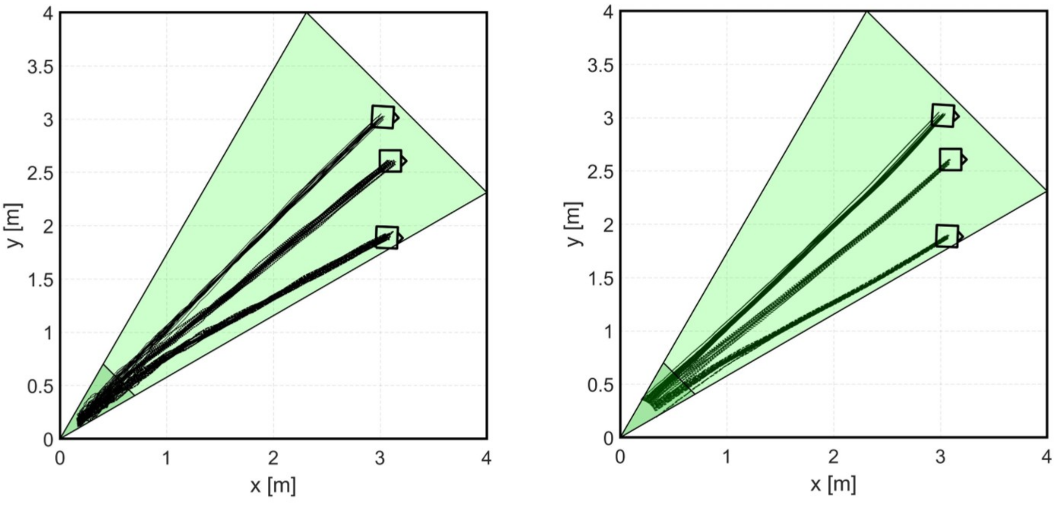

(a) Simulation Results

(b) Experimental Results

Figure 6.41: Simulation and experimental results for 3 different ICs, considering 20 repetitions for each one.

A zoom-in of the terminal region, both for simulations and experiments, is represented in Figure 6.42, where a relevant difference between the simulated trajectories (Figure 6.42a) and the experimental ones (Figure 6.42b) with respect to the stopping condition. In the simulations, the chaser trajectory were stopped when the relative distance with respect to the *virtual* target was lower than a certain threshold (0.18 m). On the other hand, in the experimental setup, the target is a real FSS, the end of the docking phase between the spacecraft were forced by the magnetic force generated between the two docking interfaces. The effects of this force are evident in Figure 6.42a, where trajectories are not funneled as in Figure 6.42b but they are distributed around the target docking interface. This discrepancy is mainly due to the fact that the magnetic force was not included in the simulation environment.

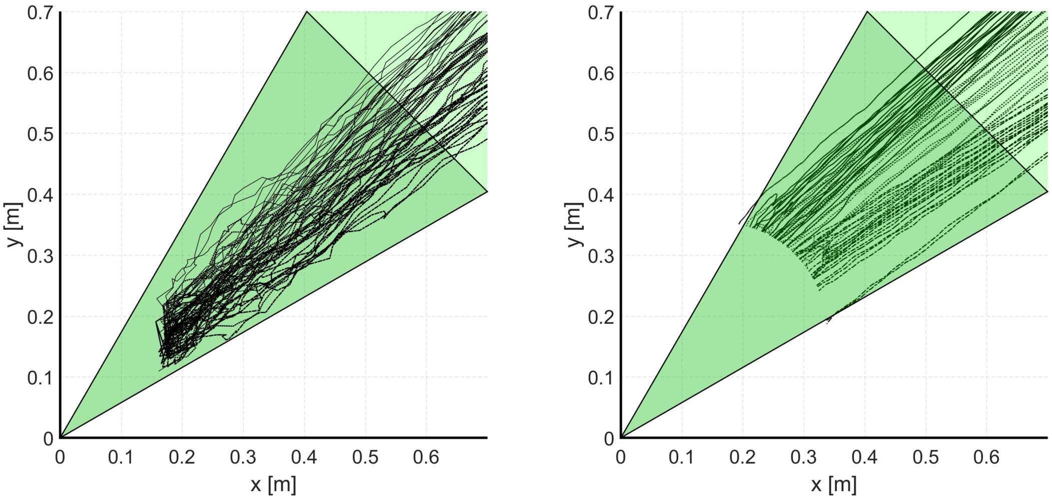

(a) Simulation Results

(b) Experimental Results

Figure 6.42: Zoom-in on the terminal region of both simulation and experimental results.

Once the OS-SMPC scheme has been validated for the real-time implementability point-of-view, Figure 6.43 depicts the control effort for all 60 experiments as a function of the time-to-dock. As it is possible to notice, in all three cases the maneuver lasted about $120 - 200$ s i.e. faster than both LQMPC and TRMPC according to the results presented in Section 6.3.3, with an average control effort between 4 Ns and 5 Ns.

In Table 6.22, the average control effort of the three MPC approaches are reported. It is possible to notice that the robust MPC scheme represents the most fuel-consuming approach, with a fuel demand about three times higher than the classical and stochastic MPC, which instead are characterized by comparable fuel consumption, in the order of 5 Ns. The fact that OS-SMPC has a much lower fuel consumption than not only TRMPC but also LQMPC results somehow surprising, but it can be explained by the much lower conservatisms of the stochastic approach.

For completeness, the computational cost of all 60 experiments is provided in

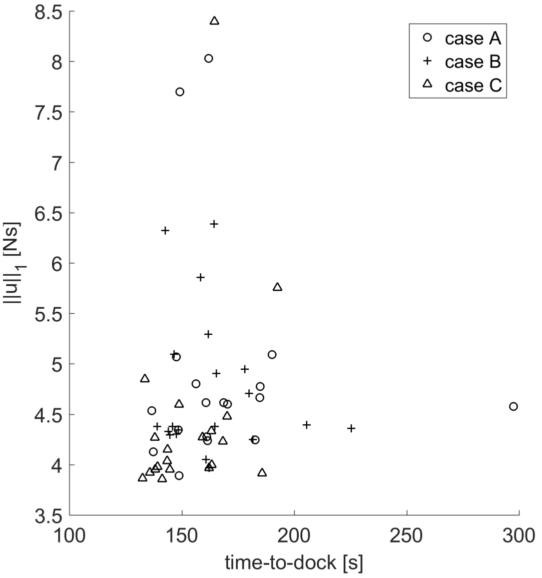

Figure 6.43: Control effort with respect to the time-to-dock results for 60 experiments.

Table 6.22: Comparison of the average control effort for three different MPC approaches adopted to control the FSS during a rendezvous maneuvers on the NPS POSEIDYN testbed: (i) LQMPC; (ii) TRMPC; (iii) OS-SMPC.

MPC approach	**Control Effort [Ns]**
LQMPC	4.99
TRMPC	14.24
OS-SMPC	4.69

Figure 6.44 in terms of average and maximum cost and it is possible to notice that all of them are close to 4s, which leaves 1s to be computationally dedicated to the other processes, considering the MPC sample time equal to 5s.

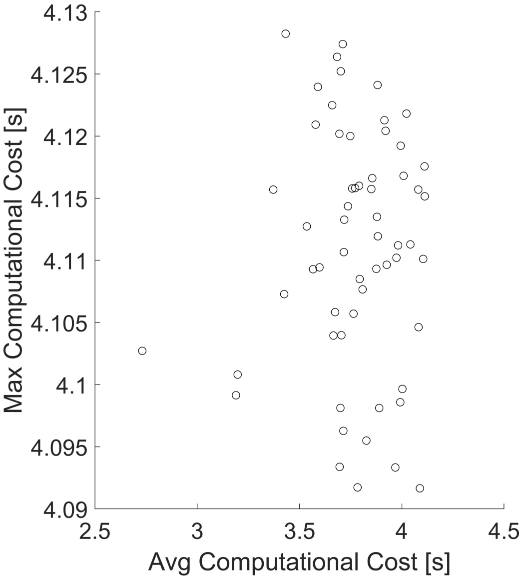

Figure 6.44: Average and maximum computational cost of all 60 experiments.

Chapter 7

Conclusions

The second space exploration era has finally began after a sudden setback due to disruptive economic efforts required to build up the ISS and to sustain the Space Shuttle operability. Starting from 2008, the international community have proposed a visionary space program that should take place in the next 25-30 years, retracing the path delineated back in 1970's, to extend (again) the human presence beyond LEO towards Mars. The envisioned incremental approach is based on several intermediate steps among which the LOP-G should represent the first cornerstone. To support the Gateway and its visiting crews, the Orion MPCV is currently under development. It will provide the transportation capabilities for 4 crewmembers together with the resupply to sustain them for at most 30 days. On the other hand, the current LOP-G design envisions an habitable volume that could allow to extend the astronauts permanence on board the Gateway up to 3 months. Thus, additional transportation systems shall be envisioned as support to the Orion spacecraft to transport cargo, equipment and resupply to and from the orbiting spaceship.

In this Thesis, an innovative transportation system is proposed. The so-called LST is envisioned as a reusable space tug, able to transfer heavy payloads released in Earth orbit by commercial launchers up to the LOP-G. Then, the LST should return to its Earth operational orbit, waiting for the next delivery in a closed-loop mission profile. The propulsive capabilities shall be provided by a cluster of high-power HETs, the same technology already under development for the first element of the Gateway, i.e. the PPE, in order to minimize the development and validation economic efforts. To preliminary assess the design of this visionary spacecraft, a tailored design tool has been realized. MISS is a flexible and reliable software suite developed in a MATLAB environment. It includes several analytical models that allow to obtain the main mission, mass and power budgets, at component level, for several e-PROP subsystem cluster architectures. Each architecture is based on one of the 125 HET operational points identified over a reference performance envelope. In particular, three case studies have been considered, each one characterized to a different crew mission duration and resupply needs, i.e. 30, 60 and 90 days corresponding to about 1.5, 3 and 4.5 tons of goods. Moreover, the possibility to exploit a fleet of spacecraft, composed by one up to 3 tugs, raised the number of case studies to nine and allowed to redefine the maximum transfer duration constraint according to the fleet configuration. An additional constraint comes from technological limitations due to HET plume impingement. Thus, the maximum number of thrusters contemporary operative has been set to 4 whereas the total number of HET allowed in the cluster architecture, between operative, stand-by and redundant thrusters, shall be limited to 10.

The first step of the design phase took care of defining the Δv budget for each of the mission phases. The results show that the total Δv demand for the EOR to and from the LOP-G is about 3.12 km/s whereas for the rendezvous maneuvers in GTO with cargo module and in NRHO with the Gateway the Δv are close to 4.5 m/s and 1.5 m/s, respectively. Then, once obtained all the 500 design solutions for each of the nine case study, a first selection process allowed to reduce the number of LST configurations to only those compliant with both mission and system constraints. The results showed that the minimum number of LST in the fleet required for the 30- and 60-days cases shall be equal to two. On the other hand, for the 90-days case the fleet shall be composed by at least three spacecraft, due to the higher resupply mass. The next step consisted in identifying the most suitable e-PROP architecture, common to all three main case study and based on the same technology in terms of HET operational point. Analyzing the feasible design results, it was possible to observe that the smallest cluster architecture should be composed by 3 HETs, two of them contemporary operated and the third only for redundancy purpose. The selected architecture results feasible for 14 different HET operative points. Thus, a trade-off analysis was performed to select the overall optimal solution with respect to the following figures of merit: (i) total power demand; (ii) LST dry mass; (iii) propellant consumption; and (iv) transfer duration. The traded results highlighted that for all three case study, the optimal solution is represented by the HET characterized by an Isp of 2600 s and 1.025 N of thrust, requiring an input power of 20 kW and an operational lifetime of 40000 h. The corresponding LST design solutions should be equipped with solar arrays with an area of about 290 m^2 whereas, during eclipses, secondary batteries would cover the total power demand required to sustain the LST and its e-PROP subsystem. To reject the heat coming from the external environment and internal equipment, deployable radiator panels with an area of about 113 m^2 should be used. All three LST share the same AOCS architecture, comprising 30 monopropellant thrusters for orbital control during ARVD maneuvers, 4 RWs for attitude control and several sensors for navigation purpose, with an overall mass of the subsystem around 313 kg. On the other hand, the three LST are in charge to transfer a different resupply mass, which implies different propellant consumption, since the Δv and Isp are the same. Thus, the sizing of Xenon and Hydrazine tanks are the only components that differ among the three design solutions. As a consequence, the total dry mass, wet mass and transfer duration are different as well. In particular, the LST total dry mass varies from about 8.5 t for the 30-days case to over 16 t for the 90-days case whereas the average transfer duration between GTO and NRHO increases from less than one year, i.e. 340 days, up to 492 days.

From an operational viewpoint, the LST should significantly rely on the ARVD technology, which has been identified as crucial for the transition of space missions from geocentric architectures to self-sustainable, autonomy and independent. Indeed, along its closed-loop mission profile, the LST should be able to safely and autonomously rendezvous with three very different target vehicles, i.e. the cargo module and the ORS in Earth proximity and the Gateway in NRHO. Thus, ARVD should become so reliable to be completely demanded to the spacecraft, without ground support. Currently, most of the spacecraft visiting the ISS are characterized by a significant level of autonomy, also during ARVD operations with very little oversight and interaction from the MCC. However, ground control is still heavily in the loop while Earth-independence and improved autonomy are key steps for outer-planet exploration for ARVD to become routine. One of the most critical technological challenge, linked to the achievement of this goal, is represented by the development and validation of innovative guidance and control algorithms. The former shall be in charge of determining the desired trajectories to be followed between spacecraft performing rendezvous maneuvers. The latter, i.e. control algorithms, shall guarantee autonomous control, allowing the chaser vehicle to follow identified by the guidance algorithm and, at the same time, fulfill safety and operational constraints even in the presence of model uncertainty and external/internal persistent disturbance affecting the operability of the spacecraft and the controllability performance. To properly validate these new guidance and control algorithms, it is mandatory to have a reliable simulation environment, where the control strategies can be preliminarily validated in terms of effectiveness. At this end, a 6 DoF orbital simulator, developed in a MATLAB/Simulink environment, has been developed in order to obtain a reliable software suite where, starting from the main outputs provided by the high-level mission analysis and the MISS design tool, the LST ARVD maneuvers could be simulated and contemporary different control strategies could be validated. An initialization environment, representing the interface with the MISS design tool, allows to set orbital parameters, initial conditions of both chaser and target vehicles in terms of attitude, position and velocity, as well as maneuver constraints. Then, chaser and target rotational and translational dynamics are modeled in a Simulink environment to simulate the ARVD maneuver where external disturbance are enforced accordingly to the orbit considered. For the LST attitude and orbital control tasks, three different MPC strategies have been designed, applied and validated. The first is a classical LQMPC, which can partially guarantee constraint satisfaction under persistent disturbance thanks to some inherent robustness. The performance of LQMPC have been compared with a TRMPC approach, a robust MPC algorithms that guarantees robustness to bounded, additive disturbance controlling the associated undisturbed dynamics. The effectiveness of this second control strategy has been observed in both GTO and NRHO, always guaranteeing LOS, terminal velocity and attitude tracking constraints. On the other hand, the third control strategy, the so-called OS-SMPC, was not inherited from literature but fully developed within this project. Indeed, recently SMPC approaches have gained popularity for processes where a stochastic model can be formulated to represent the uncertainty and disturbance and constraints violation does not correspond to compromise the application or lose the mission. Indeed, a probabilistic model allows to optimize average performance or appropriate risk measures, and to introduce the so-called *chance constraints*. This type of constraints seem more appropriate in real-world applications such as ARVD maneuvers where a (very) small probability of constraint violation can be allowed, especially if it corresponds to a higher cost-effectiveness of the application itself. A crucial issue typically encountered in the design of SMPC algorithms is the derivation of computationally tractable methods to propagate the uncertainty for evaluating the cost function and the chance constraints. Among the different methods proposed in literature, the scenario approach represents one of the most promising when the computational capability of the stochastic algorithm represents a stringent constraint for the chosen application and several types of stochastic uncertainty are involved and can enter nonlinearly in the system. The drawback of propagating the uncertainty as a finite number of scenarios to be considered at each step, requiring that different samples need to be drawn at each step, has been recently overcome by the introduction of the *offline sampling* strategy. It allows to reduce the computational effort made online by means of a pre-processing of data made offline. Combining all these needs, the innovative OS-SMPC scheme developed solves the nontrivial problem of extending the previous result into a comprehensive framework, able to tackle situations in which *both* additive disturbances and parametric uncertainties are simultaneously present in a computationally tractable manner. Thus, for the first time, a complete and integrated framework, able to cope simultaneously with additive random noise and parametric stochastic uncertainty has been developed and it has been demonstrated recursive feasibility and the presence of an asymptotic performance bound, which partially solves the problem of asymptotic stability. Indeed, due to the presence of additive disturbance, the state does not converge to the origin. The presented theory results particularly attractive for real-world applications, since the design can be based on real data gathered from experiments or high fidelity simulations.

Starting from the comparison among LQMPC and TRMPC performance in the presence of external disturbances, the major difference can be observed with respect to the attitude control where the classical MPC approach results not able to steer the LST attitude to the desired one, i.e. perfect alignment among docking interfaces. TRMPC guarantees always constraint satisfaction and the performance are not compromised by the presence of persistent noise, at the cost of a higher control effort in the Cislunar environment. On the other hand, in GTO the robust algorithm allows to save propellant since it maintains the LST closer to the orbital plan during the radial boost phase than the LQMPC. Another difference among the two approaches can be observed in terms of maneuver duration since TRMPC takes longer to drive the LST to reach the target vehicles both in GTO and NRHO. However, both controllers allow to satisfy the operational constraints in terms of allocated Hydrazine mass and maneuver duration, defined during the LST mission analysis and design phase. For the first time, a SMPC approach has been exploited for ARVD maneuver and, more in general, for aerospace applications. The developed OS-SMPC algorithm has been exploited for both attitude and orbital control of LST during rendezvous maneuver with cargo module and LOP-G. The results obtained running 50 simulations have shown that, for the rotational dynamics, the controller tries to steer the attitude to a neighborhood of the desired and in the majority of the cases, the tracking constraints are satisfied. Analogously, the LST angular velocity is driven to zero in both GTO and NRHO. For the orbital control, two main observations can be made, separating the in-plane motion to the out-of-plane component. Indeed, in the orbital plan, a quasi perfect overlapped of the rendezvous trajectories can be observed and the LST is always driven to properly reach and enter the LOS approach corridor at the end of the close-range phase. In particular for the ARVD maneuver with the cargo module, the LST is almost perfectly aligned with the target at the beginning of the final approach phase, i.e. along the V-bar axis. On the other hand, for the ARVD with the Gateway, the LST enters the LOS corridor almost 6 m far from the approach axis but still in the LOS constraint. Differently, the out-of-plane component of the motion results significantly affected by the external disturbances, especially in GTO, and this drives the chaser quite far from the orbital plane during the radial boost maneuver. Consequently, in GTO the LST starts the final approach maneuver quite far from the desired axis but the OS-SMPC is able to fast drive the spacecraft within the LOS corridor and reach the target, i.e. the cargo module, within the enforced terminal constraints. On the other hand, the LST in NRHO is subject to external disturbances of lower intensity and thus the spacecraft remains closer to the orbital plane during the close-range maneuver and at the beginning of the final approach phase the maximum distance from the approach axis is within 5 m. However, due to the convergence of the pitch angle to a neighborhood of the ideal attitude, in most cases the LST stays far from the orbital plane and in some cases does not allow to complete the rendezvous maneuver properly. On the other hand, these results can be still considered as reliable since for berthing maneuvers, less demanding constraints can be envisioned. The last two parameters analyzed are those related to the constraints coming from the mission analysis and LST design phase: Hydrazine consumption and maneuver duration. It has been shown that, even if the OS-SMPC implies longer maneuvers, the 12 h constraint is still guaranteed, i.e. the

ARVD lasts about 2 h, but with the drawback of higher propellant consumption, in the order of 50% higher than LQMPC and TRMPC one. Another significant point was to demonstrate the real-time computational applicability of the proposed OS-SMPC approach. Thus, the execution time required to solve on-line the MPC problem has been tracked and the results have showed that, despite very few peaks, the OS-SMPC problem can always be solved within the time allocated to the control problem, considering hardware with computational capabilities similar to the one of the computer exploited for performing the simulations, i.e. an Intel Core i7-7500 CPU, 2.70 GHz with 16 GB of RAM and 512 GB solid-state drive.

Another crucial task related to the validation process of innovative control algorithms for space application is the analysis of real-time computational applicability. Thus, to complete the algorithms verification process, all three MPC strategies have been experimentally validated at the NPS Spacecraft Robotics Laboratory exploiting spacecraft mock-up, i.e. the FSS. Running the algorithms on the on-board micro-controller, it was demonstrated their effectiveness and real-time computational applicability. In particular, focusing on the robust approach, the chaser FSS always satisfied the hard state and control constraints and successfully docked with the target FSS. On the other hand, the deterministic LQMPC was not always able to satisfy the operational and saturation constraints, especially, in terms of cone boundaries and it implies that the chaser FSS was not able to dock the target during some experiments. Moreover, the results shown that both control approaches can be implemented on-board for the real-time control of the final phase of the rendezvous maneuver, with a comparable computational effort, even if the fuel consumption is higher when the robust approach is adopted. Hence, if the constraint satisfaction represents the main mission requirement, the TRMPC guarantees better performance. In order to reduce the control effort related to the robust scheme, a fuel-saving strategy, based on a LASSO approach, has been proposed and experimental validated. The results have shown that, comparing the control effort obtained with the traditional classic and robust approaches with those obtained applying the fuel-efficient approach, it is possible to obtain fuel saving from 30% up to 50%, aiming the TRMPC to become more affordable from a control effort point-of-view, still guaranteeing robust constraint satisfaction. The last experimental campaign was dedicated to the validation of the new OS-SMPC control strategy. A significant part of the preparatory work was dedicated to the selection of the optimal solver that could provide fast-computing capabilities while handling a significant number of constraints. Then, the real-time computational applicability has been confirmed via an extensive experimental campaigns where different initial conditions have been considered. In particular, it is important to highlight that the real-time implementability has been validated also exploiting a micro-controller with lower computational capabilities, i.e. an Intel Atom 1.6 GHz 32-bit processor, with 2 GB of RAM and an 8 GB solid-state drive. Last, despite the results obtained in simulations, comparing the average control effort of the three MPC approaches, it was observed an opposite behavior. Indeed, while the TRMPC scheme represented the most fuel-consuming approach, LQMPC and OS-SMPC were characterized by comparable fuel consumption. The fact that OS-SMPC has much lower fuel consumption than not only TRMPC but also LQMPC was somehow surprising, but it can be explained by the much lower conservatisms of the stochastic approach.

Future works shall be addressed mainly in two directions. First, the STAR orbital simulator shall be integrated with a reliable low-thrust EOR tool in order to properly simulate the whole LST mission profile and obtain the exact transfer duration and propellant consumption. Indeed, the current version of the STAR software allows only to simulate the dynamics of the chaser vehicle during the ARVD maneuvers, relying on the main outcomes provided by the preliminary design phase for the analysis initialization. rely on a simulation environment where the complete mission can be simulated together with the chaser and target vehicles. In particular when electric propulsion is envisioned as in the case under analysis, it is crucial to provide a reliable software that allows to properly propagate the spacecraft motion during the EOR phases, according to the selected mission profile. In addition to that, the low-thrust trajectories that the LST shall perform exploiting the HET cluster would be affected by the control strategies selected not only for the thrusters management but also for the thrust profile, in terms of magnitude and direction. Furthermore, the LST would undergo the effects due to the disturbance affecting the spacecraft during the entire transfer. Thus, suitable control strategies shall be selected and integrated also for the LST attitude control during the EOR phases. Then, the resulting simulator shall be further integrated with the MISS design tool to realize a complete software suite that, starting from a reference scenario, allows to provide a comprehensive modeling framework for integrated high-power electric spacecraft and trajectory design.

The second major effort shall be put into improving and extending the applicability of the OS-SMPC control strategy, starting from demonstrating that the minimal Robust Positively Invariant set $S_K(\infty)$ is asymptotically stable in probability for the closed-loop system under the proposed OS-SMPC algorithm. This asymptotic behavior has been already proved in [164], where a similar sampling-based approach was proposed to control a linear, time-variant system involving additive, bounded disturbance and subject to chance constraints on the state and hard constraints on the input. Moreover, the applicability of the proposed OS-SMPC scheme shall be extended to the case on nonlinear systems, which would allow to broaden the applicability to a larger number of applications. Concurrently, further analysis shall be done to identify a (presumingly) different solver, compliant with the computational requirements and of both the proposed algorithm and the selected hardware performance and calculation speed. Additional investigations shall be addressed to analyze the effect of controlling a system where some states are non measurable, potentially exploiting a controller-observer approach and obtaining an output-feedback OS-SMPC algorithm. Moreover, the assumptions of iid uncertainty and disturbance shall be replaced with more realistic ones, possibly exploiting modeling hypothesis that better fit with real-world applications, e.g. rendezvous maneuvers in the deep space, providing more reliable results. Hence, future analysis shall focus on validating the effectiveness of the OS-SMPC approach when dealing with unstructured, time-varying uncertainty. A possible scenario could be represented by the combination of the aforementioned stochastic MPC algorithm with a complementary filter, that would allow to deal with unknown, unstructured uncertainty.

Last, further experimental campaigns shall be performed to complete the TRMPC and OS-SMPC algorithms validation process, comparing their performance with other schemes proposed in literature, such as the *Contraction Theory Approach* described in [194], where the initial state is also an optimization variable.

Appendix A

Multi-Scenario SEP Platforms Design Exploiting MISS

Relevant efforts have been done in the last decades on developing improved HET for space transportation and exploration missions thanks to their peculiarities such as high efficiency, favorable power-to-thrust ratio and relatively long operational lifetime, features of which novel near-Earth and deep space applications could benefit. Among them, according to the current market outlook and the strategic decisions of national and international space agencies, three different mission families have been identified as more interesting to be further investigated: (i) orbit raising of telecommunication and navigation satellites from their LEO injection orbit up to the GEO operational ones; (ii) unmanned cargo transfer, in analogy to the scenario envisioned for the LOP-G replenishment concept; and (iii) disposal or de-orbiting of modules and payloads for improving the waste management of space missions.

As anticipated in Chapter 3, the MISS software suite has been developed to provide a reliable and flexible design tool able to preliminary size various high-power electric spacecraft which propulsive core is based on HET. The flexibility of MISS has been validated within the GSTP Programme "High Power Hall Effect Thruster subsystem for space transportation and exploration" funded by the European Space Agency (Contract 4000122232). The project, led by SITAEL S.p.A., aims to the development of an improved 20kW-class HET, i.e. the HT20k XC, starting from the company experience gained during the last decade on HET. Moreover, the employability of the HT20k XC is investigated considering possible realistic mission scenarios in which the identified transportation systems could benefit from adopting this enabling technologies. In particular, 33 different mission concepts have been identified, distributed among the three mission families introduced before. In particular:

- The *telecommunication* mission concept envisions the adoption of electric spacecraft to provide orbit raising capabilities to telecommunication and navigation satellites up to the GEO, after their injection in LEO. Two scenarios have been identified, both with the same satellite injection orbit, i.e. a 300 km LEO, as well as the reference satellite mass, i.e. 4 t as the average mass of current telecommunication/navigation satellites. On the other hand, each one is characterized by a different parking orbit for the electric platform:

  1. the first one, i.e. TELECOMM #1, envisages that the parking orbit is a circular orbit with an altitude 50 km lower than GEO, i.e. orbital radius of 42114 km;
  2. the second one, i.e. TELECOMM #2, envisages that the parking orbit is a circular orbit with an altitude of 350.

- The *disposal* mission family envisions 7 different mission concepts, as here briefly reported:

  1. DISP #1: de-orbiting of ISS modules , once the Station will reach the its EOL. The reference module mass has been set to 24968 kg, i.e. equal to the heaviest ISS module to de-orbit;
  2. DISP #2: de-orbiting of LEO satellites located in the *grey* area of space in which the current regulation allows both to de-orbit the satellite or transfer it to a Earth graveyard orbit, i.e. 1400 km of orbital altitude. The reference satellite mass has been set to 18000 kg, i.e. equal to the heaviest module currently located in a 14000 km LEO to de-orbit;
  3. DISP #3: transfer to internal Earth graveyard of LEO satellites located in the *grey* area of space in which the current regulation allows both to de-orbit the satellite or transfer it to a Earth graveyard orbit. Reference orbit and module mass set analogously to the previous scenario;
  4. DISP #4: same of DISP #3 but in this scenario, the transportation system for the disposal has its parking orbit to an altitude of 35736 km instead of 1450 km;
  5. DISP #5: disposal of GEO satellites in the external Earth graveyard orbit. The reference satellite mass has been set to 4000 kg, i.e. equal to the average mass of the current satellites located in GEO;
  6. DISP #6: support to LOP-G waste management, disposing the Gateway waste in one of the external Earth graveyard orbits. The mass to dispose ha been evaluated according to the guidelines provided in [33] and set to 200 kg for a 4 members crew spending 30 days on the LOP-G;
  7. DISP #7: as for the DISP #6, the mission scenario is intended to support the LOP-G waste management but, in this case, a Lunar graveyard orbit is envisioned, located into the region of lunar frozen orbit with an altitude of 8800 km.

- The *transportation* mission family includes the following mission scenario, in addition to the LST one:
    1. TRANS #1: orbit raising of cargo module from a 300 km LEO up to GEO;
    2. TRANS #2: cargo, dedicated hardware, robotic systems and infrastructures transferred from the LOP-G down to a 100 km Low Lunar Orbit;
    3. TRANS #3: in analogy to TRANS #2, cargo, dedicated hardware, robotic systems and infrastructures transferred from a ISS-like habitable station, orbiting in a High Mars Orbit with a periastrum altitude of 3746 km and apoastrum altitude of 37149 km, down to a 150 km Low Mars Orbit.

  For all these scenarios, the cargo mass has been set to four different levels, in this way envisioning a greater variety of mission scenarios, from 5 t up to 20 t.

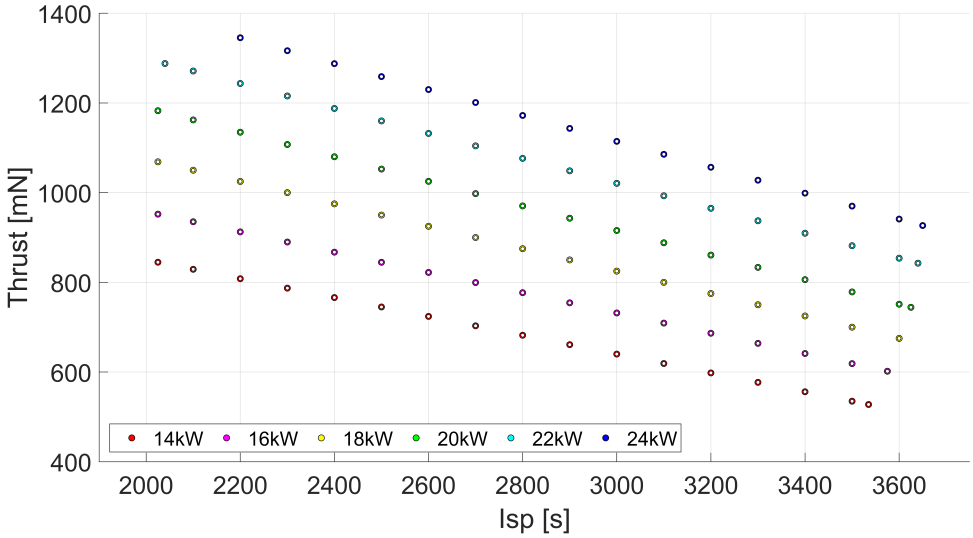

Figure A.1: HT20k XC expected performance.

The aims of this analysis are twofold: (i) on one side, to provide the preliminary design of electric platforms able to transfer the designated payload, considering different cluster architectures, in compliance with mission and system constraints; and (ii) on the other side, to preliminary define an area over the HT20k reference performance map, represented in Figure A.1, which corresponding operational points provide at least one feasible design solution for the highest number of mission scenarios envisioned. In analogy to the selection process described in Section 3.1.4, all the design solutions obtained for the 33 mission scenarios have been filtered applying two selection criteria in a row: (i) first, the mission duration requirement identified within the specific traffic plane of each mission scenario; and then (ii) the e-PROP cluster architecture constraints, in which the total number of HT20k contemporary operated is limited to 6. The main difference with respect to the LST mission concept is related to the HET reference performance map considered (see Figure A.1), in which 103 operational points have been identified: Moreover, the HT20k lifetime range has been envisioned ranging from 10000 h up to 30000 h, obtaining a total of 3090 design solutions analyzed for each mission scenario.

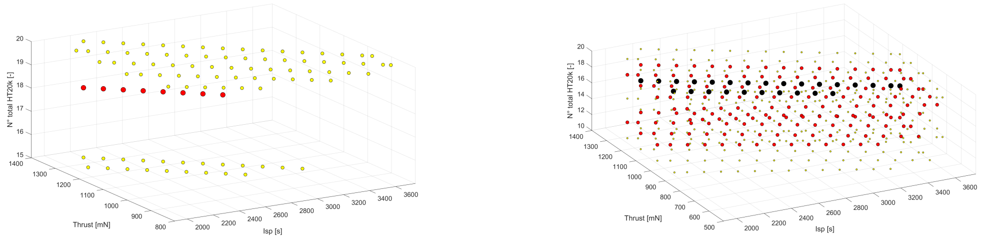

(a) TELECOMM #2 (b) DISP #6

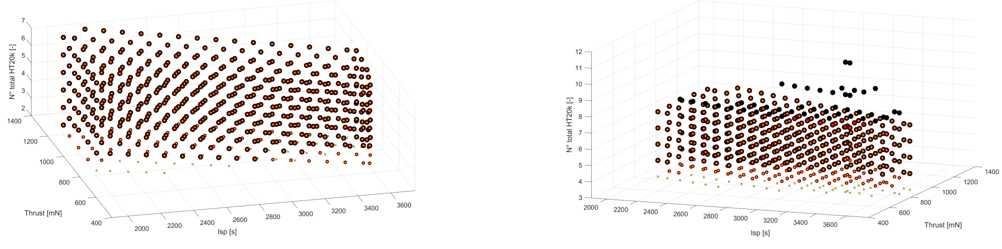

(c) TRANS #3 (5t) (d) TRANS #3 (10t)

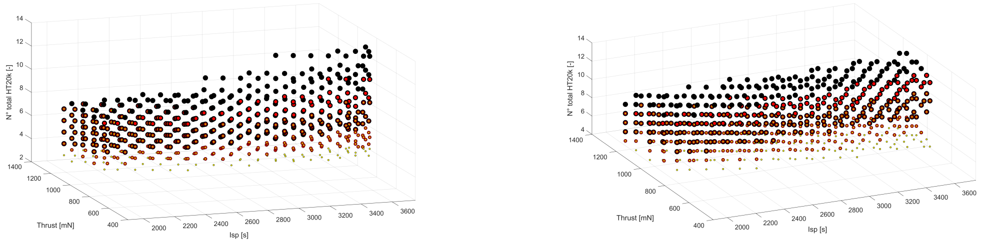

(e) TRANS #3 (15t) (f) TRANS #3 (20t)

Figure A.2: Telecommunication scenario #2, Disposal scenario #6 and Transportation scenario #3 with 5/10/15/20 t cargo modules – Feasible working points over the reference performance map and with respect to the total number of HT20k in the e-PROP cluster. Three lifetime level for HT20k: (i) 20000 h (black circle); (ii) 25000 h (red circle); (iii) 30000 h (yellow circle).

After the selection process, some of the envisioned scenarios result not feasible exploiting the HT20k technology under the mission and system constraints. On the other hand, 6 scenarios present at least one design solution compliant with all the requirements and constraints. They are: (i) TELECOMM #2; (ii) DISP #6; (iii) TRANS #3 (5/10/15/20 t). Moreover, the LOP-G replenishment concept has been included in this analysis, i.e. TRANS #4, and 4 other mission scenarios are added, each one related to a different crew permanence on board the Gateway, i.e. 30/60/90/180 days. Each feasible solution corresponds to a peculiar HT20k operational point and specific lifetime, and characterized by a e-PROP cluster architecture, as represented in Figure A.2. Further results are presented in the following Sections, first in terms of the four main parameters characterizing the electric spacecraft, i.e. thrust, wet mass, power demand and transfer duration, and then identifying the HT20k nominal operational points that should be considered for the next development phase of this thruster in order to be exploitable within the highest number of applications.

A.1 Transfer Duration

In this Section, each selected scenario and its feasible design solutions are described in terms of transfer duration, defined as the time required to the spacecraft to transfer the specific cargo from the cargo injection orbit to the target operational one, starting from the spacecraft parking orbit. As recalled in Chapter 3, the transfer duration is approximated as a polynomial function of the thrust-over-mass ratio, peculiar for each scenario. Thus, the following results provide the transfer duration as a function of three parameters: (i) total thrust available, given by the number of operative HT20k times the specific thrust value with respect to its operational point; (ii) the total wet mass of the spacecraft, including the cargo mass; and (iii) the platform total power demand, i.e. the designated input power times the number of operative HETs in the cluster.

It is possible to observe some common behaviors, shared among all the scenarios and here reported:

1. The transfer duration trend with respect to all three parameters could be approximated, in almost all the scenarios, as a hyperbole with an horizontal asymptote, highlighting the deep interdependence among these three parameters, i.e. thrust, mass and power.

2. For the same design solution, i.e. same thrust, wet mass and power demand, the transfer duration decreases if the thruster lifetime increases.

3. To reduce the transfer duration, the thrust available has to be increased faster, i.e. greater punctual slope inclination, than the platform wet mass.

4. If the power demand increases, the transfer duration can be reduced but still the corresponding thrust-over-mass has to increase as well. Indeed, at the same power level, it is shown that multiple solutions correspond to different mission duration.

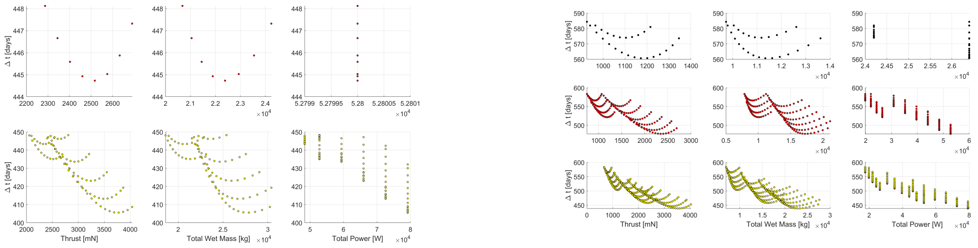

(a) Telecomm

(b) Disposal

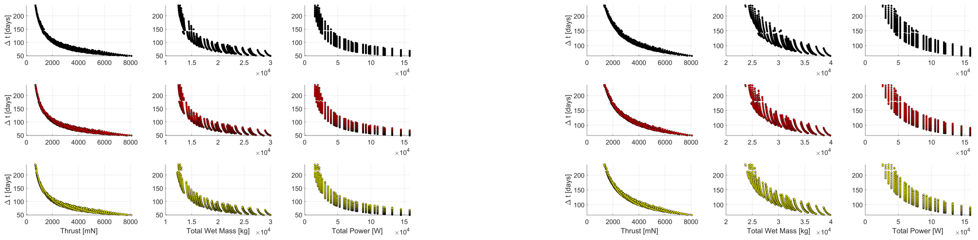

(c) Transportation 5t

(d) Transportation 10t

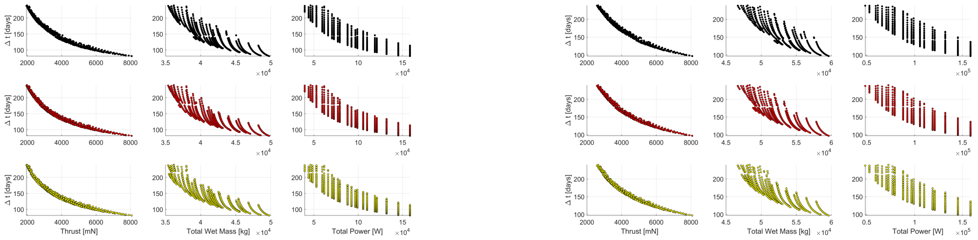

(e) Transportation 15t

(f) Transportation 20t

Figure A.3: Telecommunication scenario #2, Disposal scenario #6 and Transportation scenario #3 with 5/10/15/20 t cargo modules – Transfer duration with respect to total thrust available (left), total wet mass (center), and total power demand (right). Three lifetime levels for HT20k: (i) 20000 h (black circle); (ii) 25000 h (red circle); (iii) 30000 h (yellow circle).

Moreover, peculiar behaviors are shown within each scenario. In particular:

- Figure A.3a provides the transfer duration overview within the telecommunication scenario with respect to the total thrust available, the platforms total wet mass and their power demand. First, it is important to highlight that no feasible solutions are provided considering a HT20k with a 20000 h lifetime. On the other hand, the two lifetime levels show quite different behavior. In particular, for the 25000 h scenario, the transfer duration slightly varies, i.e. from 445 to 448 days, at different values of thrust and mass and it presents a minimum at about 2.5 N of thrust for a 22.5 t spacecraft. On the other hand, it is still possible to identify local minima but no symmetry is shown by the corresponding curves with respect to this minima for the 30000 h. Moreover, the transfer duration gap between the minimum and maximum is much higher than the 25000h case, i.e. almost 1.5months. Last, an interesting behavior is shown by the Δt-power demand subplot at 30000 h, where a relevant increase in the power demand correspond to a significant decrease in the transfer duration for those platform design in which the thrust-over mass ratio increase as well.

A.2 Optimal Nominal Operational Points

In this Section, the performance maps of all the 10 selected scenarios have been overlapped to identify which working point(s) is compliant with all the mission scenarios. In particular, the scenarios have been split in two groups. In the first group, all the four sub-cases of the transportation scenario as well as the disposal and telecommunication scenarios are included. The second one envisages the LST concept considering four scenarios, each one related to a different crew mission duration: (i) 30 days; (ii) 60 days; (iii) 90 days; and (iv) 180 days, i.e. the maximum duration envisioned according to the current plans for the Gateway. Moreover, the performance map overlapping has been done for different lifetime level. Hence, Figure A.4 provides the feasible working points for 20000 h, 25000 h and 30000 h for transportation, disposal and telecommunication scenarios. On the other hand, the performance maps for the LOP-G replenishment scenario are represented in Figure A.5.

First, no HT20k working point at 20000 h corresponds to a feasible telecommunication platform. The minimum lifetime that provides at least one common working point within the first group, corresponding to a 24 kW HT20k with a thrust higher than 1.1 N and an Isp between 2200 s and 2900 s, is 25000 h (Figure A.4.b). Moreover, increasing the lifetime to 30000 h (see Figure A.4.c) provides a wider area on the performance map in which all the scenarios present at least one feasible solutions. Indeed, it is possible to observe that the minimum input power is reduced to 16 kW and there are working points with a input voltage higher than 700V that are in common among all these scenarios (for input power greater or equal to 18 kW).

On the other hand, for what concern the LOP-G replenishment scenario, Figure A.5.a, i.e. 20000 h lifetime, highlights that all the identified working points provide

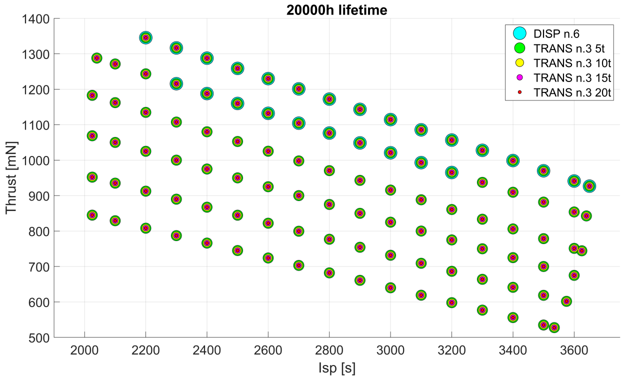

(a) 20000 h

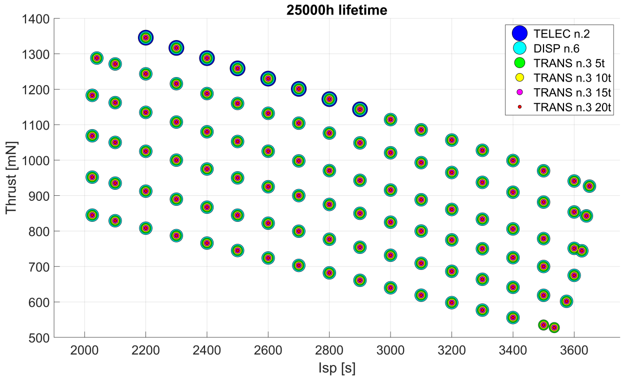

(b) 25000 h

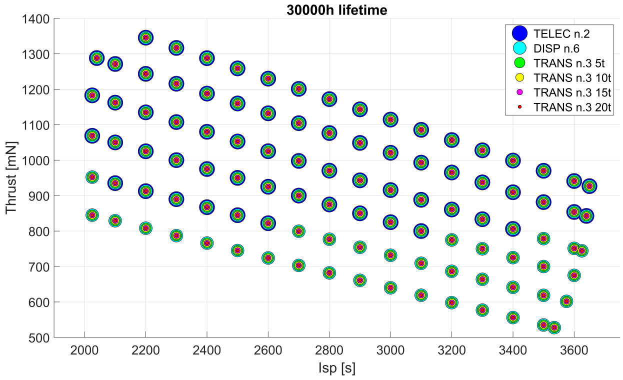

(c) 30000 h

Figure A.4: Performance map for transportation, disposal and telecommunication scenarios.

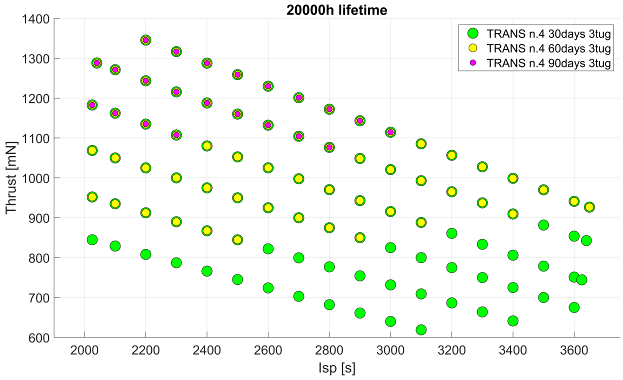

(a) 20000 h

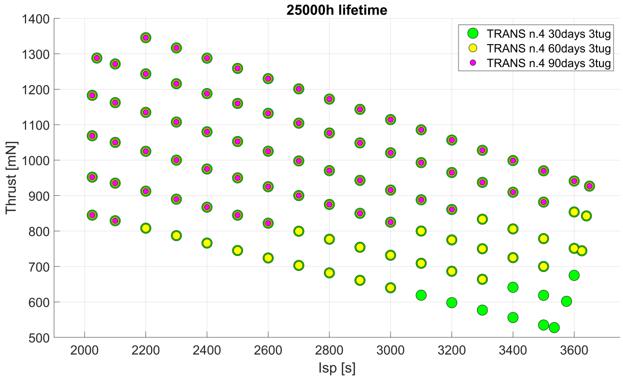

(b) 25000 h

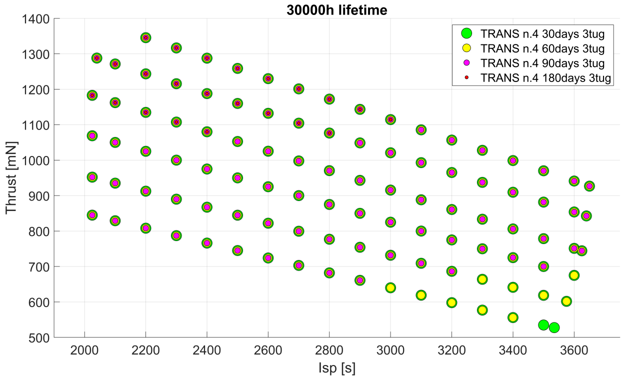

(c) 30000 h

Figure A.5: Performance map for LOP-G replenishment scenarios.

at least one feasible solutions for the 30-days scenario. Furthermore, it is evident that only HT20k operational points characterized by an input power higher than 20 kW and a thrust greater than 1050 mN are compliant with 30/60/90 days scenarios, whereas there are no feasible solutions for the 180 days sub-case. The shared area significantly increases for the 25000 h case, as shown in Figure A.5.b, providing feasible operational points for input power from 14 kW up to 24 kW and thrust higher than 900 mN. Figure A.5.c, on the other hand, sees again a reduction of the area in which finally all four sub-cases present compliant design solutions. In particular, no working point with an input voltage higher than 650V covers the need of all the scenarios and the minimum input power is equal to 20 kW, corresponding to a thrust higher than 1 N.

In conclusion, overlapping the 30000 h reference maps, i.e. the minimum lifetime requirement that covers all the case studies, have been overlapped to identify the area of HT20k performance map shared among all the mission scenarios, highlighted in red dashed rectangles in Figure A.6.

Analyzing the results depicted in Figure A.6, the following mission-driven requirements related to the HT20k technology have been derived:

- The HT20k thrust shall be between 1050 mN and 1350 mN;
- The HT20k specific impulse shall be between 2050 s and 3000 s;
- The HT20k input power shall be greater than or equal to 20 kW;
- The HT20k propellant mass flow shall be at least 38 mg/s;
- The HT20k lifetime shall be at least 30000 h;
- The HT20k input voltage shall be at most 825 V;
- The HT20k current shall be at least 42A;
- The e-PROP subsystem efficiency shall be at least 59%.

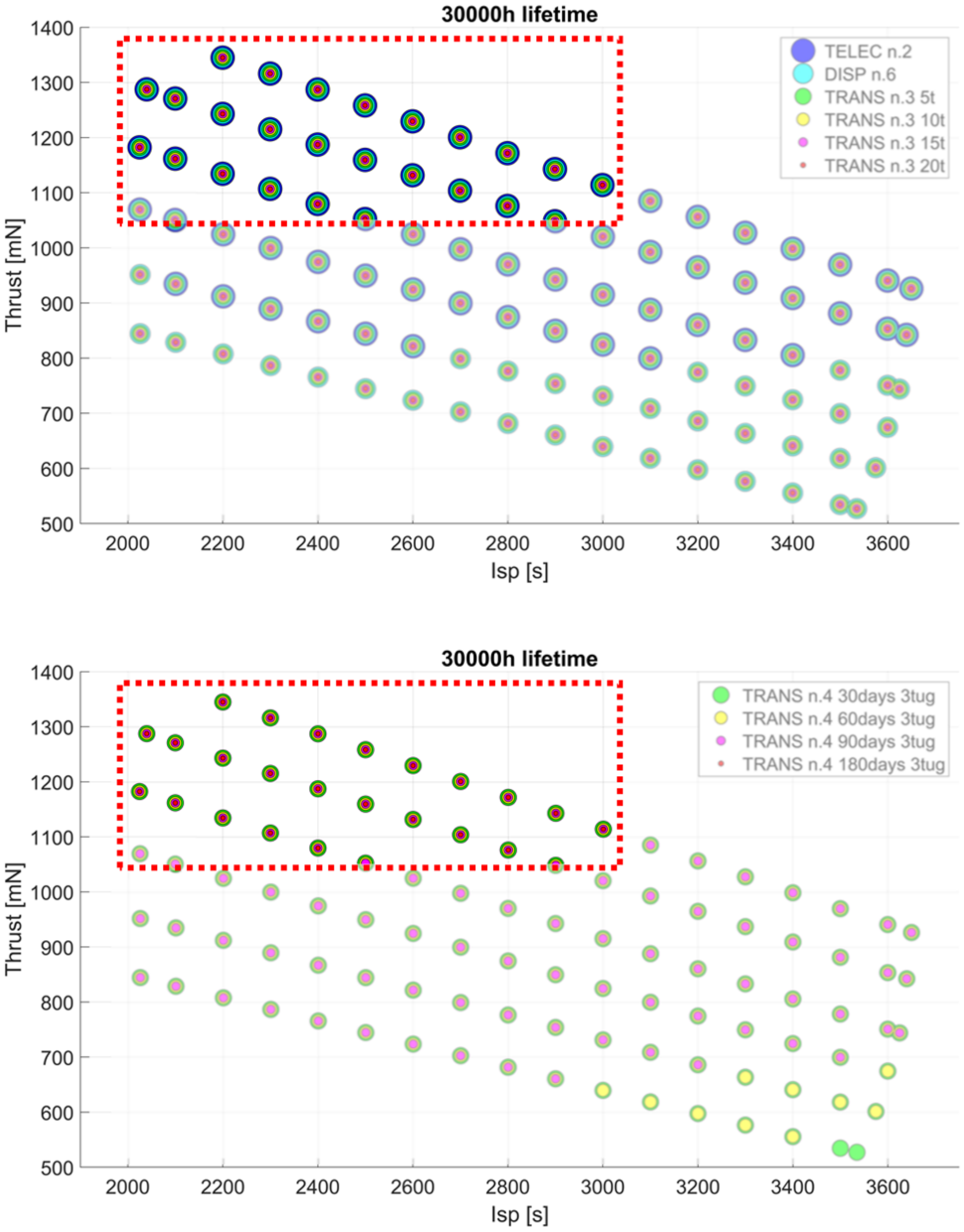

Figure A.6: Overlapped performance maps for all 10 selected scenarios. The red dashed rectangle highlights the area of the map shared among all the feasible concepts.

Appendix B

Real-Time Implementability Validation of Proposed MPC Schemes for Fixed-Wing UAVs

The real-time implementability of the control strategies discussed in Chapter 5 has been further investigated extending the field of application to fixed-wing UAV. Commonly known as drones, are being widely studied and developed due to their mission flexibility, reconfigurable architecture and cost effectiveness. The list of practical and potential applications of UAVs is wide, well beyond the boundaries of conventional remote sensing scenarios, as thoroughly described in [195]. Some typical fields of application are rescue and civil protection, precision farming, and urban monitoring, among which some common features can be identified: (i) high variability, such as the need of producing low-cost UAVs induces uncertainty in their characteristics; and (ii) safety issues, such as the need of guaranteeing the mission compliance with guaranteed deviation from the planned trajectory. In particular, the precision agriculture sector has seen a significant growth in the UAV exploitation, due to the great benefits given by the use of these platforms and the tools they incorporate, providing farmers with useful information ans ensuring the required efficiency and flexibility.

The challenges introduced by this new field of application are first due to the much faster dynamics characterizing the UAV dynamics with respect the spacecraft dynamics, mainly for what concerns the attitude dynamics. Second, from an implementation viewpoint, the class of mini/ micro UAVs shares limitations with most computer embedded systems: limited space and limited power resources, increasing computation requirements, complexity of the applications, as highlighted in [196]. For these reasons, the UAVs have been selected as additional *case-study* to validate the effectiveness of the proposed control algorithms, including also HIL tests, as described in the following Sections.

B.1 MH850 Fixed-Wing Mini-UAV and On-Board Systems

In recent years, fixed-wing UAVs have seen an revived interested with respect to the *multi-rotor* ones, thanks to their capability of performing longer missions, covering larger areas, and having lower construction costs. For this reason, the aircraft considered for the validation of the guidance and control scheme proposed is the MH850, a fixed-wing UAV (Figure B.1) belonging to the *MicroHawk family* of UAVs [197]. Developed for low cost alpine surveillance missions, the MH850 has a tailless configuration with an expanded poly-propylene wing (wingspan of 85 cm), a sintered nylon fuselage, trailing edge elevon, guaranteeing symmetric deflection for elevator δ_e and antisymmetric for aileron δ_a, and non-movable vertical fins at wingtips. Furthermore, it is equipped with an electric brushless motor and a Lithium polymer battery of 5000 mAh with two cells 2S (input voltage 7.4 V and discharge efficiency 0.875), which can guarantee and endurance close to 1 hour at an airspeed of 13.5 m/s and at an altitude of 100 m.

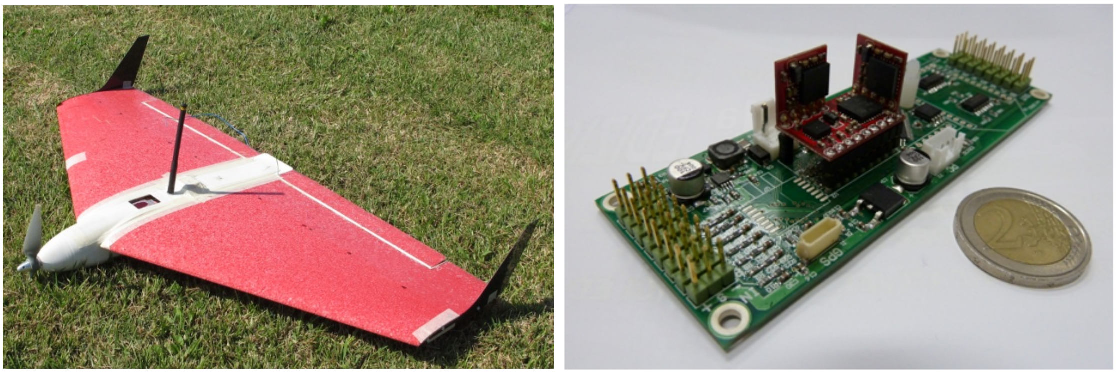

Figure B.1: The MH850 mini-UAV [197] and the custome-made autopilot (credit: Politecnico di Torino).

The flight autonomy of the MH850 is provided by the custom-made autopilot represented in Figure B.1, which has been developed by the Flight Mechanics group from the Department of Mechanical and Aerospace Engineering of Politecnico di Torino and it is characterized by an open architecture re-programmable in flight. Moreover, real-time telemetry related to the on-board sensors, i.e. GPS, barometric sensor, differential pressure and three-axis gyroscope and accelerometers, are sent to the ground control station thanks to a Radiomodem Xbee Pro S1, which guarantee the communication link. The ATXMEGA256A3U-3U microcontroller with a 256Kb flash memory and 16Kb of RAM completes the MH850 equipment.

The UAV rigid-body motion, assuming a flat non-rotating Earth, is described by a set of nonlinear equations, function of forces and moments acting on the vehicle and referred to a body-fixed reference frame. In the longitudinal plane, the longitudinal and vertical components of the total airspeed V, u and w respectively, the angle of attack $\alpha \simeq \frac{w}{V}$, the pitch angle θ and the pitch rate q are the state variables. On the other hand, the lateral component of the total airspeed v, the roll and yaw rates, p and r, respectively, and the roll angle ϕ are the state variables in the lateral-directional plane. Considering the forces and moments acting on the aircraft, $[F_X\ F_Y\ F_Z]^T$ and $[L\ M\ N]^T$, respectively, and that the aircraft control can be obtained exploiting the trailing edge elevon, i.e. symmetric deflection for elevator δ_e and antisymmetric for aileron δ_a, the UAV dynamics and kinematics are described by the following nonlinear model, as defined in [198]

- Longitudinal plane:

$$\begin{aligned}
\dot{u} &= \frac{F_X}{m} + qw - rv + g\sin\theta, \\
\dot{w} &= \frac{F_Z}{m} + pv - qu - g\cos\theta\cos\phi, \\
\dot{q} &= \frac{M}{J_y} + \frac{[J_{xz}(r^2 - p^2) + pr(J_z - J_x)]}{J_y}, \\
\dot{\theta} &= q\cos\phi - r\sin\phi.
\end{aligned}$$

- Lateral-directional plane:

$$\begin{aligned}
\dot{v} &= \frac{F_Y}{m} - pw + ru - g\cos\theta\sin\phi, \\
\dot{p} &= \frac{L}{J_x} + [J_{xz}(\dot{r} + pq) + qr(J_y - J_z)]J_x, \\
\dot{r} &= \frac{N}{J_z} + \frac{[J_{xz}(\dot{p} - pq) + pq(J_x - J_y)]}{J_z}, \\
\dot{\phi} &= p + q\sin\phi\tan\theta + r\cos\phi\tan\theta, \\
\dot{\psi} &= \frac{q\sin\phi}{\cos\theta} + \frac{r\cos\phi}{\cos\theta}.
\end{aligned}$$

where m is the aircraft mass and J_i are the moments of inertia with $i = x, y, z, xz$.

For the evaluation of the aircraft navigation, the vehicle-carried vertical reference frame is considered, which is centered in the aircraft center of gravity and the X_V axis is directed North, the Y_V axis towards East and the axis Z_V is along the local gravity acceleration vector. Thus, integrating the following equation, the position vector $[x\ y\ h]^T$ can be obtained

$$\begin{aligned}
V_N &= u\cos\theta\cos\psi + v(\sin\phi\sin\theta\cos\psi - \cos\phi\sin\psi) + w(\cos\phi\sin\theta\cos\psi + \sin\phi\sin\psi), \\
V_E &= u\cos\theta\sin\psi + v(\sin\phi\sin\theta\sin\psi + \cos\phi\cos\psi) + w(\cos\phi\sin\theta\sin\psi - \sin\phi\cos\psi), \\
V_D &= u\sin\theta + v\cos\theta\sin\phi + w\cos\phi\cos\theta,
\end{aligned}$$

where $[V_N\ V_E\ V_D]^T$ are the components of the total airspeed along the three axes in the so-called North-East-Down (NED) frame.

To complete the UAV model exploited for the validation of the controllers in the following Sections, the battery model to evaluate its consumption is here reported

$$\begin{aligned} I &= I_0 + \tfrac{dI}{d\tau}\tau, && \text{(B.1)} \\ V &= (\omega - r_1\tau)\tfrac{V_0}{\omega_0}, && \text{(B.2)} \end{aligned}$$

with

$$r_1 = -\frac{\omega_0}{\tau_{ST}} \quad \text{and} \quad \frac{dI}{d\tau} = \frac{I_{ST} - I_0}{\tau_{ST}},$$

where I_0 is related to the lost of current, I_{ST} is the stall current and τ_{ST} is the stall torque. V_0 and ω_0 are the nominal voltage and rpm values. The torque τ is evaluated starting from the blade element theory [199], using a Clark-YM15 airfoil with 250 mm of diameter. The charge level at the time $t+1$ is

$$E_b^{t+1} = E_b^t - \frac{V^t I^t}{\eta_b} t,$$

with $\eta_b = 0.85$ propeller efficiency and I^t and V_t are the current and the voltage, respectively, evaluated at the time t as in Eq. (B.1).

B.2 Guidance and Control Strategies

The key feature of the proposed approach is the design of combined guidance and control algorithms able to perform the desired mapping, guaranteeing robustness of the system to uncertainties and disturbances, reducing the flight time and optimizing the path while maintaining the trajectories in a pre-defined neighborhood on the nominal one with high probability. The guidance segment assumes a relevant role for the accomplishment of the UAV mission, providing a feasible trajectory, combined with the control system. The proposed software is able not only to maximize the performance of the on-board sensors, but also to improve the stability of the platform. Moreover, the same controller can be used for different UAVs, with similar but not identical characteristics, that can cover a bigger area with reduction of the cost and equipped with different payloads.

In the following Sections, the guidance algorithm exploited is briefly described in Section B.2.1 whereas in Section B.2.2, the effectiveness of the TRMPC scheme is validated, comparing the performance with those obtained exploiting an $\mathcal{L}_1$ controller. Then, the real-time implementability of the robust MPC is validated via HIL simulations applying the controller to a precision farming case-study. On the other hand, the OS-SMPC algorithm has been slightly modified, obtaining a tracking scheme to be applied for mapping applications in different scenario, as presented in Section B.2.3.

It is important to highlight that, in both cases, the path-following control of the UAV has been separated into different layers: (i) an inner loop for pitch θ and roll ϕ attitude and airspeed u; (ii) an outer loop for heading angle ψ and altitude h. Moreover, the effectiveness of the combined guidance and control strategies has been validated including both atmospheric disturbances, i.e. wind turbulence, as random and bounded noise, model uncertainties in terms of airspeed and mass variations on speed V and mass m, and platform inaccuracies, such as variations on the moments of inertia J.

B.2.1 Guidance Algorithm

The guidance algorithm adopted in this study and combined with both control schemes, i.e. TRMPC and OS-SMPC, has been proposed in [200] and is here briefly described. The guidance law is based on the definition of a set of waypoints with assigned NED coordinates, including the starting point, i.e. the point where the UAV finishes its climb and the autonomous flight starts. To guarantee the kinematic feasibility of the assigned trajectory in terms of speed and turn rate, a trajectory smoother is implemented. The performance of the guidance algorithm is evaluated as Cross-Track Error (CTE) ϵ_r. Defined the UAV real position P_{UAV} as East and North coordinates, i.e. E_{UAV} and N_{UAV} respectively, and the segment connecting two consecutive waypoints, i.e. the former $\mathrm{WP}_n(E_n, N_n)$ and the next $\mathrm{WP}_{n+1}(E_{n+1}, N_{n+1})$, the CTE can be expressed as

$$\epsilon_r = \frac{|E_{UAV} - \mathrm{m}N_{UAV} - (E_n - \mathrm{m}N_n)|}{\sqrt{\mathrm{m}^2 + 1}}, \tag{B.3}$$

with $\mathrm{m} = \frac{E_{n+1}-E_n}{N_{n+1}-N_n}$ (see Figure B.2).

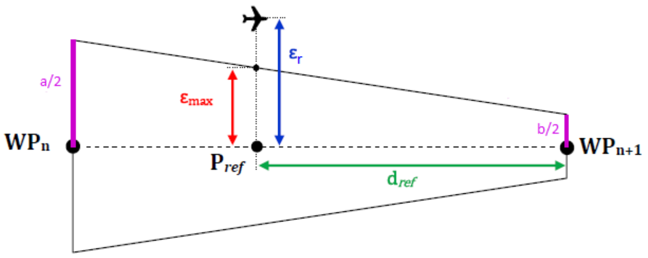

Figure B.2: CTE and reference distances.

A look-ahead or proximity distance is included to define the minimum distance of the UAV from the next waypoint. When the distance between the aircraft and the next waypoint is less than this pre-defined value, the waypoint is reached and the aircraft can move to the next waypoint.

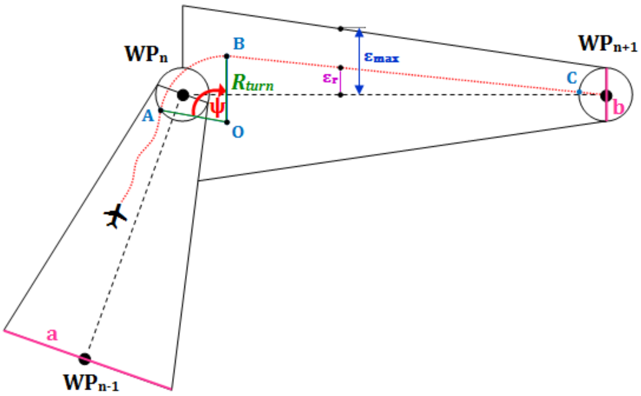

Figure B.3: Guidance phases.

The guidance sequence can be divided in three phases, as described in [200] and represented in B.3:

1. waypoint approach: assuming that the aircraft is flying with a fixed speed at a defined altitude, this phase is identified by the red dotted line before point A in Figure B.3. It is assumed that the waypoint has been reached when the FW-UAV flies into the imaginary circle centered in the waypoint WP$_n$ with radius equal to the defined proximity distance, i.e. fixed to 20 m in th following applications according to the MH850 dynamic constraint in terms of minimum turn radius.

2. aircraft turn around the waypoint: this segment is identified by the red dotted curve between points A and B in B.3.

3. straight flight: starts at the end of the last turn and ends at the beginning of the next turn, represented by the red spotted line between the points B and C in Figure B.3.

Moreover, a no-correction zone is included, in which the corrections on the heading angle are imposed only when the UAV CTE is larger than an assigned value (i.e. maximum acceptable CTE).

B.2.2 Tube-based Robust MPC for Precision Farming

As anticipated, TRMPC has been adopted to control both the inner and outer navigation loops of the longitudinal dynamics, including the airspeed longitudinal component u and the altitude h, as well as the roll angle ϕ. On the other hand, a PID controls the heading angle ψ. The reference signals to track are fed to the simulator as step and doublet inputs, as shown in Figure B.4. Moreover, while the initial conditions for the linear model are set to zero, for the nonlinear model, the following equilibrium flight conditions have been adopted: (i) $V_0 = 13.5$ m/s; (ii) $h_0 = 100$ m; (iii) angle-of-attack $\alpha_0 = 5.18$ deg; (iv) ramp angle $\gamma = 0$, i.e. $\theta_0 = 5.18$ deg. Last, the TRMPC performance applied to the linear model have been compared with those obtained adopting a $\mathcal{L}_1$ controller, showing the higher reliability of the robust controller in the presence of disturbances.

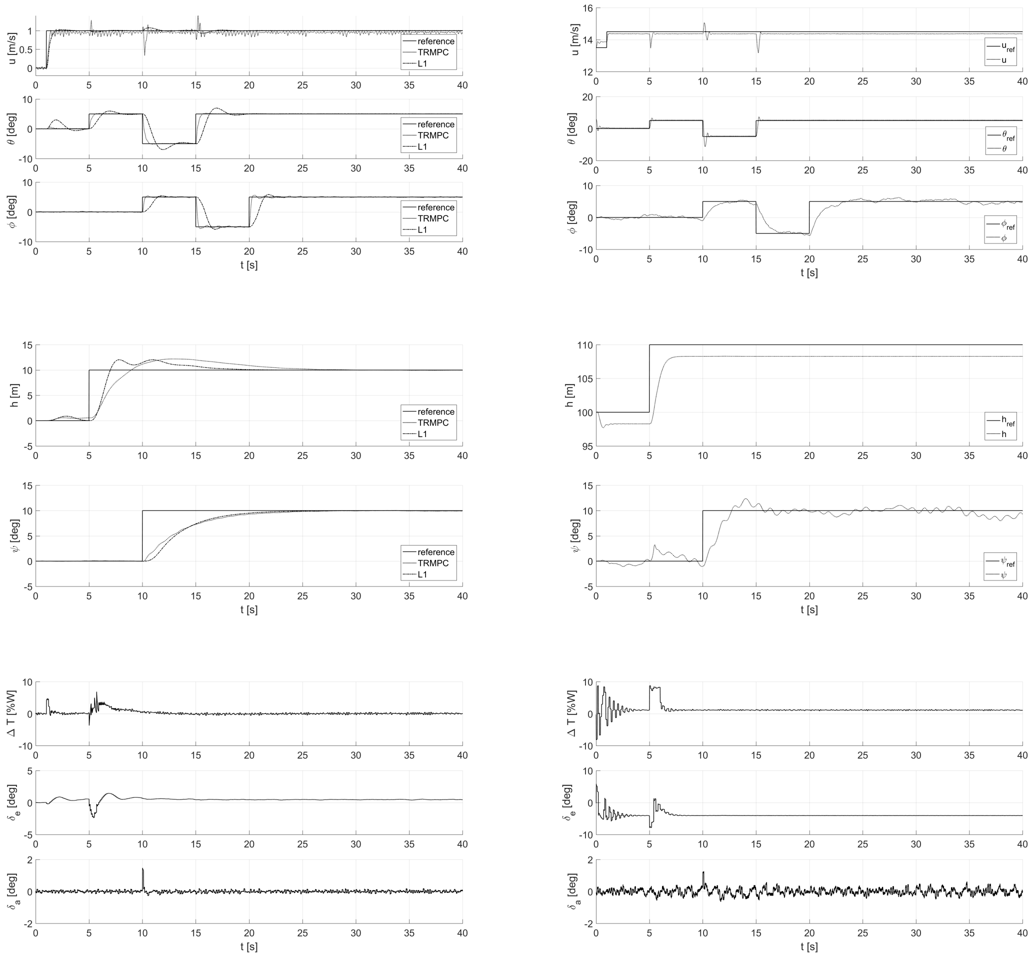

Figure B.4: Inner and outer variables behavior and control actions for both linear (left column) and nonlinear (right column) models exploiting TRMPC.

Comparing the results among linear and non linear models it is possible to highlight that in both cases the controller provides the required robustness to disturbances, maintaining the state variables within the allowed boundaries and providing a remarkable tracking capability. In particular, TRMPC is able to better follow the reference signal for the outer loop navigation when the linearized dynamics is envisioned. Another relevant difference can be spotted in the control action trend. Indeed, the adoption of a nonlinear model implies relevant interconnection among state variables characterized by different dynamic rate. Typically, these variables are controlled separately, in order to properly tune the parameters in compliance with the specific needs. In this work, on the other hand, the controller is exploited for both inner and outer loop variables, resulting in a higher control effort than the linear case, as shown in the last two plots in Figure B.4.

The next step consisted in envisioning three different scenarios analyzed to preliminary assess the effectiveness of the guidance and control scheme here proposed and to compare the performance obtained both with SIL and HIL simulations. In particular, three standard paths have been considered:

1. a square pattern, identified by four waypoints, one for each corner, plus the initial one corresponding to the center of the square itself. This kind of path could be representative of a civil protection scenario where a high-risk area shall be monitored;
2. a butterfly pattern, also in this case defined by four waypoints plus the central one. It could be envisioned for patrolling tasks over an area of interest, such as industrial warehouses and criminal neighborhood;
3. a snake pattern, which turns are identified through 8 waypoints, one of them representing the starting point for the autonomous flight. This last case of study could be envisioned for precision farming applications in which large area shall be monitored to estimate sensitive vegetation indexes or where UAVs are exploited either to properly distribute fertilizer and to irrigate the field.

For all these case studies, the same initial conditions have been considered. Moreover, the MPC parameters have been set uniformly within all the scenarios as well as the sample times: (i) system dynamics 0.01 s; (ii) TRMPC sample time = 0.1 s. For what concern the other MPC parameters, they are reported in Table B.1. Instead, for the robustly stabilizing feedback gain matrix K, it has been evaluated offline exploiting typical robust tools. For each case study, ten SIL and ten HIL simulations have been performed exploiting a MATLAB/Simulink simulator running over a Intel Core i7 − 7500U CPU @2.70 GHz with 16 GB of RAM and 512 GB solid-state drive and the XMOS board for HIL simulations.

In terms of uncertainties and disturbance included in the model, a ±15% variation of cruise speed, UAV mass and inertia has been considered, together with a fixed-direction wind turbulence, representing a bounded persistent disturbance affecting the system and modeled as random noise with uniform distribution and

Table B.1: TRMPC parameters.

Parameter	Value
N_{long}	30
N_{lat}	30
$diag(Q_{long})$	$[10^6,4 \times 10^1,4 \times 10^1,4 \times 10^1,10^5]$
$diag(R_{long})$	$[4 \times 10^2, 3 \times 10^{-6}]$
$diag(Q_{lat})$	$[10^1,10^1,10^1,10^4]$
R_{lat}	10^4

maximum intensity of ±1 m/s. Moreover, additional external disturbances have been included as affecting the other states and their values are reported in Table B.2.

Table B.2: Additive disturbances considered.

LONG. disturbance	Disturbance value	LAT.-DIR. disturbance	Disturbance value
d_u [m/s]	1.5	d_v [m/s]	1.5
d_α [rad]	10^{-2}	d_p [rad/s]	10^{-2}
d_θ [rad]	10^{-2}	d_r [rad/s]	10^{-2}
d_q [rad/s]	10^{-2}	d_ϕ [rad]	10^{-2}
d_h [m]	10^{-1}		

Figure B.5, Figure B.6 and Figure B.7 provide the SIL and HIL simulation results obtained for all the three case studies, i.e. the square, butterfly and snake paths, respectively. In all the figures, the trapezoidal corridors refer to the guidance constraints, described in Section B.2.2, which bases are centered in two consecutive waypoints. All three scenarios shown that the TRMPC is able to follow the trajectory reference provided by the guidance algorithm, maintaining the UAV within the pre-defined track, both in SIL and HIL simulations.

Moreover, it is possible to observe that even during turns, the controller is able to limit the UAV drift while maintaining the longitudinal airspeed within the boundary constraints, aiming to the position constraints compliance as well. The mission accomplishment is also guaranteed by the proper tracking of the roll angle signal, which defines the aircraft turning according to the waypoints position.

To properly compare the TRMPC effectiveness among SIL and HIL simulations,

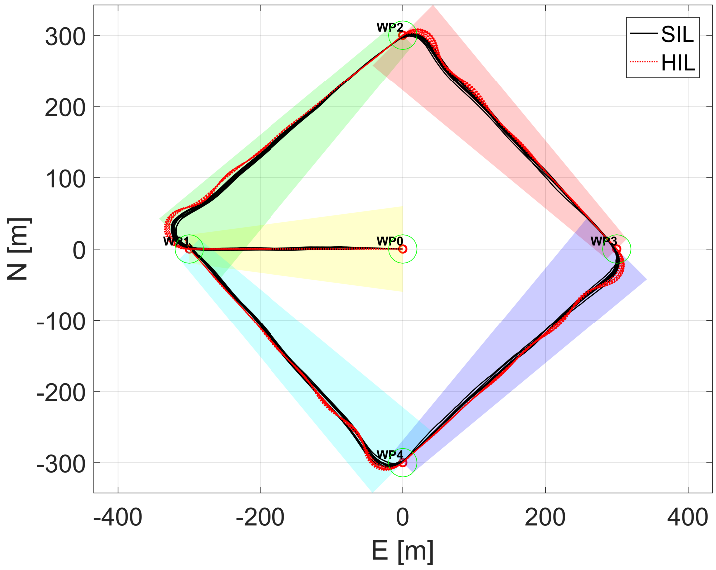

Figure B.5: SIL vs HIL for a square pattern.

the reader is referred to Figure B.8 where an ad-hoc zoom-in is provided for all three case studies to better highlight the differences among the two sets of results. On one side, Figure B.8 confirms the effectiveness of the guidance and control scheme in tracking the pattern to follow both in SIL and HIL simulations. On the other side, it appears clear that the internal communication delays introduced by the micro-controller slightly affect the controller performance, mainly in correspondence of the UAV turns around the waypoint.

Indeed, when the UAV heading angle is subject to a relevant change in its reference signal, corresponding to the most critical part of the entire mission profile, the inherent delays act as an additional disturbance affecting the system dynamics and the control performance as well. In this case, the TRMPC takes longer to damp the following oscillations, as highlighted in both Figure B.8 (a) and Figure B.8 (b).

Then, the TRMPC computational affordability has been validated analyzing the related Elapsed Real Time exploiting the *Real-Time Pacer* Simulink Toolbox (version 1.0.0.1) developed by Gautam Vallabha, which allows to force a simulation to run in real (wall clock) time. Indeed, the RealTime Pacer block slows down the simulation time so that is synchronizes with real elapsed time. As described in [201], the matching between simulation time and elapsed real time is approximate, with expected differences on the order of $10 - 30$ ms. Figure B.9 provide the computational load required for all three case studies during the HIL runs as the ratio between the simulated time and the elapsed one. As it is possible to notice, for all the case study, the elapsed time is much lower than the simulated one, i.e. 150s for

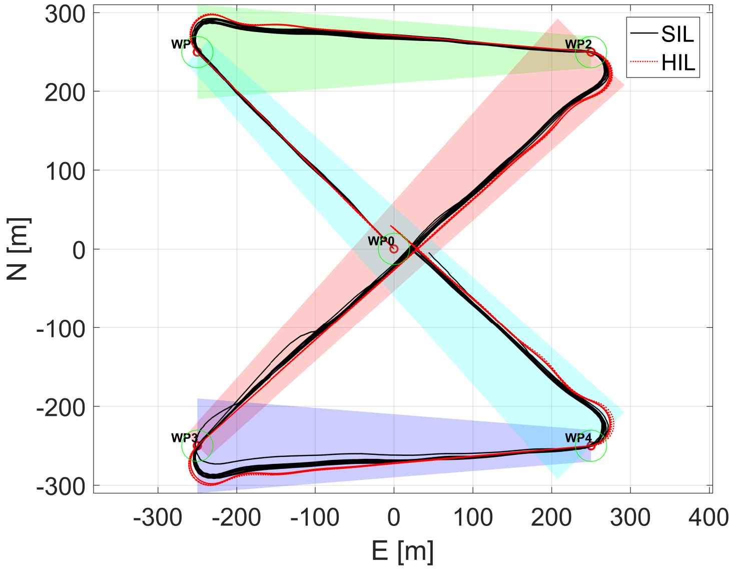

Figure B.6: SIL vs HIL for a butterfly pattern.

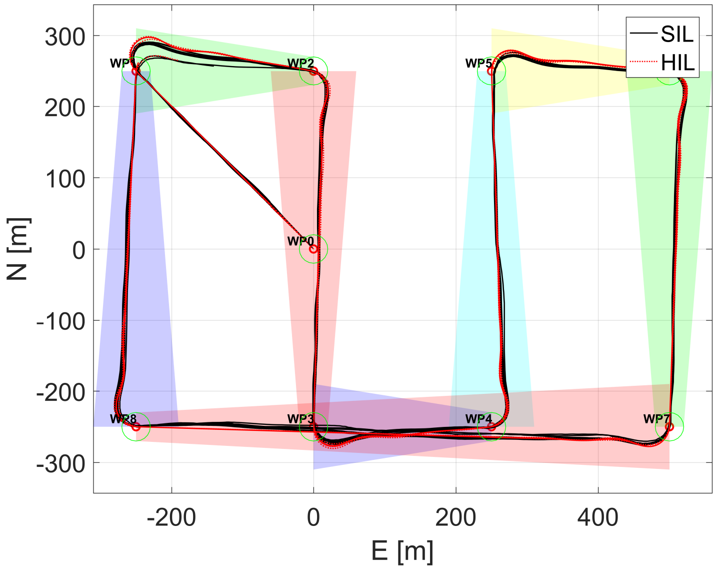

Figure B.7: SIL vs HIL for a 8-waypoints snake pattern.

the square pattern, 190 s for the butterfly and 350 s for the snake. Indeed, the average percentage is about 17%, thus implying potential real-time implementability of the proposed guidance and control scheme on the selected autopilot.

The last step consists in applying the TRMPC scheme to a real applications, in

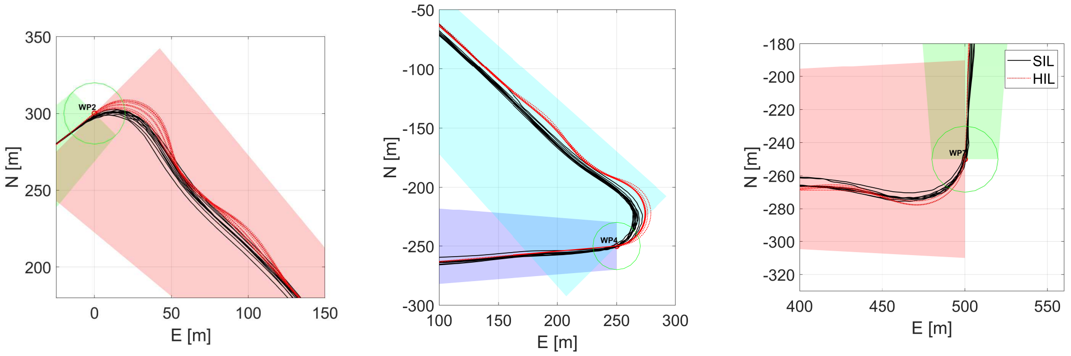

(a) square (b) butterfly (c) snake

Figure B.8: Zoom-in on the square, butterfly and snake patterns.

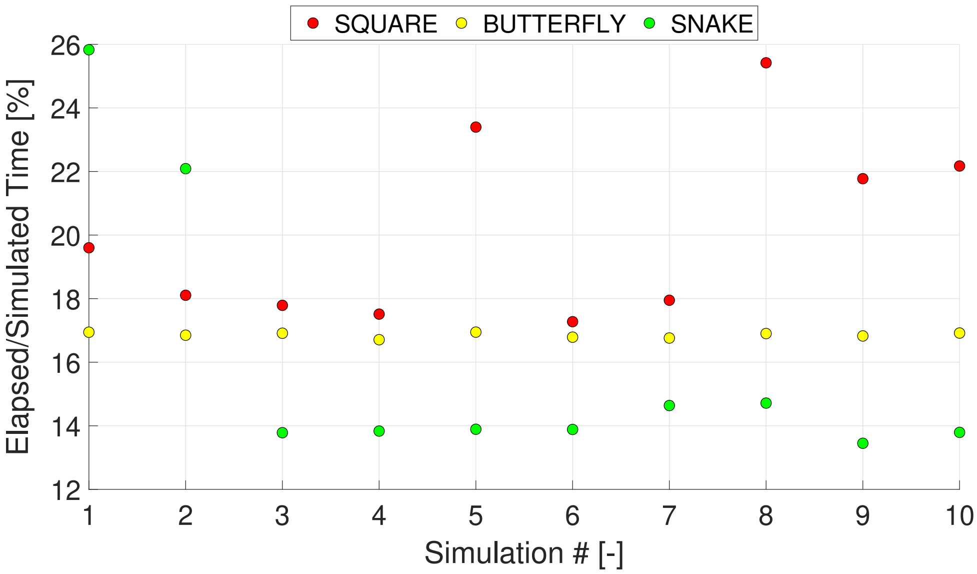

Figure B.9: Elapsed-over-simulated time for the three case study.

this case precision farming. In particular, the scenario chosen envisions the monitoring of a paddy field in Olcenengo, Piedmont, Italy (45°22′22.2″N, 8°17′34.3″E) to obtain information about the Normalized Difference Vegetation Index to assess whether the target being observed contains live green vegetation or not. Assuming that the MH850 is equipped with a specific payload, the OptRx® crop sensor from AG Leader (www.agleader.com), a snake-path has been identified over a 200X150 m rectangular-shape area, where the grid width is defined according to the specific payload requirements (see [202] for further details). In this case, considering an flight altitude of 100 m, the grid size (yellow and green strips) has been set to 20 m and is defined including a 10% of both overlap and sidelap requirements. Moreover, the coverage area includes also an additional 10 m band for the flight path in order to allow the stabilization of the UAV for a straight flight after each turn. Both SIL and HIL simulations have been performed to validate the guidance and control strategy, considering the following initial conditions: (i) altitude $h_0 = 100$ m; (ii) airspeed $V_0 = 13.5$ m/s; (iii) angle-of-attack $\alpha_0 = 5.18$ deg; (iv) ramp angle $\gamma_0 = 0$ deg and the main results are provided in Figure B.10 and Figure B.11.

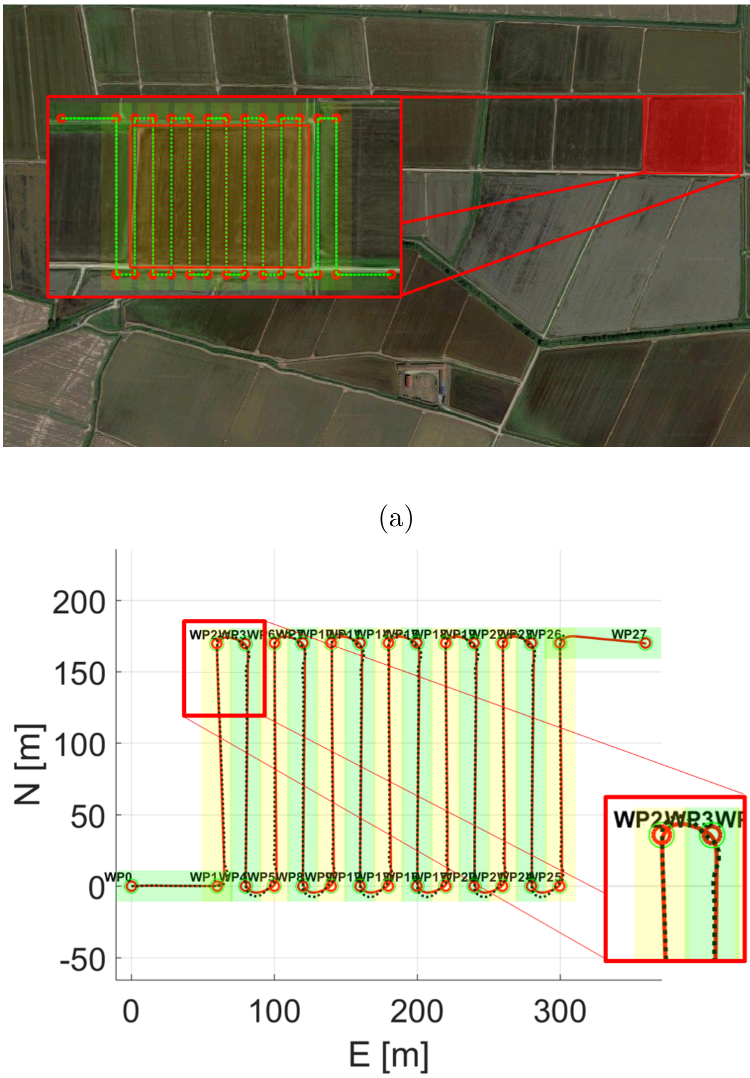

(a)

(b)

Figure B.10: (a) Monitored portion of field at Olcenengo, Italy, overlapped with a snake-path. (b) Comparison among SIL (red line) and HIL (dotted black line) trajectories.

It is possible to observe not only the adherence among SIL and HIL simulations,

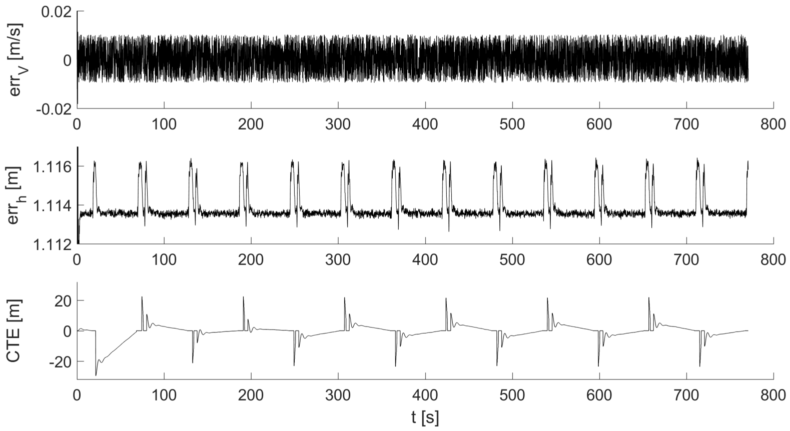

Figure B.11: Deviations between actual airspeed and altitude with respect to the references, and CTE for the UAV position.

corroborating the real-time implementability of the control strategy even with low-computational hardware, but also the robustness with respect to the 0.5 m/s wind turbulence considered. Indeed, the UAV always remains within the highlighted strips, guaranteeing the optimal performance of the payload as well.

B.2.3 Offline-Sampling Stochastic MPC for Multi-Scenario Mapping

For the validation of the OS-SMPC algorithm, other two scenarios have been considered, in addition to the precision farming application already presented in Section B.2.2:

- **rescue and civil protection:** square-patterns, normally covering a pre-assigned sequence of waypoints with selectable levels of persistence (monitoring or ground tracking). In the frame of UAV for civil protection, the selected area is a high-risk landslides area close to the Taro River, Parma, Italy (45°29′43.1″N,9°47′47.3″E), where the overfly is required to monitor the landslide movement in the Boceto area to prevent catastrophic consequences such as those occurred in February 2014.
- **urban monitoring:** complex 3D flight paths, highly connected with the requirements for safety of citizens and collision avoidance, related to buildings, obstacles and other vehicles. A neighborhood in the Downtown Miami's Brickell Financial District, Miami, FL, USA (25°45′31.3″N,80°11′28.3″W), around the Four Season Hotel and Tower, has been chosen for the urban scenario, where the local police enforcement has already started exploiting drones for drug interdiction, patrol missions, and criminal surveillance. In this case,

the selected waypoints have been identified with respect to the buildings-to-be-monitored location and the safety-area around them, set to be compliant with (possible) risk-mitigation rules, obtaining a piecewise-linear pattern as shown in Figure B.14.

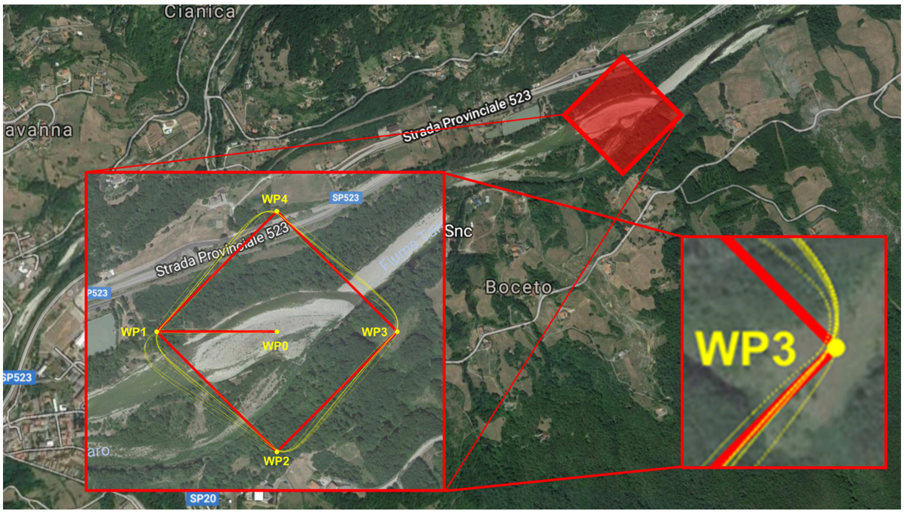

Figure B.12: 20 different square-trajectories over the Taro River, Borgo Val di Taro, Parma, Italy. The area covered has an extension of about 180 ha.

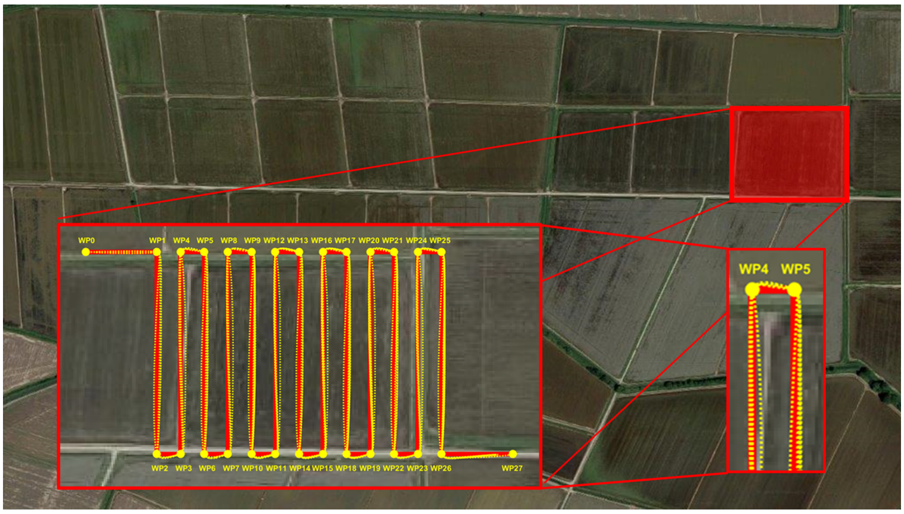

Figure B.13: 20 different snake-trajectories over a paddy field in Olcenengo, Vercelli, Italy.

In general, for all three scenarios, we can notice a *tangible* effectiveness of the proposed control strategy since the UAV results able to properly follow the path

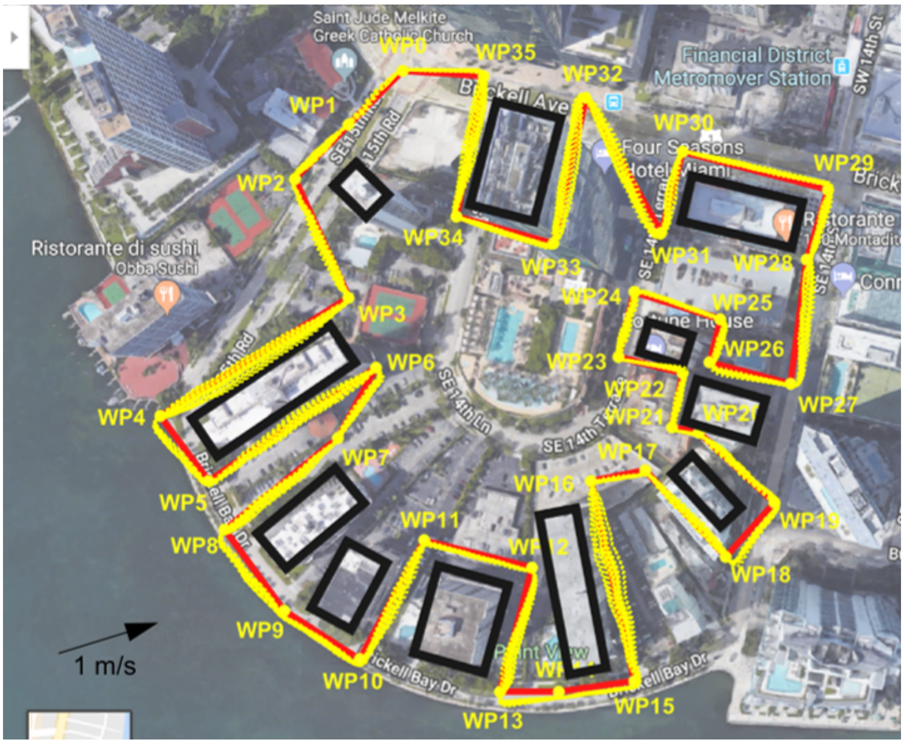

Figure B.14: 20 different piecewise-linear trajectories over Downtown Miami's Brickell Financial District, around the Four Season Hotel and Tower - 2D trajectories.

provided by the guidance algorithm, as shown in Figure B.12, Figure B.13 and Figure B.14, even in the presence of a 1 m/s fixed-direction wind turbulence.

Last, the effectiveness of the tracking OS-SMPC scheme has been compared with an LQMPC and Figure B.15 highlights how the presence of wind significantly influence the control capabilities of the LQMPC (black trajectory) which has shown effective behavior if the MPC sample time is reduced to 0.01 s, i.e. the same of the UAV dynamics. On the other hand, the remarkable tracking capabilities provided by the OS-SMPC remains acceptable with a sample time of 0.1 s, which should allow the real-time feasibility, compromised for a much shorter time-step and reduced hardware computational capabilities.

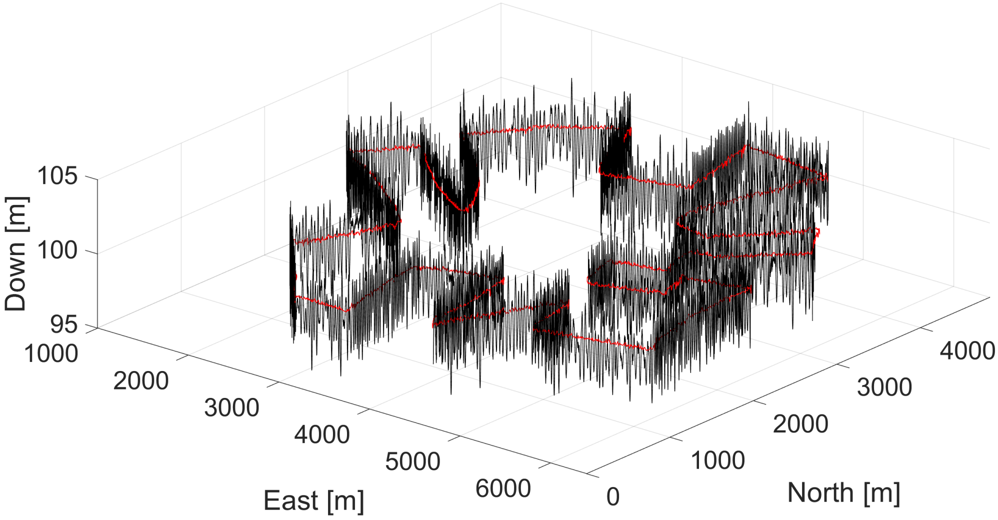

Figure B.15: LQMPC 3D trajectory (black line) and OS-SMPC 3D trajectory (red line).

Additional Notes

Author’s Comments about Autoplagiarism

- Part of the work described in Chapter 2 and Chapter 3 has been previously published in [203], [204], [205], [206], [207], [208], [209], [210], [211], [212], and [213].

- Part of the work described in Chapter 4 and Chapter 5 has been previously published in [214], [215], [206], [216], [217], [218], [213], [219], and [220].

- Part of the work described in Chapter 6 has been previously published in [216], [217], [218], [221], [213], and [220].

- Part of the work described in Appendix A has been previously published in [209], [222], [223], and [224].

- Part of the work described in Appendix B has been previously published in [225], [226], and [227].

Bibliography

[1] *The Post-Apollo Space Program: Directions for the Future*. Tech. rep. NASA Space Task Group, 1969.

[2] *Summary Report Future Programs Task Group*. Tech. rep. NASA Future Program Task Group, 1965.

[3] T.H. Sharpe and G. Von Tiesenhausen. *Space Flight Evolution*. Tech. rep. NASA Marshall Space Flight Center, 1970.

[4] International Space Exploration Coordination Group. *The Global Exploration Strategy: The Framework for Coordination*. Tech. rep. 2007.

[5] International Space Exploration Coordination Group. *The Global Exploration Roadmap - September 2011*. Tech. rep. 2011.

[6] International Space Exploration Coordination Group. *The Global Exploration Roadmap - August 2013*. Tech. rep. 2013.

[7] International Space Exploration Coordination Group. *The Global Exploration Roadmap - January 2018*. Tech. rep. 2018.

[8] National Research Council and others. *NASA Space Technology Roadmaps and Priorities: Restoring NASA's Technological Edge and Paving the Way for a New Era in Space*. National Academies Press, 2012.

[9] R. Myers and C. Carpenter. "High Power Solar Electric Propulsion for Human Space Exploration Architectures". In: *32nd International Electric Propulsion Conference (IEPC)*. 2011, pp. 2011–261.

[10] *NASA Seeks Information for Gateway Cargo Delivery Services*. 2018. URL: `https://www.nasa.gov/feature/nasa-seeks-information-for-gateway-cargo-delivery-services`.

[11] C.M. Jewison. "Guidance and Control for Multi-Stage Rendezvous and Docking Operations in the Presence of Uncertainty". PhD thesis. Massachusetts Institute of Technology, 2017.

[12] D. Zimpfer, P. Kachmar, and S. Tuohy. "Autonomous Rendezvous, Capture and In-Space Assembly: Past, Present and Future". In: *1st Space Exploration Conference: Continuing the Voyage of Discovery*. 2005.

[13] K.J. Schlager. “Systems Engineering-Key to Modern Development”. In: *IRE Transactions on Engineering Management* 3 (1956), pp. 64–66.

[14] E.C. Honour. “INCOSE: History of the International Council on Systems Engineering”. In: *Systems Engineering: The Journal of The International Council on Systems Engineering* 1.1 (1998), pp. 4–13.

[15] T. Robertson. “INCOSE Systems Engineering Handbook”. In: *INSIGHT* 1.2 (1998), pp. 20–20.

[16] R. Shishko and R. Aster. “NASA Systems Engineering Handbook”. In: *NASA Special Publication* 6105 (1995).

[17] J.R. Wertz and W.J. Larson. *Space Mission Analysis and Design.* Microcosm Press and Kluwer Academic Publishers, El Segundo, CA, USA, 1999.

[18] N. Viola et al. “Functional Analysis in Systems Engineering: Methodology and Applications”. In: *Systems Engineering-Practice and Theory.* InTech, 2012.

[19] P.K. McConnaughey et al. *Draft Launch Propulsion Systems Roadmap.* Tech. rep. 2010.

[20] United Launch Alliance. *Delta IV Launch Services User’s Guide - June 2013.* Tech. rep. 2018.

[21] International Launch Services. *Proton Launch System - Mission Planner’s Guide - Revision 7 - July 2009.* Tech. rep. 2009.

[22] SpaceX. *SpaceX Falcon Heavy.* 2018 (accessed August 22, 2018). URL: `https://www.spacex.com/falcon-heavy`.

[23] S.S. Pietrobon. “Fly Me to the Moon on an SLS Block II”. In: *Proceedings of International Astronautical Congress (IAC).* 2017.

[24] ArianeSpace. *Ariane 5 User’s Manual - Issue 5 Revision 2 - October 2016.* Tech. rep. 2016.

[25] ArianeSpace. *Ariane 6 User’s Manual - Issue 1 Revision 0 - March 2018.* Tech. rep. 2018.

[26] R. Whitley et al. “Global Exploration Roadmap Derived Concept for Human Exploration of the Moon”. In: *Proceedings of Global Space Exploration Conference (GLEX).* 2017.

[27] Guardabasso, P. et al. “Lunar Outpost Sustaining Human Space Exploration by Utiizing In-Situ Resources with a Focus on Propellat Production”. In: *Proceedings of International Astronautical Congress (IAC).* 2018.

[28] A.E.M. Casini et al. “Analysis of a Moon Outpost for Mars Enabling Technologies through a Virtual Reality Environment”. In: *Acta Astronautica* 143 (2018), pp. 353–361.

[29] S. Li et al. “Direct Evidence of Surface Exposed Water Ice in the Lunar Polar Regions”. In: *Proceedings of the National Academy of Sciences* (2018).

[30] B. Hill. ““The Next Great Steps”: Space Policy Directive-1”. In: (2018).

[31] K. Timmons et al. “The Orion Spacecraft as a Key Element in a Deep Space Gateway”. In: *2018 IEEE Aerospace Conference*. 2018.

[32] K. Kubicek and B. Woolford. *Man-Systems Integration Standards*. Tech. rep. NASA-STD-3000, 1995.

[33] W.J. Larson and L.K. Pranke. *Human Spaceflight Mission Analysis and Design*. New York: McGraw—Hill, 1999.

[34] J. Geffre, D. Cooke, and J. Carpenter. *Lunar L1 Gateway Conceptual Design Report - EX15-01-001*. Tech. rep. NASA, 2001.

[35] S. Ross and M. Lo. “The Lunar L1 Gateway-Portal to the Stars and Beyond”. In: *Proceedings of AIAA Space 2001*. 2001.

[36] R. Whitley and R. Martinez. “Options for Staging Orbits in Cislunar Space”. In: *Proceedings of IEEE Aerospace Conference*. 2016.

[37] M.L. McGuire et al. “Low Thrust Cis-Lunar Transfers Using a 40 kW-Class Solar Electric Propulsion Spacecraft”. In: *Proceedings of AAS/AIAA Astrodynamics Specialist Conference*. 2017.

[38] D. Smitherman and G. Woodcock. “Space Transportation Infrastructure Supported by Propellant Depots”. In: *Proceedings of AIAA SPACE 2011*. 2011.

[39] J. Goff et al. “Realistic Near-Term Propellant Depots: Implementation of a Critical Spacefaring Capability”. In: *Proceedings of AIAA SPACE 2009*. 2009.

[40] B. Kutter et al. “A Practical, Affordable Cryogenic Propellant Depot based on ULA’s Flight Experience”. In: *Proceedings of AIAA SPACE 2008*. 2008, p. 7644.

[41] E. Henderson and M. Holderman. “Technology Applications that Support Space Exploration”. In: *Proceedings of 47th AIAA/ASME/SAE/ASEE Joint Propulsion Conference and Exhibit*. 2011.

[42] *Seeking a Human Spaceflight Program Worthy of a Great Nation - Review of US Human Spaceflight Plans Committee*. Tech. rep. U.S. Human Spaceflight Plans Committee, 2009.

[43] K. Geurts. “Electric Propulsion and Spacecraft Trajectory Design”. PhD Dissertation. Università degli Studi di Pisa, 2008.

[44] D. Manzella. “Low Cost Electric Propulsion Thruster for Deep Space Robotic Missions”. In: *Proceeding of 2007 NASA Science Technology Conference*. 2007.

[45] B.E. Beal. “Clustering of Hall Effect Thrusters for High-Power Electric Propulsion Applications”. PhD Dissertation. University of Michigan, 2004.

[46] R.R. Hofer and T.M. Randolph. “Mass and Cost Model for Selecting Thruster Size in Electric Propulsion Systems”. In: *Journal of Propulsion and Power* 29.1 (2012), pp. 166–177.

[47] *COBHAM Xenon Propellant Tank Factsheet.* Tech. rep. COBHAM, 2009.

[48] C.A. Paissoni. *Electric Propulsion for a Cislunar Space Tug: Preliminary Sizing and Investigation on Mutual Influences.* Master Thesis. 2017.

[49] S. Mazouffre. “Electric Propulsion for Satellites and Spacecraft: Established Technologies and Novel Approaches”. In: *Plasma Sources Science and Technology* 25.3 (2016), p. 033002.

[50] V. Kim et al. “Electric Propulsion Activity in Russia”. In: *IEPC Paper* 5 (2001), p. 2001.

[51] R.R. Hofer et al. “Development Approach and Status of the 12.5 kW HERMeS Hall Thruster for the Solar Electric Propulsion Technology Demonstration Mission”. In: *34th International Electric Propulsion Conference (IEPC).* 2015.

[52] R. Hofer et al. “Development Status of the 12.5 kW Hall Effect Rocket with Magnetic Shielding (HERMeS)”. In: *35th International Electric Propulsion Conference (IEPC).* 2017.

[53] D.A. Herman et al. “Overview of the Development and Mission Application of the Advanced Electric Propulsion System (AEPS)”. In: *35th International Electric Propulsion Conference (IEPC).* 2017.

[54] J.R. Brophy. “Legacy of the Asteroid Redirect Robotic Mission (ARRM)”. In: *35th International Electric Propulsion Conference (IEPC).* 2017.

[55] Andreussi, T. et al. “Development Status of Sitael’s 20 kW-Class Hall Thruster”. In: *10th 3AF Space Propulsion.* 2018.

[56] M. Andrenucci, F. Battista, and P. Piliero. “Hall Thruster Scaling Methodology”. In: *29th International Electric Propulsion Conference (IEPC).* 2005.

[57] T. Misuri et al. “High Power Hall Thruster Design Options”. In: *30th International Electric Propulsion Conference (IEPC).* 2007.

[58] *MegaFlex™ Solar Array Systems Factsheet.* Tech. rep. Northrop Grumman, 2018.

[59] *UltraFlex™ Solar Array Systems Factsheet.* Tech. rep. Northrop Grumman, 2018.

[60] *GS YUASA LSE134 Lithium-Ion Battery Factsheet.* Tech. rep. GS YUASA, 2012.

[61] *CDF Study Report - CLEO/P - Assessment of a Europa Penetrator Mission as Part of NASA Clipper Mission*. Tech. rep. ESA CDF Team, 2015.

[62] *CDF Study Report - SPP Executive Summary - Consolidated Data for Small Planetary Platforms in NEO and MAB*. Tech. rep. ESA CDF Team, 2018.

[63] *20N Chemical Monopropellant Hydrizine Thruster*. Tech. rep. arianeGROUP, 2018.

[64] *Rockwell Collins RDR 68-3 Reaction Wheel Factsheet*. Tech. rep. Rockwell Collins, 2018.

[65] F.L. Markley and J.L. Crassidis. *Fundamentals of Spacecraft Attitude Determination and Control*. Springer, 2014.

[66] W. Fehse. *Automated Rendezvous and Docking of Spacecraft*. Cambridge university press, 2003.

[67] R. Biesbroek. *Lunar and Interplanetary Trajectories*. Springer, 2016.

[68] *Margin Philosophy for Science Assessment Studies - Issue 1 Revision 3 - June 2012*. Tech. rep. ESA European Space Research and Technology Centre, 2012.

[69] P.M. Vernicari. *Cost Analysis of a Lunar Space Tug*. Master Thesis. 2017.

[70] R.R. Hofer and T.M. Randolph. “Mass and Cost Model for Selecting Thruster Size in Electric Propulsion Systems”. In: *Journal of Propulsion and Power* 29.1 (2012), pp. 166–177.

[71] B. Aldrin. “Line-of-Sight Guidance Techniques for Manned Orbital Rendezvous”. PhD thesis. Massachusetts Institute of Technology, 1963.

[72] M.E. Polites. *An Assessment of the Technology of Automated Rendezvous and Capture in Space*. Tech. rep. 1998.

[73] M.E. Polites. “Technology of Automated Rendezvous and Capture in Space”. In: *Journal of Spacecraft and Rockets* 36.2 (1999), pp. 280–291.

[74] M. Ganet et al. “ATV GNC During Rendezvous with ISS”. In: *DCSSS Conference*. 2002.

[75] J. Tsukui et al. “Automatic Rendezvous to the International Space Station”. In: *Proceeding of the 7th International Symposium on Artificial Intelligence, Robotics and Automation in Space: i-SAIRAS*. 2003.

[76] Z. Jianping. “A Review of Tiangong-1/Shenzhou-8 Rendezvous and Docking Mission [J]”. In: *Manned Spaceflight* 1 (2012), p. 004.

[77] D.C. Woffinden and D.K. Geller. “Navigating the Road to Autonomous Orbital Rendezvous”. In: *Journal of Spacecraft and Rockets* 44.4 (2007), pp. 898–909.

[78] D.E. Hastings and C. Joppin. “On-orbit Upgrade and Repair: the Hubble Space Telescope Example”. In: *Journal of Spacecraft and Rockets* 43.3 (2006), pp. 614–625.

[79] E.N. Hartley. “A Tutorial on Model Predictive Control for Spacecraft Rendezvous”. In: *European Control Conference (ECC)*. 2015.

[80] L.S. Breger and J.P. How. “Safe Trajectories for Autonomous Rendezvous of Spacecraft”. In: *Journal of Guidance, Control, and Dynamics* 31.5 (2008), pp. 1478–1489.

[81] J.R. Wertz and R. Bell. “Autonomous Rendezvous and Docking Technologies: Status and Prospects”. In: *Space Systems Technology and Operations*. Vol. 5088. International Society for Optics and Photonics. 2003, pp. 20–31.

[82] ISECG. *International Deep Space Interoperability Standards*. Tech. rep. 2018.

[83] U. Eren et al. “Model Predictive Control in Aerospace Systems: Current State and Opportunities”. In: *Journal of Guidance, Control, and Dynamics* 40.7 (2017), pp. 1541–1566.

[84] M.J. Sidi. *Spacecraft Dynamics and Control: A Practical Engineering Approach*. Vol. 7. Cambridge university press, 2000.

[85] R.R. Bate, D.D. Mueller, and J.E. White. *Fundamentals of Astrodynamics*. Courier Corporation, 1971.

[86] W.H. Clohessy. “Terminal Guidance System for Satellite Rendezvous”. In: *Journal of the Aerospace Sciences* 27.9 (1960), pp. 653–658.

[87] J. Tschauner and P. Hempel. “Rendezvous Zu Einem in Elliptischer Bahn Umlaufenden Ziel”. In: *Astronautica Acta* 11.2 (1965).

[88] K. Yamanaka and F. Ankersen. “New State Transition Matrix for Relative Motion on an Arbitrary Elliptical Orbit”. In: *Journal of Guidance, Control, and Dynamics* 25.1 (2002), pp. 60–66.

[89] A.J. Sinclair, R.E. Sherrill, and T.A. Lovell. “Geometric Interpretation of the Tschauner–Hempel Solutions for Satellite Relative Motion”. In: *Advances in Space Research* 55.9 (2015), pp. 2268–2279.

[90] R.G. Melton. “Time-Explicit Representation of Relative Motion Between Elliptical Orbits”. In: *Journal of Guidance, Control, and Dynamics* 23.4 (2000), pp. 604–610.

[91] A. Imani and B. Beigzadeh. “Robust Control of Spacecraft Rendezvous on Elliptical Orbits: Optimal Sliding Mode and Backstepping Sliding Mode Approaches”. In: *Proceedings of the Institution of Mechanical Engineers, Part G: Journal of Aerospace Engineering* 230.10 (2016), pp. 1975–1989.

[92] R. Vazquez, F. Gavilan, and E.F Camacho. “Trajectory Planning for Spacecraft Rendezvous in Elliptical Orbits with On/Off Thrusters”. In: *IFAC Proceedings Volumes* 47.3 (2014), pp. 9703–9708.

[93] J.R. Wertz. *Spacecraft Attitude Determination and Control.* Vol. 73. Springer Science & Business Media, 2012.

[94] I. Harris and W. Priester. “Time-Dependent Structure of the Upper Atmosphere”. In: *Journal of the Atmospheric Sciences* 19.4 (1962), pp. 286–301.

[95] C.F. Harding. “Effect of Gravity Gradient Torque on the Motion of the Spin Axis of an Asymmetric Vehicle”. In: (1966).

[96] R.C. Domingos, R. Vilhena De Moraes, and A.F. Bertachini De Almeida Prado. “Third-Body Perturbation in the Case of Elliptic Orbits for the Disturbing Body”. In: *Mathematical Problems in Engineering* (2008).

[97] J.T. Betts. “Optimal Interplanetary Orbit Transfers by Direct Transcription”. In: *Journal of the Astronautical Sciences* 42.3 (1994), pp. 247–268.

[98] W.M. Folkner, J.G. Williams, and D.H. Boggs. “The Planetary and Lunar Ephemeris DE 421”. In: *JPL IOM 343R-08-003* (2008).

[99] R.H. Battin. *An Introduction to the Mathematics and Methods of Astrodynamics, Revised Edition.* American Institute of Aeronautics and Astronautics, 1999.

[100] N. Bloise et al. “Obstacle Avoidance with Potential Field Applied to a Rendezvous Maneuver”. In: *Applied Sciences* 7.10 (2017), p. 1042.

[101] N. Silva, F. Martel, and P. Delpy. “Automated Transfer Vehicle Thrusters Selection and Management Function”. In: *6th International ESA Conference on Guidance, Navigation and Control Systems.* 2006.

[102] D. Berthelier et al. “Automated Transfer Vehicle (ATV) Nominal Software GNC Numerical Validation Overview”. In: *6th International ESA Conference on Guidance, Navigation and Control Systems.* 2006.

[103] Y. Luo, J. Zhang, and G. Tang. “Survey of Orbital Dynamics and Control of Space Rendezvous”. In: *Chinese Journal of Aeronautics* 27.1 (2014), pp. 1–11.

[104] E. Capello et al. ““Flyable” Guidance and Control Algorithms for Orbital Rendezvous Maneuver”. In: *SICE Journal of Control, Measurement, and System Integration* 11.1 (2018), pp. 14–24.

[105] X. Yang and X. Cao. “A New Approach to Autonomous Rendezvous for Spacecraft with Limited Impulsive Thrust: Based on Switching Control Strategy”. In: *Aerospace Science and Technology* 43 (2015), pp. 454–462.

[106] R. Bevilacqua, J.S. Hall, and M. Romano. “Multiple Spacecraft Rendezvous Maneuvers by Differential Drag and Low Thrust Engines”. In: *Celestial Mechanics and Dynamical Astronomy* 106.1 (2010), p. 69.

[107] M. Dentis, E. Capello, and G. Guglieri. “A Novel Concept for Guidance and Control of Spacecraft Orbital Maneuvers”. In: *International Journal of Aerospace Engineering* 2016 (2016).

[108] L. Sun and W. Huo. “6-DOF Integrated Adaptive Backstepping Control for Spacecraft Proximity Operations”. In: *IEEE Transactions on Aerospace and Electronic Systems* 51.3 (2015), pp. 2433–2443.

[109] M. Leomanni et al. “An MPC-Based Attitude Control System for All-Electric Spacecraft with On/Off Actuators”. In: *IEEE 52nd Annual Conference on Decision and Control (CDC)*. IEEE. 2013, pp. 4853–4858.

[110] W. Yang, S. Li, and N. Li. “Station-Keeping Control Method for GEO Satellite Based on Relative Orbit Dynamics”. In: *11th World Congress on Intelligent Control and Automation (WCICA)*. IEEE. 2014, pp. 1682–1687.

[111] Q. Wang, J. Yuan, and Z. Zhu. “The Application of Error Quaternion and PID Control Method in Earth Observation Satellite’s Attitude Control System”. In: *1st International Symposium on Systems and Control in Aerospace and Astronautics*. IEEE. 2006.

[112] X. Chen et al. “Optimal Combined Reaction-Wheel Momentum Management for Earth-Pointing Satellites”. In: *Journal of Guidance, Control, and Dynamics* 22.4 (1999), pp. 543–550.

[113] D.Y. Lee et al. “Geometric Mechanics Based Nonlinear Model Predictive Spacecraft Attitude Control with Reaction Wheels”. In: *Journal of Guidance, Control, and Dynamics* 40.2 (2016), pp. 309–319.

[114] A. Sanyal, L. Holguin, and S.P. Viswanathan. “Guidance and Control for Spacecraft Autonomous Chasing and Close Proximity Maneuvers”. In: *IFAC Proceedings Volumes* 45.13 (2012), pp. 753–758.

[115] D. Perez and R. Bevilacqua. “Lyapunov-Based Spacecraft Rendezvous Maneuvers using Differential Drag”. In: *AIAA Guidance, Navigation, and Control Conference*. American Institute of Aeronautics and Astronautics, 2011.

[116] X. Yang and H. Gao. “Robust Reliable Control for Autonomous Spacecraft Rendezvous with Limited-Thrust”. In: *Aerospace Science and Technology* 24.1 (2013), pp. 161–168.

[117] L. Walker. “Automated Proximity Operations Using Image-Based Relative Navigation”. In: 2012.

[118] N. Chan and S. Mitra. “Verifying Safety of an Autonomous Spacecraft Rendezvous Mission”. In: *arXiv preprint arXiv:1703.06930* (2017).

[119] N. Chan and S. Mitra. "Verified Hybrid LQ Control for Autonomous Spacecraft Rendezvous". In: *IEEE 56th Annual Conference on Decision and Control (CDC)*. IEEE. 2017, pp. 1427–1432.

[120] L. Guarnaccia, R. Bevilacqua, and S.P. Pastorelli. "Suboptimal LQR-Based Spacecraft Full Motion Control: Theory and Experimentation". In: *Acta Astronautica* 122 (2016), pp. 114–136.

[121] R. Bevilacqua, T. Lehmann, and M. Romano. "Development and Experimentation of LQR/APF Guidance and Control for Autonomous Proximity Maneuvers of Multiple Spacecraft". In: *Acta Astronautica* 68.7-8 (2011), pp. 1260–1275.

[122] S.B. McCamish et al. "Flight Testing of Multiple-Spacecraft Control on SPHERES during Close-Proximity Operations". In: *Journal of Spacecraft and Rockets* 46.6 (2009), pp. 1202–1213.

[123] H. Gao, X. Yang, and P. Shi. "Multi-Objective Robust H_∞ Control of Spacecraft Rendezvous". In: *IEEE Transactions on Control Systems Technology* 17.4 (2009), pp. 794–802.

[124] C. Andrade et al. "Robust Control Applied Towards Rendezvous and Docking". In: *European Control Conference (ECC)*. IEEE. 2009, pp. 1854–1859.

[125] S.N. Wu et al. "Robust Control for Spacecraft Rendezvous with a Noncooperative Target". In: *The Scientific World Journal* 2013 (2013).

[126] G. Franzini, L. Pollini, and M. Innocenti. "H-Infinity Controller Design for Spacecraft Terminal Rendezvous on Elliptic Orbits using Differential Game Theory". In: *American Control Conference (ACC)*. IEEE. 2016, pp. 7438–7443.

[127] E. Capello et al. "Sliding-Mode Control Strategies for Rendezvous and Docking Maneuvers". In: *Journal of Guidance, Control, and Dynamics* 40.6 (2017), pp. 1481–1487.

[128] E. Capello, E. Punta, and G. Bartolini. "Simplex Sliding Mode Control Strategies for Spacecraft Rendezvous Maneuvers". In: *IFAC-PapersOnLine* 50.1 (2017), pp. 8496–8501.

[129] Q. Li, J. Yuan, and H. Wang. "Sliding Mode Control for Autonomous Spacecraft Rendezvous with Collision Avoidance". In: *Acta Astronautica* 151 (2018), pp. 743–751.

[130] A. Imani and B. Beigzadeh. "Robust Control of Spacecraft Rendezvous on Elliptical Orbits: Optimal Sliding Mode and Backstepping Sliding Mode Approaches". In: *Proceedings of the Institution of Mechanical Engineers, Part G: Journal of Aerospace Engineering* 230.10 (2016), pp. 1975–1989.

[131] Q. Zhan and V.G. Grassi. “An Industrial Approach to Implementing MPC in Speciality Chemical Plant”. In: *IFAC Proceedings Volumes* 32.2 (1999), pp. 6603–6608.

[132] V. Manikonda et al. “A Model Predictive Control-Based Approach for Spacecraft Formation Keeping and Attitude Control”. In: *American Control Conference (ACC).* Vol. 6. IEEE. 1999, pp. 4258–4262.

[133] A. Richards and J.P. How. “Model Predictive Control of Vehicle Maneuvers with Guaranteed Completion Time and Robust Feasibility”. In: *American Control Conference (ACC).* Vol. 5. IEEE. 2003, pp. 4034–4040.

[134] A. Richards and J. How. “Performance Evaluation of Rendezvous using Model Predictive Control”. In: *AIAA Guidance, Navigation, and Control Conference and Exhibit.* 2003, p. 5507.

[135] H. Park, S. Di Cairano, and I. Kolmanovsky. “Linear Quadratic Model Predictive Control Approach to Spacecraft Rendezvous and Docking”. In: *Proceedings of 21st AAS/AIAA Space Flight Mechanics Meeting, Spaceflight Mechanics, Part III of Advances in the Astronautical Sciences.* Vol. 140. 2011.

[136] H. Park, S. Di Cairano, and I. Kolmanovsky. “Model Predictive Control for Spacecraft Rendezvous and Docking with a Rotating/Tumbling Platform and for Debris Avoidance”. In: *American Control Conference (ACC).* IEEE. 2011, pp. 1922–1927.

[137] E.N. Hartley et al. “Model Predictive Control System Design and Implementation for Spacecraft Rendezvous”. In: *Control Engineering Practice* 20.7 (2012), pp. 695–713.

[138] R. Vazquez, F. Gavilan, and E.F. Camacho. “Model Predictive Control for Spacecraft Rendezvous in Elliptical Orbits with On/Off Thrusters”. In: *IFAC-PapersOnLine* 48.9 (2015), pp. 251–256.

[139] M. Saponara et al. “Model Predictive Control Application to Spacecraft Rendezvous in Mars Sample Return Scenario”. In: (2013).

[140] M. Leomanni, E. Rogers, and S.B. Gabriel. “Explicit Model Predictive Control Approach for Low-Thrust Spacecraft Proximity Operations”. In: *Journal of Guidance, Control, and Dynamics* 37.6 (2014), pp. 1780–1790.

[141] A. Weiss et al. “Model Predictive Control for Spacecraft Rendezvous and Docking: Strategies for Handling Constraints and Case Studies”. In: *IEEE Transactions on Control Systems Technology* 23.4 (2015), pp. 1638–1647.

[142] M. Cannon and B. Kouvaritakis. *Model Predictive Control—Classical, Robust and Stochastic.* Springer: New York, NY, USA, 2016.

[143] F. Gavilan, R. Vazquez, and E.F. Camacho. “Robust Model Predictive Control for Spacecraft Rendezvous with Online Prediction of Disturbance Bounds”. In: (2011).

[144] A.T. Schwarm and M. Nikolaou. “Chance-Constrained Model Predictive Control”. In: *AIChE Journal* 45.8 (1999), pp. 1743–1752.

[145] F. Gavilan, R. Vazquez, and E.F. Camacho. “Chance-Constrained Model Predictive Control for Spacecraft Rendezvous with Disturbance Estimation”. In: *Control Engineering Practice* 20.2 (2012), pp. 111–122.

[146] S. Zhu et al. “Robust Model Predictive Control for Multi-Step Short Range Spacecraft Rendezvous”. In: *Advances in Space Research* 62.1 (2018), pp. 111–126.

[147] M. Farina, L. Giulioni, and R. Scattolini. “Stochastic Linear Model Predictive Control with Chance Constraints-A Review”. In: *Journal of Process Control* 44 (2016), pp. 53–67.

[148] J.M. Grosso et al. “Chance-Constrained Model Predictive Control for Drinking Water Networks”. In: *Journal of Process Control* 24.5 (2014), pp. 504–516.

[149] H.A. Nasir, A. Carè, and E. Weyer. “A Randomised Approach to Flood Control using Value-at-Risk”. In: *2015 IEEE 54th Annual Conference on Decision and Control (CDC)*. IEEE. 2015, pp. 3939–3944.

[150] D. Van Hessem and O. Bosgra. “Stochastic Closed-Loop Model Predictive Control of Continuous Nonlinear Chemical Processes”. In: *Journal of Process Control* 16.3 (2006), pp. 225–241.

[151] R.M. Vignali et al. “Energy Management of a Building Cooling System with Thermal Storage: An Approximate Dynamic Programming Solution”. In: *IEEE Transactions on Automation Science and Engineering* 14.2 (2017), pp. 619–633.

[152] L. Blackmore, M. Ono, and B.C. Williams. “Chance-Constrained Optimal Path Planning with Obstacles”. In: *IEEE Transactions on Robotics* 27.6 (2011), pp. 1080–1094.

[153] R. Tempo, G.C. Calafiore, and F. Dabbene. *Randomized Algorithms for Analysis and Control of Uncertain Systems: with Applications*. Springer Science & Business Media, 2012.

[154] G.C. Calafiore and M.C. Campi. “The Scenario Approach to Robust Control Design”. In: *IEEE Transactions on Automatic Control* 51.5 (2006), pp. 742–753.

[155] G. Schildbach et al. "The Scenario Approach for Stochastic Model Predictive Control with Bounds on Closed-Loop Constraint Violations". In: *Automatica* 50.12 (2014), pp. 3009–3018.

[156] D.Q. Mayne, M.M. Seron, and S.V. Raković. "Robust Model Predictive Control of Constrained Linear Systems with Bounded Disturbances". In: *Automatica* 41.2 (2005), pp. 219–224.

[157] L. Chisci, J.A. Rossiter, and G. Zappa. "Systems with Persistent Disturbances: Predictive Control with Restricted Constraints". In: *Automatica* 37.7 (2001), pp. 1019–1028.

[158] S.V. Raković et al. "Homothetic Tube Model Predictive Control". In: *Automatica* 48.8 (2012), pp. 1631–1638.

[159] J.B. Rawlings and D.Q. Mayne. *Model Predictive Control: Theory and Design.* Nob Hill Pub. Madison, Wisconsin, 2009.

[160] D.Q. Mayne. "Model Predictive Control: Recent Developments and Future Promise". In: *Automatica* 50.12 (2014), pp. 2967–2986.

[161] M. Lorenzen et al. "Scenario-based Stochastic MPC with Guaranteed Recursive Feasibility". In: *2015 IEEE 54th Annual Conference on Decision and Control (CDC).* IEEE. 2015, pp. 4958–4963.

[162] M. Lorenzen et al. "Stochastic MPC with Offline Uncertainty Sampling". In: *Automatica* 81 (2017), pp. 176–183.

[163] M. Lorenzen et al. "An Improved Constraint-Tightening Approach for Stochastic MPC". In: *American Control Conference (ACC).* IEEE. 2015, pp. 944–949.

[164] M. Lorenzen et al. "Constraint-Tightening and Stability in Stochastic Model Predictive Control". In: *IEEE Transactions on Automatic Control* 62.7 (2017), pp. 3165–3177.

[165] G.C. Calafiore. "On the Expected Probability of Constraint Violation in Sampled Convex Programs". In: *Journal of Optimization Theory and Applications* 143.2 (2009), pp. 405–412.

[166] G. Schildbach, L. Fagiano, and M. Morari. "Randomized Solutions to Convex Programs with Multiple Chance Constraints". In: *SIAM Journal on Optimization* 23.4 (2013), pp. 2479–2501.

[167] D.P. Bertsekas and I.B. Rhodes. "On the Minimax Reachability of Target Sets and Target Tubes". In: *Automatica* 7.2 (1971), pp. 233–247.

[168] D.P. Bertsekas. *Dynamic Programming and Optimal Control.* Academic Press, New York, 1976.

[169] A.C. Bartlett, C.V. Hollot, and H. Lin. “Root Locations of an Entire Polytope of Polynomials: It Suffices to Check the Edges”. In: *Mathematics of Control, Signals and Systems* 1.1 (1988), pp. 61–71.

[170] B.R. Barmish and E.I. Jury. “New Tools for Robustness of Linear Systems”. In: *IEEE Transactions on Automatic Control* 39.12 (1994), pp. 2525–2525.

[171] SV Rakovic and KI Kouramas. “The Minimal Robust Positively Invariant Set for Linear Discrete Time Systems: Approximation Methods and Control Applications”. In: *45th IEEE Conference on Decision and Control (CDC).* IEEE. 2006, pp. 4562–4567.

[172] S.V. Rakovic et al. “Approximation of the Minimal Robustly Positively Invariant Set for Discrete-Time LTI Systems with Persistent State Disturbances”. In: *42nd IEEE Conference on Decision and Control (CDC).* Vol. 4. IEEE. 2003, pp. 3917–3918.

[173] H. Niederreiter. *Random Number Generation and Quasi-Monte Carlo Methods.* Vol. 63. Siam, 1992.

[174] G.C. Calafiore and L. Fagiano. “Stochastic Model Predictive Control of LPV Systems via Scenario Optimization”. In: *Automatica* 49.6 (2013), pp. 1861–1866.

[175] G.C. Calafiore and M.C. Campi. “The Scenario Approach to Robust Control Design”. In: *IEEE Transactions on Automatic Control* 51.5 (2006), pp. 742–753.

[176] M. Vidyasagar. *Learning and Generalisation: with Applications to Neural Networks.* Springer Science & Business Media, 2013.

[177] *Active Thermal Control System (ATCS) Overview.* Tech. rep. Boeing.

[178] Vicon Motion Systems Limited. *Vicon Tracker User Guide.* Tech. rep. 2016.

[179] R. Zappulla, J. Virgili-Llop, and M. Romano. “Spacecraft Thruster Control via Sigma–Delta Modulation”. In: *Journal of Guidance, Control, and Dynamics* 40.11 (2017), pp. 2928–2933.

[180] R. Zappulla et al. “Dynamic Air-Bearing Hardware-In-the-Loop Testbed to Experimentally Evaluate Autonomous Spacecraft Proximity Maneuvers”. In: *Journal of Spacecraft and Rockets* 54.4 (2017), pp. 1–15.

[181] G.C. Calafiore and L. Fagiano. “Robust Model Predictive Control via Scenario Optimization”. In: *IEEE Transactions on Automatic Control* 58.1 (2012), pp. 219–224.

[182] CPLEX User’s Manual. *IBM ILOG CPLEX Optimization Studio, Version 12, Release 6.* Tech. rep. 2015.

[183] MOSEK ApS. *MOSEK FAQ, Release 8.1.0.42.* Tech. rep. 2018.

[184] Gurobi Optimization, Inc. *GUROBI Optimizer Reference Manual, Version 7.5.* Tech. rep. 2017.

[185] Y. Wang and S. Boyd. "Fast Model Predictive Control using Online Optimization". In: *IEEE Transactions on Control Systems Technology* 18.2 (2010), pp. 267–278.

[186] J. Currie, A. Prince-Pike, and D.I. Wilson. "Auto-Code Generation for Fast Embedded Model Predictive Controllers". In: *Proceedings of International Conference Mechatronics and Machine Vision in Practice.* 2012.

[187] S.J. Wright. *Applying New Optimization Algorithms to Model Predictive Control.* Tech. rep. 1996.

[188] J. Mattingley and S. Boyd. "CVXGEN: A Code Generator for Embedded Convex Optimization". In: *Optimization and Engineering* 13.1 (2012), pp. 1–27.

[189] M. Nagahara, J. Østergaard, and D.E. Quevedo. "Discrete-Time Hands-Off Control by Sparse Optimization". In: *EURASIP Journal on Advances in Signal Processing* 2016.1 (2016), p. 76.

[190] R. Li and Y.J. Shi. "The Fuel Optimal Control Problem of a Hypersonic Aircraft with Periodic Cruising Mode". In: *Mathematical and Computer Modelling* 55.11-12 (2012), pp. 2141–2150.

[191] A. L'Afflitto and W.M. Haddad. "A Variational Approach to the Fuel Optimal Control Problem for UAV Formations". In: *Recent Advances in Aircraft Technology (R. Agarwal, ed.), Boston, MA: InTech* (2012).

[192] E.N. Hartley, M. Gallieri, and J.M. Maciejowski. "Terminal Spacecraft Rendezvous and Capture with LASSO Model Predictive Control". In: *International Journal of Control* 86.11 (2013), pp. 2104–2113.

[193] J. Lofberg. "YALMIP: A Toolbox for Modeling and Optimization in MATLAB". In: *IEEE International Symposium on Computer Aided Control Systems Design.* IEEE. 2004, pp. 284–289.

[194] S. Singh, M. Pavone, and J.E. Slotine. "Tube-Based MPC : a Contraction Theory Approach". In: 2016.

[195] K.P. Valavanis and G.J. Vachtsevanos. *Handbook of Unmanned Aerial Vehicles.* Springer Netherlands, 2015.

[196] E.L. Pastor, J. Lopez, and P. Royo. "A Hardware/Software Architecture for UAV Payload and Mission Control". In: *Proceedings of IEEE/AIAA Conference on Digital Avionics Systems* (2006).

[197] E. Capello et al. "Preliminary Assessment of Flying and Handling Qualities for mini-UAVs". In: *Journal of Intelligent and Robotic Systems* 65.1 (2012), pp. 43–61.

[198] B. Etkin and L. Reid. *Dynamics of Flight: Stability and Control.* New York: John Wiley and Sons, 1996.

[199] G.D. Padfield. *Helicopter Flight Dynamics: The Theory and Application of Flying Qualities and Simulation Modeling.* AIAA education series. American Institute of Aeronautics and Astronautics, 1996.

[200] E. Capello, G. Guglieri, and G. Ristorto. "Guidance and Control Algorithms for Mini-UAV Autopilots". In: *Aircraft Engineering and Aerospace Technology* 89.1 (2017), pp. 133–144.

[201] G. Vallabha. *Real-Time Pacer for Simulink.* 2016. URL: `https://it.mathworks.com/matlabcentral/fileexchange/29107-real-time-pacer-for-simulink` (visited on 04/24/2018).

[202] L. Novaro Mascarello, F. Quagliotti, and G. Ristorto. "A Feasibility Study of an Harmless Tiltrotor for Smart Farming Applications". In: *Proceedings of International Conference on Unmanned Aircraft Systems (ICUAS).* 2017.

[203] M. Mammarella et al. "A Sustainable Bridge between Low Earth Orbits and Cislunar Infrastructures: the Lunar Space Tug". In: *Proceedings of 67th International Astronautical Congress (IAC).* 2016.

[204] M. Mammarella et al. "How the Lunar Space Tug can Support the Cislunar Station". In: *10th IAA Symposium on the Future of Space Exploration: Towards the Moon Village and Beyond.* 2017.

[205] M. Mammarella et al. "The Lunar Space Tug: A Sustainable Bridge between Low Earth Orbits and the Cislunar Habitat". In: *Acta Astronautica* 138 (2017), pp. 102–117.

[206] M. Mammarella, G. Guglieri, and N. Viola. "Missions, Architectures and Technologies for a Lunar Space Tug in Support of Cislunar Infrastructures". In: *Proceedings of 68th International Astronautical Congress (IAC).* 2017.

[207] M. Mammarella et al. "The Lunar Space Tug in the Future Space Exploration Scenario". In: *Proceedings of 68th International Astronautical Congress (IAC).* 2017.

[208] M. Mammarella et al. "Electric Propulsion for High-Power Deep Space Transportation System: Investigation on Mutual Influences and Preliminary Sizing". In: *Proceedings of 68th International Astronautical Congress (IAC).* 2017.

[209] M. Mammarella et al. "Mission Scenarios for High-Power Electric Platforms". In: *Proceedings of Space Propulsion 2018.* 2018.

[210] M. Mammarella, P.M. Vernicari, and N. Viola. "Design and Cost Analysis of High-Power Solar Electric Propulsion Platforms". In: *Proceeding of Space Propulsion 2018.* 2018.

[211] M. Mammarella et al. “How the Lunar Space Tug Can Support the Cislunar Station”. In: *Acta Astronautica* (2018).

[212] M. Mammarella et al. “Electric Propulsion, an Enabling Technology for the Deep Space Gateway”. In: *Proceedings of AIAA SPACE 2018*. 2018.

[213] M. Mammarella, E. Capello, and G. Guglieri. “Robust Model Predictive Control for Automated Rendezvous Maneuvers in Near-Earth and Moon Proximity”. In: *Proceedings of AIAA SPACE 2018*. 2018.

[214] M. Mammarella. “Guidance and Control Algorithms for Space Rendezvous and Docking Maneuvers”. In: *Proceedings of Pegasus-AIAA Student Conference*. 2016.

[215] M. Mammarella, E. Capello, and G. Guglieri. “A Comprehensive Analysis of Guidance and Control Algorithms for Orbital Rendezvous Maneuvers”. In: *Proceedings of AIAA SPACE 2016*. 2016.

[216] M. Mammarella et al. “Spacecraft Proximity Operations Via Tube-Based Robust Model Predictive Control with Additive Disturbances”. In: *Proceedings of 68th International Astronautical Congress (IAC)*. 2017.

[217] M. Mammarella et al. “A General Sampling-Based SMPC Approach to Spacecraft Proximity Operations”. In: *Proceedings of 56th IEEE Conference on Decision and Control 2017*. 2017.

[218] M. Mammarella et al. “Tube-Based Robust Model Predictive Control for Spacecraft Proximity Operations in the Presence of Persistent Disturbance”. In: *Aerospace Science and Technology* 77 (2018), pp. 585–594.

[219] M. Mammarella et al. “Attitude Control of a Small Spacecraft for Earth Observation via Tube-based Robust Model Predictive Control”. In: *Proceedings of AIAA SPACE 2018*. 2018.

[220] M. Mammarella et al. “An Offline-Sampling SMPC Framework with Application to Autonomous Space Maneuvers”. In: *IEEE Transactions on Control Systems Technology* (2018).

[221] Martina Mammarella et al. “An Offline-Sampling SMPC Framework with Application to Automated Space Maneuvers”. In: *arXiv preprint arXiv:1803.01652* (2018).

[222] M. Mammarella et al. “How to Sustain the Deep Space Gateway with Reusable High-Power Electric Platforms”. In: *Proceedings of AIAA SPACE 2018*. 2018.

[223] C.A. Paissoni et al. “Deep Space transportation enhanced by 20kW-class Hall Effect Thruster”. In: *Proceedings of 69th International Astronautical COngress (IAC)*. 2018.

[224] M. Mammarella et al. “A 20kW-class Hall Effect Thruster to Enhance Present and Future Space Missions”. In: *Proceedings of 69th International Astronautical COngress (IAC)*. 2018.

[225] M. Mammarella and E. Capello. “A Robust MPC-Based Autopilot for Mini UAVs”. In: *Proceedings of International Conference on Unmanned Aircraft Systems (ICUAS)*. 2018.

[226] M. Mammarella et al. “Sample-Based SMPC for Tracking Control of Fixed-Wing UAV”. In: *IEEE Control Systems Letters* (2018).

[227] M. Mammarella, E. Capello, and F. Dabbene. “Sample-Based SMPC for Tracking Control of Fixed-Wing UAV: Multi-Scenario Mapping”. In: *arXiv preprint arXiv:1805.05879* (2018).

This Ph.D. thesis has been typeset by means of the TEX-system facilities. The typesetting engine was pdfLATEX. The document class was `toptesi`, by Claudio Beccari, with option `tipotesi=scudo`. This class is available in every up-to-date and complete TEX-system installation.